

博士論文

**Tailoring SWCNTs and MoS<sub>2</sub> based nanomaterials  
for application in photovoltaic devices**

(光電変換デバイス応用に向けた単層 CNT 及び  
MoS<sub>2</sub> 由来ナノ材料の開発)

銭 洋

**Tailoring SWCNTs and MoS<sub>2</sub> based nanomaterials  
for application in photovoltaic devices**  
(光電変換デバイス応用に向けた単層 CNT 及び  
MoS<sub>2</sub> 由来ナノ材料の開発)

**Yang QIAN**

銭 洋

A dissertation presented in partial fulfillment of  
the requirements for the degree of  
**Doctor of Philosophy**

東京大学大学院工学系研究科機械工学専攻

Department of Mechanical Engineering

The University of Tokyo

August 2019

# Contents

<b>Contents</b> .....	<b>i</b>
<b>Abstract</b> .....	<b>vii</b>
<b>List of Figures</b> .....	<b>xiii</b>
<b>List of Tables</b> .....	<b>xx</b>
<b>Terminology</b> .....	<b>xxi</b>
<b>Chapter 1 General Introduction</b> .....	<b>1</b>
1.1 World of Low-Dimensional Nanomaterials.....	1
1.2 SWCNTs.....	3
1.2.1 Atomic Structure of SWCNTs.....	3
1.2.2 Structure-Related Properties of SWCNTs .....	5
1.3 Low-Dimensional MoS <sub>2</sub> .....	10
1.3.1 Atomic Structure of MoS <sub>2</sub> .....	11
1.3.2 Structure-Related Properties of MoS <sub>2</sub> .....	12
1.4 Renewable Energy Resources .....	14
1.5 Solar Cells .....	17
1.6 Development of Next-Generation Solar Cells.....	20
1.7 Application of Low-Dimensional Nanomaterials in Solar Cells.....	22

## Contents

---

1.8	Motivation and Purpose of this Dissertation .....	26
1.9	Organization of this Dissertation .....	28
<b>Chapter 2</b>	<b>General Experimental Methodology .....</b>	<b>30</b>
2.1	Metrology of Low-Dimensional Nanomaterials.....	30
2.1.1	SEM.....	30
2.1.2	TEM.....	31
2.1.3	Raman Spectroscopy .....	33
2.1.3.1	Raman Spectroscopy of SWCNTs.....	35
2.1.3.2	Raman Spectroscopy of MoS <sub>2</sub> .....	36
2.1.4	PL .....	38
2.1.5	UV-Vis-NIR Spectroscopy .....	39
2.1.6	XPS.....	40
2.2	Metrology of Nanomaterial Solar Cells .....	42
2.2.1	<i>J-V</i> Characterizations.....	42
2.2.2	Four-Point Probe Measurement.....	44
2.3	SWCNT-Si Solar Cells .....	47
2.3.1	Synthesis of SWCNT Film.....	47
2.3.2	Fabrication of SWCNT-Si Solar Cells.....	50
2.3.3	Performance of Pristine SWCNT-Si Solar Cells .....	54
2.4	Synthesis of MoS <sub>2</sub> .....	57

## Contents

---

2.4.1	LPCVD System .....	57
2.4.2	Reactions during CVD Process .....	59
<b>Chapter 3 Multifunctional Effect of <i>p</i>-Doping, Anti-Reflection, and Encapsulation by Polymeric Acid for High-Efficiency and Stable SWCNT-Si Solar Cells .....</b>		<b>61</b>
3.1	Literature Review and Introduction.....	61
3.2	Experimental Methods.....	63
3.2.1	Preparation of Dopant.....	63
3.2.2	Characterizations .....	64
3.3	SWCNT-Si Solar Cells with Record-High Efficiency and Stability .....	65
3.3.1	<i>J-V</i> Characteristics .....	65
3.3.2	Characterization of Stability in various Environments .....	66
3.3.3	Record-High Stable Efficiency.....	69
3.4	Mechanism Discussions .....	71
3.4.1	Anti-Reflection Mechanism of Nafion for SWCNT-Si Solar Cells ...	71
3.4.2	<i>p</i> -Doping Mechanism of Nafion for SWCNT-Si Solar Cells .....	79
3.5	Summary.....	89
<b>Chapter 4 Controlled Synthesis of SWCNTs and MoS<sub>2</sub> based Nanomaterials and their Application in Photovoltaic Devices.....</b>		<b>90</b>
4.1	Controlled Synthesis of 2D MoS <sub>2</sub> .....	90
4.1.1	Literature Review and Introduction.....	90

## Contents

---

4.1.1.1	Review of Top-Down Approach .....	90
4.1.1.2	Review of Bottom-Up Approach .....	91
4.1.1.3	Introduction.....	93
4.1.2	Controlled Synthesis of Monolayer MoS <sub>2</sub> .....	95
4.1.2.1	Effect of Substrate Preparation Method.....	96
4.1.2.2	Effect of Carrier Gas Flow Rate .....	97
4.1.2.3	Effect of Sulfur Evaporation Temperature.....	98
4.1.2.4	Effect of MoO <sub>3</sub> Sublimation and Growth Temperature .....	99
4.1.2.5	Effect of Growth Duration and MoO <sub>3</sub> Amount.....	100
4.1.2.6	Continuous Monolayer MoS <sub>2</sub> Film.....	101
4.1.3	Summary.....	102
4.2	Controlled Synthesis of 1D SWCNTs and MoS <sub>2</sub> based vdW Heterostructures.....	104
4.2.1	Literature Review and Introduction.....	104
4.2.2	Experimental Methods.....	105
4.2.3	Synthesis Results .....	107
4.2.3.1	MoS <sub>2</sub> NT-SWCNT 1D vdW Heterostructure.....	107
4.2.3.2	MoS <sub>2</sub> NT-BNNT-SWCNT 1D vdW Heterostructure.....	110
4.2.4	Summary.....	112
4.3	Application of SWCNTs and MoS <sub>2</sub> based Nanomaterials in Photovoltaic	

## Contents

---

Devices .....	114
4.3.1 Literature Review and Introduction.....	114
4.3.2 MoS <sub>2</sub> NT as Light-Absorbing Layer in Photovoltaic Devices .....	115
4.3.2.1 C <sub>60</sub> -MoS <sub>2</sub> NT-SWCNT Device Performance.....	117
4.3.2.2 C <sub>60</sub> -SWCNT Device Performance .....	118
4.3.2.3 C <sub>60</sub> -MoS <sub>2</sub> NT-BNNT-SWCNT Device Performance.....	119
4.3.2.4 Mechanism Discussions.....	120
4.3.3 MoS <sub>2</sub> NT-SWCNT as Electron Transport Layer and Cathode in Perovskite Solar Cells.....	121
4.3.3.1 MoS <sub>2</sub> NT-SWCNT Device Performance .....	123
4.3.3.2 MoS <sub>2</sub> NT-BNNT-SWCNT Device Performance.....	123
4.3.3.3 Mechanism Discussions.....	125
4.3.4 MoS <sub>2</sub> NT-SWCNT as Hole Transport Layer and Anode in Perovskite Solar Cells .....	126
4.3.4.1 Device Performance.....	127
4.3.4.2 Mechanism Discussions.....	128
4.3.5 Summary.....	129
<b>Chapter 5 Closing Remarks.....</b>	<b>131</b>
5.1 Summaries of this Dissertation.....	131
5.2 Vision for Next-Generation Solar Cells.....	133

## Contents

---

5.3 Future Perspectives of this Dissertation .....	136
<b>Bibliography.....</b>	<b>137</b>
<b>Appendix .....</b>	<b>152</b>
<b>Publication List.....</b>	<b>156</b>
<b>Acknowledgments.....</b>	<b>160</b>

# Abstract

### 1. Introduction and motivation of this dissertation

As energy is closely related to our human society development, how to obtain energy and how to guarantee sufficient energy have become important issues for a long time. Traditional energy sources such as fossil fuels and nuclear energy suffer from the significant issues of shortage, pollution, and unsafety. In order to solve these issues, renewable energy has attracted much attention in recent years, within which the solar energy has been regarded as a promising next-generation energy source. Photovoltaic (PV) devices, especially solar cells, which are used to cultivate solar energy, are being vibrantly developed. Although several kinds of solar cells have achieved high efficiency of over 20%, the current issues in these solar cells include high cost, inflexibility, heavyweight, and so on. There is an urgent need for the development of next-generation PV devices.

On the other hand, the diversity of low-dimensional nanomaterials has been enriched by both the dimensionalities and new compounds. The 1-dimensional (1D) single-walled carbon nanotube (SWCNT) and 2-dimensional (2D) MoS<sub>2</sub> are both the representatives of their dimensions and elements, with excellent physical, chemical, and mechanical properties. Moreover, the diversity of low-dimensional nanomaterial world has also been enriched by the method of "tailoring". As the properties of these materials can be tuned by carrier doping and structural transformation, we can develop different tailoring methods for different application purposes, such as nanomaterial PV devices. For PV

device applications, the low-dimensional nanomaterials can reduce the usage of high-cost materials, and they have tunable physical properties with flexible and lightweight nature. These advantages enable them to be promising candidates for next-generation PV devices.

### **2. Purpose of this dissertation**

This dissertation focuses on the tailoring methods of SWCNTs and MoS<sub>2</sub> based nanomaterials for the application purpose of PV devices, especially solar cells.

The SWCNT transparent conductive film (TCF) in SWCNT-Si solar cells is one of the crucial factors for improving performance. Both the conductivity and transmittance of SWCNT film need to be high in order to have excellent performance in SWCNT-Si solar cells, but this always includes a trade-off. Moreover, SWCNT shows a hole-transporting property in solar cells, which is tunable by carrier doping. As a result, the first purpose of this dissertation is to explore novel and outstanding tailoring methods for SWCNT TCF, and to apply the tailored SWCNT TCF to SWCNT-Si solar cells to achieve higher performance than the state of the art. Furthermore, this process can shed some light on the mechanisms of SWCNT-Si solar cells.

The second purpose of this dissertation is to explore the possibility of applying SWCNTs and MoS<sub>2</sub> based nanomaterials in PV devices. Although MoS<sub>2</sub> only has a thickness of nanometer level, its light-absorbing efficiency has been calculated to be about one order of magnitude higher than that of traditional PV materials. Thus, using MoS<sub>2</sub> as the light-absorbing material in PV devices can have the advantages of cost-reduction, flexible applications, and gaining insights for developing low-dimensional nanomaterial PV devices. On the other hand, MoS<sub>2</sub> may also contribute to other functional layers of solar cells after tailoring. In order to achieve the second purpose, tailoring

SWCNTs and MoS<sub>2</sub> based nanomaterials by synthesis and structural transformation methods are discussed in this dissertation, as well as the application of the synthesized SWCNTs and MoS<sub>2</sub> based nanomaterials in PV devices.

### **3. Organization and contents of this dissertation**

In Chapter 1, this dissertation begins with a brief introduction of the world of low-dimensional nanomaterials, followed by the discussions of the structures and structure-related properties of SWCNTs and MoS<sub>2</sub>, which are the two basic low-dimensional nanomaterials that this dissertation focuses on. Then, renewable energy resources are introduced, with a specific emphasis on solar cells for solar energy harvesting. Subsequently, the development of next-generation solar cells is discussed, of which the nanomaterial solar cells are the applications that this dissertation studies for low-dimensional nanomaterials. The application of low-dimensional nanomaterials in solar cells are introduced in a general manner, with the detailed and specific introductions provided in the following experimental chapters. The motivation and purpose of this dissertation are also introduced in Chapter 1.

The general experimental methodology is introduced in Chapter 2. The first part is about the metrology for the low-dimensional nanomaterials and nanomaterial solar cells, with the discussions of the mechanisms of these methods. The second part is about the fabrication of SWCNT-Si solar cells and the properties of the as-fabricated pristine SWCNT-Si solar cells. We applied the randomly-oriented SWCNT films that can be dry-transferred onto arbitrary substrates. The pristine SWCNT-Si solar cell showed the best power conversion efficiency (PCE) with 90%-transparency SWCNT film and was stable in air for over one month. The third part is about the structure of a semi-automated low-

## Abstract

---

pressure chemical vapor deposition (LPCVD) system that I constructed for synthesizing MoS<sub>2</sub> based nanomaterials, and about the reactions during the CVD process. The specific experimental methodology will be introduced in the following experimental chapters.

Chapter 3 presents the results of tailoring SWCNTs for application in SWCNT-Si solar cells. We report a polymeric acid, which can induce a multi-effect of permanent and strong *p*-doping, anti-reflection, and encapsulation of SWCNT-Si solar cells. Nafion, the polymeric acid was reported to dope carbon electrodes effectively and exhibit a permanent doping effect in organic light-emitting devices and organic solar cells. Interestingly, when Nafion was used in SWCNT-Si solar cells to dope the SWCNT top electrode, its effect was not only limited to a *p*-dopant but led to a favorable anti-reflection effect and an encapsulation effect as well. The device PCE increased from 9.5% to 14.4% owing to the increases in all the three photovoltaic parameters, specifically, short-circuit current density ( $J_{SC}$ ), open-circuit voltage ( $V_{OC}$ ), and fill factor (FF) upon a simple spin-coating of the polymeric acid. The increase in  $J_{SC}$  came from the inaugurated light absorption from the anti-reflection effect as evidenced by both empirical and computational analyses in this work. The anti-reflection effect was greater than that of PMMA owing to the intrinsically low refractive index of Nafion. The improvement in FF came from the improved conductivity of SWCNT films by the strong *p*-doping of the polymeric acid. There was a significant increase in  $V_{OC}$  as well, which is attributed to the strong Fermi level downshift and the densification effect of SWCNTs, thanks to the highly electronegative fluorinated chains and the viscous nature of the polymeric acid, respectively. The polymeric acid functioned as an excellent encapsulation layer as well. The polymeric acid-coated SWCNT-Si solar cells withstood submersion to chloroform, HNO<sub>3</sub>, and water for more than 10 days, which was by far more stable than the PMMA-

## Abstract

---

coated SWCNT-Si solar cells. The obtained stable PCE of 14.4% currently stands the highest among the reported carbon nanotube-based Si solar cells with similar active areas.

In Chapter 4, the investigations of tailoring SWCNT and MoS<sub>2</sub> based nanomaterials and their application to PV devices are discussed. First, the results of the controlled synthesis of 2D MoS<sub>2</sub> nanomaterials are presented. Through the LPCVD system that I constructed, a 2D MoS<sub>2</sub> monolayer film with over 99% coverage was synthesized after tuning various synthesis parameters to the optimal conditions. Second, we tried to synthesize 1D MoS<sub>2</sub> nanotube (MoS<sub>2</sub>NT) onto 1D nanostructures. With the optimized synthesis parameters for 2D MoS<sub>2</sub> monolayer film, a heterostructure of an SWCNT wrapped with a single-walled MoS<sub>2</sub>NT has been discovered, which is also the first evidence of a single-walled MoS<sub>2</sub>NT. Furthermore, with the heterostructure of 1D boron nitride nanotube (BNNT)-SWCNT, a novel type of 1D semiconductor-insulator-metal (MIS) van der Waals (vdW) heterostructure of MoS<sub>2</sub>NT-BNNT-SWCNT has been synthesized with MoS<sub>2</sub>NT as the semiconducting tubular layer. Third, the possibility of applying the as-synthesized SWCNTs and MoS<sub>2</sub> based nanomaterials in PV devices are discussed with various device structures. For the light-absorbing layer function, C<sub>60</sub>-MoS<sub>2</sub>NT-BNNT-SWCNT PV device showed higher photocurrent than that of C<sub>60</sub>-MoS<sub>2</sub>NT-SWCNT because of the charge separation facilitation of BNNT. For the electron transport layer (ETL) and cathode multifunction, we have substituted two layers of PCBM and SWCNT in inverted-type perovskite solar cells with one multifunctional layer of MoS<sub>2</sub>NT-(BNNT)-SWCNT. The integration of ETL and cathode in one layer can allow easier fabrication than the layer-stacking, and thus reduce the size of the device and the amount of used materials. The BNNT again facilitated the charge separation, resulting in the improvement of  $V_{OC}$  and PCE. Moreover, there is a trade-off between the tunneling

and blocking effects of BNNT for electrons and holes. For the hole transport layer (HTL) and anode multifunction, MoS<sub>2</sub>NT-SWCNT was applied to normal-type perovskite solar cells and improved the PCE by the excellent hole-extraction ability of MoS<sub>2</sub>NT. A PCE of 15.0% has been achieved after the application of spiro-MeOTAD. These results have demonstrated prototypes for the promising application of 1D vdW heterostructures in PV devices.

Finally, the summaries, my vision for next-generation solar cells, and the future perspectives of the research in this dissertation are presented in Chapter 5.

#### **4. Conclusions and future perspectives of this dissertation**

First, SWCNT film has been tailored by Nafion to improve SWCNT-Si solar cell performance successfully. The performance of SWCNT-Si solar cell has been improved to record-high efficiency and stability. Mechanism discussions show that Nafion has the superior multifunction of *p*-type doping, anti-reflection, and encapsulation.

Second, MoS<sub>2</sub> monolayer film has been synthesized by a home-made LPCVD system. A heterostructure of an SWCNT wrapped with a single-walled MoS<sub>2</sub>NT has been discovered, which is also the first evidence of a single-walled MoS<sub>2</sub>NT. Furthermore, a 1D MIS vdW heterostructure of MoS<sub>2</sub>NT-BNNT-SWCNT has been synthesized for the first time.

Third, the MoS<sub>2</sub>NT-BNNT-SWCNT 1D vdW heterostructures have shown promising applications in PV devices with different multifunctions of light-absorbing layer, ETL/cathode, and HTL/anode. The further improvements of the tailoring methods and the device structures will lead to novel applications of both the SWCNT and MoS<sub>2</sub> based nanomaterials and the 1D vdW heterostructures in PV devices.

## List of Figures

Figure 1.1 Schematics of low-dimensional nanomaterials. (a) 0D fullerene. (b) 1D SWCNT. (c) 2D graphene. (d) 2D MoS<sub>2</sub>, which is a representative of TMDCs. (a), (b), and (c) are reproduced from <http://www.photon.t.u-tokyo.ac.jp>. (d) is reprinted from [7], Copyright (2011), with permission from Nature Publishing Group. .... 2

Figure 1.2 Unrolled hexagonal lattice of an SWCNT. The chiral vector  $C_h$  and translational vector  $T$  are presented for the case of  $C_h = 4a_1 + 2a_2$  SWCNT. The angle between  $a_1$  and  $C_h$  gives the chiral angle  $\theta$  ( $0 \leq \theta \leq 30^\circ$ ). .... 3

Figure 1.3 (a) Real lattice space of graphene. A unit cell is shown as a blue dashed rhombus with two carbon atoms (A and B).  $a_1$  and  $a_2$  are unit vectors. (b) Reciprocal lattice space of graphene. The grey hexagonal area is the first Brillouin zone.  $b_1$  and  $b_2$  are unit vectors. .... 6

Figure 1.4 (a) 3D band structure of graphene. Reproduced from <http://www.photon.t.u-tokyo.ac.jp>. (b) 3D band structure of SWCNT. Reprinted from [10], Copyright (2005), with permission from Elsevier. .... 7

Figure 1.5 SWCNT ( $n, m$ ) indices, the so-called chiral map. A red solid point denotes metallic SWCNTs, and a black open circle denotes semiconducting SWCNTs. Reproduced from <http://www.photon.t.u-tokyo.ac.jp>. .... 8

Figure 1.6 eDOS of (4, 2), (6, 5), (12, 6), and (16, 0) SWCNTs. Reproduced from <http://www.photon.t.u-tokyo.ac.jp>. .... 9

Figure 1.7 Photograph of a piece of bulk MoS<sub>2</sub> crystal, which was purchased from 2D Semiconductors Inc. .... 10

Figure 1.8 The element distribution of MX<sub>2</sub> TMDCs in a periodic table. Reprinted from [16], Copyright (2015), with permission from Nature Publishing Group. .... 11

Figure 1.9 Schematics of the structural polytypes of MoS<sub>2</sub>: 1T, 2H, and 3R. Reprinted from [17], Copyright (2012), with permission from Nature Publishing Group. .... 12

Figure 1.10 DFT calculated band structures of MoS<sub>2</sub>. The blue line is VBM, and the red line is CBM. From left to right: bulk, quadrilayer, bilayer, monolayer. The solid arrows indicate the lowest energy transitions. Reprinted from [20], Copyright (2010), with

## List of Figures

---

permission from ACS. ....	13
Figure 1.11 Schematics illustrating how a solar cell works. ....	17
Figure 1.12 Solar cell market share by solar cell type.....	18
Figure 1.13 Two approaches for developing next-generation solar cells. ....	20
Figure 1.14 (a) 20.6% inverted-type perovskite solar cells with polymer-optimized PCBM ETL. Reprinted from [29], Copyright (2019), with permission from ACS. (b) 12.4% pristine graphene-Si solar cells with the optimization of interfacial oxide layer. Reprinted from [30], Copyright (2015), with permission from ACS.....	22
Figure 1.15 (a) SWCNT dye-sensitized solar cells. Reprinted from [31], Copyright (2011), with permission from ACS. (b) SWCNT-Si solar cells. Reprinted from [32], Copyright (2014), with permission from RSC. (c) SWCNT organic solar cells. Reprinted from [33], Copyright (2015), with permission from ACS. (d) SWCNT perovskite solar cells. Reprinted from [34], Copyright (2017), with permission from ACS.....	23
Figure 2.1 SEM image of (a) an SWCNT film, and (b) CVD synthesized monolayer MoS <sub>2</sub> . ....	31
Figure 2.2 (a) A scanned film of TEM. (b) CCD image of TEM. (c) Crystal planes of Co nanoparticles, with the lattice space of 0.2046 nm, which is assigned to (1 1 1) lattice plane. (d) SAED patterns of Co nanoparticles, with the assigned lattice planes on each diffraction ring.....	33
Figure 2.3 (a) Example Raman spectrum taken from vertically-aligned SWCNTs. The inset is the RBM. The excitation laser is 532 nm.....	34
Figure 2.4 Example Raman spectrum taken from vertically-aligned SWCNTs. The inset is the RBM. The excitation laser is 532 nm. ....	35
Figure 2.5 (a) Typical atomic vibrational modes of MoS <sub>2</sub> . (b) Raman spectra of thin and bulk MoS <sub>2</sub> as a focus on E <sub>2g</sub> <sup>1</sup> and A <sub>1g</sub> modes. (c) Raman shifts of E <sub>2g</sub> <sup>1</sup> and A <sub>1g</sub> modes (left vertical axis) and their difference (right vertical axis) as a function of MoS <sub>2</sub> layer thickness. (b) (c) are reprinted from [48], Copyright (2010), with permission from ACS. ....	37
Figure 2.6 Typical PL spectrum of monolayer MoS <sub>2</sub> . The positions of A exciton and B exciton are written beside the peaks. ....	38
Figure 2.7 (a) Transmittance spectrum of an SWCNT film. The transmittance at 550 nm is 90.1%. (b) Reflectance spectrum of SWCNT film on Si.....	40

## List of Figures

---

Figure 2.8 Co 2 <i>p</i> region in the XPS spectrum of Co <sub>3</sub> O <sub>4</sub> crystal.....	41
Figure 2.9 AM1.5G spectrum. Reprinted from [49], Copyright (2012), with permission from RSC.....	42
Figure 2.10 (a) <i>J-V</i> light characteristics of a solar cell. (b) Equivalent circuit of a solar cell. (c) <i>J-V</i> light and dark characteristics of a solar cell, with the schematics for the calculation of <i>R<sub>S</sub></i> and <i>R<sub>SH</sub></i> . (d) Calculation of the ideality factor <i>n</i> . ....	43
Figure 2.11 Schematic of four-point probe measurement using van de Pauw method. .	45
Figure 2.12 (a) SEM image of a TCF90 SWCNT film. (b) TEM image of a TCF90 SWCNT film. (c) SEM image of a TCF90 SWCNT film on SWCNT-Si solar cell. The contrast is clear for active window, suspended region, and electrode. ....	48
Figure 2.13 Characterizations of TCF60, TCF70, TCF80, and TCF90 SWCNT films. (a) RBM region of Raman spectra. The excitation laser is 532 nm. RBM was normalized by G band. (b) G/D band region of Raman spectra. (c) Transmittance spectra. (d) Relationship between sheet resistance and transparency. The red dashed line shows a near-linear relationship, which is fitted by ordinary least squares regression model. ....	49
Figure 2.14 Schematics of SWCNT-Si solar cells. (a) Optical image of an as-fabricated SWCNT-Si solar cell. (b) Top-view drawing. (c) Side-view drawing. (d) 3D drawing.	51
Figure 2.15 (a) <i>J-V</i> curves of the SWCNT-Si solar cells with the TCF60, TCF70, TCF80, and TCF90 SWCNT films, under 100 mW/cm <sup>2</sup> AM1.5G illumination. The dashed lines are the dark current. (b) <i>J-V</i> curves of the as-realized SWCNT-Si solar cell with TCF90 and were measured again after 1.5-month exposure in ambient environment, under 100 mW/cm <sup>2</sup> AM1.5G illumination. ....	54
Figure 2.16 Schematics of the MoS <sub>2</sub> LPCVD system.....	57
Figure 2.17 (a) Main interface of LPCVD controlling software. (b) Picture of the MoS <sub>2</sub> LPCVD system.....	59
Figure 3.1 (a) Chemical structure of Nafion. (b) Illustration of a simple application of aqueous Nafion to an SWCNT-Si solar cell, inducing an anti-reflection effect and <i>p</i> -doping at the same time. ....	63
Figure 3.2 (a) <i>J-V</i> curves of the pristine SWCNT-Si solar cell, the Nafion-applied SWCNT-Si solar cell, the PMMA-applied SWCNT-Si solar cell, and the HNO <sub>3</sub> -applied SWCNT-Si solar cell, under 100 mW/cm <sup>2</sup> AM1.5G illumination. (b) Dark <i>J-V</i> curves of the pristine SWCNT-Si solar cell, the Nafion-applied SWCNT-Si solar cell, the PMMA-	

## List of Figures

---

applied SWCNT-Si solar cell, and the HNO <sub>3</sub> -applied SWCNT-Si solar cell with logged $I$ - $V$ curves in the inset.....	65
Figure 3.3 (a) Stability data showing the doping effectiveness change of the SWCNT films after a Nafion application and the PCE change of the Nafion-applied SWCNT-Si solar cell. (b, c, d, e) Normalized PCE of SWCNT-Si solar cells, PMMA-applied SWCNT-Si solar cells, and Nafion-applied SWCNT-Si solar cells submerged to (b) chloroform, (c) 60 v/v% HNO <sub>3</sub> , and (d) water, and (e) under constant illumination of UV. ....	67
Figure 3.4 Reported PCEs of CNT electrode-based Si solar cells with similar active areas (6–10 mm <sup>2</sup> ) to the devices of this work.....	69
Figure 3.5 (a) Cross-sectional SEM images of different concentrations of Nafion/SWCNT layers on Si substrates and their thicknesses. (b) The measured total thicknesses of Nafion/SWCNT layers on Si, depending on the nominal concentration of Nafion. ....	71
Figure 3.6 RIs of SWCNT film, Nafion film, and Nafion-applied SWCNT film, all on Si substrates. ....	72
Figure 3.7 (a) RCWA-simulated reflectance spectral mapping over the total Nafion/SWCNT thickness. (b) RCWA-simulated absorptance spectral mapping over the total Nafion/SWCNT thickness. ....	73
Figure 3.8 (a) PCE and $J_{SC}$ rend over the nominal concentration of Nafion. (b) RCWA-simulated absorptance as a function of the total Nafion/SWCNT thickness at the wavelength of 600 nm. (c) Sheet resistance changes of SWCNT films upon doping by Nafion with different concentrations, and (d) $V_{OC}$ and FF of Nafion-applied SWCNT-Si solar cells in different Nafion concentrations.....	74
Figure 3.9 UV-Vis-NIR experimental results. (a) Reflectance, (b) absorptance, (c) transmittance spectra of a Si substrate, an SWCNT film on a Si substrate, and Nafion-applied SWCNT films on Si substrates, where the Nafion nominal concentrations are 5%, 10% , and 20%.....	75
Figure 3.10 RCWA-simulated (a) reflectance, (b) absorptance, and (c) transmittance of a Si substrate and Nafion-applied SWCNT films on Si substrates, where the Nafion concentrations are 5%, 10%, and 20%; and (d) the combination of reflectance, transmittance, and absorptance for the 10 v/v% Nafion concentration. ....	76
Figure 3.11 RCWA-simulated (a) reflectance and (b) absorptance data; empirical (c) reflectance and (d) absorptance data of a Si substrate, a 5 v/v% Nafion-coated Si substrate,	

## List of Figures

---

a 10 v/v% Nafion-coated Si substrate, and a 20 v/v% Nafion-coated Si substrate. ....	77
Figure 3.12 FDTD full-vector simulation for the light wave of 600 nm on a Si substrate and Nafion-applied SWCNT films on Si substrates, where the Nafion concentrations are 5%, 10%, and 20%. ....	78
Figure 3.13 IPCE spectra and integrated $J_{SC}$ of a Nafion-applied SWCNT-Si solar cell, a PMMA-applied SWCNT-Si solar cell, and an $HNO_3$ -applied SWCNT-Si solar cell. ...	79
Figure 3.14 (a) Illustration of the Nafion-applied SWCNT-Si solar cell, (b) illustration of the PYS measurement conducted on both sides of a Nafion-applied SWCNT film, and (c) the corresponding PYS data. ....	80
Figure 3.15 (a) XPS carbon peaks of an SWCNT film, a 2.5 v/v% Nafion-applied SWCNT film, and an $HNO_3$ -applied SWCNT film. (b) XPS scan of the entire range of SWCNT films with different nominal Nafion concentrations. (c) the carbon XPS peaks of the SWCNT films with different nominal Nafion concentrations. ....	82
Figure 3.16 (a) Band structure of SWCNT-Si solar cells by Schottky barrier model. (b) Band structure of SWCNT-Si solar cells by $p-n$ junction model.....	83
Figure 3.17 TCAD simulation modeling and four selected data showing that more band bending is induced by lower Fermi level.....	84
Figure 3.18 TCAD-simulated $J-V$ curves of SWCNT-Si solar cells with different Fermi levels of the SWCNT films. ....	85
Figure 3.19 EIS spectra of SWCNT-Si solar cells with different treatments and a high-frequency parallel resistor-capacitor circuit as an inset.....	86
Figure 3.20 (a) Sample information for QSSPC measurement. (b) QSSPC lifetimes of bare Si wafer, pristine SWCNT-laminated Si, ethanol-applied SWCNT-laminated Si, $HNO_3$ -applied SWCNT-laminated Si, PMMA-applied SWCNT-laminated Si, and Nafion-applied SWCNT-laminated Si.....	88
Figure 4.1 Monolayer $MoS_2$ synthesized by APCVD method at Jing Kong lab, Massachusetts Institute of Technology (MIT) [126]: (a) optical image, (b) Raman, and (c) PL. Monolayer $MoS_2$ film synthesized by LPCVD method: (d) optical image, (e) single-crystalline domains, and (f) PL, reprinted from [128], Copyright (2014), with permission from ACS.....	94
Figure 4.2 (a) A schematic of LPCVD synthesis. (b) Experimental flow of a $MoS_2$ LPCVD process. ....	95

## List of Figures

---

Figure 4.3 Effect of substrate preparation method on MoS <sub>2</sub> synthesis results, characterized by SEM. (a) Without KOH pre-processing. (b) With 5-min KOH pre-processing. (c) With 10-min KOH pre-processing. ....	96
Figure 4.4 Effect of Ar carrier gas flow rate on MoS <sub>2</sub> synthesis results, characterized by SEM. (a) 50 sccm. (b) 10 sccm. ....	97
Figure 4.5 Effect of S evaporation temperature on MoS <sub>2</sub> synthesis results, characterized by SEM. (a) 100 °C. (b) 110 °C. (c) 120 °C. (d) 130 °C. ....	98
Figure 4.6 Effect of MoO <sub>3</sub> sublimation and growth temperature on MoS <sub>2</sub> synthesis results, characterized by SEM. (a) 530 °C. (b) 570 °C. (c) 600 °C. ....	99
Figure 4.7 Effect of MoO <sub>3</sub> amount and growth time on MoS <sub>2</sub> synthesis results, characterized by SEM. (a) 30 min. (b) 50 min. (c) 70 min. ....	100
Figure 4.8 As-synthesized continuous monolayer MoS <sub>2</sub> film by LPCVD. (a) Optical image, along with the comparison with bare SiO <sub>2</sub> /Si substrate. (b) SEM image of the center of substrate. (c) Raman. (d) PL. ....	102
Figure 4.9 (a) A schematic of a 1D vdW heterostructure of MoS <sub>2</sub> NT-BNNT-SWCNT. (b) A schematic of the LPCVD synthesis of MoS <sub>2</sub> NT onto 1D nanostructures. ....	105
Figure 4.10 Comparisons of MoS <sub>2</sub> NT-SWCNT and SWCNT films. (a) SEM characterizations. (b) Raman spectra. (c) UV-Vis-NIR absorption spectra. ....	107
Figure 4.11 (a) 1D MoS <sub>2</sub> NT-SWCNT nanostructure that was characterized by HR-TEM, HAADF-STEM, and EELS mapping. (b) Typical diameter characterization of a MoS <sub>2</sub> NT-SWCNT. (c) The strain energy of a single-walled MoS <sub>2</sub> NT as a function of tube diameter calculated by Stillinger-Weber (denoted as SW) type potential and DFT simulation. .	108
Figure 4.12 Comparisons of SWCNT, BNNT-SWCNT, and MoS <sub>2</sub> NT-BNNT-SWCNT films. (a) Optical images against a printed logo of the University of Tokyo. The scale bar is 5 mm. (b) Raman spectra. (c) UV-Vis-NIR absorption spectra. ....	111
Figure 4.13 TEM characterizations of the MoS <sub>2</sub> NT-BNNT-SWCNT 1d vdW heterostructures. (a) TEM. The scale bar is 5 nm. (b) EELS mapping. (c) SAED patterns. ....	112
Figure 4.14 (a) A schematic of the C <sub>60</sub> -MoS <sub>2</sub> NT-SWCNT PV device structure. (b) Energy band diagram of the C <sub>60</sub> -MoS <sub>2</sub> NT-SWCNT PV device. ....	116
Figure 4.15 Fabrication and characterizations of the C <sub>60</sub> -MoS <sub>2</sub> NT-SWCNT PV device. (a) A schematic of the sample preparation method. (b) Optical image. (c) <i>J-V</i> characteristics	

## List of Figures

---

in a range of -1 V to 1 V. (d) $J$ - $V$ characteristics in a range of -2 mV to 2 mV.....	118
Figure 4.16 $J$ - $V$ characteristics of the C <sub>60</sub> -SWCNT device. ....	119
Figure 4.17 Fabrication and characterizations of C <sub>60</sub> -MoS <sub>2</sub> NT-BNNT-SWCNT PV device. (a) A schematic of the sample preparation method. (b) Optical image. (c) $J$ - $V$ characteristics in a range of -2 mV to 2 mV. ....	120
Figure 4.18 (a) Comparison of the $J$ - $V$ characteristics of the C <sub>60</sub> -MoS <sub>2</sub> NT-SWCNT and the C <sub>60</sub> -MoS <sub>2</sub> NT-BNNT-SWCNT PV devices, under 100 mW/cm <sup>2</sup> AM1.5G illumination. (b) Energy band diagram of the C <sub>60</sub> -MoS <sub>2</sub> NT-BNNT-SWCNT PV device.....	121
Figure 4.19 (a) A schematic of the MoS <sub>2</sub> NT-SWCNT on top of an inverted-type perovskite solar cell. (b) Energy band diagram of the MoS <sub>2</sub> NT-SWCNT as ETL and cathode in perovskite solar cells.....	122
Figure 4.20 $J$ - $V$ characteristics of (a) the MoS <sub>2</sub> NT-SWCNT and (b) the SWCNT on top of inverted-type perovskite solar cells, under 100 mW/cm <sup>2</sup> AM1.5G illumination.....	123
Figure 4.21 (a) Comparison of the $J$ - $V$ characteristics of the MoS <sub>2</sub> NT-SWCNT, MoS <sub>2</sub> NT- BNNT(3hr)-SWCNT, and MoS <sub>2</sub> NT-BNNT(1hr)-SWCNT on top of inverted-type perovskite solar cells, under 100 mW/cm <sup>2</sup> AM1.5G illumination. The dashed lines are the dark current. (b) Energy band diagram of the MoS <sub>2</sub> NT-BNNT-SWCNT as ETL and cathode in perovskite solar cells.....	124
Figure 4.22 (a) A schematic of the MoS <sub>2</sub> NT-SWCNT on top of a normal-type perovskite solar cell. (b) Energy band diagram of the MoS <sub>2</sub> NT-SWCNT as HTL and anode in perovskite solar cells. ....	126
Figure 4.23 Comparison of the $J$ - $V$ characteristics of the SWCNT, the MoS <sub>2</sub> NT-SWCNT, and the MoS <sub>2</sub> NT-SWCNT with the spiro-MeOTAD coated on top, on top of normal-type perovskite solar cells, under 100 mW/cm <sup>2</sup> AM1.5G illumination. ....	127
Figure 4.24 Raman spectra of the SWCNT film before and after MoS <sub>2</sub> NT coating. (a) G band region. (b) 2D band region.....	129
Figure A.1 (a) Schematic of the thin interfacial oxide layer between SWCNT film and $n$ - Si. (b) Illustration of the characterization process for Si oxide thickness from XPS spectra. .....	156
Figure A.2 Full-range XPS surface survey spectra of the RCA2-cleaned $n$ -Si substrates. (a) Before BHF cleaning. (b) After BHF cleaning. ....	158

## List of Tables

Table 2.1 The PCE, $FF$ , $J_{SC}$ , and $V_{OC}$ of the SWCNT-Si solar cells with the TCF60, TCF70, TCF80, and TCF90 SWCNT films, as well as $R_S$ , $R_{SH}$ , and $n$ . The transparency and $R_{sheet}$ characteristics of SWCNT films are also presented. ....	55
Table 2.2 The PCE, $FF$ , $J_{SC}$ , and $V_{OC}$ of the as-realized SWCNT-Si solar cell with the TCF90 SWCNT film and measured again after 1.5-month exposure in the ambient environment. ....	56
Table 3.1 PV parameters of the SWCNT-Si solar cell, the Nafion-applied SWCNT-Si solar cell, the PMMA-applied SWCNT-Si solar cells, and the $HNO_3$ -applied SWCNT-Si solar cell, under $100 \text{ mW/cm}^2$ AM1.5G illumination. ....	66
Table 3.2 Record table of the reported CNT-based Si solar cells with details including active area, CNT type, doping treatment, anti-reflection coating, and stability. ....	70
Table 3.3 Implied $V_{OC}$ from different work functions by TCAD simulation. ....	85
Table 3.4 EIS fitting data of the pristine and doped SWCNT-based Si solar cells at 0.5 V over the high-frequency range of 10 kHz to 1 MHz under AM1.5G illumination ( $100 \text{ mW/cm}^2$ ). ....	87
Table 3.5 Implied $V_{OC}$ calculated from the QSSPC data of SWCNTs on $n$ -Si wafers treated by different substances. ....	88
Table 4.1 Comparison of the characteristics of the $C_{60}$ - $MoS_2$ NT-SWCNT and the $C_{60}$ - $MoS_2$ NT-BNNT-SWCNT PV devices. ....	121
Table 4.2 Comparison of the characteristics of the $MoS_2$ NT-SWCNT, $MoS_2$ NT-BNNT(3hr)-SWCNT, and $MoS_2$ NT-BNNT(1hr)-SWCNT on top of inverted-type perovskite solar cells. ....	125
Table 4.3 Comparison of the characteristics of the SWCNT, the $MoS_2$ NT-SWCNT, and the $MoS_2$ NT-SWCNT with the spiro-MeOTAD coated on top, on top of normal-type perovskite solar cells. ....	128
Table 5.1 Comparison of different types of solar cells with respect to their different characteristics. ....	135

# Terminology

0D: 0-dimensional	GaAs: gallium arsenide
1D: 1-dimensional	HAADF-STEM: high-angle annular
2D: 2-dimensional	dark-field scanning transmission electron
ABF-STEM: annular bright-field	microscopy
scanning transmission electron	hBN: hexagonal boron nitride
microscopy	HOMO: highest occupied molecular
AFM: atomic force microscope	orbital
AM: air mass	HR-TEM: high-resolution transmission
APCVD: atmospheric-pressure chemical	electron microscopy
vapor deposition	HTL: hole transport layer
BHF: buffered hydrogen fluoride	IPA: isopropyl alcohol
BNNT: boron nitride nanotube	IPCE: incident photon-to-current
CBM: conduction band minimum	efficiency
CCD: charge-coupled device	ITO: indium tin oxide
$C_{CT}$ : charge transport capacitance	$I$ - $V$ : current-voltage
CdTe: cadmium telluride	$J_{SC}$ : short-circuit current density
CIGS: copper indium gallium selenide	$J$ - $V$ characteristic: current density-voltage
CNT: carbon nanotube	characteristic
CVD: chemical vapor deposition	KPI: key performance indicator
DFT: density functional theory	LPCVD: low-pressure chemical vapor
eDOS: electronic density of states	deposition
EELS: electron energy loss spectroscopy	LUMO: lowest unoccupied molecular
EIS: electrochemical impedance	orbital
spectroscopy	MIS: metal-insulator-semiconductor
EQE: external quantum efficiency	MOCVD: metal-organic chemical vapor
ETL: electron transport layer	deposition
FDTD: finite-difference time-domain	MoS <sub>2</sub> NT: molybdenum disulfide
FET: field effect transistor	nanotube
FF: fill factor	MWCNT: multi-walled carbon nanotube
FiT: feed-in tariff	PCBM: [6,6]-phenyl-C <sub>61</sub> -butyric acid
FTO: fluorine-doped tin oxide	methyl ester

## Terminology

---

PCE: power conversion efficiency	scm: standard cubic centimeters per minute
PEDOT:PSS: poly(3,4-ethylenedioxythiophene) polystyrene sulfonate	SEM: scanning electron microscopy
PL: photoluminescence	SWCNT: single-walled carbon nanotube
PMMA: poly(methyl methacrylate)	TCAD: technology computer-aided design
PV: photovoltaic	TCF: transparent conductive film
PVD: physical vapor deposition	TEM: transmission electron microscopy
PYS: photoelectron yield spectroscopy	TMDC: transition metal dichalcogenide
QSSPC: quasi-steady-state photoconductance	UV: ultraviolet
RBM: radial breathing mode	UV-Vis-NIR: ultraviolet-visible-near infrared
$R_{CT}$ : charge transfer resistance	VBM: valence band maximum
RCWA: rigorous coupled-wave analysis	$V_d$ : built-in potential
RI: refractive index	vdW: van der Waals
$R_S$ : series resistance	$V_{OC}$ : open-circuit voltage
$R_{SH}$ : shunt resistance	XPS: x-ray photoelectron spectroscopy
SAED: selected area electron diffraction	

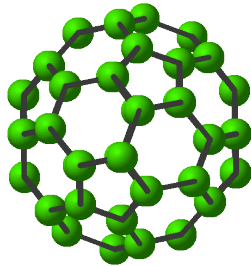
# Chapter 1      General Introduction

## 1.1      World of Low-Dimensional Nanomaterials

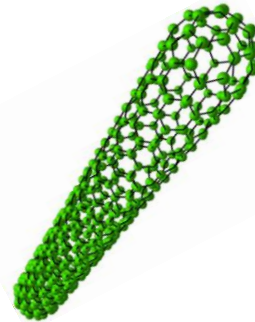
Dimensionality has been an important characteristic of materials. With different dimensions, substantial variations of electronic structures and fundamental properties have been observed [1]. The nanotechnology, which is based on nanomaterials with reduced dimensionality, has been influencing we human beings over the last semicentury. As said by the American physicist Richard Feynman, "There's Plenty of Room at the Bottom," there are plenty of discoveries after we opened the door of low-dimensional nanomaterials.

The big bang of the world of low-dimensional nanomaterials started from fullerene, which is a new allotrope of carbon discovered in 1985 [2]. This so-called buckyball dramatically reduced the dimensionality of materials from 3D to 0D, with the scale down to the nanometer level. Another boom came when in 1991, Iijima et al. discovered MWCNT [3], and two years later, SWCNT was also discovered [4]. The collection of MWCNT and SWCNT is called CNT, which showed us with 1D nanomaterial for the first time. The exciting story did not end. In 2004, Geim and Novoselov et al. extracted graphene from graphite by Scotch tape, which is a 2D nanomaterial [5]. Not only has the graphene itself contributed to the world of low-dimensional nanomaterials, but also the technique of exfoliation has given us hints about producing the "2D nanomaterials beyond graphene" [6]. As the layered structure of graphite is prevalent in the natural world, a treasure house of 2D nanomaterials, including hBN and TMDCs, can be handily produced and studied. The schematics of low-dimensional nanomaterials are shown in Figure 1.1. During this new era of nanoscience and nanotechnology, two Nobel Prizes have been awarded in 1996 and 2010 respectively, for the discovery of fullerene and graphene.

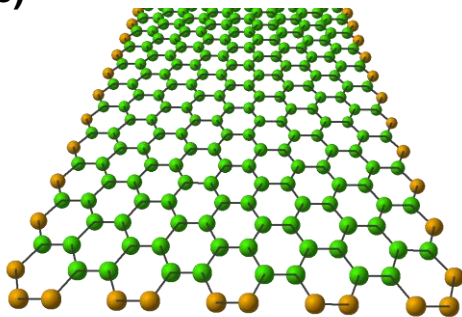
(a)



(b)



(c)



(d)

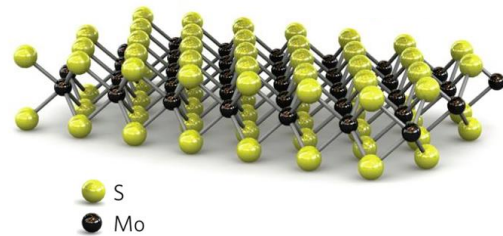


**Figure 1.1 Schematics of low-dimensional nanomaterials. (a) 0D fullerene. (b) 1D SWCNT. (c) 2D graphene. (d) 2D MoS<sub>2</sub>, which is a representative of TMDCs. (a), (b), and (c) are reproduced from <http://www.photon.t.u-tokyo.ac.jp>. (d) is reprinted from [7], Copyright (2011), with permission from Nature Publishing Group.**

## 1.2 SWCNTs

Rolling up an  $sp^2$ -bonded 2D graphene sheet (one layer of graphite) into a tubular structure can yield an SWCNT. Depending on the way the graphene is rolled up, *i.e.*, the rolling direction and diameter of tubes, SWCNT can have tunable electronic structures and thus tunable properties, which is one of the most charming points in the research of SWCNT [8].

### 1.2.1 Atomic Structure of SWCNTs

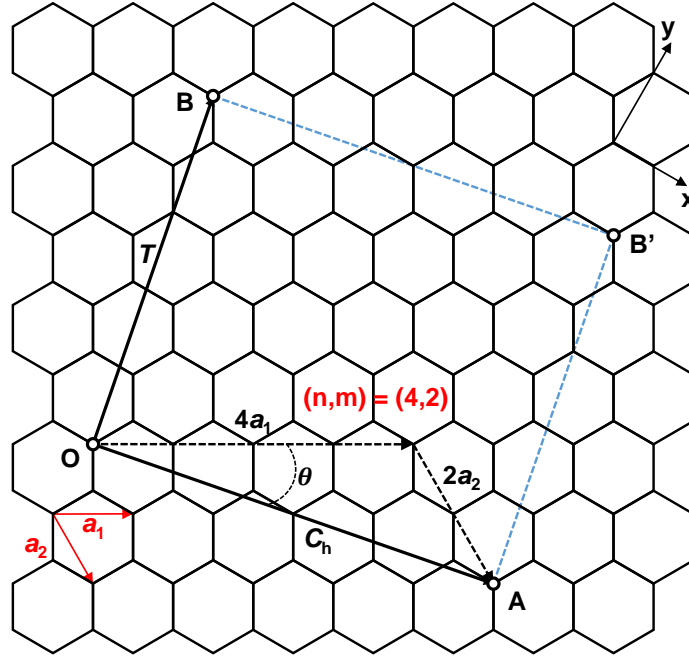


**Figure 1.2** Unrolled hexagonal lattice of an SWCNT. The chiral vector  $C_h$  and translational vector  $T$  are presented for the case of  $C_h = 4a_1 + 2a_2$  SWCNT. The angle between  $a_1$  and  $C_h$  gives the chiral angle  $\theta$  ( $0 \leq \theta \leq 30^\circ$ ).

Figure 1.2 shows the unrolled graphene sheet. The distance between carbon atoms is  $a_{c-c}$  ( $=1.42 \text{ \AA}$ ). In the Cartesian  $x$ - $y$  coordinate, the unit vectors  $a_1$  and  $a_2$  are expressed as

$$\mathbf{a}_1 = (a, 0), \quad \mathbf{a}_2 = \left( \frac{1}{2}a, -\frac{\sqrt{3}}{2}a \right) \quad (1.1)$$

where

$$a = \sqrt{3} \times a_{c-c} = \sqrt{3} \times 1.42 \text{ \AA} = 2.46 \text{ \AA} \quad (1.2)$$

A chiral vector  $\mathbf{C}_h$  showing how SWCNT is rolled up from graphene, *i.e.*, the structure of the SWCNT, is defined as

$$\mathbf{C}_h = n\mathbf{a}_1 + m\mathbf{a}_2 \equiv (n, m) \quad (1.3)$$

which is often described by the pair of indices  $(n, m)$  that denote the number of unit vectors in the hexagonal honeycomb lattice contained in the vector  $\mathbf{C}_h$ . The nanotube diameter  $d_t$  can be written in terms of the integers  $(n, m)$  as

$$d_t = \frac{|\mathbf{C}_h|}{\pi} = \frac{a\sqrt{m^2 + mn + n^2}}{\pi} \quad (1.4)$$

As shown in Figure 1.2, the angle between the chiral vector  $\mathbf{C}_h$  and  $\mathbf{a}_1$  is named as the chiral angle  $\theta$ , which is given by

$$\theta = \cos^{-1}\left(\frac{2n + m}{2\sqrt{n^2 + nm + m^2}}\right) \quad \left(|\theta| \leq \frac{\pi}{6}\right) \quad (1.5)$$

An example of (4,2) SWCNT is shown in Figure 1.2. For armchair SWCNT,  $(n, n)$ ,  $\theta$  equals  $30^\circ$ , while for zigzag SWCNT,  $(n, 0)$ ,  $\theta$  is  $0^\circ$ . The chiral angle for chiral tubes such as  $(4, 2)$  is between  $0^\circ$  and  $30^\circ$ . So far, the atomic structure of an SWCNT is described by its unit cell OBB'A. The other unit vector which is vertical to the chiral vector  $\mathbf{C}_h$  in the unit cell is labeled as translational vector  $\mathbf{T}$ . The translational vector  $\mathbf{T}$  is the shortest repeat distance along the SWCNT axis and is described as

$$\mathbf{T} = t_1\mathbf{a}_1 + t_2\mathbf{a}_2 \equiv (t_1 + t_2) \quad (1.6)$$

where  $(t_1, t_2)$  correlates to  $(n, m)$  as

$$t_1 = \frac{(2m + n)}{d_R}, \quad t_2 = -\frac{(2n + m)}{d_R} \quad (1.7)$$

where  $d_R$  is the greatest common divisor of  $(2n+m, 2m+n)$

$$d_R = \begin{cases} d & \text{if } n - m \text{ is not a multiple of } 3d \\ 3d & \text{if } n - m \text{ is a multiple of } 3d \end{cases} \quad (1.8)$$

where  $d$  is the greatest common divisor of  $(n, m)$ . The number of the hexagons contained in one unit cell of SWCNT is given as

$$N = \frac{|\mathbf{C}_h \times \mathbf{T}|}{|\mathbf{a}_1 \times \mathbf{a}_2|} = \frac{2(n^2 + nm + m^2)}{d_R} \quad (1.9)$$

The number of carbon atoms contained in one unit cell is  $2N$ .

## 1.2.2 Structure-Related Properties of SWCNTs

As mentioned in Section 1.2.1, the electronic structure of an SWCNT is tunable due to its rolling-up way of graphene. The structure-related electronic structures of SWCNTs have attracted a large amount of research and is crucial to the optical and electrical applications of SWCNTs [9]. In order to understand the electronic structure of an SWCNT, we need to consider the electronic structure of its "nominal" origin, graphene.

One carbon atom has four valence electrons, of which two are in  $2s$  orbital, and the other two are in  $2p$  orbital. By orbital hybridization, one electron of  $2s$  orbital moves to  $2p$  orbital, resulting in three electrons in  $sp^2$  orbital and one electron in  $2p_z$  orbital. In graphene, the  $\sigma$  band is formed from  $sp^2$  orbital, and  $\pi$  band is formed from  $2p_z$  orbital. The electronic properties of graphene are related to the  $\pi$  band near Fermi level.

It is necessary to consider the reciprocal lattice space to calculate the  $\pi$  band of graphene. The real lattice space is shown in Figure 1.3a. The unit vectors are  $\mathbf{a}_1$  and  $\mathbf{a}_2$ , and the unit cell containing two carbon atoms is shown as the blue dashed rhombus. Then, the reciprocal lattice space is shown in Figure 1.3b. The unit vectors in reciprocal lattice space are defined as

$$\mathbf{b}_1 = \left( \frac{1}{\sqrt{3}}, 1 \right) \frac{2\pi}{a}, \quad \mathbf{b}_2 = \left( \frac{1}{\sqrt{3}}, -1 \right) \frac{2\pi}{a} \quad (1.10)$$

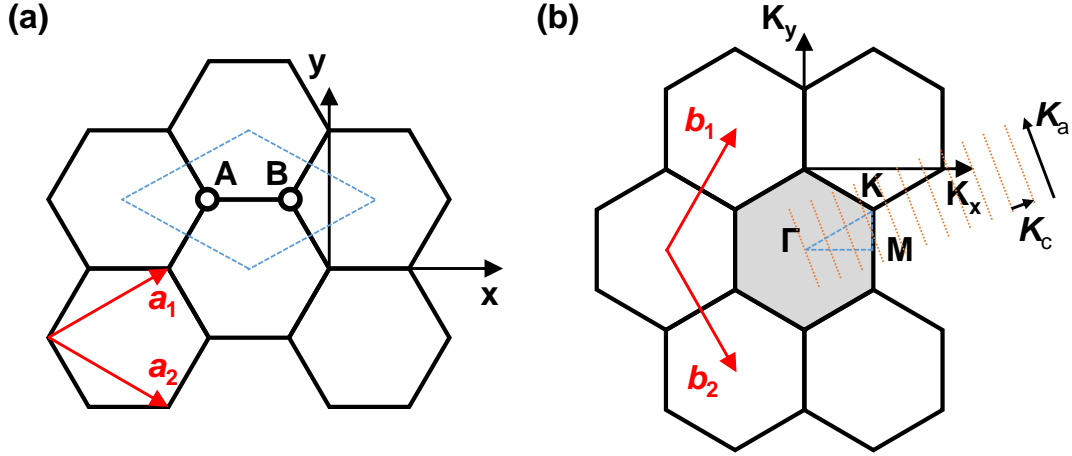


**Figure 1.3 (a) Real lattice space of graphene. A unit cell is shown as a blue dashed rhombus with two carbon atoms (A and B).  $a_1$  and  $a_2$  are unit vectors. (b) Reciprocal lattice space of graphene. The grey hexagonal area is the first Brillouin zone.  $b_1$  and  $b_2$  are unit vectors.**

The first Brillouin zone is the grey hexagonal area. In this Brillouin zone, three high symmetry points,  $\Gamma$ ,  $K$ , and  $M$  are defined as the center, the corner, and the center of the edge, respectively.

The energy dispersion of graphene is calculated by the tight-binding approximation of the  $2p_z$  orbital between the two carbon atoms, A and B:

$$w(\mathbf{k}) = \sqrt{1 + 4 \cos \frac{\sqrt{3} \mathbf{k}_x a}{2} \cos \frac{\mathbf{k}_y a}{2} + 4 \cos^2 \frac{\mathbf{k}_y a}{2}} \quad (1.11)$$

$$E_{\text{graphene}}^{\pm}(\mathbf{k}) = \frac{\varepsilon_{2p} \pm tw(\mathbf{k})}{1 \pm sw(\mathbf{k})} \quad (1.12)$$

where  $\varepsilon_{2p} = 0$ ,  $t = -3.033$  eV, and  $s = 0.129$ . The plus sign is the bonding  $\pi$  band, and the minus sign is the anti-bonding  $\pi^*$  band. The 3D  $\pi$  band structure of graphene in the first Brillouin zone is shown in Figure 1.4a. The lower part is  $\pi^*$  band, while the upper part is  $\pi$  band. Because they are touching each other at the  $K$  point, it shows that graphene is a zero-bandgap semiconductor.

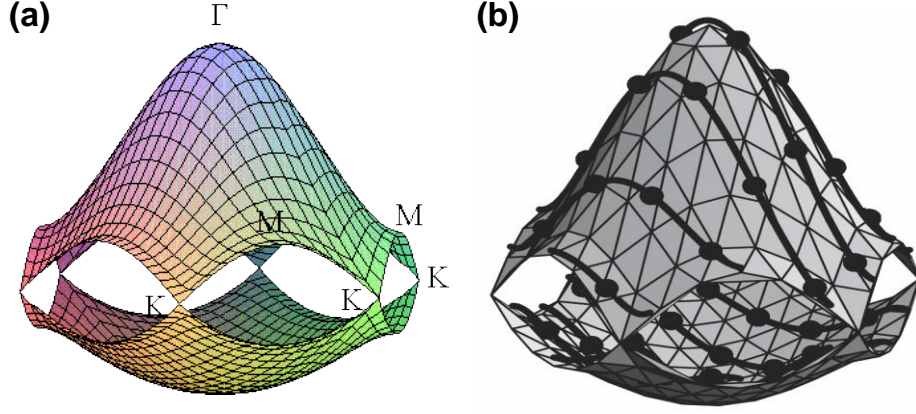


**Figure 1.4** (a) 3D band structure of graphene. Reproduced from <http://www.photon.t.u-tokyo.ac.jp>. (b) 3D band structure of SWCNT. Reprinted from [10], Copyright (2005), with permission from Elsevier.

Then we consider the electronic structure of SWCNT based on that of graphene. The corresponding reciprocal vectors of the unit vectors  $\mathbf{C}_h$  and  $\mathbf{T}$  at circumferential direction and axial direction are defined as  $\mathbf{K}_c$  and  $\mathbf{K}_a$  through the following equations.

$$\begin{aligned} \mathbf{C}_h \cdot \mathbf{K}_c &= 2\pi, \quad \mathbf{T} \cdot \mathbf{K}_c = 0, \\ \mathbf{C}_h \cdot \mathbf{K}_a &= 0, \quad \mathbf{T} \cdot \mathbf{K}_a = 2\pi \end{aligned} \quad (1.13)$$

Then,  $\mathbf{K}_c$  and  $\mathbf{K}_a$  can be obtained as

$$\mathbf{K}_c = \frac{1}{N} (-t_2 \mathbf{b}_1 + t_1 \mathbf{b}_2), \quad \mathbf{K}_a = \frac{1}{N} (m \mathbf{b}_1 - n \mathbf{b}_2) \quad (1.14)$$

From the Bloch wave theory and periodic boundary conditions on circumferential direction of SWCNT, the wave vectors can be determined as

$$\begin{aligned} E_\mu(k) &= E_{\text{graphene}}^\pm(\mathbf{k}) \left( \frac{\mathbf{K}_a}{|\mathbf{K}_a|} + \mu \mathbf{K}_c \right), \\ \left( \mu = 0, 1, \dots, N-1, \text{ and } -\frac{\pi}{|\mathbf{T}|} < k < \frac{\pi}{|\mathbf{T}|} \right) \end{aligned} \quad (1.15)$$

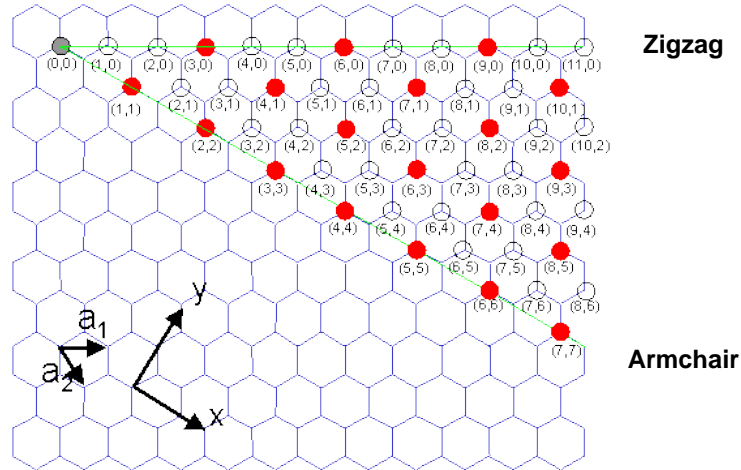


**Figure 1.5** SWCNT  $(n, m)$  indices, the so-called chiral map. A red solid point denotes metallic SWCNTs, and a black open circle denotes semiconducting SWCNTs. Reproduced from <http://www.photon.t.u-tokyo.ac.jp>.

These  $N$  discrete cutting lines are in parallel with  $\mathbf{K}_a$  with the interval of  $|\mathbf{K}_c|$ , as shown in Figure 1.3b. The 3D  $\pi$  band structure of SWCNT with the cutting lines is shown in Figure 1.4b. Depending on the chiralities of SWCNTs, if the cutting lines pass through the K point, the SWCNT is metallic; if not, the SWCNT is semiconducting. In a simple way, if  $(n - m)$  is the multiple of 3, the SWCNT is metallic; if not, the SWCNT is semiconducting. A graphical illustration of this chirality related electronic property is the chiral map, as shown in Figure 1.5.

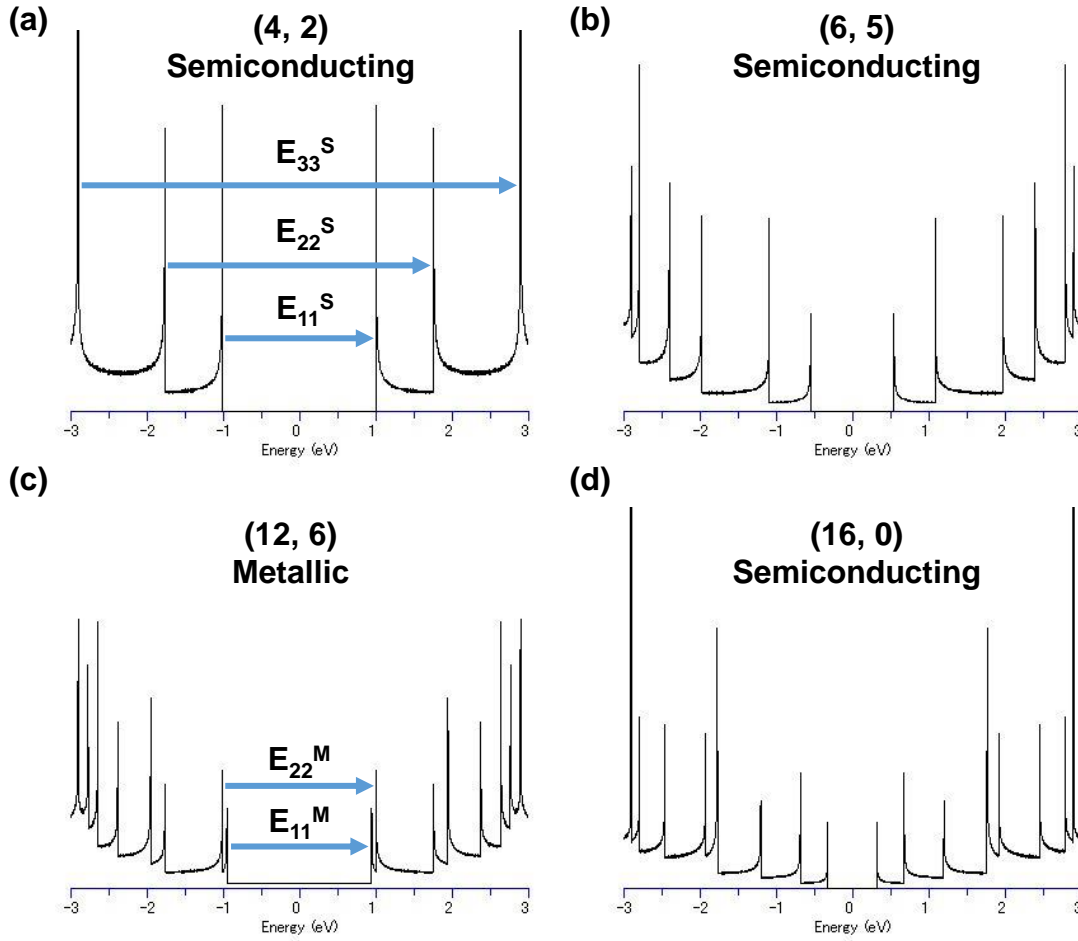


**Figure 1.6 eDOS of (4, 2), (6, 5), (12, 6), and (16, 0) SWCNTs. Reproduced from <http://www.photon.t.u-tokyo.ac.jp>.**

The eDOS of SWCNT can be obtained by tight-binding approximation and shows sharp peaks of van Hove singularities. Figure 1.6 shows the eDOS of SWCNTs with four famous chiralities. The energy separation between  $i$ th valence band and conduction band is called  $E_{ii}$ . For the metallic SWCNTs,  $E_{ii}$  is written as  $E_{ii}^M$ ; while for the semiconducting SWCNTs,  $E_{ii}$  is  $E_{ii}^S$ . The (4, 2) SWCNT is the smallest nanotube that can be synthesized so far [11], with the theoretical bandgap of about 2 eV. In contrast, the (12, 6) SWCNT has a continuous band structure and is hence metallic.

### 1.3 Low-Dimensional MoS<sub>2</sub>



**Figure 1.7 Photograph of a piece of bulk MoS<sub>2</sub> crystal, which was purchased from 2D Semiconductors Inc.**

MoS<sub>2</sub> is not a new material. The oldest known bulk MoS<sub>2</sub> sample can be dated to over 2.9 billion years ago [12]. A piece of bulk MoS<sub>2</sub> crystal (2D semiconductors Inc.) is shown in Figure 1.7. Even the low-dimensional MoS<sub>2</sub> is not new: few-layer MoS<sub>2</sub> single crystals have been reported in 1966 [13]. However, the application of MoS<sub>2</sub> has been restricted to lubricant and industrial catalyst for a long time, until the discovery of graphene. The unique electronic properties of graphene have given us hints to study 2D TMDCs (MX<sub>2</sub>) [14], which consists of transition metal and chalcogen with a ratio of 1:2. Figure 1.8 shows the element distribution of TMDCs in a periodic table. 2D MoS<sub>2</sub> belongs to the family of 2D TMDCs and is the representative of semiconducting 2D TMDCs in terms of the atomic structure and electronic properties [15]. Typically, each layer of a TMDC has a thickness of 6–7 Å [14].

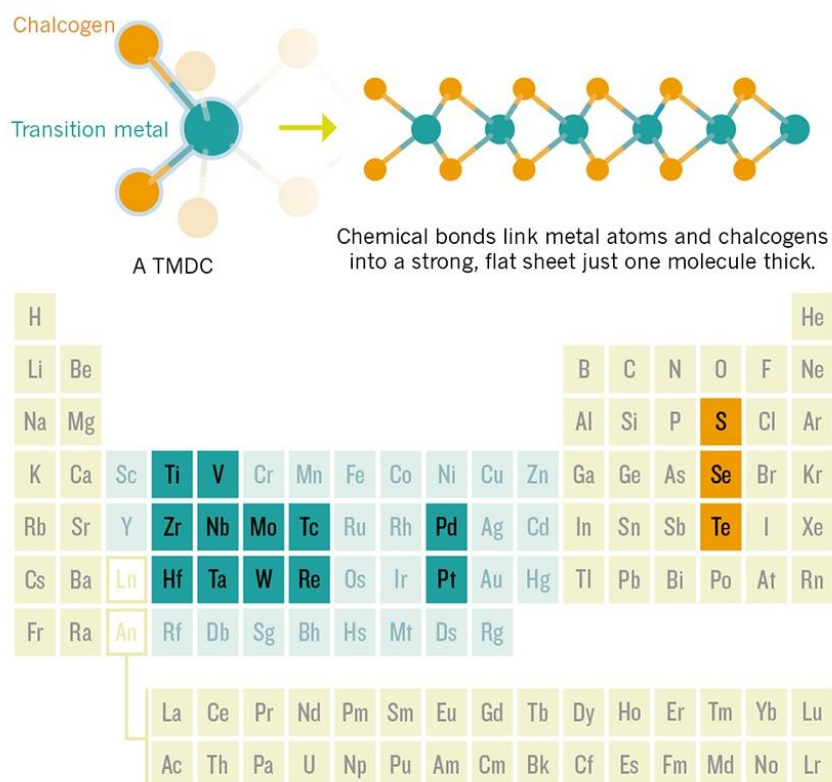


**Figure 1.8** The element distribution of  $\text{MX}_2$  TMDCs in a periodic table. Reprinted from [16], Copyright (2015), with permission from Nature Publishing Group.

### 1.3.1 Atomic Structure of $\text{MoS}_2$

As shown in Figure 1.1d, for monolayer  $\text{MoS}_2$ , one layer of Mo atoms is sandwiched between two layers of S atoms. The S atoms are hexagonal close packing, and bond with Mo atoms by either trigonal prismatic or octahedral geometry, resulting in no dangling bond of S. The absence of dangling bonds makes  $\text{MoS}_2$  a layered material, and the layers are held together by weak vdW forces. As a result, bulk  $\text{MoS}_2$  is an excellent lubricant, and monolayer  $\text{MoS}_2$  has high chemical stability.

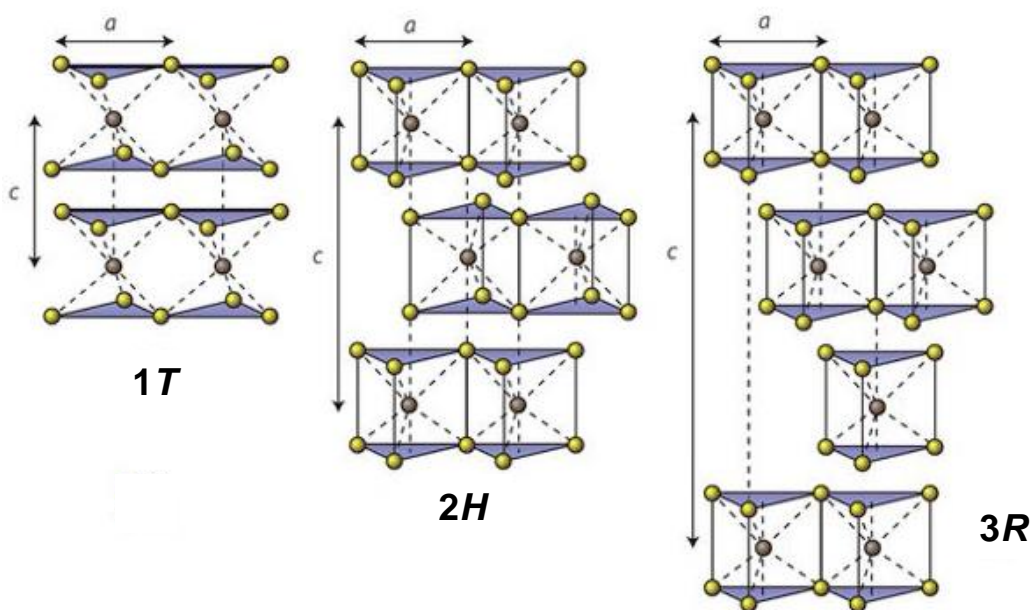


**Figure 1.9** Schematics of the structural polytypes of MoS<sub>2</sub>: *1T*, *2H*, and *3R*. Reprinted from [17], Copyright (2012), with permission from Nature Publishing Group.

There are three phases of MoS<sub>2</sub> depends on its symmetry: *1T*, *2H*, and *3R* (*T*–trigonal, *H*–hexagonal, and *R*–rhombohedral), where the digit indicates the number of layers in a crystallographic unit cell. Figure 1.9 illustrates the structural differences between these three symmetries. *1T* phase displays metallic behavior, while *2H* and *3R* phases display semiconducting behavior. Different synthesis methods produce MoS<sub>2</sub> with different phases. Natural MoS<sub>2</sub> is usually in *2H* and *3R* phases, while *2H* phase is dominant and more stable [18]. In this dissertation, hereafter, the thermodynamically stable phase of *2H* MoS<sub>2</sub> is discussed.

### 1.3.2 Structure-Related Properties of MoS<sub>2</sub>

The bulk MoS<sub>2</sub> is an indirect bandgap semiconductor with a bandgap of  $\approx 1\text{--}1.3$  eV. With the decrease of the thickness (number of layers), the indirect bandgap increases and becomes a direct bandgap of  $\approx 1.9$  eV when it is monolayer [19], which has a strong PL intensity. From the calculation results of DFT [20], the intrinsic mechanism can be revealed.

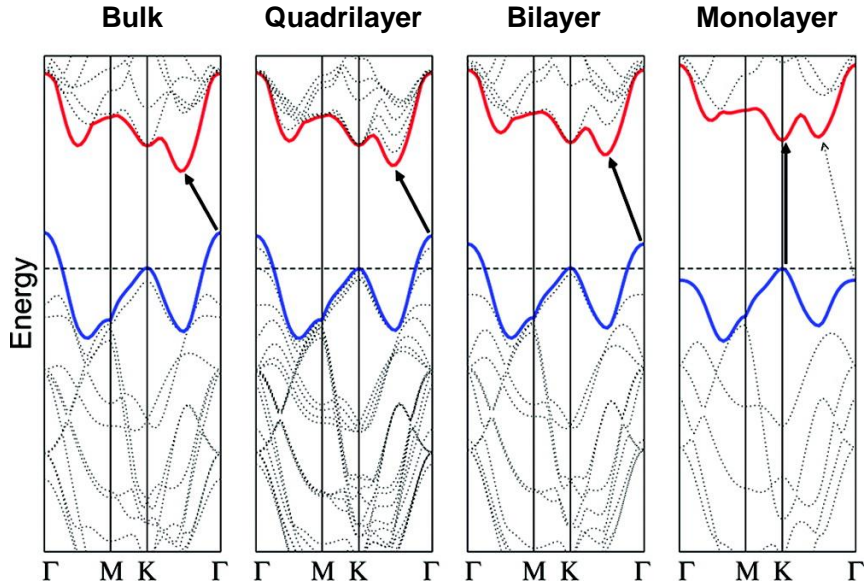


**Figure 1.10** DFT calculated band structures of MoS<sub>2</sub>. The blue line is VBM, and the red line is CBM. From left to right: bulk, quadrilayer, bilayer, monolayer. The solid arrows indicate the lowest energy transitions. Reprinted from [20], Copyright (2010), with permission from ACS.

As shown in Figure 1.10,  $\Gamma$ , K, and M. The VBM and CBM at K point ( $\text{VBM}_K$  and  $\text{CBM}_K$ ) are primarily composed of the  $d$  orbital of Mo atom, and the VBM at  $\Gamma$  point ( $\text{VBM}_\Gamma$ ) and CBM along K- $\Gamma$  ( $\text{CBM}_{K-\Gamma}$ ) are originated from the combination of the  $d$  orbital of Mo atom and  $p_z$  orbital of S atom. Because Mo atom is in the middle of S-Mo-S sandwich structure, the electronic states at K point have little influence from interlayer coupling effect. On the other hand, the  $\text{VBM}_\Gamma$  and  $\text{CBM}_{K-\Gamma}$ , which are related to the indirect bandgap, are significantly influenced by the interlayer coupling of the S atoms at the outer side. When there is only one layer, the absence of interlayer coupling finally makes the indirect bandgap larger than the direct bandgap at K point, which means MoS<sub>2</sub> monolayer becomes direct bandgap semiconductor. The thickness-related band structure and bandgap of MoS<sub>2</sub> allow it to respond to incident light with different wavelengths by different thicknesses, which is useful in optoelectronics. It is noteworthy to mention that if we consider spin-orbit coupling of monolayer MoS<sub>2</sub> as well, a field called "valleytronics" can be opened up in the research of TMDCs [21].

### 1.4 Renewable Energy Resources

As energy is closely related to our human society development, how to obtain energy and how to guarantee sufficient energy have become critical issues for a long time. For the former issue, traditional energy resources of fossil fuel, which consists of oil, coal, and natural gas, have been exploited for thousands of years. However, there have always been problems accompanying the process of exploiting energy, and these problems have led to significant disputes across geographical regions. Most of these problems can be summarized using a notion called "energy security".

Energy security is a major issue for our world in modern society. As the development of the economy highly depends on the richness of energy, how to guarantee sufficient energy is an inevitable affair for all the governments who focus on economic development. The definition of energy security is that it is the uninterrupted availability of energy resources at an affordable price [22]. There have been many kinds of issues related to energy security.

First, one intrinsic problem is that: as fossil fuels need thousands of years to form naturally, we usually regard them as nonrenewable energy resources. Consequently, the depletion issue has been more and more urgent as we are now consuming fossil fuels at an exponential curve. In addition, the regions with a large number of fossil fuels are suffering from the side effect of over-exploitation. For example, the coal-producing cities in China have the problem of coal mine collapse, and the cities after depletion are even abandoned by younger generations.

Second, the concentration of reserves in the politically unstable region is one of the fundamental problems of energy security. As different countries have a different amount of traditional energy resources, the issue of energy security is even severer in certain countries that do not have many natural resources. For example, the Middle East has a large amount of crude oil, which attracts the superpower's eyes for obtaining these resources with carrots and sticks. During this process, the outbreak of wars is a proof for the importance of energy security.

Third, because most of the traditional energy resources are being traded among international markets, market volatility has been a threat for both the buyers and sellers

## Chapter 1 General Introduction

---

of energy resources. The unsustainable and unstable nature of fossil fuels has caused the high correlation with the international situation, such as resource nationalism, diplomatic weapon usage of energy resources, political and military turbulence, natural disasters, accidents, strikes, terrorist attacks, piracy, and so on. For example, the Oil Shock in the 1970s caused the oil price surge in many countries, and the economy suffered from the recession.

Besides the energy security issues, traditional energy resources also suffer from the significant issues of pollution and unsafety. The generation of CO<sub>2</sub> during the consumption process of fossil fuels is being criticized for the global warming problem. In China, the consumption of coals for heating in the winter season has caused the air pollution issue by sulfur oxides and dust contained in the exhaust gas, which forces the government to close down the plants and transfer to cleaner energy resources. Nuclear energy seems to have become a solution, which needs less space and cost. However, the Chernobyl disaster and Fukushima Daiichi nuclear disaster are reminding us of the great side effects. It has been an urgent issue to find alternative safer solutions.

One solution to the previously discussed issues is to develop renewable energy resources. As renewable energy resources exist over vast geographical areas, they are among the best alternatives to the concentrated traditional energy resources. Moreover, pollution and safety issues can be solved as well. The mainstream renewable energy resources are wind power, hydropower, geothermal energy, biomass, and solar energy, [23].

Wind energy is cultivated by wind turbines to transform mechanical energy into electric energy. There are on-shore and off-shore wind farms as wind farms have low energy density and require large space to install. One adverse effect caused by the installation of wind turbines is that the ecosystem of birds and fishes may be affected.

Hydro energy is harnessed from the energy of falling water or fast-running water. People build dams over the rivers to increase the height difference of water for larger gravitational potential energy. However, there has also been a concern that the dams may cause damage to the ecosystem.

Geothermal energy is generated from the earth's magmatic activity. We can use the

## Chapter 1 General Introduction

---

heat directly for hot spring or indirectly by turbines to transform into electricity. Biomass energy is a traditional renewable energy resource which is using materials from plants or animals. There have been concerns about the deforestation and the release of greenhouse gases when consuming biomass energy.

The solar energy has been regarded as a promising next-generation energy resource. PV solar cell devices, which are used to harvest solar energy, are being vibrantly developed. Although several kinds of PV solar cells have achieved high PCE of over 20%, the current issues in these solar cells include high cost, inflexibility, heavyweight, glare, and so on. There is an urgent need for the development of next-generation solar cells.

Among the above-mentioned promising resources, solar energy harvesting has attracted much attention for a long period due to the excellent accessibility over the universe. We can use sunlight to heat the water and cook or to produce electricity by PV solar cells.

Although renewable energy is emerging and promising, there are still several general issues hindering renewable energy development, such as the intermittency, grid development requirement, long payback period, and so on.

## 1.5 Solar Cells

As introduced in Section 1.4, solar cell is one kind of technologies that can harvest solar energy efficiently. The basic mechanism of a solar cell is about transforming photon energy into electric energy, as shown in Figure 1.11. The photon in the light will be converted into electron-hole pairs by semiconducting light-absorbing materials to recombine at the outer circuit for electrical current. As a result, the light-absorbing layer is the most important component in solar cells. Besides, there are other important components of the electrode materials, structures, and active area design. PCE and cost are the two fundamental properties for solar cells. However, both of them have not been developed sufficiently, which highly requires next-generation solar cells.

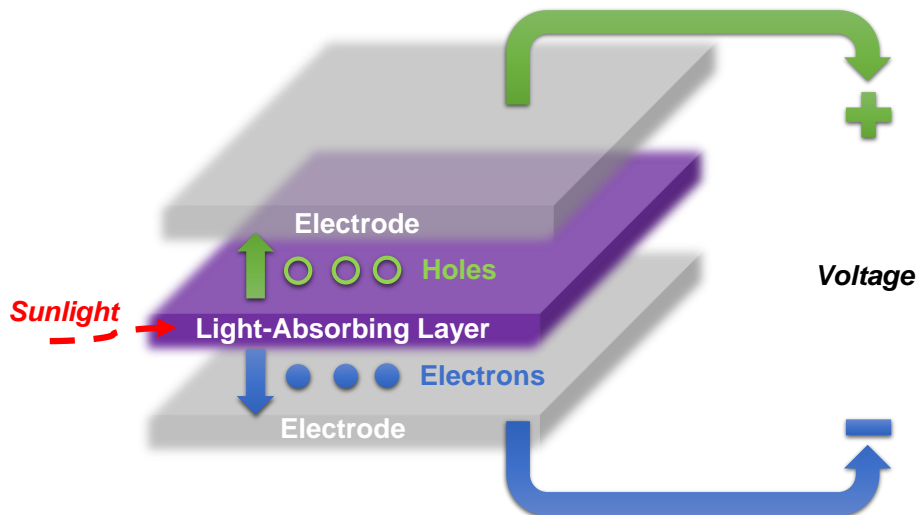


**Figure 1.11 Schematics illustrating how a solar cell works.**

To date, Si solar cells are the most mature technology among all solar cells owing to their superior stability and high efficiency. Their high performance comes from intrinsically stable Si substrates possessing a favorable bandgap to absorb light efficiently. There are mainly three types of Si solar cells: monocrystalline, multicrystalline, and amorphous Si solar cells. A PCE of over 26% has been achieved for single-junction monocrystalline Si solar cells in the laboratory [24], which is approaching the Shockley-Queisser limit of about 32% [25]. For the commercial single-junction crystalline cells that can be purchased in the market, they typically have the PCE of around 20%. Although

## Chapter 1 General Introduction

---

the Si solar cell technology is mature, it has many disadvantages. The synthesis of high-purity Si and the fabrication process of Si solar cells are expensive and thus result in the high price of Si solar cells without regard to subsidies. The fabrication process also consumes a large amount of energy that is not environmentally friendly. The brittleness of Si is also a major disadvantage for flexible applications.

Other types of commercialized solar cells include thin-film solar cells, such as the CdTe and CIGS solar cells. Moreover, for space-based solar cells, because we care the efficiency more than the cost, GaAs thin-film solar cells have been used with high efficiency as well as high cost.

From the market share in Figure 1.12, we can find that Si solar cells are occupying over 95% of the PV solar cell market [26]. The global solar energy market size has been estimated by Allied Market Research to reach \$422 billion by 2022 [27]. This is highly correlated with the policies as Si solar cell's intrinsic price still cannot beat the traditional energy resources. However, the macro trend is a continuously growing curve as transferring to clean energy resources has been a global consensus.

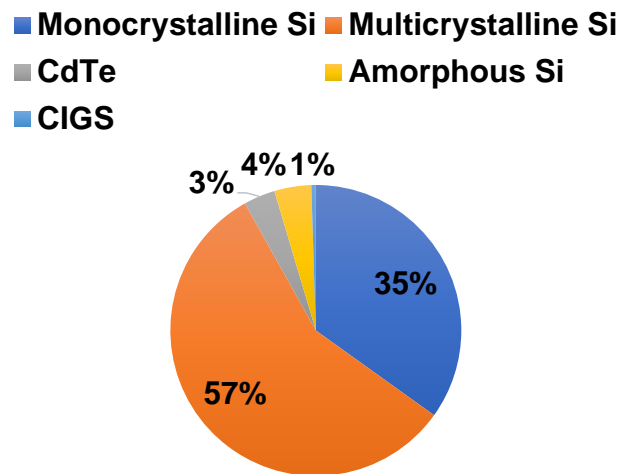


**Figure 1.12 Solar cell market share by solar cell type.**

There are also several kinds of "tailoring" methods to boost the PCE of solar cells. Most of them are playing with the light. For example, anti-reflection coating using polymer material can reduce light reflection and thus promote light absorption. The

## Chapter 1 General Introduction

---

concentration method can use a convex lens to have more light concentrated on the identical active area. The texture method is another way of trapping more sunlight in the light absorption layer by making the surface rougher, such as a pyramid structure.

As PV market is still highly policy-oriented, the FiT is a widely implemented policy to facilitate the market development of renewable energy resources, mostly solar cells. The current mechanism for FiT is: first, businesses of companies and individuals generate power from renewable energy farms; second, they can sell electricity to electric power companies, with a fixed tariff over a duration, which is determined by the government with respecting the opinions of special committees; third, the surcharge adjustment organization reimburses electric power companies for the purchase costs; fourth, the electric power companies sell electricity to electricity consumers by the price that is set by government. The government also approves the renewable-energy-harvesting facilities for businesses that meet the requirement of stability and efficiency. Although FiT has been effective for solar cell market development, a recent movement is that the governments are cutting the FiT with the goal of achieving grid parity. The grid parity means that the cost of renewable energy generated electricity is the same or even lower than that of traditional energy resources. As a result, the current PV solar cell industry should find ways to reduce their cost in order to maintain profits. This may be achieved by the development of novel low-cost solar cells.

Overall, the current issues of commercial solar cells include complex fabrication process, high cost, inflexibility, heavyweight, pollution of the semiconductor industry, energy storage, and so on. Besides, the uncertainty of investment by government and private investors is a general concern.

## 1.6 Development of Next-Generation Solar Cells

In order to address the above issues for traditional commercial solar cells, next-generation solar cells are being vibrantly developed in laboratories. There are mainly two approaches to developing next-generation solar cells, as shown in Figure 1.13. One is to replace the high-cost light-absorbing materials with novel low-cost materials that are more suitable for light harvesting. Because the solar spectrum has ununiform intensity, developing materials with better bandgap will have more light absorbed and electricity generated. The other one is to replace the high-cost electrodes with novel low-cost transparent conductive materials. For the former approach, novel organic and perovskite materials are being rapidly developed in the last two decades. For the latter approach, nanomaterials, especially the carbon nanomaterials, have been demonstrated to be the feasible alternative electrodes.

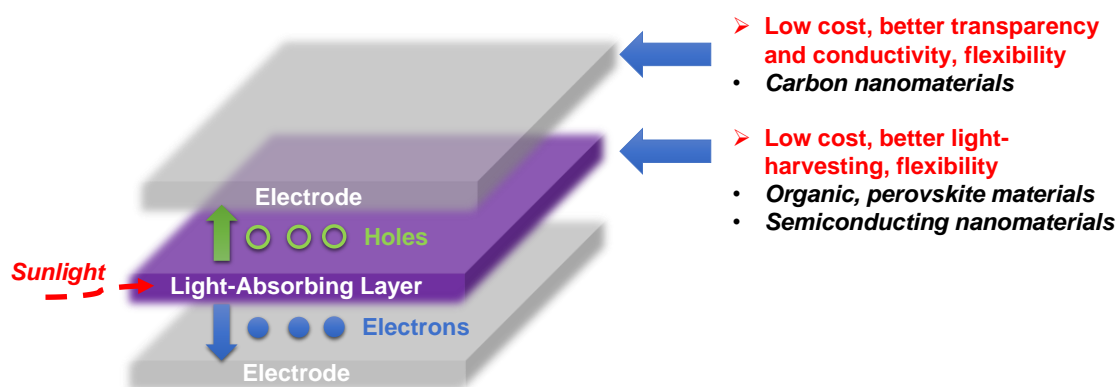


**Figure 1.13 Two approaches for developing next-generation solar cells.**

The organic solar cells are using low-cost organic semiconductors as the light-absorbing layer. Because of the liquid solution process, they can be easily scaled up. They typically consist of several layers of electron donor, electron acceptor, and electrodes. The highest PCE has been certified to be about 15% [28].

The perovskite solar cells, which are the rising star in the research of solar cells, are firstly reported in 2009 but have now reached an efficiency of over 20%. It uses lead halide-based material to function as the light-absorbing layer. Other layers include the electron transport and hole transport layers, as well as the electrodes.

## Chapter 1 General Introduction

---

The nanomaterial solar cells are being developed in order to further solve the problems that we found in next-generation solar cells. For the electrodes, organic and perovskite solar cells usually use ITO as the TCF. However, as ITO is made of the rare earth metal of Indium, it is highly subject to the price change of Indium. Moreover, ITO is brittle in mechanical property. In contrast, nanomaterials can also function as TCF in solar cells with flexibility. Because of these outstanding properties, people are using nanomaterials to replace ITO electrodes in solar cells. Moreover, for the light-absorbing layer, a huge library of semiconducting nanomaterials can be explored to have comparative advantages than traditional PV materials.

Overall, the current issues for these next-generation solar cells are the uniformity of materials caused by the immature synthesis methods, the relatively low efficiency, instability in the ambient environment, scale-up issue, toxicity of the perovskite materials, and so on.

## 1.7 Application of Low-Dimensional Nanomaterials in Solar Cells

In recent decades, low-dimensional nanomaterials are emerging to make considerable contributions to the development of solar cells due to the reduced usage of high-cost materials and tunable physical properties. Both the 0D, 1D, and 2D nanomaterials have been applied to solar cells, with different research stages.

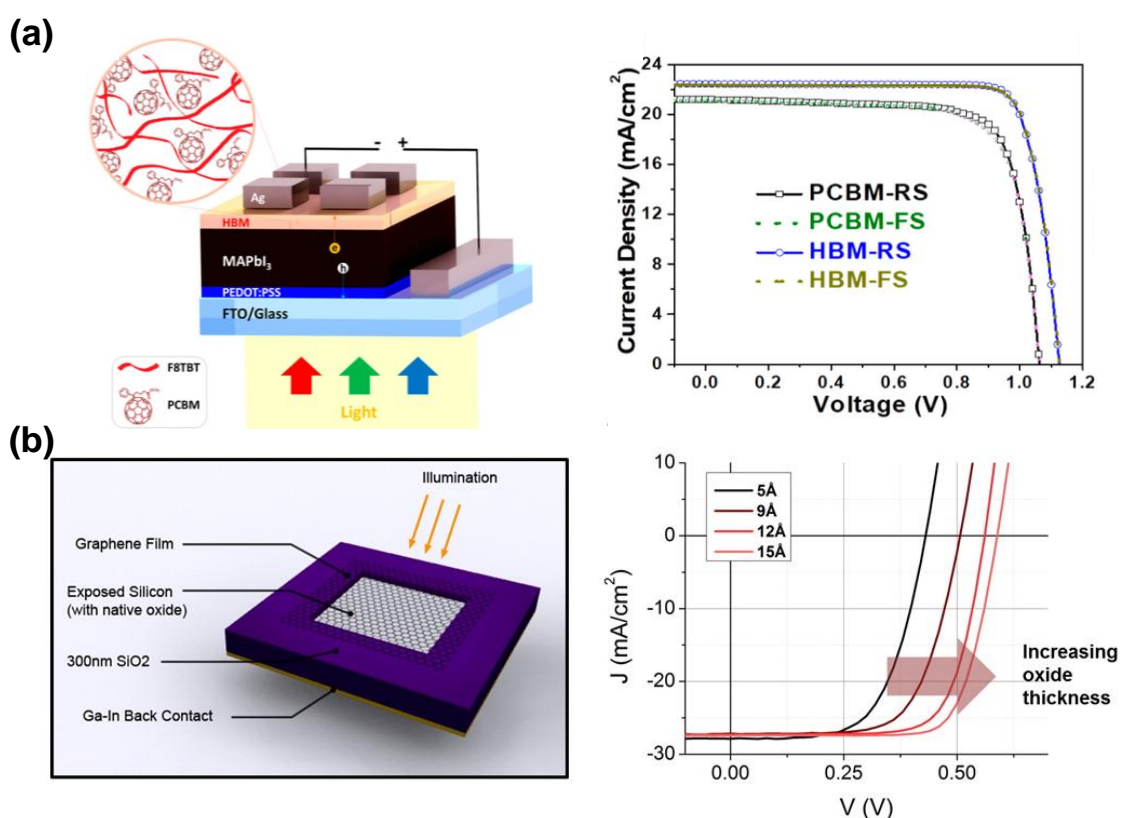


**Figure 1.14 (a) 20.6% inverted-type perovskite solar cells with polymer-optimized PCBM ETL. Reprinted from [29], Copyright (2019), with permission from ACS. (b) 12.4% pristine graphene-Si solar cells with the optimization of interfacial oxide layer. Reprinted from [30], Copyright (2015), with permission from ACS.**

In regard to 0D nanomaterials, PCBM, which is a derivative of fullerene, is a famous material for organic and perovskite solar cells. PCBM functions as the electron acceptor in solar cells, with the advantage of solution processability and device flexibility. The

## Chapter 1 General Introduction

perovskite solar cells using PCBM as part of the ETL can have a PCE of 20.6% by academic research [29], as shown in Figure 1.14a.

In regard to 1D nanomaterials, SWCNTs have been demonstrated to be promising in next-generation solar cells. Most SWCNTs have a length of 100 nm to several centimeters and a diameter of several nanometers, producing a high aspect ratio. As a result, SWCNTs have extremely high electrical conductivity, carrier mobility, mechanical strength, and flexibility; in addition, they are relatively lightweight. They also have high chemical stability because of the  $sp^2$ -bond of carbon atoms. Last but not least, carbon is earth-abundant that SWCNTs have a low-cost perspective. These superior properties endow SWCNTs with solar cell applications.

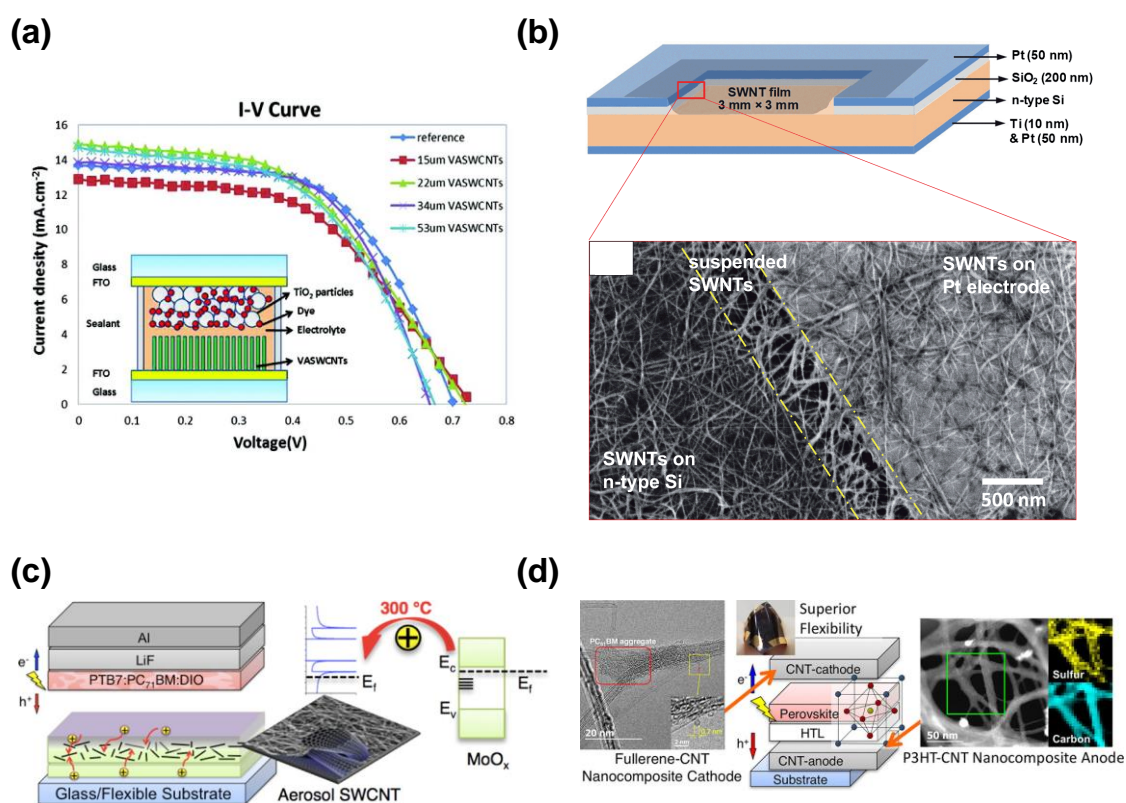


**Figure 1.15** (a) SWCNT dye-sensitized solar cells. Reprinted from [31], Copyright (2011), with permission from ACS. (b) SWCNT-Si solar cells. Reprinted from [32], Copyright (2014), with permission from RSC. (c) SWCNT organic solar cells. Reprinted from [33], Copyright (2015), with permission from ACS. (d) SWCNT perovskite solar cells. Reprinted from [34], Copyright (2017), with permission from ACS.

So far, there are mainly four kinds of solar cell applications of SWCNTs: dye-sensitized solar cells, Si solar cells, organic solar cells, and perovskite solar cells. As shown in Figure 1.15a, SWCNTs can act as the counter electrode in dye-sensitized solar cells which can have a comparable performance to Pt electrode [31]. As shown in Figure 1.15b, a TCF that constructed from SWCNTs can be applied to Si solar cells, in which the *n*-Si and SWCNT form heterojunction solar cells [32]. The PCE of SWCNT-Si solar cells has been improved by an order of magnitude over the last decade [32,35–39]. The detailed literature review and introduction of SWCNT-Si solar cells can be found in Chapter 3. In addition, as shown in Figure 1.15c, the SWCNT TCF can also be applied to organic solar cells for the purpose of replacing high-cost and inflexible ITO electrode [33]. The SWCNT TCF is also effective in perovskite solar cells, in which it can act as both the cathode and the anode [34,40], as shown in Figure 1.15d.

In regard to 2D nanomaterials, graphene can function as the TCF in solar cells to replace traditional TCFs. For example, the graphene-Si solar cells have been researched so far and a record PCE of 12.4% has been achieved for pristine solar cells [30], as shown in Figure 1.14b. For the function of TCF, SWCNT and graphene are similar, however, the structural variations of SWCNT give SWCNT TCF more variability in device structure and performance than graphene TCF [41]. Moreover, the network structure of SWCNT TCF makes it easier to scale up. Recently, there has been more and more research about the "2D nanomaterials beyond graphene". One major reason is that these materials have more variability in electronic properties than graphene while keeping the 2D layered structure. The detailed literature review and introduction of these pieces of research can be found in Chapter 4.

These low-dimensional nanomaterial solar cells are expected to bring about new markets. Their flexibility and lightweight nature can help the application in wearable devices. The lightweight nature can also promote the efficient design of other parts. For example, as the MoS<sub>2</sub> solar cells can be approximately 10 times lighter than Si solar cells because of the higher power density, we can allocate the reduced weight to other functional parts of the device: if it is a solar-cell-charged smartphone, larger size can be realized with the same weight. In addition, the semi-transparent solar cells enabled by thinner nanomaterials can be applied to windows to have hybrid functions.

## Chapter 1 General Introduction

---

There are also side effects of the commercialization of nanomaterial solar cells. For example, the emergence of new manufactures can cause pain to the traditional Si solar cell manufacturers. Also, the transfer from Si solar cells to nanomaterial solar cells in the same company may have a cannibalization effect, as well as the re-education problem for exiting employees. These traditional manufacturers may be the significant supporters for employment so that the government does not want them to fade away. The conflict between traditional and emerging manufacturers is an important issue for policymakers. In order to overcome this issue, the application pace should not be too fast, by a gradual transit to next-generation solar cells. With respect to the research development, because the technologies for nanomaterial solar cells are still immature, the government should balance the investment in academia and industry, with the policy tools of subsidies and tax.

## 1.8 Motivation and Purpose of this Dissertation

From the history of low-dimensional nanomaterials, especially at the genesis, carbon is a keyword. Why carbon is so outstanding? One reason is that carbon is one of the most abundant elements on the earth. The small size of carbon allows it to form multiple bonds with many small atoms and generate the compounds that are inevitable for everyone and almost everything. Most importantly, the allotropes of carbon are extremely stable to air as well as many chemicals. However, is carbon enough for everything? The answer is apparently no. Nowadays, we are talking about the "Diversity and Inclusion". The diversity of low-dimensional nanomaterial world is enriched by the addition of compounds with other elements. The new properties and combinations have fascinated us to explore them for the sake of human knowledge and development. For example, as graphene is a zero-bandgap material, MoS<sub>2</sub> can provide the advantage of opening the bandgap to be applied to various electronic devices as a 2D nanomaterial.

The diversity of low-dimensional nanomaterial world is also enriched by the method of "tailoring". As the properties of these materials can be tuned by carrier doping and structural transformation, we can develop different tailoring methods for different application purposes. This dissertation focuses on the tailoring methods of SWCNTs and MoS<sub>2</sub> based nanomaterials for the application purpose of solar cells.

The SWCNT TCF in SWCNT-Si solar cells is one of the crucial factors for improving performance. Both the conductivity and transmittance of SWCNT film need to be high in order to have excellent performance in SWCNT-Si solar cells, but this always includes a trade-off. Moreover, SWCNT shows a hole-transporting property in solar cells [33], which is tunable by carrier doping. As a result, the first purpose of this dissertation is to explore novel and outstanding tailoring methods for SWCNT TCF, and to apply the tailored SWCNT TCF to SWCNT-Si solar cells to achieve higher performance than the state of the art. Furthermore, this process can shed some light on the mechanisms of SWCNT-Si solar cells.

The second purpose of this research is to explore the possibility of applying SWCNTs and MoS<sub>2</sub> based nanomaterials in PV devices. From the research of SWCNT-Si solar cells, it is an intuitive idea that the part of Si can be replaced by semiconducting

## Chapter 1 General Introduction

---

low-dimensional nanomaterials. Although MoS<sub>2</sub> only has a thickness of nanometer level, as discussed in Chapter 4, its light-absorbing efficiency has been calculated to be about one order of magnitude higher than that of traditional PV materials. Thus, replacing Si by MoS<sub>2</sub> can have the advantages of cost-reduction, flexible applications, and gaining insights for developing low-dimensional nanomaterial PV devices. On the other hand, MoS<sub>2</sub> may also contribute to other functional layers of solar cells after tailoring. In order to achieve the second purpose, tailoring SWCNTs and MoS<sub>2</sub> based nanomaterials by synthesis and structural transformation methods are discussed in this dissertation, as well as the application of the synthesized SWCNTs and MoS<sub>2</sub> based nanomaterials in PV devices.

### 1.9 Organization of this Dissertation

This dissertation begins with a brief introduction of the world of low-dimensional nanomaterials, followed by the discussions of the structures and structure-related properties of SWCNTs and MoS<sub>2</sub>, which are the two basic low-dimensional nanomaterials that this dissertation focuses on. Then, renewable energy resources are introduced, with a specific emphasis on solar cells for solar energy harvesting. Subsequently, the development of next-generation solar cells is discussed, of which the nanomaterial solar cells are the applications that this dissertation studies for low-dimensional nanomaterials. The application of low-dimensional nanomaterials in solar cells are introduced in a general manner, with the detailed and specific introductions provided in the following experimental chapters. The motivation and purpose of this dissertation are also introduced in Chapter 1.

The general experimental methodology is introduced in Chapter 2. The first part is about the metrology for the low-dimensional nanomaterials and nanomaterial solar cells, with the discussions of the mechanisms of these methods. The second part is about the fabrication of SWCNT-Si solar cells and the properties of the as-fabricated pristine SWCNT-Si solar cells. The third part is about the structure of MoS<sub>2</sub> LPCVD system and the reactions during CVD process. The specific experimental methodology will be introduced in the following experimental chapters.

Chapter 3 presents the results of tailoring SWCNTs for application in SWCNT-Si solar cells. A novel polymeric acid of Nafion has been applied to SWCNT TCF to introduce the multifunction of acid doping, anti-reflection, and encapsulation into SWCNT-Si solar cells. The mechanisms for the Nafion-applied SWCNT-Si solar cells are discussed through various characterization and simulation methods.

In Chapter 4, the investigations of tailoring MoS<sub>2</sub> based nanomaterials and its application to PV devices are discussed. First, the results of the controlled synthesis of 2D MoS<sub>2</sub> nanomaterials are presented. Through the LPCVD system that I constructed, 2D MoS<sub>2</sub> monolayers can be synthesized after tuning various synthesis parameters. Second, a novel type of 1D vdW structure has been synthesized with MoS<sub>2</sub> as the semiconducting tube layer. Third, application of the as-synthesized SWCNTs and MoS<sub>2</sub>

## **Chapter 1 General Introduction**

---

based nanomaterials in PV devices are discussed with various device structures.

Finally, the summaries, my vision for next-generation solar cells, and the future perspectives of the research in this dissertation are presented in Chapter 5.

## Chapter 2      General Experimental Methodology

In this chapter, the general experimental methodology will be introduced, which is the base to conduct the research in this dissertation. The specific experimental methodology will be introduced in each experimental chapter.

### 2.1      Metrology of Low-Dimensional Nanomaterials

The experimental advances of low-dimensional nanomaterials can never be enabled without the development of metrological technology. As the scale of these nanomaterials is usually at nm level, we need to employ microscopy and spectroscopy to help us obtain the information of the low-dimensional nanomaterials that we produced.

#### 2.1.1      SEM

The resolution of optical microscopy  $\sigma$  can be defined as

$$\sigma = \frac{0.61 \times \lambda}{n \times \sin \theta} \quad (2.1)$$

where  $\lambda$  is the wavelength of light,  $n$  is the RI,  $\theta$  is one-half of the objective's opening angle. From this equation, it can be found that it is difficult to obtain the resolution that is less than the visible spectrum (400–700 nm). As a result, nanostructures that have sub-hundred-nanometer scale cannot be resolved using optical microscopy. Since electrons have a much smaller wavelength (the higher acceleration voltage, the smaller wavelength),

electron microscopy can have hundreds of times better resolution than that of the optical microscopy. SEM is one of the electron microscopies that obtains the image through detecting the second electrons scattered by the sample.

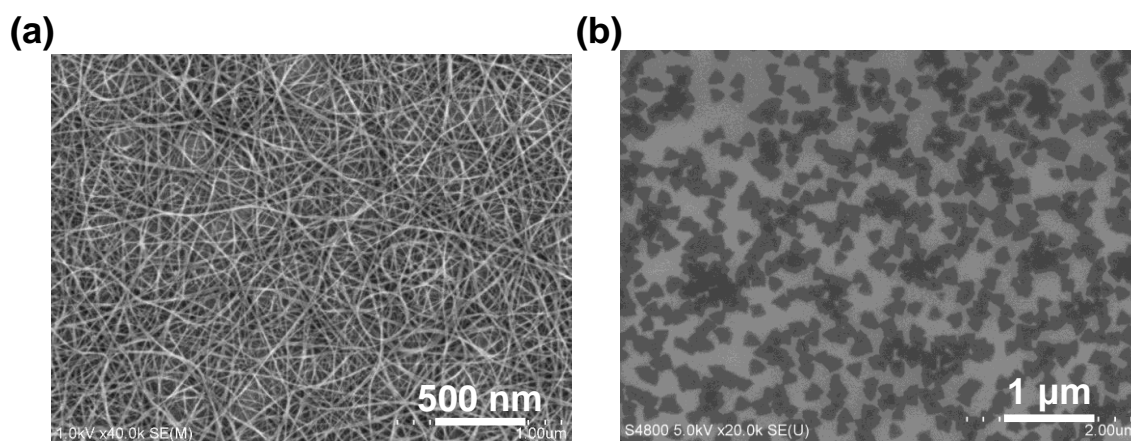


**Figure 2.1 SEM image of (a) an SWCNT film, and (b) CVD synthesized monolayer MoS<sub>2</sub>.**

Figure 2.1 shows the SEM images of vertically-aligned SWCNTs and monolayer MoS<sub>2</sub>. In practice, usually, 1.0 kV is selected for the imaging of SWCNTs, which avoids the damage to the sample while still retains a high resolution. For MoS<sub>2</sub> characterization, as MoS<sub>2</sub> is not as conductive as SWCNTs, a higher acceleration voltage of 5.0 kV is employed. In order to avoid the charging effect of the sample, a higher working distance of 30 mm is selected. In addition, an upper detector shows better resolution in the case of MoS<sub>2</sub> as the depth information is enhanced.

### 2.1.2 TEM

Besides SEM, there is another kind of electron microscopy that is even more powerful, which is called TEM. In SEM, the resolution is still not high enough to image

the catalysts of SWCNTs (the diameter is usually sub-10 nm) and also single SWCNT. However, TEM uses acceleration voltage of several hundred kV that makes the resolution high enough for catalysts, even the crystal planes and atoms. Being different from SEM, the TEM image is obtained through the detection of the transmitted electrons that get across the samples. As a result, the samples for TEM should be thin enough to allow electrons to get through them. The transmitted electrons are then focused by the objective lens into an image on the phosphor screen, or film, or CCD camera, depending on the user's needs. Figure 2.2a shows the scanned film of TEM image, on which the SWCNTs and catalysts are clearly confirmed if we enlarge it. Figure 2.2b shows the CCD image that was directly observed and saved on computer.

One superior ability of TEM is to characterize the catalyst nanoparticles and determine the chemical states of them. If the resolution is high enough, we can directly observe the lattice planes by TEM image, as shown in Figure 2.2c. By measuring the distance between each lattice plane, as well as the angle between different lattice planes, a chemical state of the nanoparticle can be determined. SAED is a way to study the chemical states of a large number of nanoparticles. Electrons that scattered by different lattice planes of the nanoparticles in the selected area will be collected into different rings on the patterns, as shown in Figure 2.2d. The radius of each ring  $R$  is defined as

$$R = \frac{L \times \lambda}{D_{hkl}} \quad (2.2)$$

where  $L$  is the camera constant (usually 80 cm or 60 cm for JEOL JEM-2000EX II),  $\lambda$  is the wavelength of the electron, and  $D_{hkl}$  is the lattice spacing of a lattice plane ( $h k l$ ). ( $h k l$ ) is the Miller index of lattice plane. The lattice information of crystals can be found from the databased of Powder Diffraction File. From the calculated lattice spacing as well

as the intensity of each ring, chemical states of the nanoparticles in the selected area can be determined. Moreover, TEM is also useful in characterizing the structure of nanotubes by taking nano-area electron diffraction patterns [42].

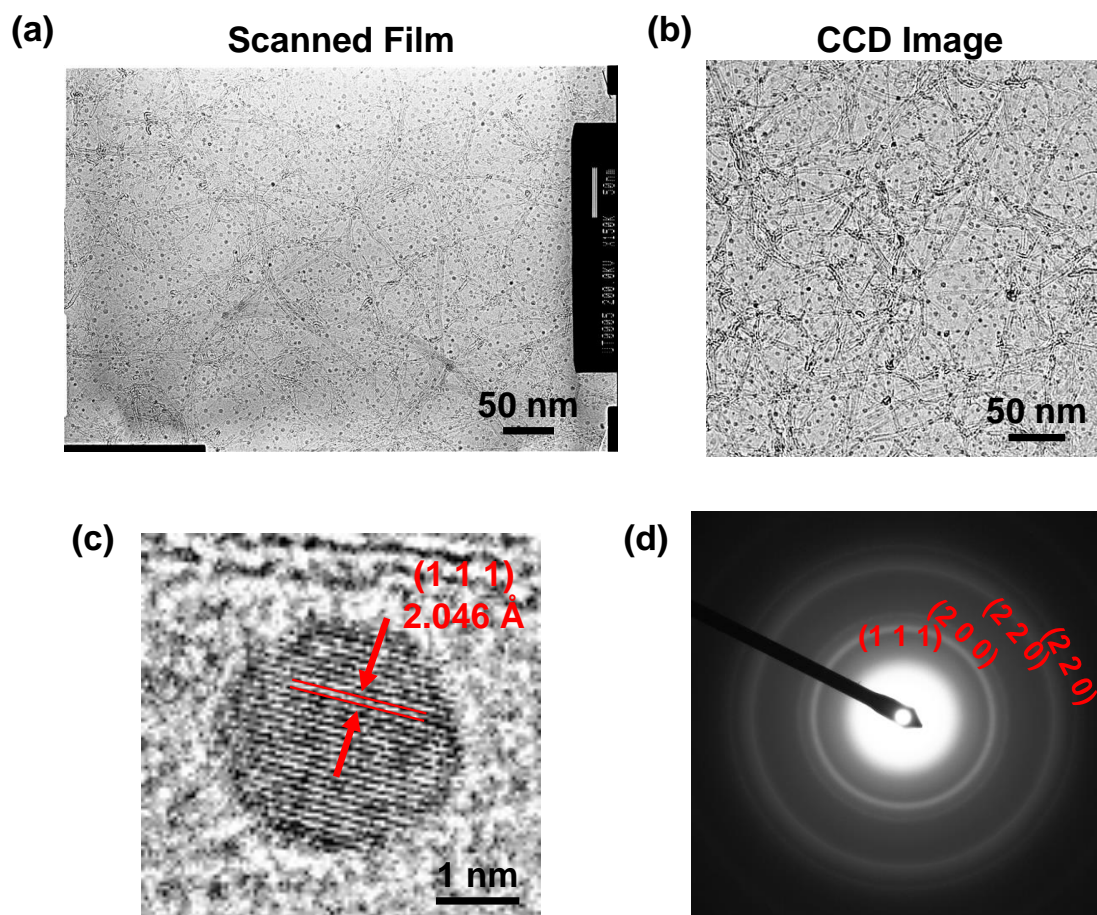


**Figure 2.2** (a) A scanned film of TEM. (b) CCD image of TEM. (c) Crystal planes of Co nanoparticles, with the lattice space of 0.2046 nm, which is assigned to (1 1 1) lattice plane. (d) SAED patterns of Co nanoparticles, with the assigned lattice planes on each diffraction ring.

### 2.1.3 Raman Spectroscopy

The Raman spectroscopy is a powerful and convenient optical tool to study low-

dimensional nanomaterials. It uses the information from Raman scattering, which is the inelastic scattering of a photon. When an incident light (usually a strong intensity laser beam) is shed on the material, a molecule in the material is excited to higher energy states by absorbing a photon. Then, a photon can be either elastically or inelastically scattered. The elastic scattering of a photon is called Rayleigh scattering, which means that the material then reemits a photon with almost the same energy as the original photon. In contrast, if a molecule does not relax back to the original energy state, a photon with lower energy than original photon is reemitted. This phenomenon is called Stokes Raman scattering. On the other hand, if the scattered photon has higher energy than the original photon, the phenomenon is called anti-Stokes Raman scattering. The wavenumber difference between the incident photon and the reemitted photon is Raman shift (in the unit of  $\text{cm}^{-1}$ ). These processes are illustrated in Figure 2.3.

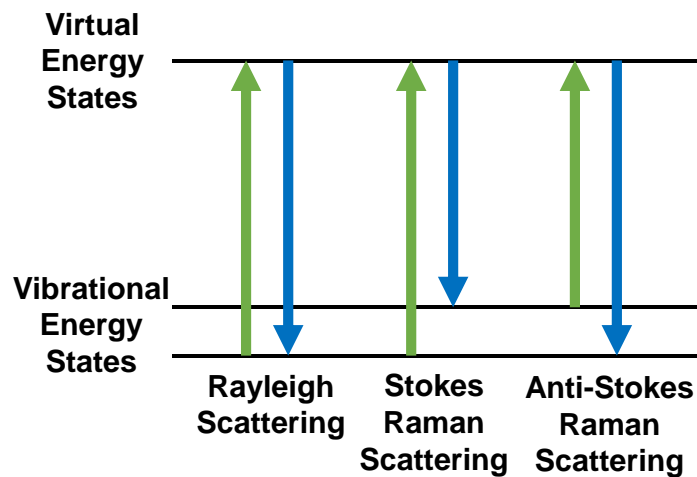


**Figure 2.3 (a) Example Raman spectrum taken from vertically-aligned SWCNTs.**

**The inset is the RBM. The excitation laser is 532 nm.**

### 2.1.3.1 Raman Spectroscopy of SWCNTs

The main features in the Raman spectra of SWCNTs are RBM, G band, and D band [8,10]. An example Raman spectrum of vertically aligned SWCNTs is shown in Figure 2.4.

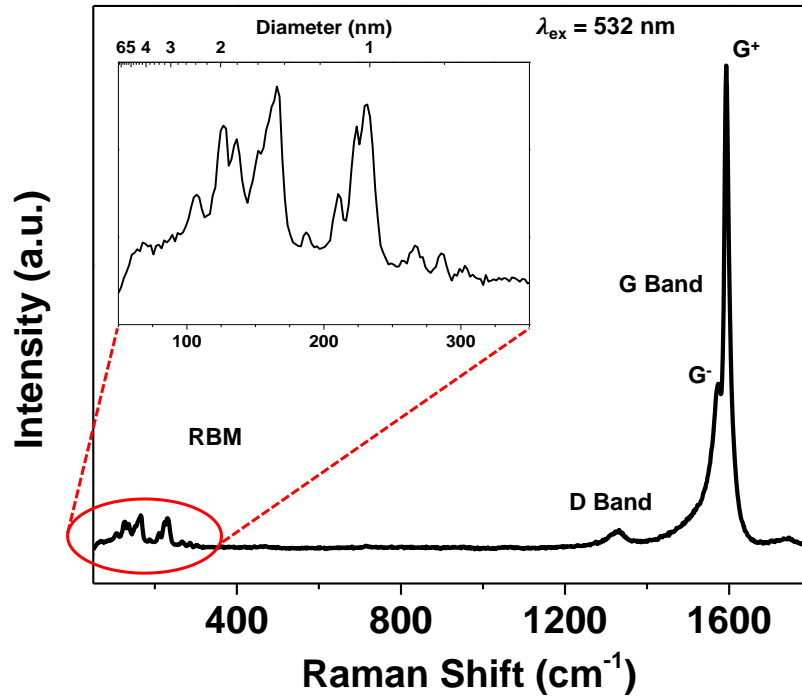


Figure 2.4 Example Raman spectrum taken from vertically-aligned SWCNTs. The inset is the RBM. The excitation laser is 532 nm.

RBM is a first-order Raman mode that generates from the coherent movement of all the carbon atoms in the radial direction of SWCNT. The frequency  $\omega_{RBM}$  has a range of 100–500 cm<sup>-1</sup>. According to the RBM-Diameter equation [43]:

$$\omega_{RBM} = 217.8/D_t + 15.7 \quad (2.3)$$

we can roughly calculate that the diameter of SWCNTs from the peaks in RBM. As

different chiralities of SWCNTs correspond to different  $E_{ii}$ , the excitation laser with the energy that is close to  $E_{ii}$  can give rise to a strong peak in RBM by resonant Raman effect. As a result, we need to use multiple excitation lasers to fully assign the chiralities of SWCNTs. This process of assignment can be guided by Kataura plots [44].

The dominant peak at  $\approx 1590 \text{ cm}^{-1}$  is the G band. It is a first-order Raman peak that corresponds to the in-plane vibrational mode of carbon atoms in SWCNT. The position of G band can be used to investigate the charge transfer of SWCNTs [45], which is employed in the doping research of SWCNTs. G band is split into  $G^+$  and  $G^-$  modes. The analysis of the relationship between these two modes can give information about the diameter as well as help identifying semiconducting or metallic SWCNTs [46].

Another band is called D band, which is the disorder-induced band at  $\approx 1350 \text{ cm}^{-1}$  that is related to the defects in the SWCNTs or the presence of amorphous carbon materials. The G/D ratio (intensity of G band/intensity of D band) is a direct method to characterize the crystallinity of SWCNTs.

### 2.1.3.2 Raman Spectroscopy of MoS<sub>2</sub>

The thickness of MoS<sub>2</sub> not only influences its electronic energy dispersion but also affects its phonon dispersion. Figure 2.5a shows the typical vibrational modes of MoS<sub>2</sub>. The most widely researched and useful modes are  $E_{2g}^1$  and  $A_{1g}$  modes, which depend remarkably on the thickness. Their Raman spectra and thickness-related properties are shown in Figure 2.5b and c.  $E_{2g}^1$  is an in-plane vibration mode, and the peak has red-shift with the increase of thickness;  $A_{1g}$  is an intralayer vibration mode, the peak has blue-shift with the increase of thickness. This characteristic provides a corresponding relationship between the peak-to-peak distance  $\Delta$  and thickness, which is a convenient method for

identifying the number of layers in MoS<sub>2</sub>. In general,  $\Delta \leq 20 \text{ cm}^{-1}$  corresponds to monolayer, while  $20 \text{ cm}^{-1} < \Delta \leq 22 \text{ cm}^{-1}$  means bilayer. The detailed explanation of this phenomenon can be found in the literature [47]. The excitation laser for characterizing the MoS<sub>2</sub> related nanomaterials in this dissertation is 532 nm.

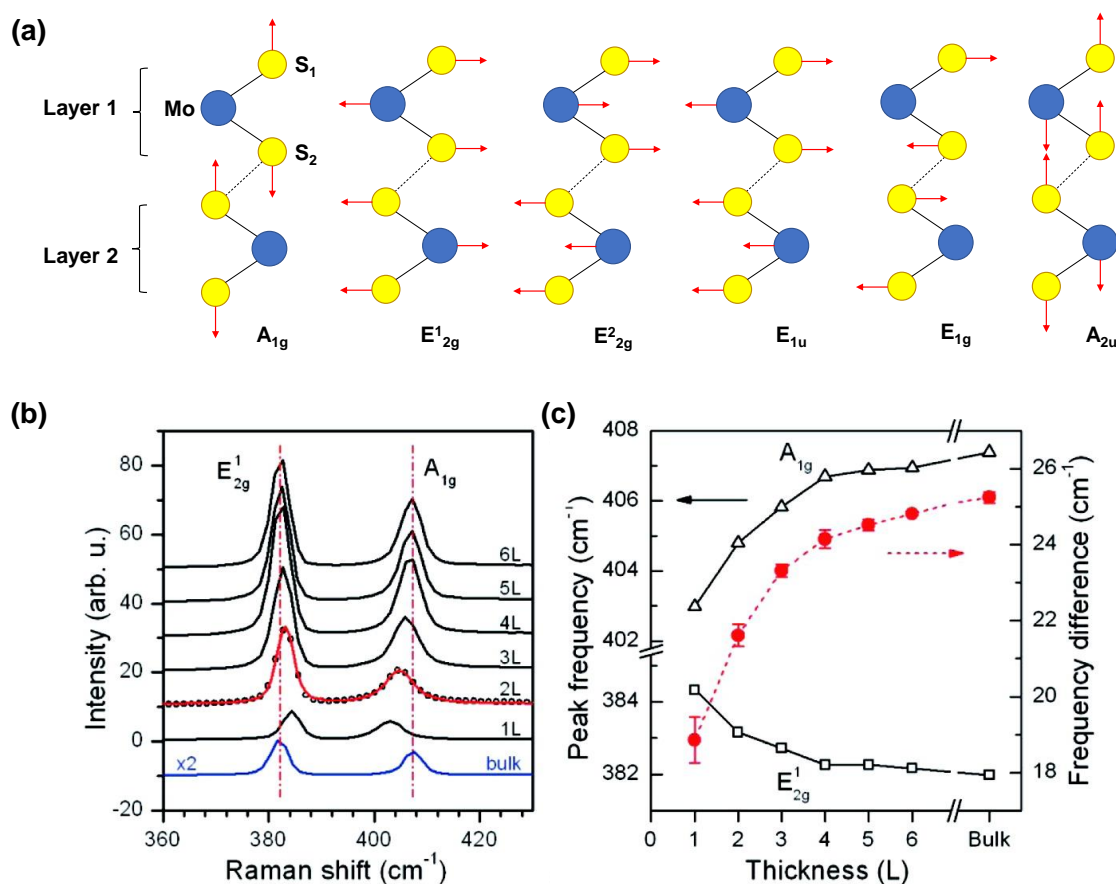


**Figure 2.5** (a) Typical atomic vibrational modes of MoS<sub>2</sub>. (b) Raman spectra of thin and bulk MoS<sub>2</sub> as a focus on E<sup>1</sup><sub>2g</sub> and A<sub>1g</sub> modes. (c) Raman shifts of E<sup>1</sup><sub>2g</sub> and A<sub>1g</sub> modes (left vertical axis) and their difference (right vertical axis) as a function of MoS<sub>2</sub> layer thickness. (b) (c) are reprinted from [48], Copyright (2010), with permission from ACS.

### 2.1.4 PL

PL measures the luminescence spectrum of materials. When the incident light with the energy larger than the material's bandgap is shed onto the material, the electrons in the material can be excited and reemits the photon with the energy equaling its bandgap.

As monolayer MoS<sub>2</sub> is a direct-bandgap material while other thicknesses are not, the information obtained by PL can tell us about the bandgap of MoS<sub>2</sub> as well as whether the MoS<sub>2</sub> is monolayer. Figure 2.6 shows a typical PL spectrum of a monolayer MoS<sub>2</sub> sample. The A exciton and B exciton are the two excitons that generated from the direct excitonic transitions in monolayer MoS<sub>2</sub>, while the difference is originated from the valence band spin-orbit coupling [19,20]. For indirect-bandgap MoS<sub>2</sub> samples that are not monolayer, such strong PL peaks are not observed.

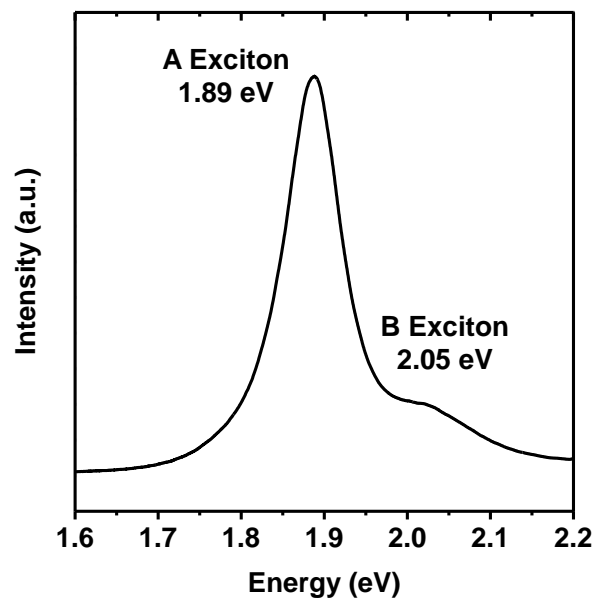


**Figure 2.6 Typical PL spectrum of monolayer MoS<sub>2</sub>. The positions of A exciton and B exciton are written beside the peaks.**

In practice, PL can be obtained by the same instrument for Raman spectroscopy. Because the grating limits the detectable range, it is being rotated during the PL measurement to have a wider PL spectrum.

### 2.1.5 UV-Vis-NIR Spectroscopy

UV-Vis-NIR spectroscopy can give three characteristics of materials, absorbance ( $A$ ) or absorptance ( $A'$ ), transmittance ( $T$ ), and reflectance ( $R$ ). These three characteristics have the following relationship:

$$1 = A' + T + R \quad (2.4)$$

In practice,  $A$  is directly measured instead of  $A'$ .  $A$  and  $T$  have the following relationship:

$$A = -\log_{10} T \quad (2.5)$$

while  $I_0$  is the incident light intensity, and  $I$  is the received light intensity.  $T$  and  $R$  are both measured by the ratio of received light intensity to induced light intensity:

$$T = \frac{I}{I_0}, R = \frac{I'}{I_0} \quad (2.6)$$

The difference is, in the transmission measurement, the received light is transmitted by the sample, while in the reflectance measurement, the light is reflected by the sample.

The transmittance of SWCNT film applied in solar cells can be measured by UV-Vis-NIR spectroscopy. An example of a transmittance spectrum is shown in Figure 2.7a. Usually, the transparency of SWCNT film is defined at the transmittance at the wavelength of 550 nm, which is the wavelength that has the highest spectral irradiance over AM1.5G spectrum. From the transmittance spectrum of SWCNT film, we can know how much light can pass through the film at a specific wavelength, which is a basic

characteristic of TCF.

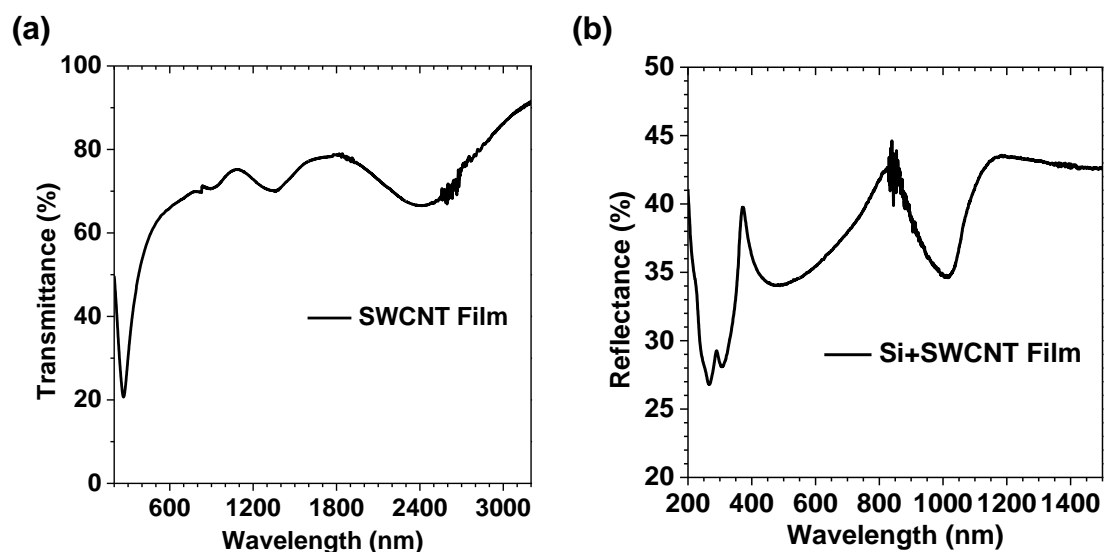


**Figure 2.7 (a) Transmittance spectrum of an SWCNT film. The transmittance at 550 nm is 90.1%. (b) Reflectance spectrum of SWCNT film on Si.**

A typical reflectance spectrum of SWCNT film on Si is shown in Figure 2.7b. From this spectrum, we can characterize the reflectance ability of the sample. For solar cells, it is better to have lower reflectance to allow the light-absorbing layer to absorb more light, especially around the visible wavelength range.

### 2.1.6 XPS

XPS is a powerful tool to obtain the chemical information of materials. All-elements XPS depth profile can provide information regarding the thickness of the sample. Ar sputtering is required for depth profile, which is a destructive method.

The X-ray source was Al-K $\alpha$  (1486.6 eV) operating at 24.2 W, and the charge-up shift of binding energies was corrected by referring to the C 1s peak at 284.6–285.0 eV.

The analysis was performed using MultiPak. An example of the Co 2*p* region in the XPS spectrum of Co<sub>3</sub>O<sub>4</sub> crystal is shown in Figure 2.8.

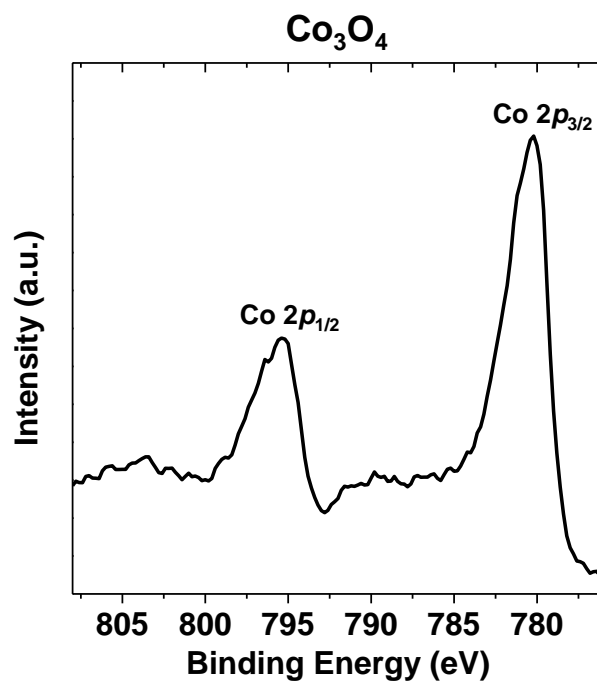


Figure 2.8 Co 2*p* region in the XPS spectrum of Co<sub>3</sub>O<sub>4</sub> crystal.

## 2.2 Metrology of Nanomaterial Solar Cells

In order to understand the nature of nanomaterial solar cell and gain insights into how to improve the solar cell, metrology of nanomaterial solar cells includes electrical characterizations of both the nanomaterial and the solar cell.

### 2.2.1 $J$ - $V$ Characterizations

The performance of SWCNT-Si solar cells was characterized by semiconductor parameter analyzer.  $J$ - $V$  curves are the basic characteristics of solar cells. AM1.5G illumination (Figure 2.9) was generated by solar simulator to measure the light current of solar cell. The dark current of solar cell was measured under dark condition.

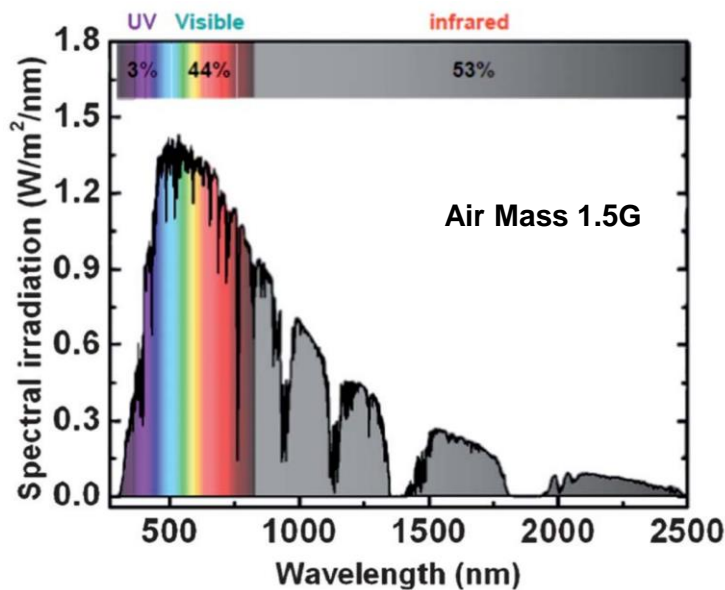


Figure 2.9 AM1.5G spectrum. Reprinted from [49], Copyright (2012), with permission from RSC.

Figure 2.10a shows the typical  $J$ - $V$  light characteristic of SWCNT-Si solar cell. The

PCE is defined as

$$PCE(\%) = \frac{P_M}{P_{AM1.5G}} \times 100 \quad (2.7)$$

where  $P_M$  is the maximum power point of the  $J$ - $V$  curve.  $P_{AM1.5G}$  is  $100 \text{ mW/cm}^2$ .  $J_{SC}$  is the current through the solar cell when the voltage across the solar cell is zero.  $V_{OC}$  is the maximum voltage available from a solar cell, and this occurs at zero current. The FF is defined as

$$FF(\%) = \frac{P_m}{J_{SC} \times V_{OC}} \times 100 \quad (2.8)$$

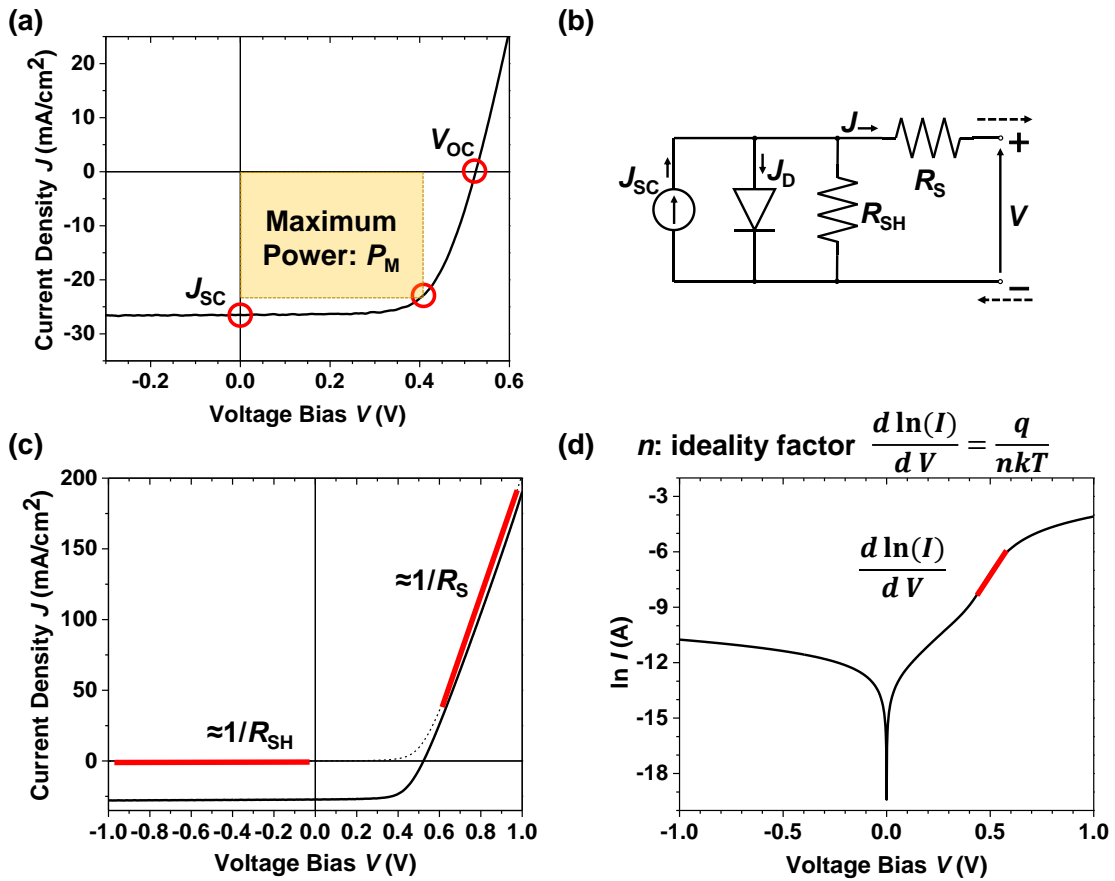


Figure 2.10 (a)  $J$ - $V$  light characteristics of a solar cell. (b) Equivalent circuit of a solar cell. (c)  $J$ - $V$  light and dark characteristics of a solar cell, with the schematics for the calculation of  $R_S$  and  $R_{SH}$ . (d) Calculation of the ideality factor  $n$ .

Figure 2.10b shows the equivalent circuit of a solar cell. In this circuit, the series resistance  $R_S$  and shunt resistance  $R_{SH}$  are also the important parameters of a solar cell. A direct and approximated calculation way for  $R_S$  and  $R_{SH}$  is from the dark current of solar cell, as shown in Figure 2.10c. When  $R_S \ll R_{SH}$ , the slope of the linear curve beyond  $V_{OC}$  is the reciprocal value of  $R_S$ , and the slope of the linear curve at the left of origin is the reciprocal value of  $R_{SH}$ .

Another important value for Si solar cell is the ideality factor  $n$ , which shows how close a solar cell is to an ideal diode. The ideality factor  $n$  is defined as

$$n = \frac{q}{\frac{d \ln(I)}{dV} kT} \quad (2.9)$$

where  $q$  is the absolute value of electron charge,  $k$  is the Boltzmann's constant,  $T$  is the absolute temperature.  $\frac{d \ln(I)}{dV}$  can be generated from the slope of  $I$ - $V$  curve on a logarithmic scale ranging from 0.45 V to 0.55 V, as shown in Figure 2.10d. Normally, the ideality factor of Si solar cell should be as close as 1 in order to be an ideal diode.

### 2.2.2 Four-Point Probe Measurement

Besides the transmittance, the sheet resistance is also a basic characteristic of TCF. The sheet resistance of the SWCNT films was measured by a four-point probe method.

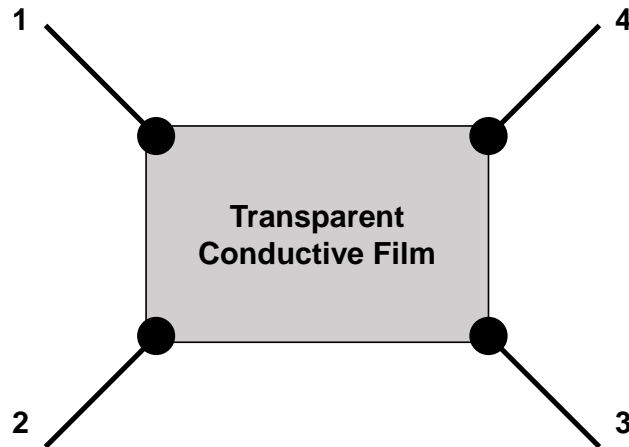


**Figure 2.11 Schematic of four-point probe measurement using van de Pauw method.**

As shown in Figure 2.11, the van der Pauw method was used for the measurement [50], which requires four times' measurements:

- 1) apply current at probe 1 and 2, and measuring the voltage at probe 3 and 4 ( $V_{12,34}$ );
- 2) apply current at probe 3 and 4, and measuring the voltage at probe 1 and 2 ( $V_{34,12}$ );
- 3) apply current at probe 2 and 3, and measuring the voltage at probe 4 and 1 ( $V_{23,41}$ );
- 4) apply current at probe 4 and 1, and measuring the voltage at probe 2 and 3 ( $V_{41,23}$ ).

The average sheet resistance of each measurement was then calculated, which are  $R_{12,34}$ ,  $R_{34,12}$ ,  $R_{23,41}$ , and  $R_{41,23}$ , respectively. The van der Pauw formula is defined as

$$e^{-\pi R_{\text{vertical}}/R_{\text{sheet}}} + e^{-\pi R_{\text{horizontal}}/R_{\text{sheet}}} = 1 \quad (2.10)$$

where

$$R_{\text{vertical}} = \frac{R_{12,34} + R_{34,12}}{2} \quad (2.11)$$

and

## Chapter 2 General Experimental Methodology

---

$$R_{\text{horizontal}} = \frac{R_{23,41} + R_{41,23}}{2} \quad (2.12)$$

and  $R_{\text{sheet}}$  is the sheet resistance of the measured film.

## 2.3 SWCNT-Si Solar Cells

### 2.3.1 Synthesis of SWCNT Film

The SWCNT films were synthesized by an aerosol (floating catalyst) CVD method based on ferrocene vapor decomposition in a CO atmosphere [51,52]. The catalyst precursor was vaporized by passing room temperature CO through a cartridge filled with ferrocene powder. The flow containing ferrocene vapor was then introduced into the high-temperature zone of a ceramic tube reactor through a water-cooled probe and mixed with additional CO. To obtain the stable growth of SWCNTs, a controlled amount of CO<sub>2</sub> was mixed with the CO carbon source. SWCNTs were directly collected downstream of the reactor by filtering the flow through a nitrocellulose or silver membrane filter (Millipore Corp., USA; HAWP, 0.45 μm pore diameter). The collection time is the determining factor for the transparency of SWCNT film, which results from the different densities of SWCNTs and the different thicknesses of film. Typically, TCF60, TCF70, TCF80, and TCF90 SWCNT films are named for four different transparencies.

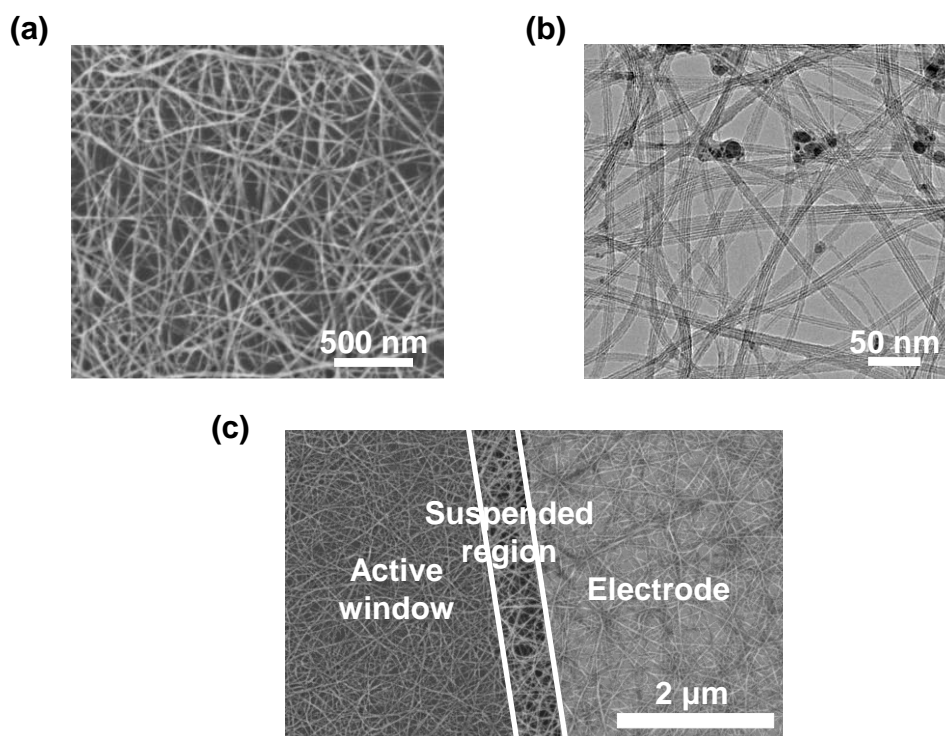


**Figure 2.12 (a) SEM image of a TCF90 SWCNT film. (b) TEM image of a TCF90 SWCNT film. (c) SEM image of a TCF90 SWCNT film on SWCNT-Si solar cell. The contrast is clear for active window, suspended region, and electrode.**

As shown in the SEM image of Figure 2.12a, the morphology of SWCNTs in TCF90 was long and straight. They were bundled and thus the diameter of the bundle from SEM was large. These SWCNTs were well-dispersed to be relatively uniform. From the TEM image in Figure 2.12b, bundles of SWCNTs were observed very clearly, and the Fe catalyst particles also remained in the film. In Figure 2.12c, the TCF90 film on SWCNT-Si solar cell was characterized by SEM. There is a suspended region of SWCNT-Si contact between the active window and electrode, but this region only has a width of less than 1 μm so it can be ignored compared to the 3-mm-width active window.

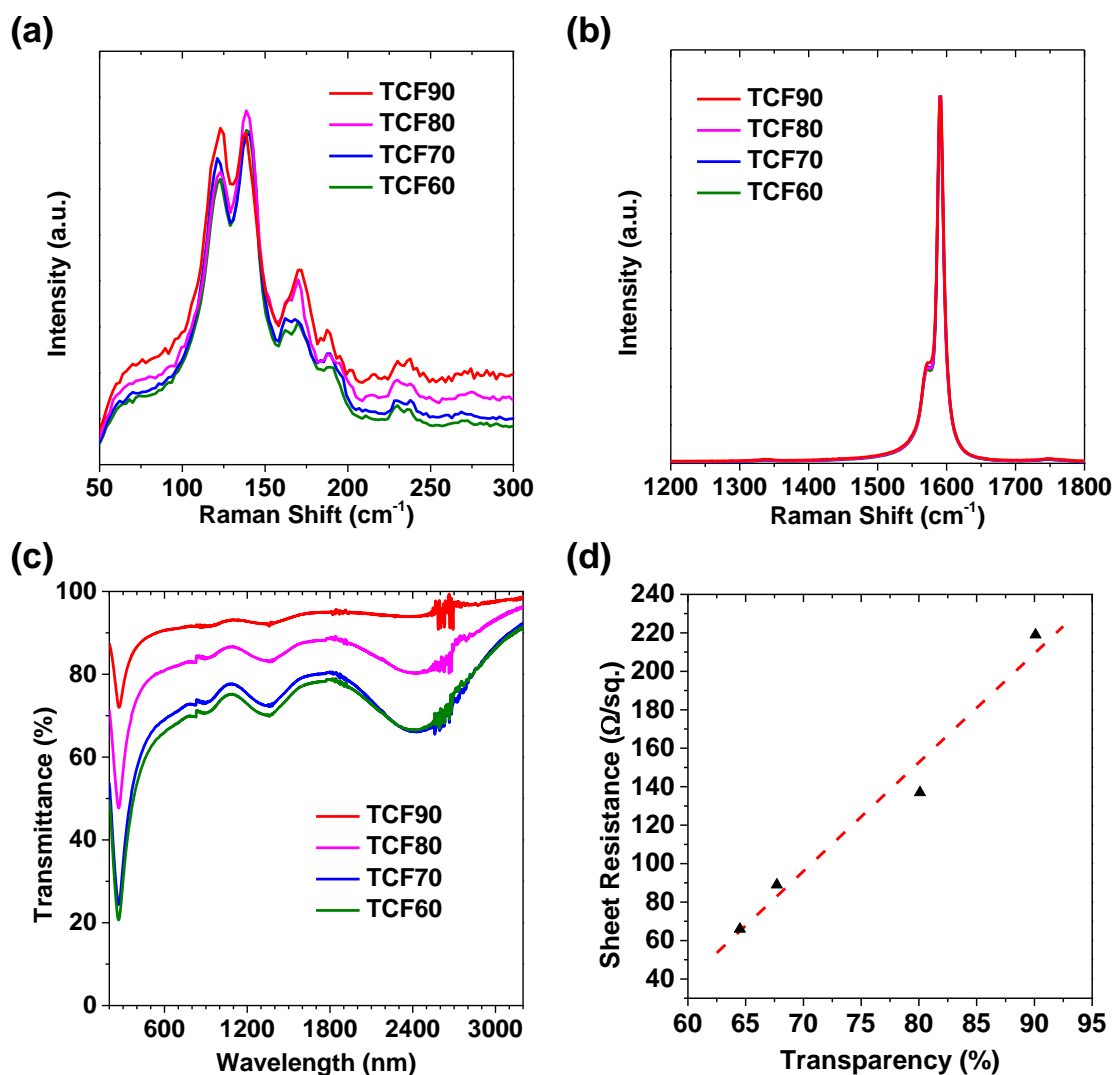


Figure 2.13 Characterizations of TCF60, TCF70, TCF80, and TCF90 SWCNT films.

(a) RBM region of Raman spectra. The excitation laser is 532 nm. RBM was normalized by G band. (b) G/D band region of Raman spectra. (c) Transmittance spectra. (d) Relationship between sheet resistance and transparency. The red dashed line shows a near-linear relationship, which is fitted by ordinary least squares regression model.

The Raman characteristics of the TCF60, TCF70, TCF80, and TCF90 SWCNT films

under the laser excitation of 532 nm are shown in Figure 2.13a and b. The RBM in Figure 2.13a shows that all the films had almost the same types of SWCNTs, with the diameter mainly ranging  $\approx 1.8$  nm. The G band in Figure 2.13b shows the extremely high G/D ratio (higher than 80), indicating the high crystallinity of these films.

The transmittance spectra of the TCF60, TCF70, TCF80, and TCF90 SWCNT films over the wavelength range of 200 nm to 3200 nm are shown in Figure 2.13c. The transparencies at 550 nm were characterized as 64.5%, 67.7%, 80.1%, and 90.1%, respectively.

The sheet resistance of the TCF60, TCF70, TCF80, and TCF90 SWCNT films were characterized by four-point probe measurement and the values are shown in Table 2.1 of 2.3.3. Figure 2.13d shows that the sheet resistance of SWCNT film has a near-linear relationship with film transparency.

### 2.3.2 Fabrication of SWCNT-Si Solar Cells

- 1) SWCNT-Si solar cell (Figure 2.14) was fabricated from a 4-inch *n*-type Si wafer with a 100-nm-thick SiO<sub>2</sub> layer on both sides (Kojundo Chemical Laboratory co., Ltd., 1–100  $\Omega\cdot\text{cm}$ ,  $\approx 521$   $\mu\text{m}$ ). The wafer was cut into 45 mm  $\times$  35 mm, which is larger than the size of sputter's sample holder. The reason for this larger size is that this size can ensure that the NaOH etching process is appropriately conducted as described in Step 3).

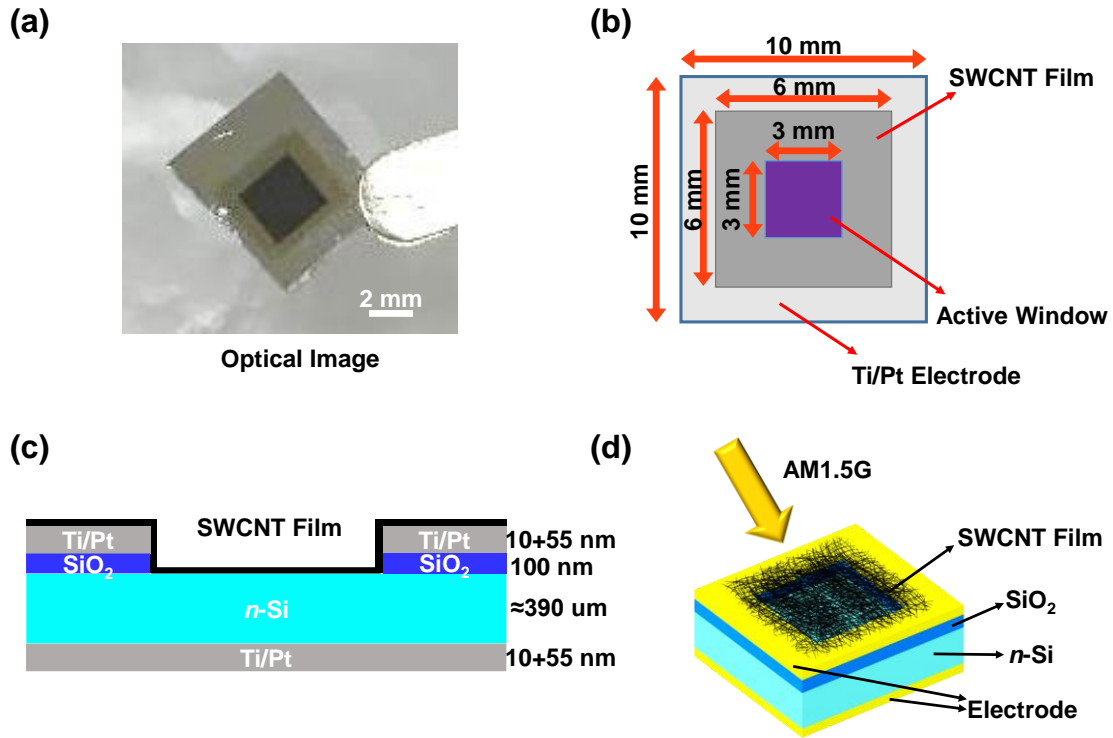


**Figure 2.14 Schematics of SWCNT-Si solar cells. (a) Optical image of an as-fabricated SWCNT-Si solar cell. (b) Top-view drawing. (c) Side-view drawing. (d) 3D drawing.**

- 2) The substrate was cleaned by RCA1 cleaning ( $\text{H}_2\text{O} : \text{NH}_4\text{OH} : \text{H}_2\text{O}_2 = 5 : 1 : 1$ ) at  $70\text{ }^\circ\text{C}$  (hotplate temperature:  $90\text{ }^\circ\text{C}$ ) for 30 min to remove the dust and organics on the surface. The concentration of  $\text{H}_2\text{O}_2$  solution is 30.0–35.5%. The concentration of  $\text{NH}_4\text{OH}$  solution is 28%. After RCA1 cleaning, the substrate was cleaned by distilled water.
- 3) The  $\text{SiO}_2$  layers on both sides of the substrate were removed by 5 M NaOH (Wako) at  $\approx 95\text{ }^\circ\text{C}$  for 20 min in a Teflon beaker (hotplate temperature:  $180\text{ }^\circ\text{C}$ , it is necessary to promote the heat conduction by Al foil and prevent the heat loss by the cover of Kim towel). After 20 min, the position of the substrate in the solution should be neither

## Chapter 2 General Experimental Methodology

---

in the bottom nor floating on the surface of the solution. This is to avoid the excess residue of NaOH on the substrate surface. After the etching process, the thickness of the Si substrate is  $\approx 390 \mu\text{m}$ .

- 4) The etched substrate was taken out from NaOH solution and quickly cleaned by RCA2 cleaning ( $\text{H}_2\text{O} : \text{HCl} : \text{H}_2\text{O}_2 = 5:1:1$ ) for 3 s. The concentration of HCl solution is 35.0–37.0%. This process should be precise to passivate the surface of Si and control the thickness of  $\text{SiO}_x$ . As the substrate was hot when taken out from NaOH, the actual RCA2 cleaning temperature was higher than room temperature.
- 5) After 3 s in RCA2 solution, the substrate was rinsed by distilled water for 3 times, 5 min each, and was blown dry by  $\text{N}_2$  gun.
- 6) The  $45 \text{ mm} \times 35 \text{ mm}$  substrate was cut into  $35 \text{ mm} \times 35 \text{ mm}$  to fit the sputter's sample holder.
- 7) The substrate was attached to sample holder by sealing the four edges with Scotch tape, and was put into sputter chamber to further dry out.
- 8) The back electrode of 10-nm Ti and 55-nm Pt was sputtered onto the backside of the etched substrate.
- 9) Physical masks (Scotch tape) for designated active areas were patterned onto the top surface of the substrate. The masks should be attached firmly to prevent the penetration of  $\text{SiO}_2$  when sputtering.
- 10) A 100-nm-thick  $\text{SiO}_2$  insulator layer and Ti/Pt electrode were sputtered onto the top surface of the substrate. The  $\text{SiO}_2$  layer was sputtered for two times, of which the interval is 30 min, in order to cool down the substrate.

## Chapter 2 General Experimental Methodology

---

- 11) The completed solar cell batch was cut into independent solar cells. The exposed Si of each solar cell also needs to be cut to avoid low  $R_{SH}$ .
- 12) The physical mask was removed and the active area was cleaned by IPA with Q tip. The residual IPA was blown dry by  $N_2$  gun. The XPS analysis of the surface after cleaning is shown in Appendix.
- 13) The SWCNT film was transferred onto the top surface of the substrate using a dry-transfer method [32]. In detail, an SWCNT film with membrane filter was cut off from the batch by scissors, and then was pressed onto the solar cell active area by another nitrocellulose membrane filter (Millipore Corp., USA; VSWP, 0.025  $\mu\text{m}$  pore diameter) to avoid contamination from gloves. It is necessary to use strong force and press many times to ensure the good contact between the film and the substrate, especially for the edge of the film.
- 14) The filtration paper attached to SWCNT film was removed by a cuspidal tweezer.
- 15) A drop of ethanol was dropped onto the SWCNT film to make good contact between SWCNTs and the substrate, as well as to densify the SWCNT film.
- 16) The SWCNT-Si solar cell was kept in air for about 1 day in order to have the ethanol evaporate fully.
- 17) The active area of each device was measured with an optical microscope (BX51, Olympus) and software (OLYMPUS Stream Start 2.1).
- 18) The SWCNT-Si solar cell was characterized by a semiconductor parameter analyzer system (Agilent 4156C) through probe station at ambient condition. For the light condition, the sunlight was simulated by a solar simulator (PEC-L01, Pecell Technologies) under AM 1.5G condition at an illumination intensity of 100  $\text{mW}/\text{cm}^2$ .

The light intensity was calibrated by a standard Si solar cell (BS-500BK, Bunkoukeiki). It is worth noting that the contact between the probe and electrode is important for a smooth curve.

### 2.3.3 Performance of Pristine SWCNT-Si Solar Cells

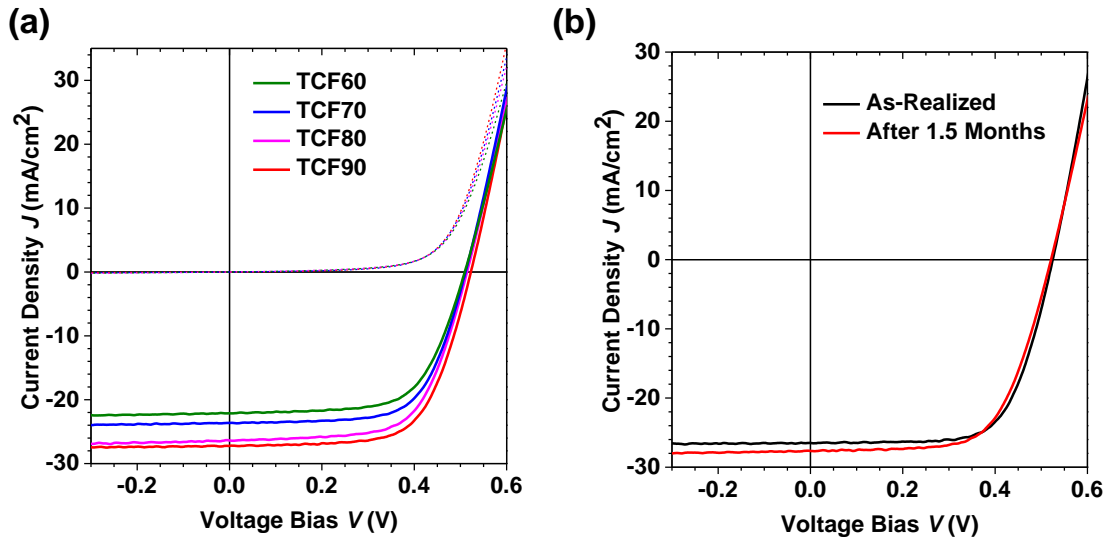


Figure 2.15 (a)  $J$ - $V$  curves of the SWCNT-Si solar cells with the TCF60, TCF70, TCF80, and TCF90 SWCNT films, under 100 mW/cm<sup>2</sup> AM1.5G illumination. The dashed lines are the dark current. (b)  $J$ - $V$  curves of the as-realized SWCNT-Si solar cell with TCF90 and were measured again after 1.5-month exposure in ambient environment, under 100 mW/cm<sup>2</sup> AM1.5G illumination.

The  $J$ - $V$  characteristics of the SWCNT-Si solar cells using the TCF60, TCF70, TCF80, and TCF90 SWCNT films were measured, as shown in Figure 2.15a. The obtained PCE values for the solar cells with the TCF60, TCF70, TCF80, and TCF90 SWCNT films were 7.3%, 8.0%, 8.8%, and 9.4%, respectively. The detailed characteristics of the fabricated solar cells are listed in Table 2.1. Although TCF60,

## Chapter 2 General Experimental Methodology

---

TCF60, and TCF80 SWCNT films had much lower sheet resistance than that of TCF90, their performances were not as good as that of TCF90 film SWCNT-Si solar cell. Only the  $FF$  retained the same level. The series resistance did not show a linear relationship with the sheet resistance, which indicates that in the range of tens to several hundred  $\Omega/\text{sq.}$ , the sheet resistance does not have much influence on the solar cell performance. The crucial factor is the transmittance of SWCNT film. Allowing more light to reach the Si surface and be absorbed by Si is a significant issue in SWCNT-Si solar cells. As TCF90 film generated the best performance, this film was utilized in SWCNT-Si solar cells for other investigations hereafter.

**Table 2.1 The PCE,  $FF$ ,  $J_{sc}$ , and  $V_{oc}$  of the SWCNT-Si solar cells with the TCF60, TCF70, TCF80, and TCF90 SWCNT films, as well as  $R_s$ ,  $R_{sh}$ , and  $n$ . The transparency and  $R_{sheet}$  characteristics of SWCNT films are also presented.**

SWCNT Film	Transparency (%)	$R_{sheet}$ ( $\Omega/\text{sq.}$ )	PCE (%)	$FF$ (%)	$V_{oc}$ (mV)	$J_{sc}$ ( $\text{mA}/\text{cm}^2$ )	$R_s$ ( $\Omega\cdot\text{cm}^2$ )	$R_{sh}$ ( $\Omega\cdot\text{cm}^2$ )	$n$
TCF60	64.5	66	7.3	64.7	510	22.1	2.6	2125	2.42
TCF70	67.7	89	8.0	66.0	512	23.6	2.3	3040	2.34
TCF80	80.1	137	8.8	64.6	516	26.4	2.6	1652	2.33
TCF90	90.1	219	9.4	65.5	524	27.2	2.3	4145	2.27

For the stability of SWCNT-Si solar cells, 1.5-month stability has been confirmed from this research. The  $J$ - $V$  curves are shown in Figure 2.15b. The detailed PCE,  $V_{oc}$ ,  $J_{sc}$ , and  $FF$  are shown in Table 2.2. The as-realized SWCNT-Si solar cell had a PCE of 9.4%. After 1.5-month exposure to ambient environment (typically 298 K, 60% humidity), the

absolute value of PCE only dropped about 0.1%. The  $J_{SC}$  increased whereas the FF and  $V_{OC}$  decreased.

This stability has been confirmed to be as long as 10 months in the previous research of our lab [32]. As this is the pristine SWCNT-Si solar cell without protection, the suitability of SWCNT-Si solar cell for practical applications has been indicated.

**Table 2.2 The PCE, FF,  $J_{SC}$ , and  $V_{OC}$  of the as-realized SWCNT-Si solar cell with the TCF90 SWCNT film and measured again after 1.5-month exposure in the ambient environment.**

TCF90	PCE (%)	FF (%)	$V_{OC}$ (mV)	$J_{SC}$ (mA/cm <sup>2</sup> )
As-Realized	9.4	67.5	526	26.5
After 1.5 Months	9.3	64.3	522	27.6

## 2.4 Synthesis of MoS<sub>2</sub>

### 2.4.1 LPCVD System

Compared with the CVD system of SWCNTs growth, the CVD system for MoS<sub>2</sub> growth is more complicated as we need to control the introduction and reaction process of two precursors. Here, a semi-automated LPCVD system has been constructed from scratch.

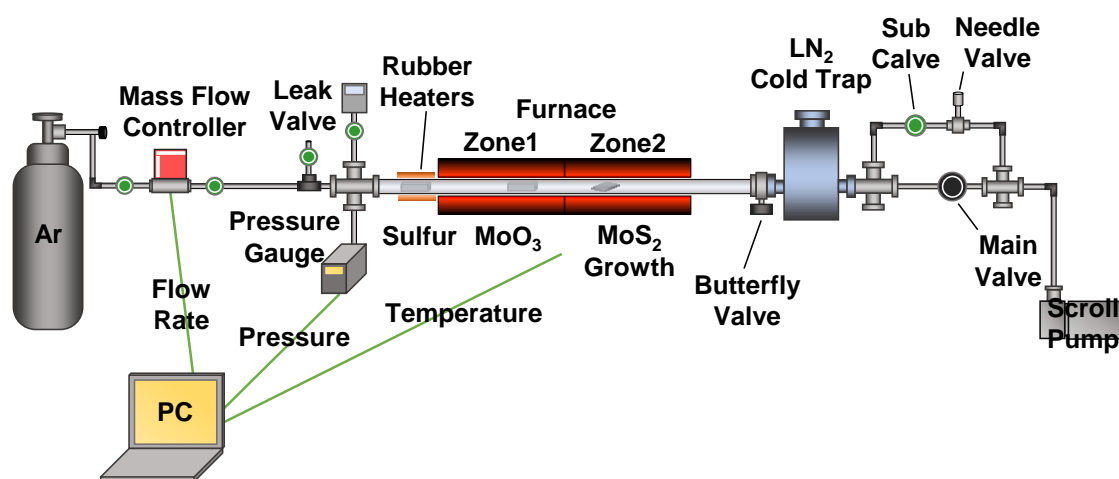


Figure 2.16 Schematics of the MoS<sub>2</sub> LPCVD system.

As shown in Figure 2.16, this LPCVD system consists of four parts: Carrier gas controlling system, reaction area, vacuum system, and CVD controlling software. The carrier gas is Ar, for the purpose of mass transfer. The mass flow controller (HORIBA STEC SEC-E40, full scale: 100 sccm) is used to control the flow of carrier gas at a precision of  $\pm 1$  sccm. A leak valve is set before the reaction area in order to introduce air when needed.

The main part of the reaction area is a two-zone ceramic furnace (Asahi Rika,

## Chapter 2 General Experimental Methodology

---

ARF2060-560-30KC), with a quartz tube of 2.54 cm (1 inch) in diameter and 1 m in length. One zone is for the sublimation of  $\text{MoO}_3$ , and another zone is for the growth of  $\text{MoS}_2$ . Because the sublimation temperature of S is relatively low ( $\approx 113\text{ }^\circ\text{C}$ ), we need an extra temperature-controlled zone outside the furnace. This zone is heated by rubber heaters that are wrapped around the quartz tube, and a fast-responsive thermal couple is attached to the quartz tube. In practice, the thermal influence from the furnace makes it difficult to control the temperature of the rubber heater. So instead of using only one rubber heater, two rubber heaters are employed, and the left one (6 inches in width) is controlled precisely for S sublimation while the right one (2 inches in width) is influenced by the furnace. As both rubber heaters are connected to the same output of temperature controller, we can ensure that the right one's temperature is higher than that of the left one to avoid the condensation of sublimated S before flowing into the furnace. Both the S and  $\text{MoO}_3$  powders are placed in quartz boats.

In the vacuum system, a scroll pump is used (ANEST IWATA, ISP-250C-SV). The base pressure is  $\approx 13\text{ Pa}$ . Because solid powders are used in this LPCVD system, in order to avoid these powders affecting the pump, a cold trap (Highlight Tech, KF40LN2CTS) is set between the reaction area and the pump. This cold trap is a Dewar bottle that is cooled down by liquid  $\text{N}_2$  ( $\approx -196\text{ }^\circ\text{C}$ ). The pressure of the system is measured by two pressure gauges, one for low pressure (Nidec Copal Electronics, PG-200-102AP-S), and one for the pressure higher than 13.33 kPa (CANON ANELVA, M-342DG-12-N25). The valves for controlling the pressure consist of a butterfly valve, a main valve, a sub valve, and a needle valve. The valves, pipelines, and connectors are mainly from Swagelok and Cosmotec.

In order to improve experimental automation and data visibility, a CVD controlling

## Chapter 2 General Experimental Methodology

software has been developed by LabVIEW (National Instruments), as shown in Figure 2.17a. This software reads and writes the growth parameters from mass flow controller, pressure gauge, and temperature controllers through DAQ-6001 (National Instruments) and Modbus Protocol. In addition, the flow rate can also be patterned by this software, which is more flexible and convenient for the experiment. The history of growth parameters is visualized and can be saved. As a result, the growth conditions can be monitored remotely and retrospectively. A picture of the as-built MoS<sub>2</sub> LPCVD system is shown in Figure 2.17b.

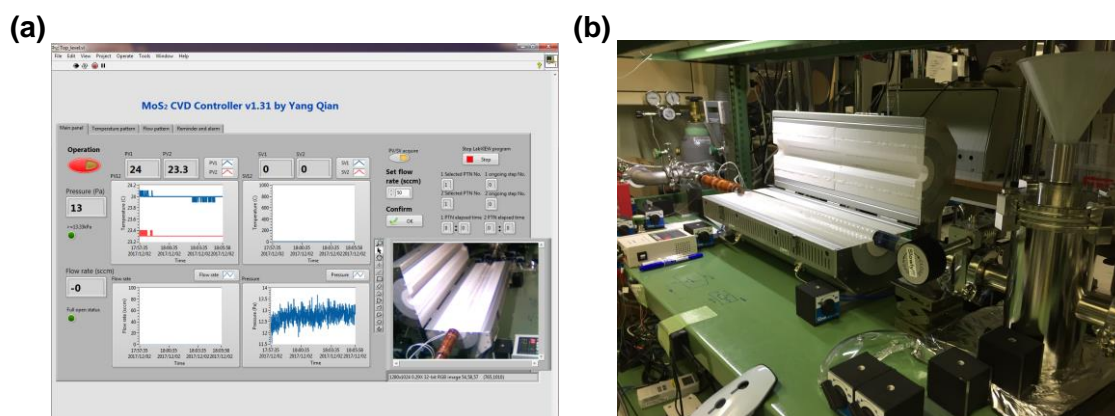


Figure 2.17 (a) Main interface of LPCVD controlling software. (b) Picture of the MoS<sub>2</sub> LPCVD system.

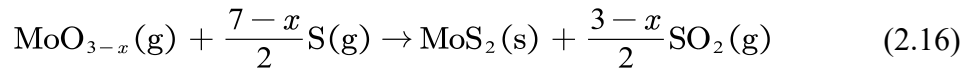
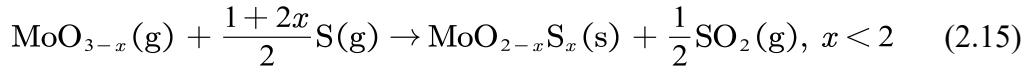
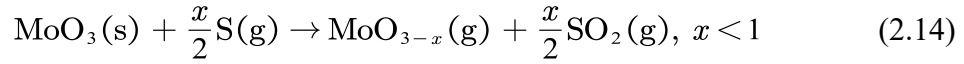
### 2.4.2 Reactions during CVD Process

For the synthesis of MoS<sub>2</sub> in LPCVD system, powders of S (sublimated, 99.0%, Wako) and MoO<sub>3</sub> (99.9%, Sigma-Aldrich) are used. The reaction between these two reagents to form MoS<sub>2</sub> are:



In order to grow high-quality MoS<sub>2</sub>, we need to consider the intermediate reactions.

During the reduction and sulfurization process of  $\text{MoO}_3$ , there are many intermediates, *e.g.*,  $\text{MoO}_{3-x}$ ,  $\text{MoO}_2$ ,  $\text{MoO}_{2-x}\text{S}_x$ , and so on. At the initial stage,  $\text{MoO}_3$  is partially reduced to  $\text{MoO}_{3-x}$  ( $x < 1$ ), which has higher volatility at a temperature lower than the melting point of  $\text{MoO}_3$  (795 °C). Then, if the amount of S in the gas phase is not enough, the  $\text{MoO}_{3-x}$  cannot be fully sulfurized and becomes  $\text{MoO}_{2-x}\text{S}_x$  ( $x < 2$ ); if the amount of S in gas phase is too high, although the  $\text{MoO}_{3-x}$  can be reduced to  $\text{MoS}_2$ , too much S is wasted and the reaction is too fast to have non-uniformity on substrate. This process is explained by the following chemical equations:



From the above chemical equations, controlling the amount and temperature of S and  $\text{MoO}_3$  is as important as controlling the substrate deposition temperature. More detailed investigations of the growth parameters will be presented in Chapter 4.

## **Chapter 3 Multifunctional Effect of *p*-Doping, Anti-Reflection, and Encapsulation by Polymeric Acid for High-Efficiency and Stable SWCNT-Si Solar Cells**

### **3.1 Literature Review and Introduction**

Increasing concerns surrounding energy issues today have led to the growing intensity of photovoltaic research [53]. Among various photovoltaics, Si solar cells are the type that made to the commercial market owing to their high PCE and superior stability [54,55]. Si solar cells in these days have become more important than ever ascribed to the emergence of perovskite-Si tandem solar cells [56–58]. Their high performance comes from intrinsically stable Si substrates, which have an ideal bandgap close to the Shockley-Queisser limit. In addition, Si solar cells possess a vital advantage of low manufacturing costs, attributed to the commercialization of *p-n* homojunction Si solar cells [59]. It is possible to amplify this trait by using planar heterojunction-type Si solar cells to reduce the fabrication cost. In fact, planar heterojunction Si solar cells have a better prospect than *p-n* homojunction Si solar cells in terms of room-temperature processability, which translate to cost reduction of up to 30% [59,60]. Such facility and low-cost advantages of the device can be enhanced even further by using CNTs or graphene [25,27,31,33,34,56–63]. These carbon electrodes can function as the *p*-type layer and electrode at the same time, which account for approximately 60% of the total

### Chapter 3 Multifunctional Effect of *p*-Doping, Anti-Reflection, and Encapsulation by Polymeric Acid for High-Efficiency and Stable SWCNT-Si Solar Cells

---

fabrication cost.

SWCNTs are eco-friendly and chemically stable transparent conductors [69,70]. Planar heterojunction solar cells with *p*-type SWCNTs and *n*-type Si have demonstrated high PCEs [27,32–34,56,59,62–63]. The unique feature of SWCNT-Si solar cells is the simple device configuration, which eliminates high-temperature diffusion and element doping processes [71], as well as minimizing the charge recombination loss at the Si interface [60,72]. Furthermore, the transparent SWCNT electrodes enable semi-transparent solar cells [36,73], which can potentially extend to tandem applications [74,75]. The performance of SWCNT-Si solar cells can easily be boosted by tailoring the SWCNT films through chemical modifications, such as chemical doping [36,39,62,64,68], anti-reflection coating [63,66,76], and encapsulation [77]. Thus far, HNO<sub>3</sub> [36,38,40] and MoO<sub>x</sub> [33,39] have been reported to dope SWCNTs effectively, improving the PCE of the device. However, those methods are limited in terms of doping effect durability. As for the anti-reflection effect, PMMA was reported to enhance the light absorption and encapsulate the device at the same time [77,78], but PMMA is easily dissolved by organic solvents and vulnerable to mechanical damage.

Herein, we report a polymeric acid, which can induce a multi-effect of permanent and strong *p*-doping, anti-reflection, and encapsulation of SWCNT-Si solar cells. Nafion, the polymeric acid was reported to dope carbon electrodes effectively and exhibit a permanent doping effect in organic light-emitting devices [79] and organic solar cells [80]. Interestingly, when Nafion was used in SWCNT-Si solar cells to dope the SWCNT top electrode, its effect was not only limited to a *p*-dopant, but led to a favorable anti-reflection effect and an encapsulation effect as well.

## 3.2 Experimental Methods

General experimental methods of the synthesis of SWCNT film and fabrication of SWCNT-Si solar cells have been presented in Chapter 2. Here, the specific methods for multifunctional-polymeric-acid-induced *p*-doping, anti-reflection, and encapsulation of SWCNT-Si solar cells are introduced.

### 3.2.1 Preparation of Dopant

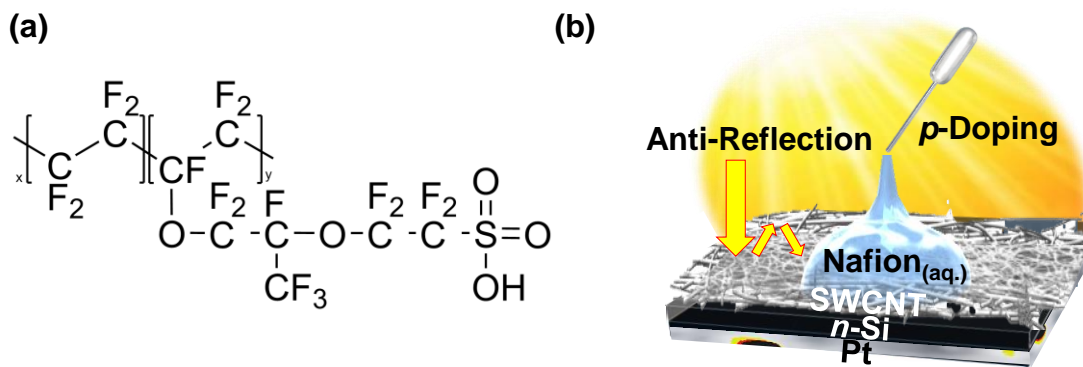


Figure 3.1 (a) Chemical structure of Nafion. (b) Illustration of a simple application of aqueous Nafion to an SWCNT-Si solar cell, inducing an anti-reflection effect and *p*-doping at the same time.

The chemical structure of Nafion is shown in Figure 3.1a. 20 wt% of Nafion perfluorinated resin solution in a mixture of lower aliphatic alcohols and water (Sigma-Aldrich) was diluted by IPA for different nominal concentrations. The obtained Nafion solution was then spin-coated on the SWCNT-Si solar cells at 7000 rpm for 60 s. The samples were subsequently dried in the ambient. The Nafion on electrode was cleaned by IPA. A schematic image of the application process of Nafion is shown in Figure 3.1b.

## Chapter 3 Multifunctional Effect of *p*-Doping, Anti-Reflection, and Encapsulation by Polymeric Acid for High-Efficiency and Stable SWCNT-Si Solar Cells

---

### 3.2.2 Characterizations

The optical reflectance and transmittance spectra were obtained by Shimadzu UV-3150. By using Agilent 4156C analyzer with a four-probe station, the sheet resistance of SWCNT films (van der Pauw method) and  $J$ - $V$  curves of the SWCNT-Si solar cells were measured. The 100 mW/cm<sup>2</sup> AM1.5G light source was provided by the solar simulator PEC-L01 (Peccell Technologies). The external quantum efficiency measurement system consisted of an MLS-1510 monochromator to scan the UV-Vis-NIR spectrum. A source measurement unit was used to record the current at each specific wavelength. The Fermi levels were measured by PYS AC-2 (Riken Keiki) in air. Kelvin probe was calibrated by Au before the measurement. XPS was performed by PHI 5000 VersaProbe using monochromatic Al K $\alpha$  radiation. The SEM analysis was conducted using Hitachi S-4800. EIS measurements were conducted by Solartron Analytical 1255B under AM1.5G light condition. Ellipsometry analysis was carried out by J.A. Woollam M-2000. Lifetime and implied  $V_{OC}$  were measured using QSSPC (WCT 120, Sinton Instrument, U.S.A). The TCAD simulation software is Atlas, Silvaco., (version 4.5.2.R).

### 3.3 SWCNT-Si Solar Cells with Record-High Efficiency and Stability

#### 3.3.1 *J-V* Characteristics

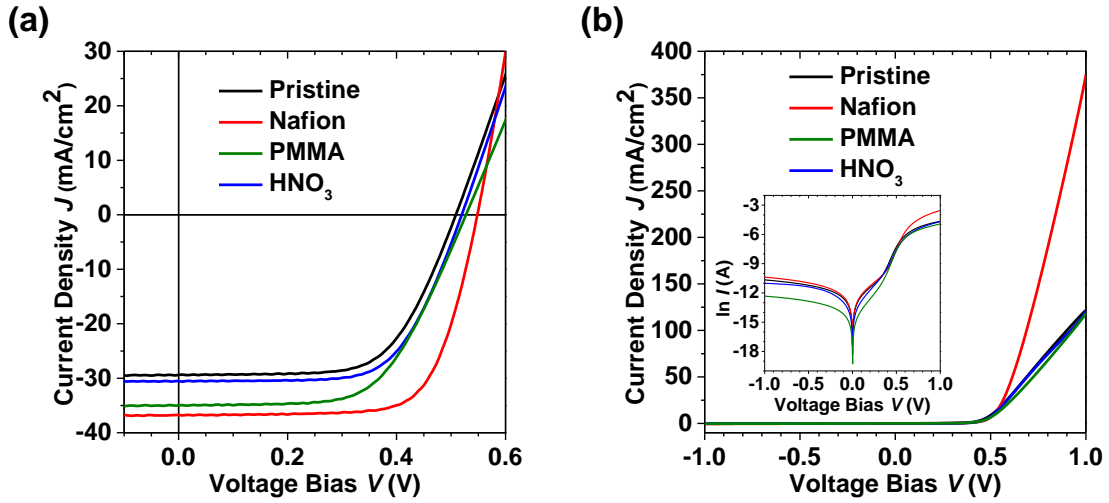


Figure 3.2 (a) *J-V* curves of the pristine SWCNT-Si solar cell, the Nafion-applied SWCNT-Si solar cell, the PMMA-applied SWCNT-Si solar cell, and the HNO<sub>3</sub>-applied SWCNT-Si solar cell, under 100 mW/cm<sup>2</sup> AM1.5G illumination. (b) Dark *J-V* curves of the pristine SWCNT-Si solar cell, the Nafion-applied SWCNT-Si solar cell, the PMMA-applied SWCNT-Si solar cell, and the HNO<sub>3</sub>-applied SWCNT-Si solar cell with logged *I-V* curves in the inset.

Nafion-applied SWCNT-Si solar cells in a configuration of Pt/*n*-Si/SWCNT/Nafion were fabricated along with the pristine SWCNT-Si solar cells, the PMMA-applied SWCNT-Si solar cells, and the HNO<sub>3</sub>-applied SWCNT-Si solar cells. The device performance was assessed and compared in terms of anti-reflection, doping effect, and

### Chapter 3 Multifunctional Effect of *p*-Doping, Anti-Reflection, and Encapsulation by Polymeric Acid for High-Efficiency and Stable SWCNT-Si Solar Cells

stability. The  $J$ - $V$  characteristics are shown in Figure 3.2, with the detailed information shown in Table 3.1. The Nafion-applied SWCNT-Si solar cell showed the highest PCE of 14.4% among the four different SWCNT-Si solar cells. All of the three PV parameters,  $J_{SC}$ ,  $V_{OC}$ , and FF increased substantially and contributed to the high PCE of the Nafion-applied SWCNT-Si solar cells.

**Table 3.1 PV parameters of the SWCNT-Si solar cell, the Nafion-applied SWCNT-Si solar cell, the PMMA-applied SWCNT-Si solar cells, and the HNO<sub>3</sub>-applied SWCNT-Si solar cell, under 100 mW/cm<sup>2</sup> AM1.5G illumination.**

Dopant	PCE (%)	FF (%)	$V_{OC}$ (mV)	$J_{SC}$ (mA/cm <sup>2</sup> )	$R_S$ ( $\Omega$ ·cm <sup>2</sup> )	$R_{SH}$ ( $\Omega$ ·cm <sup>2</sup> )
None (ref.)	9.5	63.8	509	29.4	4.5	>2.5k
Nafion	14.4	71.2	549	36.7	1.9	>2.5k
PMMA	11.1	60.0	527	35.0	5.2	>2.5k
HNO <sub>3</sub>	10.3	64.8	519	30.5	4.4	>2.5k

#### 3.3.2 Characterization of Stability in various Environments

From the aspect of real-world application, it is important for solar cells to be stable in various environments. The most possible threatens from the natural environment are air oxidation, humid weather, acid rain, organics, and UV illumination.

Chapter 3 Multifunctional Effect of *p*-Doping, Anti-Reflection, and Encapsulation by Polymeric Acid for High-Efficiency and Stable SWCNT-Si Solar Cells

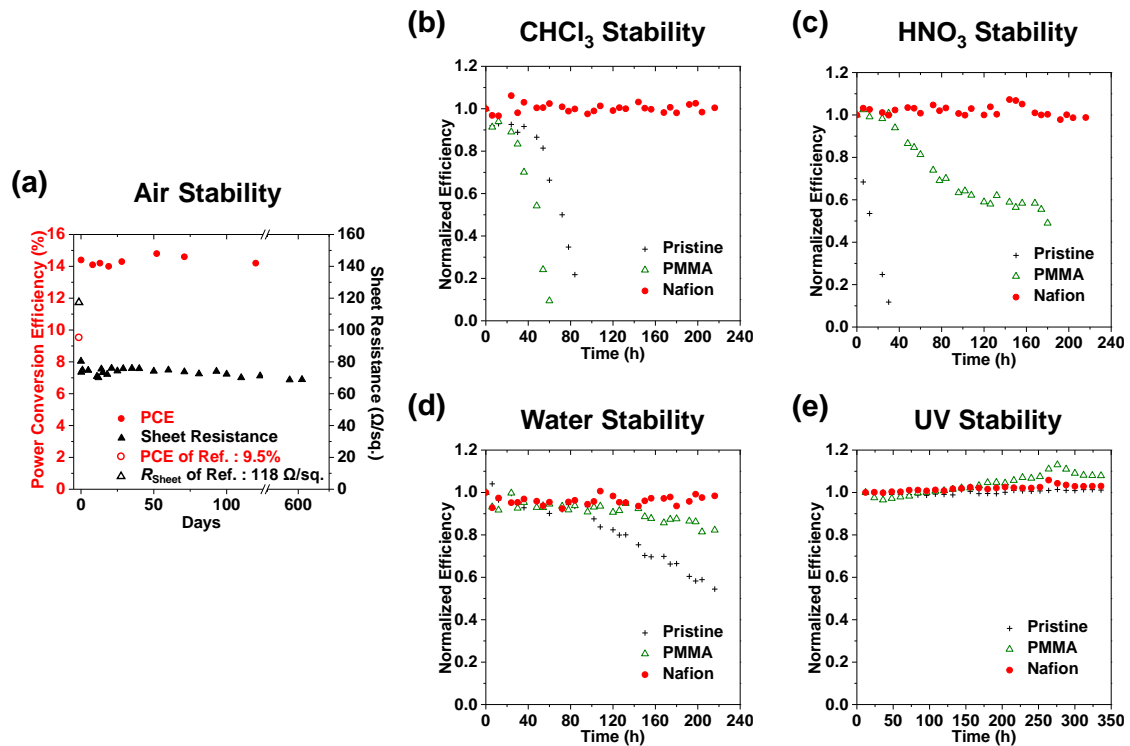


**Figure 3.3** (a) Stability data showing the doping effectiveness change of the SWCNT films after a Nafion application and the PCE change of the Nafion-applied SWCNT-Si solar cell. (b, c, d, e) Normalized PCE of SWCNT-Si solar cells, PMMA-applied SWCNT-Si solar cells, and Nafion-applied SWCNT-Si solar cells submerged to (b) chloroform, (c) 60 v/v% HNO<sub>3</sub>, and (d) water, and (e) under constant illumination of UV.

Nafion on SWCNT-Si solar cells has an encapsulation effect too as aforementioned. So far, PMMA has been employed as a means to encapsulate thin-film solar cells [77,78]. However, Nafion demonstrates by far greater encapsulating effect than PMMA in both chemical and mechanical perspectives.

Nafion doping is known to be extremely durable [79,80]. The sheet resistance change provided in Figure 3.3a shows that the doping effect is stable for 600 days. It is

### **Chapter 3 Multifunctional Effect of *p*-Doping, Anti-Reflection, and Encapsulation by Polymeric Acid for High-Efficiency and Stable SWCNT-Si Solar Cells**

---

not an exaggeration to claim that the durability of Nafion doping is permanent. Owing to the permanent doping, Nafion-applied SWCNT-Si solar cells show a constant device PCE for more than 120 days (Figure 3.3a).

Figure 3.3b reveals that the Nafion-applied SWCNT-Si solar cells retained its PCE after being submerged in chloroform ( $\text{CHCl}_3$ ) for more than 200 hours (samples were taken out for every measurement). However, both the unencapsulated SWCNT-Si solar cells and the PMMA-applied SWCNT-Si solar cells degraded under the organic solvent. In addition, the stability of the solar cells was tested under a highly concentrated strong acid,  $\text{HNO}_3$  (conc. 60 v/v%) (Figure 3.3c). The data show that both the unencapsulated SWCNT-Si solar cell and PMMA-applied SWCNT-Si solar cell degraded due possibly to  $\text{HNO}_3$  etching the Si substrates, whereas the Nafion-applied SWCNT-Si solar cell remained unchanged for more than 9 days. This is reasonable as PMMA has been reported to be damaged by strong acids [81], while nothing but pure alkali metals can damage Nafion [82]. Both the Nafion-applied SWCNT-Si solar cell and the PMMA-applied SWCNT-Si solar cell displayed great stability when submerged in water, but the unencapsulated SWCNT-Si solar cell degraded after a long time because of the physical damage caused by water which separated the SWCNT film from the Si substrate (Figure 3.3d). It should be mentioned that Nafion has advantages in terms of its hardness [83] and anti-smudge effect compared to PMMA [84]. To our surprise, all of the devices showed excellent stability under a constant UV light ( $\lambda = 280 \text{ nm}$ ) (Figure 3.3e). Seemingly slight color changes were observed in both PMMA and Nafion, yet it did not undermine the  $J_{\text{sc}}$  at all.

### 3.3.3 Record-High Stable Efficiency

To the best of our knowledge, the obtained stable PCE of the proposed Nafion-applied SWCNT-Si solar cells is the highest among the reported CNT electrode-based Si solar cells (Figure 3.4 and Table 3.2). Moreover, it is noted that such a simple treatment that inducing favorable effects in all three categories of doping, anti-reflection, and stability has not been reported.

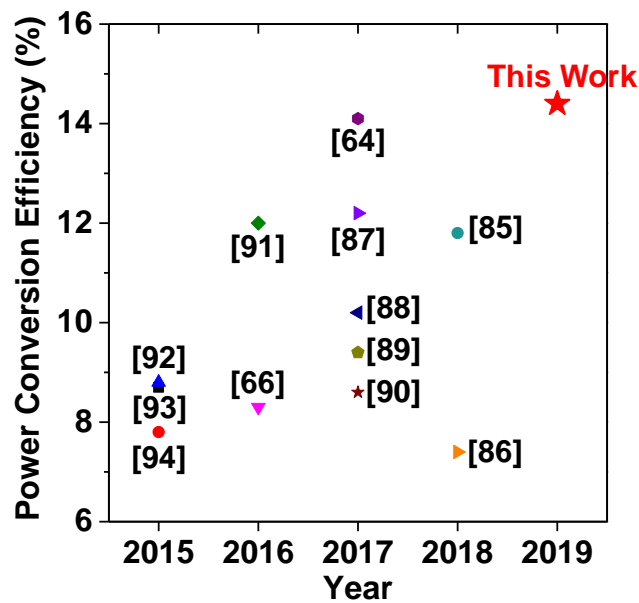


Figure 3.4 Reported PCEs of CNT electrode-based Si solar cells with similar active areas (6–10 mm<sup>2</sup>) to the devices of this work.

**Chapter 3 Multifunctional Effect of *p*-Doping, Anti-Reflection, and Encapsulation by Polymeric Acid for High-Efficiency and Stable SWCNT-Si Solar Cells**

**Table 3.2 Record table of the reported CNT-based Si solar cells with details including active area, CNT type, doping treatment, anti-reflection coating, and stability.**

Year	PCE (%)	Active Area (mm <sup>2</sup> )	CNT Type	Doping (Treatment)	Anti-Reflection Coating	Stability	Ref.
<b>This work</b>	14.4	9	SWCNT	Nafion	Nafion	≈14.2% after 120 days, resistant to CHCl <sub>3</sub> , HNO <sub>3</sub> , water, & UV	N/A
<b>2018</b>	11.8	9	SWCNT	N/A	N/A	≈11% after 9 days	[85]
<b>2018</b>	7.4	6	MWCNT	Pt nanoparticles, HNO <sub>3</sub>	N/A	N/A	[86]
<b>2017</b>	14.1	9	SWCNT	CuCl <sub>2</sub> /Cu(OH) <sub>2</sub>	CuCl <sub>2</sub> /Cu(OH) <sub>2</sub>	≈14.1% after 1 year	[64]
<b>2017</b>	12.2	9	SWCNT	N/A	N/A	N/A	[87]
<b>2017</b>	10.2	9	Mixed	PEDOT:PSS, HNO <sub>3</sub>	N/A	≈8.0% after 1 day	[88]
<b>2017</b>	9.4	8	SWCNT	Few-layer black phosphorus, SOCl <sub>2</sub>	N/A	≈3.5% after 12 days	[89]
<b>2017</b>	8.6	9	SWCNT	N/A	TiO <sub>2</sub>	N/A	[90]
<b>2016</b>	12.0	9	MWCNT	HNO <sub>3</sub>	N/A	N/A	[91]
<b>2016</b>	8.3	6	SWCNT	N/A	N/A	N/A	[66]
<b>2015</b>	8.8	9	SWCNT	Graphene, Au nanoparticles	N/A	N/A	[92]
<b>2015</b>	8.7	8	SWCNT	SOCl <sub>2</sub>	Polystyrene	≈5.6% after 7 days	[93]
<b>2015</b>	7.8	8	SWCNT	SOCl <sub>2</sub>	Polystyrene	≈4.3% after 7 days	[94]

### 3.4 Mechanism Discussions

#### 3.4.1 Anti-Reflection Mechanism of Nafion for SWCNT-Si Solar Cells

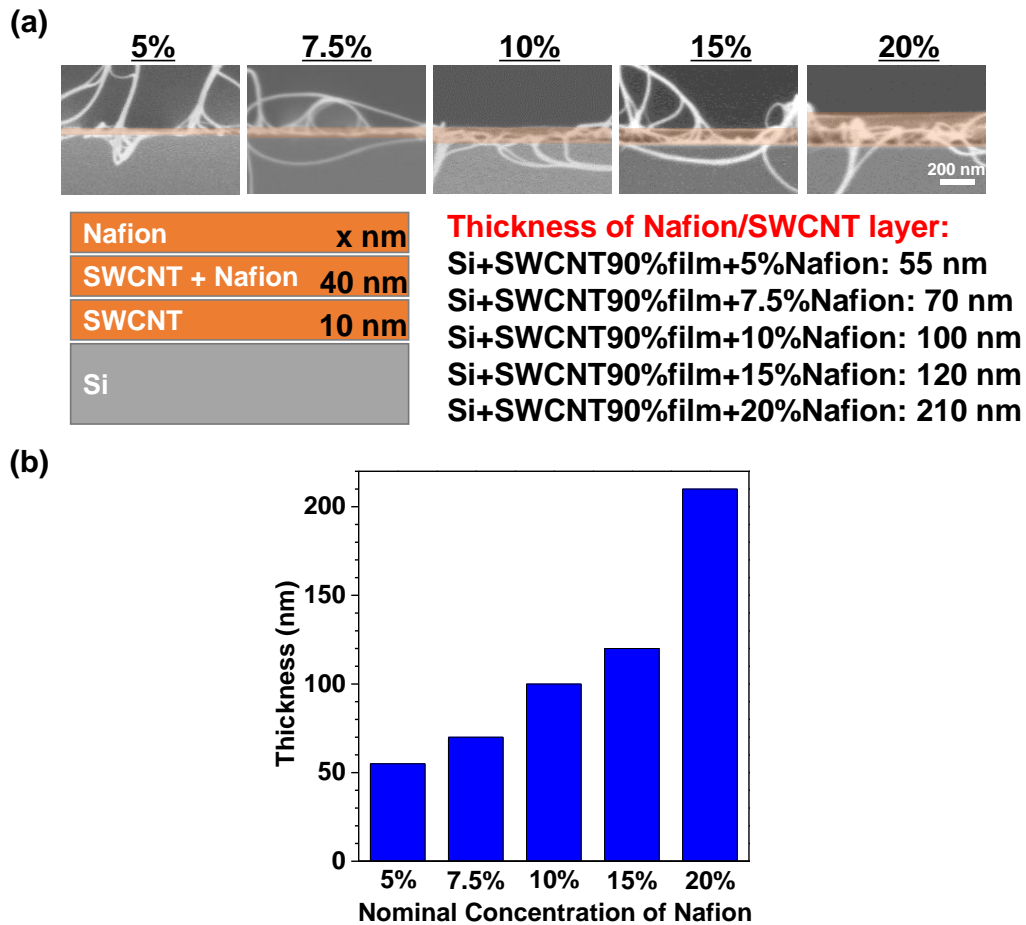


Figure 3.5 (a) Cross-sectional SEM images of different concentrations of Nafion/SWCNT layers on Si substrates and their thicknesses. (b) The measured total thicknesses of Nafion/SWCNT layers on Si, depending on the nominal concentration of Nafion.

The most notable element was  $J_{SC}$ , which increased from 29.4 mA/cm<sup>2</sup> to 36.7

### Chapter 3 Multifunctional Effect of *p*-Doping, Anti-Reflection, and Encapsulation by Polymeric Acid for High-Efficiency and Stable SWCNT-Si Solar Cells

mA/cm<sup>2</sup>.  $J_{SC}$  is dependent on the photon flux incident on solar cells, which can be enhanced by an anti-reflection effect. To investigate the anti-reflection effect of the polymeric acid coating, we firstly measured the thickness of Nafion and SWCNT layers with different nominal concentrations of the Nafion solution. Cross-sectional SEM was used to measure the thicknesses of Nafion/SWCNT layers. It was challenging to measure the thickness accurately due to the sponge-like nature of the SWCNTs (Figure 3.5). We found that the porous network of SWCNTs soaks up a certain amount of Nafion solution, which was found to be approximately 40-nm thick (Figure 3.5a).

By using ellipsometry, we obtained the RIs of the SWCNT film, the Nafion film, and the Nafion-applied SWCNT film on Si substrates, as shown in Figure 3.6.

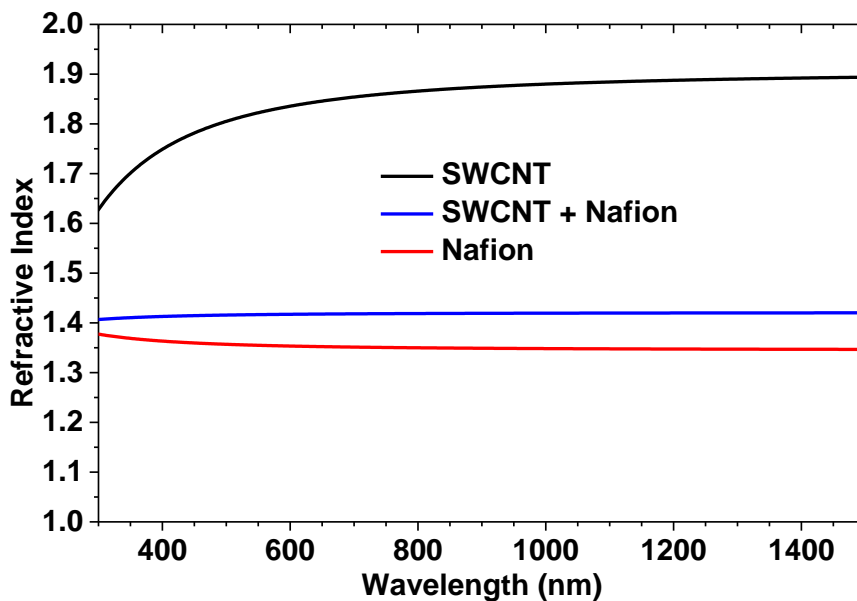


**Figure 3.6** RIs of SWCNT film, Nafion film, and Nafion-applied SWCNT film, all on Si substrates.

Using the estimated RIs, we optimized the Nafion/SWCNT layer thickness to obtain

### Chapter 3 Multifunctional Effect of *p*-Doping, Anti-Reflection, and Encapsulation by Polymeric Acid for High-Efficiency and Stable SWCNT-Si Solar Cells

minimum reflection (Figure 3.7a) and maximum absorption (Figure 3.7b) with the help from the RCWA technique. Based on the fact that SWCNT-Si solar cells have the maximum IPCE at the wavelength of 600 nm [32], the optimization was performed at this wavelength and the total thickness of 100 nm was found to give the maximum anti-reflection effect from the reflectance and absorptance spectral mappings.

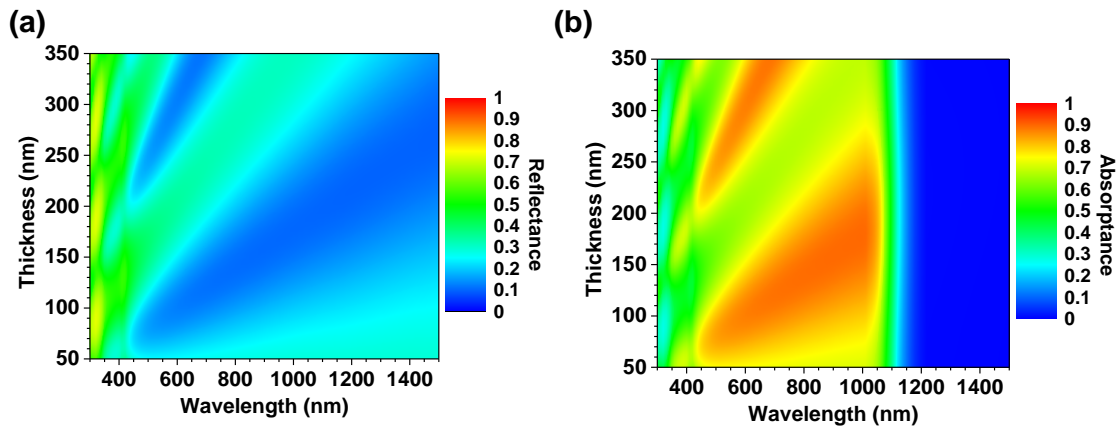


**Figure 3.7 (a) RCWA-simulated reflectance spectral mapping over the total Nafion/SWCNT thickness. (b) RCWA-simulated absorptance spectral mapping over the total Nafion/SWCNT thickness.**

Figure 3.8a shows that the  $J_{SC}$  of the Nafion-applied SWCNT-Si solar cells is maximum when the Nafion concentration is 10 v/v% under 7000 rpm, which results in a 100-nm-thick Nafion/SWCNT film. This empirical result corroborates our calculation. The variation of  $J_{SC}$  observed in Figure 3.8a is attributed to the anti-reflection effect changing with the thickness of the fabricated Nafion/SWCNT film (Figure 3.8b). The PCE value starts to decrease marginally beyond 20 v/v% of the Nafion concentration, despite the increase in  $J_{SC}$ . This is due to the decrease in FF from the decreasing doping effect when highly concentrated Nafion solution was used (Figure 3.8c and d), as too-

**Chapter 3 Multifunctional Effect of *p*-Doping, Anti-Reflection, and Encapsulation by Polymeric Acid for High-Efficiency and Stable SWCNT-Si Solar Cells**

high viscosities may hinder the Nafion from penetrating into SWCNT networks during the spin-coating process. Basically, the PCE has the same trend as  $J_{sc}$ . From an engineering point of view, by tailoring the thickness of Nafion, the PCE of Nafion-applied SWCNT-Si solar cells increased from around 12% to 14%, mainly due to the increase in  $J_{sc}$ .

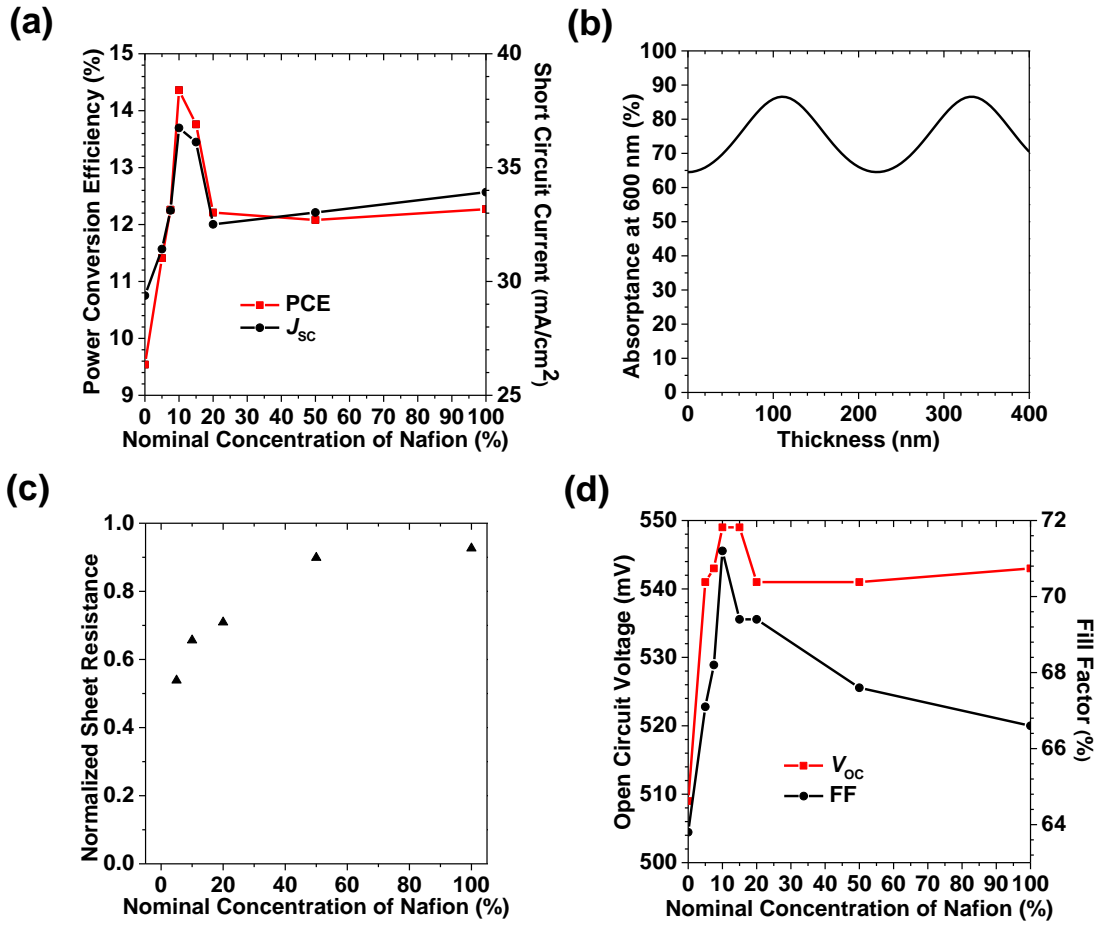


Figure 3.8 (a) PCE and  $J_{sc}$  trend over the nominal concentration of Nafion. (b) RCWA-simulated absorbance as a function of the total Nafion/SWCNT thickness at the wavelength of 600 nm. (c) Sheet resistance changes of SWCNT films upon doping by Nafion with different concentrations, and (d)  $V_{oc}$  and FF of Nafion-applied SWCNT-Si solar cells in different Nafion concentrations.

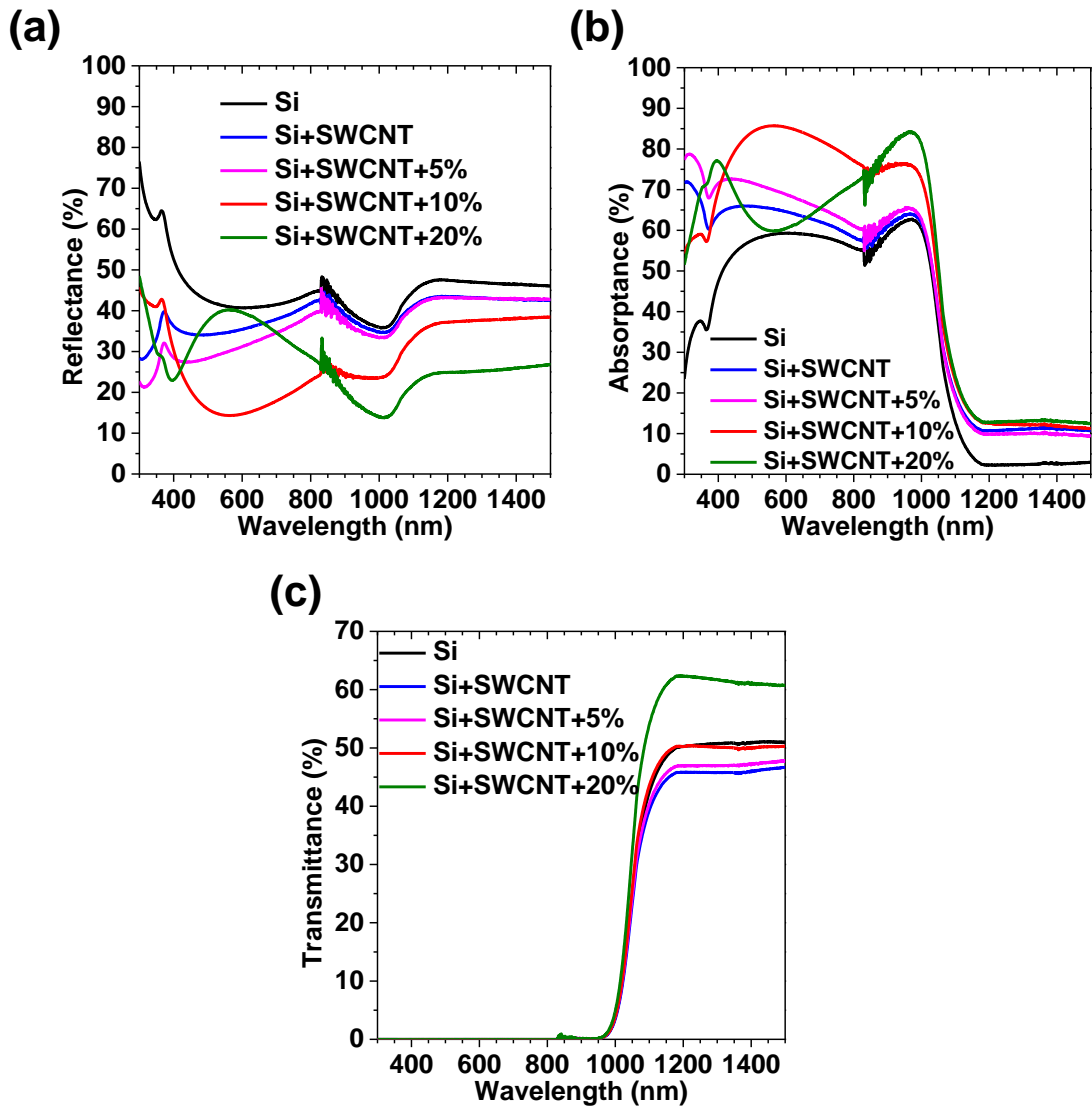


Figure 3.9 UV-Vis-NIR experimental results. (a) Reflectance, (b) absorbance, (c) transmittance spectra of a Si substrate, an SWCNT film on a Si substrate, and Nafion-applied SWCNT films on Si substrates, where the Nafion nominal concentrations are 5%, 10% , and 20%.

The UV-Vis-NIR reflectance and absorbance spectra of the SWCNT + Nafion films on Si with different concentrations show that the films with a 10 v/v% Nafion solution exhibit the minimum reflectance (Figure 3.9a) and the maximum absorbance (Figure

### Chapter 3 Multifunctional Effect of *p*-Doping, Anti-Reflection, and Encapsulation by Polymeric Acid for High-Efficiency and Stable SWCNT-Si Solar Cells

3.9b) in the wavelength region around 600 nm [32,64]. The absorptance data was obtained by subtracting the reflectance spectra and transmittance spectra from one (Figure 3.9c and Section 2.1.5).

The experimental data matches well with the RCWA-simulated results, as shown in Figure 3.10.

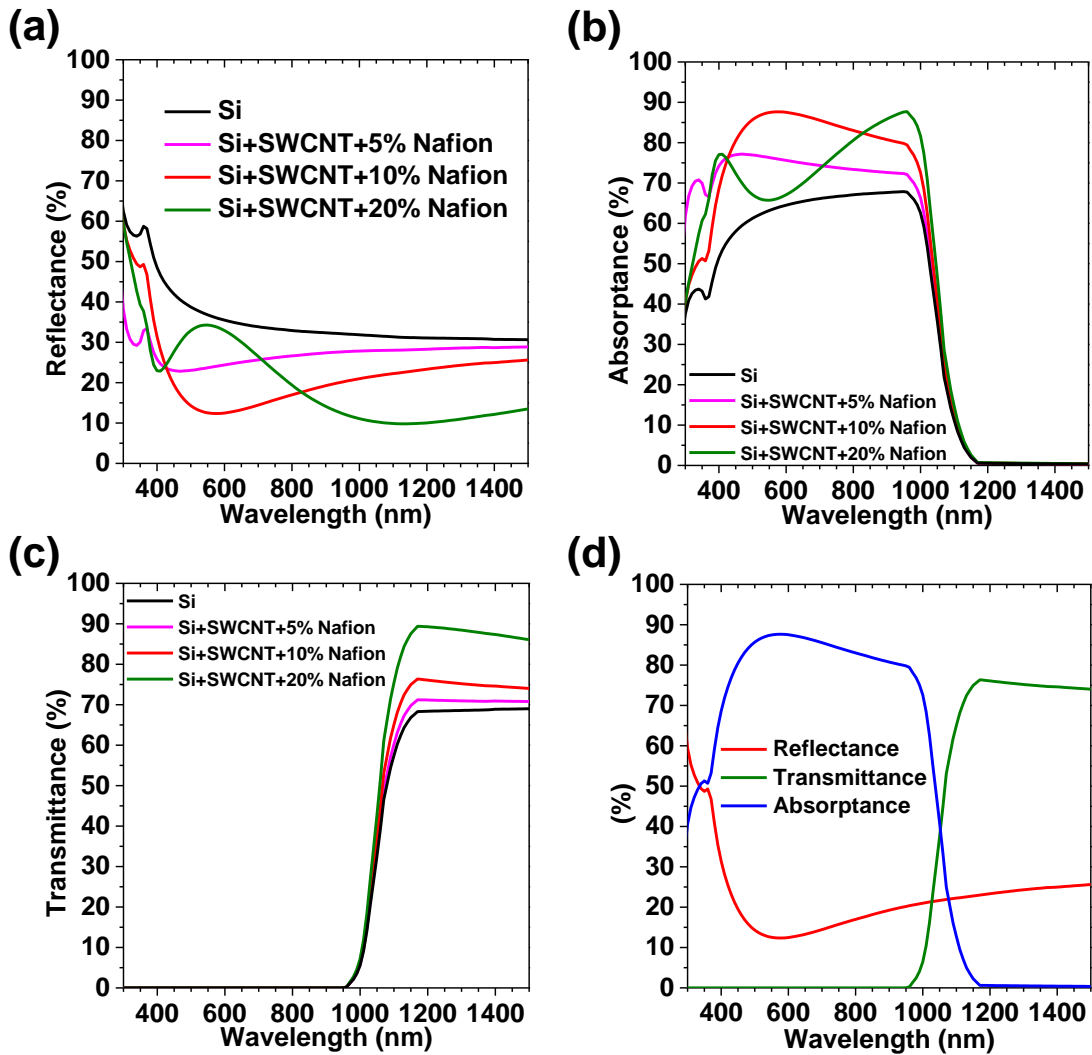


Figure 3.10 RCWA-simulated (a) reflectance, (b) absorptance, and (c) transmittance of a Si substrate and Nafion-applied SWCNT films on Si substrates, where the Nafion concentrations are 5%, 10%, and 20%; and (d) the combination of reflectance, transmittance, and absorptance for the 10 v/v% Nafion concentration.

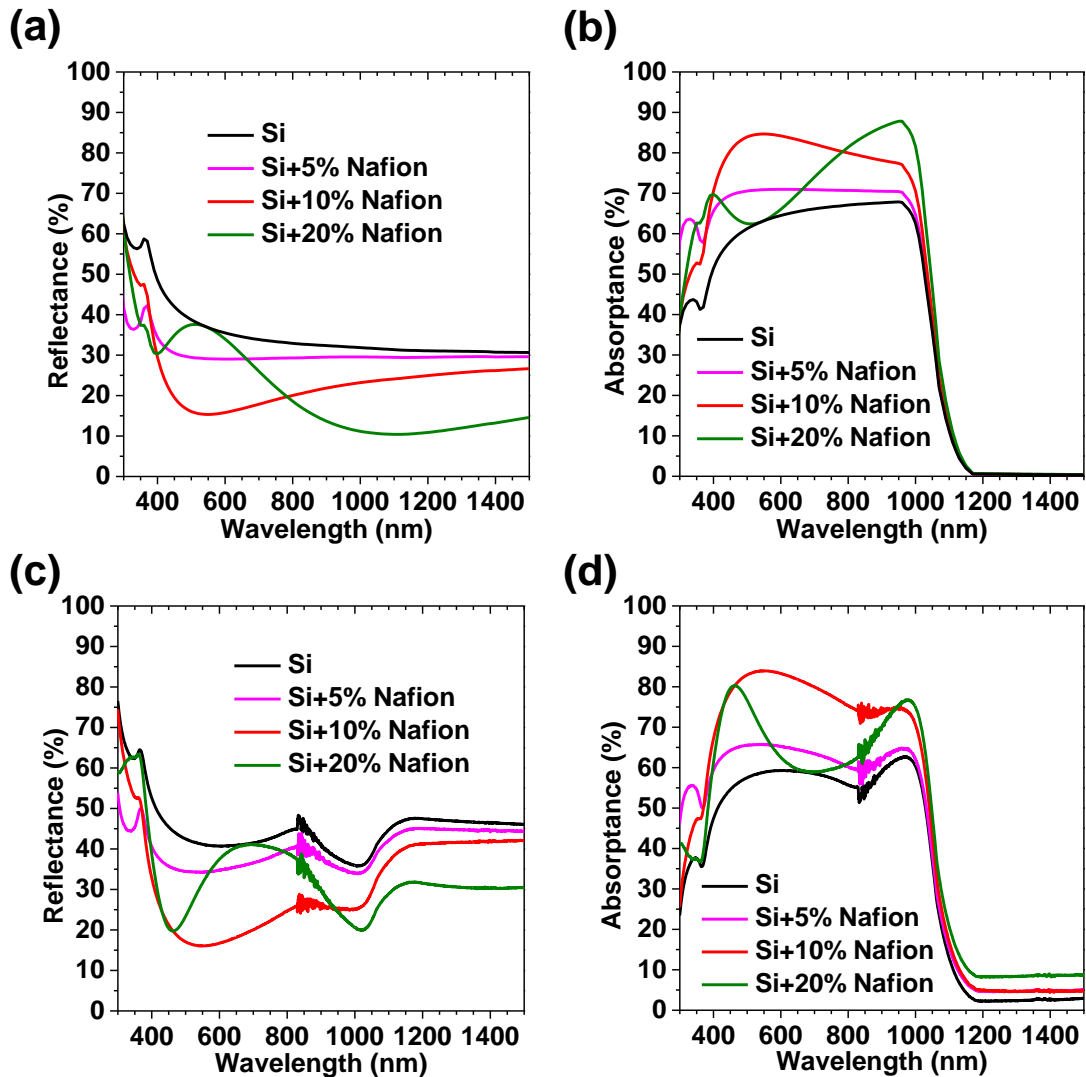


Figure 3.11 RCWA-simulated (a) reflectance and (b) absorptance data; empirical (c) reflectance and (d) absorptance data of a Si substrate, a 5 v/v% Nafion-coated Si substrate, a 10 v/v% Nafion-coated Si substrate, and a 20 v/v% Nafion-coated Si substrate.

In order to strengthen the analysis, optical analysis of the Nafion films on Si excluding SWCNTs was carried out computationally and empirically. This was to ascertain the optical effect of the approximately 40-nm thickness of Nafion penetrating

### Chapter 3 Multifunctional Effect of *p*-Doping, Anti-Reflection, and Encapsulation by Polymeric Acid for High-Efficiency and Stable SWCNT-Si Solar Cells

into the network of SWCNTs, which can undermine the accuracy of the calculation. The RCWA-simulated results and experimental results show that the 10 v/v% Nafion concentration (thickness of 90 nm in this case) still induces maximum anti-reflection effect (Figure 3.11). Therefore, we can conclude that the existence of the SWCNT layer does not play a significant role in the anti-reflection effect.

FDTD can perform a full-vector simulation of light propagation (wavelength = 600 nm) towards the surface of Si. Our simulation results show that the 10 v/v% Nafion solution spin-coated SWCNT film induces the maximum absorbance and the distance needed for a full absorption is *ca.* 10  $\mu\text{m}$  (Figure 3.12).

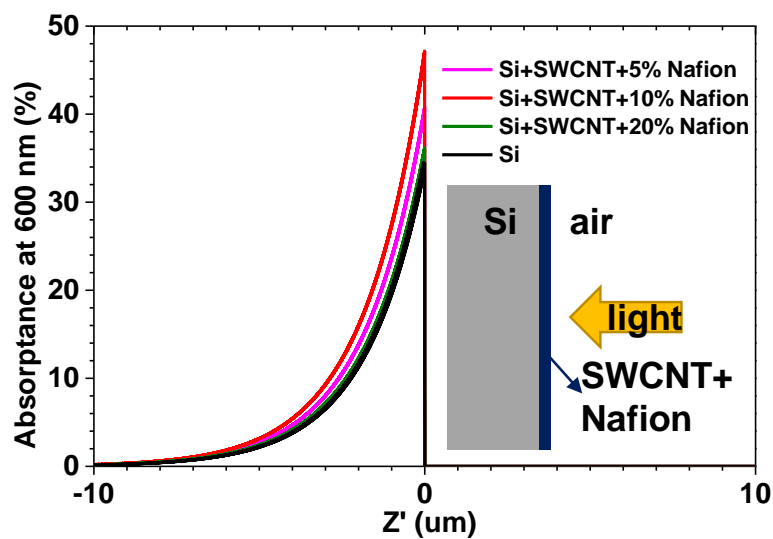


Figure 3.12 FDTD full-vector simulation for the light wave of 600 nm on a Si substrate and Nafion-applied SWCNT films on Si substrates, where the Nafion concentrations are 5%, 10%, and 20%.

IPCE data obtained in this work (Figure 3.13) and the reported values from the literature [77] confirm that the anti-reflection effect induced by Nafion is much greater

### Chapter 3 Multifunctional Effect of *p*-Doping, Anti-Reflection, and Encapsulation by Polymeric Acid for High-Efficiency and Stable SWCNT-Si Solar Cells

than that by PMMA. This, we conjecture, is due to the fact that Nafion has a lower RI ( $n \approx 1.3534$  at 600 nm) and a narrower RI dispersion than those of PMMA ( $n \approx 1.4900$  at 600 nm) [78,95,96]. The smaller difference in the RI with that of the air ( $n \approx 1.0003$  at 600 nm) leads to less surface reflection loss and the narrower RI dispersion translates to a great anti-reflection effect over a wider range of wavelengths.

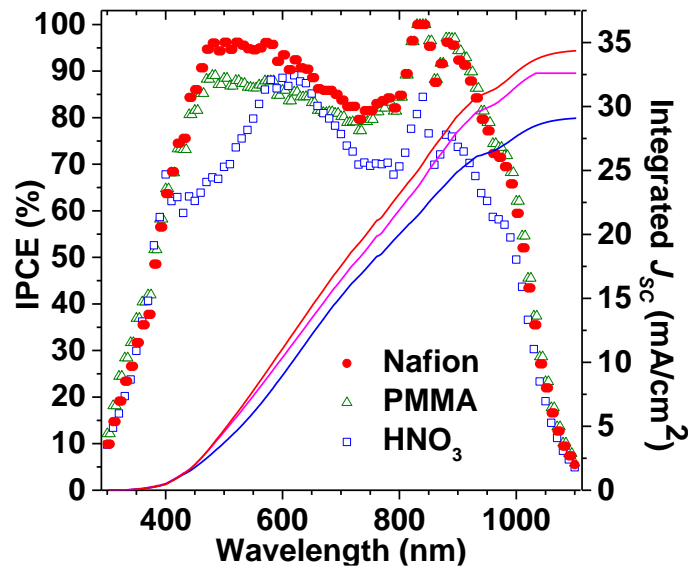


Figure 3.13 IPCE spectra and integrated  $J_{sc}$  of a Nafion-applied SWCNT-Si solar cell, a PMMA-applied SWCNT-Si solar cell, and an  $HNO_3$ -applied SWCNT-Si solar cell.

#### 3.4.2 *p*-Doping Mechanism of Nafion for SWCNT-Si Solar Cells

The application of Nafion not only induces the anti-reflection effect but also a *p*-doping effect on SWCNTs (Figure 3.14a). The Nafion-applied SWCNT-Si solar cells showed higher FF with a lower  $R_s$  than those of  $HNO_3$ -applied SWCNT-Si solar cells, indicating a stronger doping effect. Again, from an engineering point of view, this doping

### Chapter 3 Multifunctional Effect of *p*-Doping, Anti-Reflection, and Encapsulation by Polymeric Acid for High-Efficiency and Stable SWCNT-Si Solar Cells

effect roughly improved PCE from 10% to 12% (Figure 3.8a).

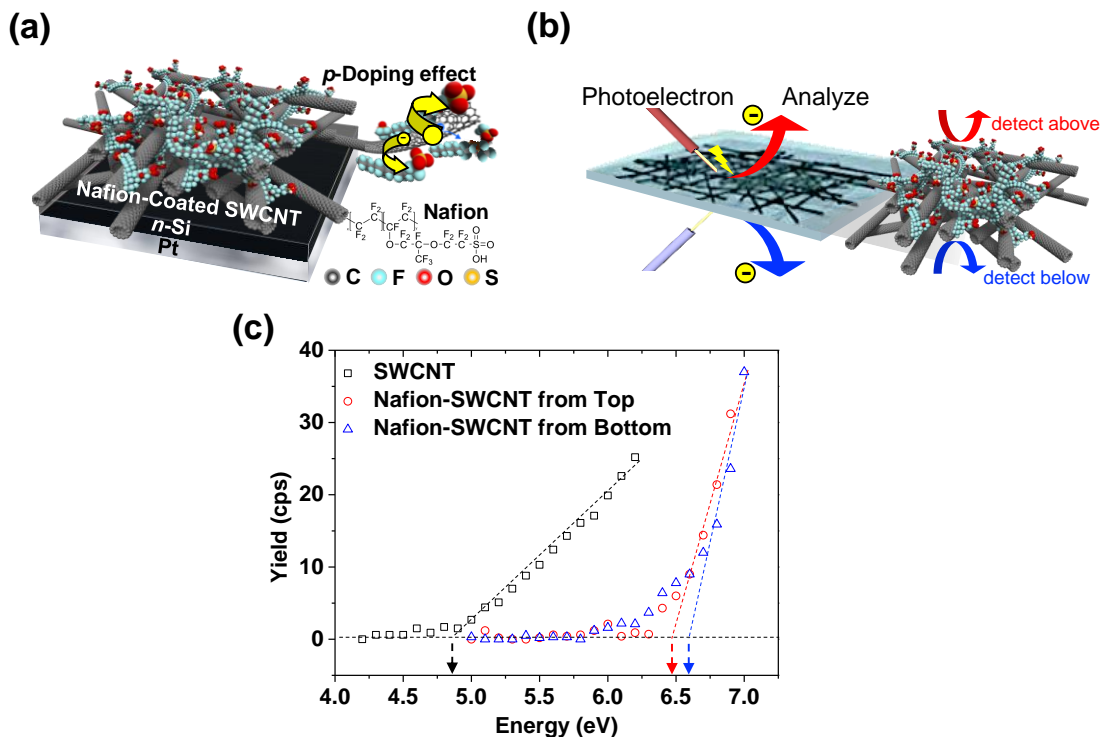


**Figure 3.14** (a) Illustration of the Nafion-applied SWCNT-Si solar cell, (b) illustration of the PYS measurement conducted on both sides of a Nafion-applied SWCNT film, and (c) the corresponding PYS data.

$V_{OC}$  of the Nafion-applied SWCNT-Si solar cells improved significantly from 509 mV to 549 mV upon Nafion doping. Fermi level of the SWCNT layers governs the Schottky barrier height which is directly related to  $V_{OC}$  in the planar heterojunction system [97]. We measured the Fermi level change of SWCNT films upon Nafion doping using PYS. Both sides of the Nafion-applied SWCNT films were measured by flipping the film using the water transfer method (Figure 3.14b). Both sides the Nafion-applied SWCNT films display the Fermi levels of around -6.5 eV (Figure 3.14c). This reveals that the doping effect by Nafion pervades thoroughly into the entire SWCNT network. The Fermi

### **Chapter 3 Multifunctional Effect of *p*-Doping, Anti-Reflection, and Encapsulation by Polymeric Acid for High-Efficiency and Stable SWCNT-Si Solar Cells**

---

level of -6.5 eV is much lower than the reported Fermi levels of SWCNTs when doped HNO<sub>3</sub> (-5.3 eV) and triflic acid (-5.4 eV), the latter of which is also a sulfuric acid, similar to Nafion [80].

This phenomenon can be understood by looking at the XPS data. The carbon peak of SWCNTs is reported to shift to lower binding energy upon *p*-doping by HNO<sub>3</sub>, because the Fermi level positions closer to the valence band edge [98,99]. The XPS data shows that HNO<sub>3</sub> doping on SWCNTs shifts the carbon peak by 0.15 eV to 284.10 eV, indicating an expected *p*-doping (Figure 3.15a). In the case of Nafion-applied SWCNTs, the carbon peak on SWCNTs was visible only when the concentration of Nafion was lowered to 2.5 v/v% because of the large molecular size of Nafion (Figure 3.15b and c). It can be seen that the carbon peak of Nafion-applied SWCNTs shifted to higher binding energy. We can speculate that this is due to the high electronegativity of fluorinated polymer backbone pulling the electrons on SWCNTs, inducing an extraordinarily strong *p*-type doping.

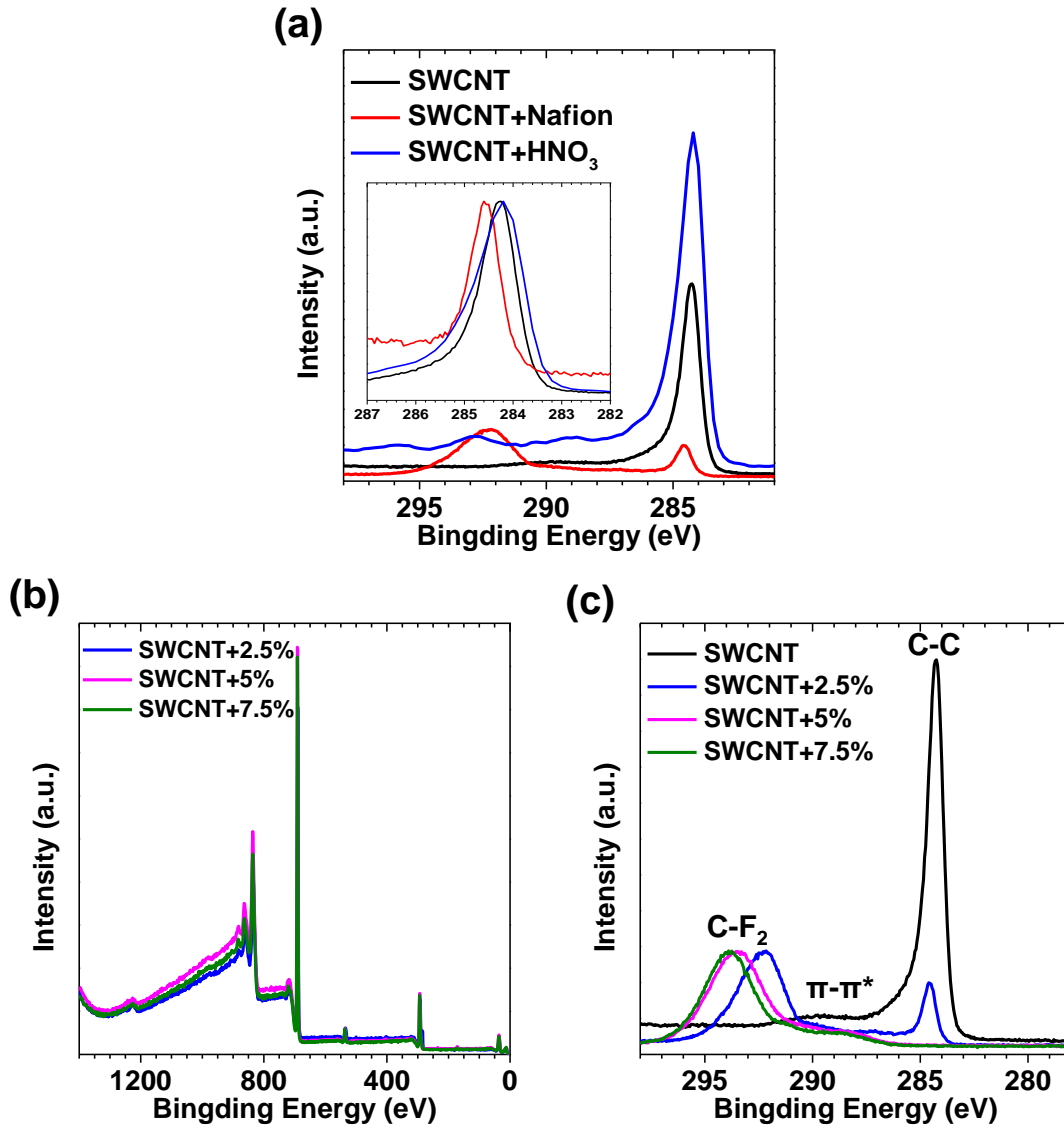
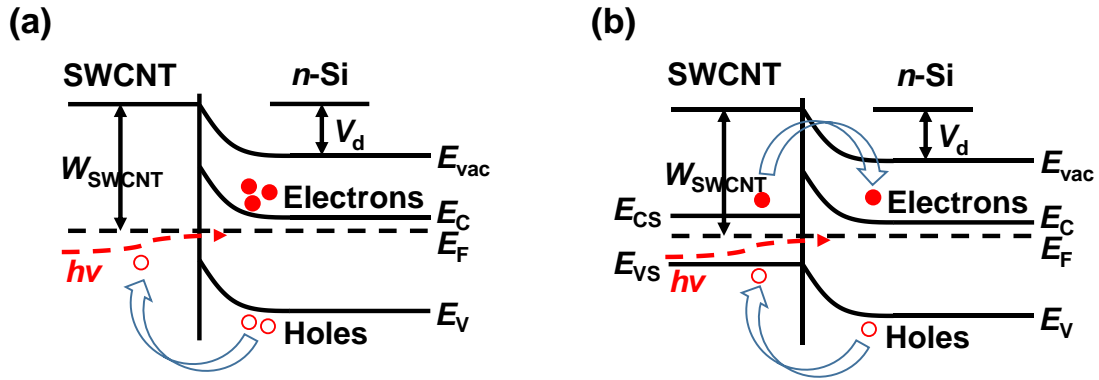


Figure 3.15 (a) XPS carbon peaks of an SWCNT film, a 2.5 v/v% Nafion-applied SWCNT film, and an HNO<sub>3</sub>-applied SWCNT film. (b) XPS scan of the entire range of SWCNT films with different nominal Nafion concentrations. (c) the carbon XPS peaks of the SWCNT films with different nominal Nafion concentrations.

TCAD simulation was used to assess the influence of the SWCNT Fermi levels on  $V_{OC}$ . There are mainly two models of SWCNT-Si solar cells: the Schottky barrier model (Figure 3.16a) and the *p-n* junction model (Figure 3.16b), depending on the electronic

**Chapter 3 Multifunctional Effect of *p*-Doping, Anti-Reflection, and Encapsulation by Polymeric Acid for High-Efficiency and Stable SWCNT-Si Solar Cells**

properties of SWCNTs. However, as our SWCNT-Si solar cell is not at the nano- or micro-scale, the model we used for TCAD is Schottky barrier model, in which we regard SWCNT film as a metal in bulk because of the bundling of SWCNTs.



**Figure 3.16 (a) Band structure of SWCNT-Si solar cells by Schottky barrier model.**

**(b) Band structure of SWCNT-Si solar cells by *p-n* junction model.**

Figure 3.17a shows the model for TCAD simulation. Figure 3.17b, c, and d show that lower Fermi levels of SWCNTs induce more band bending for SWCNT-Si solar cells. More charges accumulate at the interface of *n*-Si and SWCNT.

Chapter 3 Multifunctional Effect of *p*-Doping, Anti-Reflection, and Encapsulation by Polymeric Acid for High-Efficiency and Stable SWCNT-Si Solar Cells

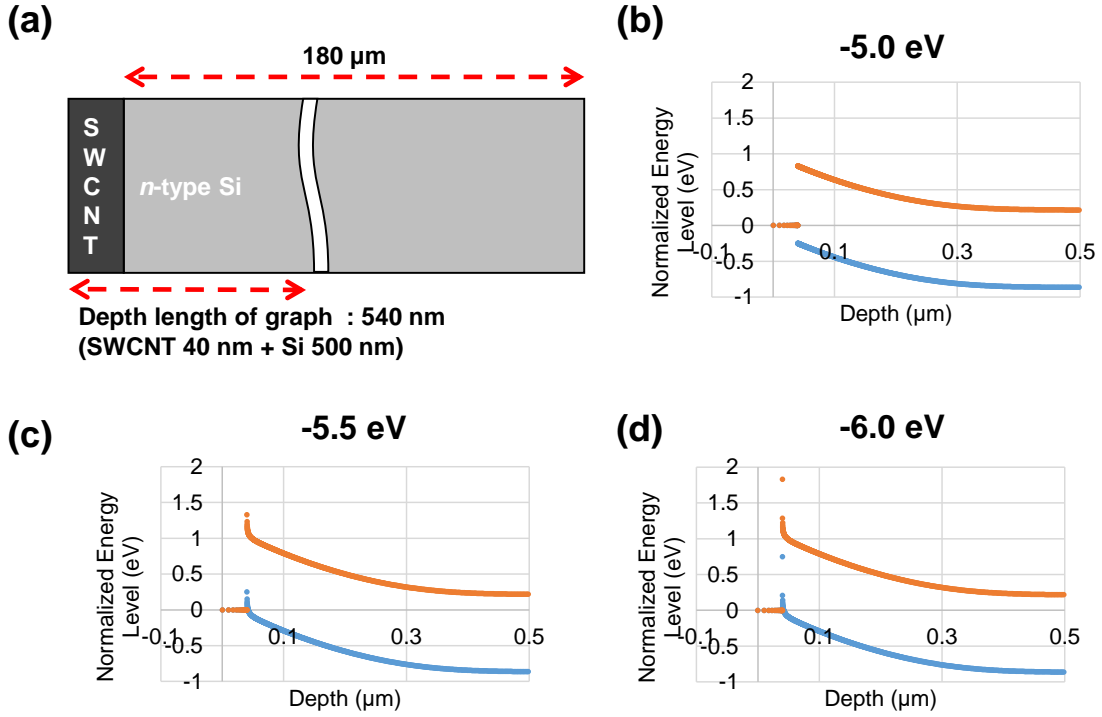


Figure 3.17 TCAD simulation modeling and four selected data showing that more band bending is induced by lower Fermi level.

Figure 3.18 shows the TCAD-simulated the  $J$ - $V$  curves of SWCNT-Si solar cell with different Fermi levels of the SWCNT layer. Lower Fermi level induces more band bending, which enhances the built-in potential  $V_d$ :

$$V_d \approx (W_{SWCNT} - \chi_{Si} - (E_C - E_F))/q \quad (3.1)$$

where  $W_{SWCNT}$  is the work function of SWCNT,  $\chi_{Si}$  is the electron affinity of Si,  $E_C$  and  $E_F$  are the energy levels of conductance band and valence band of Si, and  $q$  is the elementary electric charge of an electron. As a result, the implied  $V_{OC}$  increases as the Fermi level of the SWCNT layer decreases, which ultimately saturates at -5.5 eV (Table 3.3). This explanation also works for the *p*-*n* junction model. Although there is a marginal

**Chapter 3 Multifunctional Effect of *p*-Doping, Anti-Reflection, and Encapsulation by Polymeric Acid for High-Efficiency and Stable SWCNT-Si Solar Cells**

discrepancy between the implied  $V_{OC}$  and the empirical  $V_{OC}$ , the TCAD simulation supports our hypothesis that the high  $V_{OC}$  of the Nafion-applied SWCNT-Si solar cell is the result of the deep-lying Fermi level.

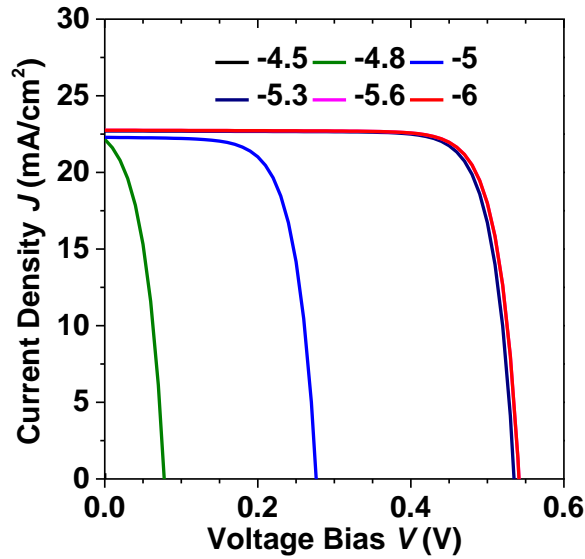


**Figure 3.18** TCAD-simulated  $J$ - $V$  curves of SWCNT-Si solar cells with different Fermi levels of the SWCNT films.

**Table 3.3** Implied  $V_{OC}$  from different work functions by TCAD simulation.

Fermi Level (eV)	Implied $V_{OC}$ (mV)
-4.5	–
-4.8	77.7
-5.0	276.3
-5.3 (HNO <sub>3</sub> Doping)	534.8
-5.5	541.3
-6.0 (Nafion Doping)	541.3

### Chapter 3 Multifunctional Effect of *p*-Doping, Anti-Reflection, and Encapsulation by Polymeric Acid for High-Efficiency and Stable SWCNT-Si Solar Cells

EIS measurement substantiates our assertion as well. EIS of the pristine and doped SWCNT-Si solar cells at 0.5 V over the high-frequency range of 10 kHz to 1 MHz under simulated AM1.5G illumination ( $100 \text{ mW/cm}^2$ ) was recorded in order to quantify the parameters of charge transport and extraction. The spectra were fitted with the resistance in series of a high-frequency parallel resistor-capacitor circuit (inset of Figure 3.19). As shown in Table 3.4, while the  $R_S$  values of the devices are similar, the charge transfer resistance  $R_{CT}$  value is the lowest for the Nafion-applied SWCNT-Si solar cells, indicating the most favorable charge transfer between the Si layer and the Nafion-applied SWCNT layer for the lowest recombination loss.

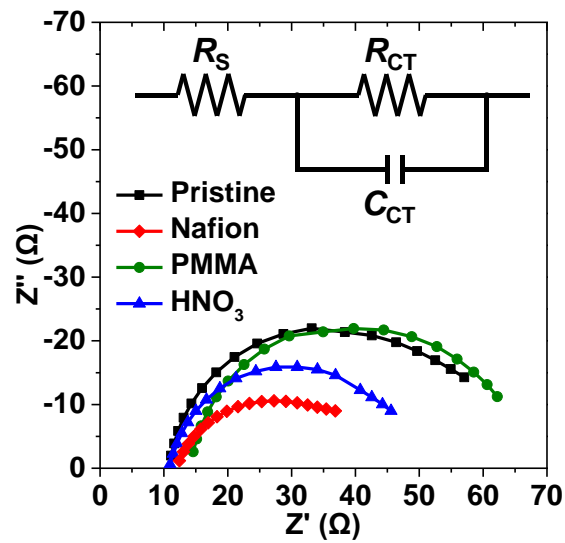


Figure 3.19 EIS spectra of SWCNT-Si solar cells with different treatments and a high-frequency parallel resistor-capacitor circuit as an inset.

**Chapter 3 Multifunctional Effect of *p*-Doping, Anti-Reflection, and Encapsulation by Polymeric Acid for High-Efficiency and Stable SWCNT-Si Solar Cells**

---

**Table 3.4 EIS fitting data of the pristine and doped SWCNT-based Si solar cells at 0.5 V over the high-frequency range of 10 kHz to 1 MHz under AM1.5G illumination (100 mW/cm<sup>2</sup>).**

<b>Dopant</b>	<b><math>R_s</math> (<math>\Omega</math>)</b>	<b><math>R_{CT}</math> (<math>\Omega</math>)</b>	<b><math>C_{CT}</math> (F)</b>
<b>None (ref.)</b>	11.3	45.4	$7.09 \times 10^{-8}$
<b>Nafion</b>	13.6	23.0	$1.33 \times 10^{-7}$
<b>PMMA</b>	14.7	47.4	$6.29 \times 10^{-8}$
<b>HNO<sub>3</sub></b>	10.0	34.7	$9.82 \times 10^{-8}$

The Fermi level explains the high  $V_{OC}$  of the Nafion-applied SWCNT-Si solar cells. However, the PMMA-applied SWCNT-Si solar cells also display rather high  $V_{OC}$  in spite of having no doping effect. To investigate the reason behind this, we carried out QSSPC decay measurement to assess the passivation effect of the various treatments we used in this work. As shown in Figure 3.20a, the sample we used in QSSPC measurement should have both sides passivated to avoid the quick recombination of photogenerated carriers. Figure 3.20b shows that the QSSPC lifetime improved upon lamination of an SWCNT film. The minority carrier lifetime was enhanced even further by a simple application of ethanol, which densifies the SWCNT film. This means that densification of SWCNTs leads to better passivation of the Si wafer surface. The application of HNO<sub>3</sub> further increases the passivation, suggesting that besides densification, doping is also related to the surface passivation by introducing a depletion layer. The PMMA application greatly boosts the QSSPC lifetime, which we believe is due to the heavy and viscous nature of PMMA. In fact, polymers, such as PEDOT:PSS, have been reported to be effective in Si surface passivation [100,101]. Nafion exhibited similarly high passivation effect, though

**Chapter 3 Multifunctional Effect of *p*-Doping, Anti-Reflection, and Encapsulation by Polymeric Acid for High-Efficiency and Stable SWCNT-Si Solar Cells**

not as good as PMMA. The implied  $V_{OC}$  values extracted from QSSPC lifetimes [102] show that PMMA-applied SWCNT-Si solar cells should give the highest  $V_{OC}$  (Table 3.5). This means that the highest empirical  $V_{OC}$  of the Nafion-applied SWCNT-Si solar cells comes from the combined effect of the low-lying Fermi level and the surface passivation effect.

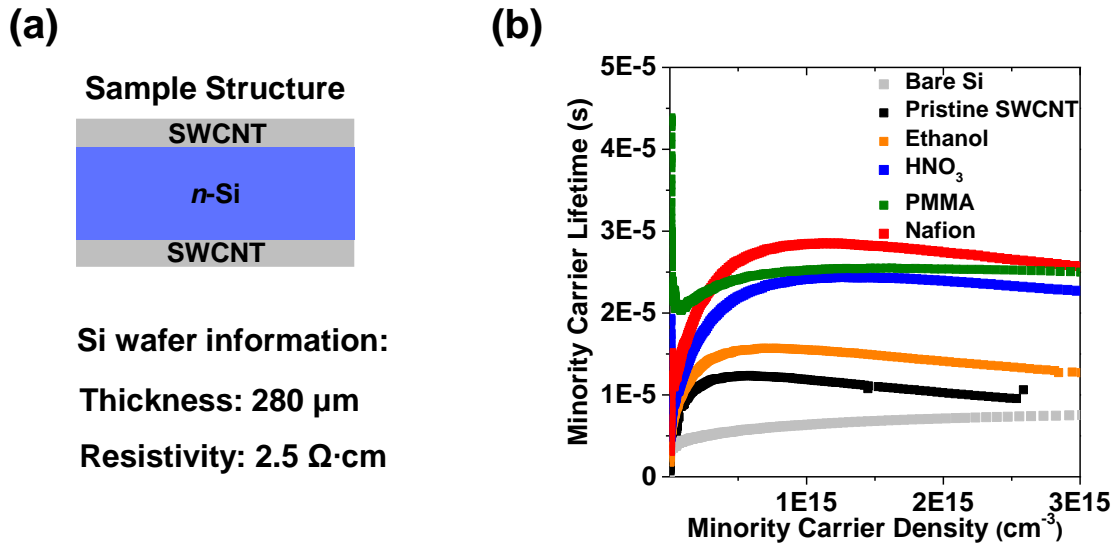


**Figure 3.20 (a) Sample information for QSSPC measurement. (b) QSSPC lifetimes of bare Si wafer, pristine SWCNT-laminated Si, ethanol-applied SWCNT-laminated Si,  $\text{HNO}_3$ -applied SWCNT-laminated Si, PMMA-applied SWCNT-laminated Si, and Nafion-applied SWCNT-laminated Si.**

**Table 3.5 Implied  $V_{OC}$  calculated from the QSSPC data of SWCNTs on *n*-Si wafers treated by different substances.**

Sample	Pristine SWCNT	Ethanol-applied SWCNT	$\text{HNO}_3$ -applied SWCNT	Nafion-applied SWCNT	PMMA-applied SWCNT
Implied $V_{OC}$ (mV)	534	539	545	555	563

### **3.5 Summary**

In this chapter, we reported a multifunctional polymeric acid called Nafion for tailoring SWCNT films in SWCNT-Si solar cells. The device PCE increased from 9.5% to 14.4% owing to the increases in all the three photovoltaic parameters, specifically,  $J_{SC}$ ,  $V_{OC}$ , and FF upon a simple spin-coating of the polymeric acid. Nafion doping introduced in this work break through the current limitations of SWCNT-Si solar cells by showcasing strong and permanent doping effect, favorable anti-reflection effect, and robust encapsulation effect, simultaneously. The increase in  $J_{SC}$  was attributed to Nafion's intrinsically low RI and optical transparency. The high FF came from the enhanced conductivity and charge transfer thanks to the highly electronegative fluorinated chains in Nafion resulting in high acidity and the Fermi level downshift. Finally, the high  $V_{OC}$  was attributed to the combined effect of the Fermi level downshift and Si surface passivation. The Nafion demonstrated superior encapsulation effect against an organic solvent, a strong acid, and water compared with widely used PMMA encapsulation. The obtained 14.4% efficiency stands the highest stable PCE among the reported CNT-based Si solar cells with an unprecedented multifunctional effect of doping, anti-reflection, and encapsulation by a single step spin-coating of polymeric acid.

## **Chapter 4      Controlled Synthesis of SWCNTs and MoS<sub>2</sub> based Nanomaterials and their Application in Photovoltaic Devices**

In this chapter, the knowledge of synthesizing and tailoring 2D MoS<sub>2</sub> by LPCVD system is introduced firstly. Then, by employing the cultivated knowledge, the line between 1D and 2D dimensionality of SWCNTs and MoS<sub>2</sub> is blurred by a novel structure called "1D vdW heterostructure". Lastly, the application of these tailored materials to PV devices is discussed.

### **4.1      Controlled Synthesis of 2D MoS<sub>2</sub>**

#### **4.1.1    Literature Review and Introduction**

The controllable synthesis of 2D MoS<sub>2</sub> is the premise of its scalable application. There are mainly two categories of synthesis methods of 2D MoS<sub>2</sub>: the top-down approach and the bottom-up approach.

##### **4.1.1.1 Review of Top-Down Approach**

The top-down approach is inspired by the pioneering research of graphene. It starts from the bulk MoS<sub>2</sub>, and exfoliates few-layer MoS<sub>2</sub> by utilizing its layered structure. There are mainly three types of methods: mechanical exfoliation and liquid-phase exfoliation.

## **Chapter 4 Controlled Synthesis of SWCNTs and MoS<sub>2</sub> based Nanomaterials and their Application in Photovoltaic Devices**

---

The mechanical exfoliation method is a convenient method for almost all layered crystals. Through attaching and detaching the tape repeatedly, the number of layers can be decreased. Then the exfoliated MoS<sub>2</sub> is attached to a target substrate by vdW forces [20,103]. Compared with other synthesis methods, the mechanical exfoliation method is simple, and the quality of the prepared sample is high for various characterizations of physical properties [104]. However, the disadvantages are: low synthesis efficiency, low uniformity, small domain ( $\mu\text{m}$  level), contamination from the residual of tape, and so on. Especially for the fabrication of devices [105], the small-domain problem causes the usage of the optical microscope during the whole process, which is extremely troublesome.

The liquid-phase exfoliation method is a more mass-productive method than the mechanical method. There are mainly two ways: ultrasonication [106,107] and chemical intercalation [108–110]. The ultrasonication uses surfactants to disperse the MoS<sub>2</sub> nanoflakes into the solution. The chemical intercalation typically uses Li and Na to intercalate between the layers of MoS<sub>2</sub>, which is followed by dispersion. Although the liquid phase exfoliation method is low cost for large-scale applications, it has the disadvantages of chemical impurities and low uniformity.

### **4.1.1.2 Review of Bottom-Up Approach**

The bottom-up approach starts from the atomic level. It creates 2D MoS<sub>2</sub> on the substrate through the nucleation and self-assembly of precursors, and this process is called "growth". Because this approach starts from scratch, its controllability is much better than that of the top-down approach, and thus is favored by the research that requires high-quality 2D MoS<sub>2</sub>. There are mainly two types of methods: the two-step growth

## Chapter 4 Controlled Synthesis of SWCNTs and MoS<sub>2</sub> based Nanomaterials and their Application in Photovoltaic Devices

---

method and the one-step growth method, which are classified by the position of precursors.

In the two-step growth method, the precursors containing Mo (and S) are first deposited onto the substrate, and are then sulfurized or decomposed into 2D MoS<sub>2</sub>. For the sulfurization method, Mo or MoO<sub>x</sub> films are deposited onto the substrate by thermal evaporation [111], e-beam evaporation [112] or sputtering [113], followed by sulfurization in CVD. For the decomposition method, (NH<sub>4</sub>)<sub>2</sub>MoS<sub>2</sub> is introduced onto the substrate firstly, followed by annealing to decompose [114,115]. Although the two-step growth method can easily synthesize a wafer-size 2D MoS<sub>2</sub> with the controllability of thickness, it has the problem of low quality: the single-crystalline domain size of MoS<sub>2</sub> is usually nm level. In addition, the synthesis of monolayer MoS<sub>2</sub> is difficult in this method.

In the one-step growth method, the precursors containing Mo and S are directly decomposed onto the substrate to form MoS<sub>2</sub> during the growth process. There are several ways to realize this process: hydrothermal and solvothermal synthesis [116–118], PVD [119–121], CVD [122–129], MOCVD [130], and so on. The hydrothermal and solvothermal synthesis of MoS<sub>2</sub> is conducted under high-temperature and high-pressure environment, resulting in a complicated structure of MoS<sub>2</sub> with various dimensionalities. PVD uses MoS<sub>2</sub> directly as the precursor, *e.g.*, a MoS<sub>2</sub> target [119] or MoS<sub>2</sub> powders [120,121], to form 2D MoS<sub>2</sub> layers on the substrate. CVD uses separate precursors of Mo and S to react in a gas phase. The first CVD growth of few-layer MoS<sub>2</sub> was reported in 2012 [122]. Single-crystalline MoS<sub>2</sub> with a domain size of hundreds of  $\mu\text{m}$  has been reported so far by using APCVD [123]. Furthermore, it has been found that seeding promoters of aromatic molecules can facilitate the nucleation of MoS<sub>2</sub> on the substrate

## Chapter 4 Controlled Synthesis of SWCNTs and MoS<sub>2</sub> based Nanomaterials and their Application in Photovoltaic Devices

---

[126]. Also, continuous poly-crystalline monolayer MoS<sub>2</sub> films have been reported through LPCVD [125,128,129], which generally have smaller single-crystalline domain size than APCVD. The advantages of CVD mainly lie in the large amount of tunable growth parameters, *e.g.*, flow rate of carrier gas, amount of precursors, temperatures, pressure, positions, and so on. Although tuning these parameters require great efforts (especially time), this method provides researchers with plenty of space to study. An advanced version of CVD is the MOCVD, which was firstly reported in 2015 [130]. This method uses the precursors of Mo(CO)<sub>6</sub> and (C<sub>2</sub>H<sub>5</sub>)<sub>2</sub>S, as well as ultra-low flow rates to allow the growth of high-quality monolayer MoS<sub>2</sub> film. However, there are concerns about the toxicity of organometals and the single-crystalline domain size of MoS<sub>2</sub> is still at several  $\mu\text{m}$  level. Another interesting research problem of monolayer MoS<sub>2</sub> crystals is about the shape. It was found that single-crystalline MoS<sub>2</sub> usually has a near-triangular shape by APCVD synthesis method, however, there are also other shapes under different synthesis methods and conditions [131].

### 4.1.1.3 Introduction

From the literature review of the synthesis methods of 2D MoS<sub>2</sub>, CVD is a promising method in regard to cost, efficiency, quality, controllability, empirical experience, and so on. In particular, for the application in PV devices, especially solar cells, which usually requires large-area uniform MoS<sub>2</sub> films, LPCVD outstands. It has been reported that continuous film can be grown by LPCVD [125,128,129], whereas the APCVD should use a vertical substrate position [132]. It has also been found that if a small amount of O<sub>2</sub> was introduced into the LPCVD system, the nucleation density dropped with the domain size became larger [129], indicating a trade-off between nucleation density and single-

## Chapter 4 Controlled Synthesis of SWCNTs and MoS<sub>2</sub> based Nanomaterials and their Application in Photovoltaic Devices

crystalline domain size. As LPCVD usually has less O<sub>2</sub> leakage than APCVD, it is easier to grow continuous MoS<sub>2</sub> films than APCVD, whereas APCVD is easier to grow large single-crystalline MoS<sub>2</sub> domains. The comparison of the experimental results of APCVD and LPCVD synthesis is shown in Figure 4.1. Moreover, under low pressure, the growth speed is much slower, which is expected to facilitate the growth of high-quality uniform MoS<sub>2</sub> films.

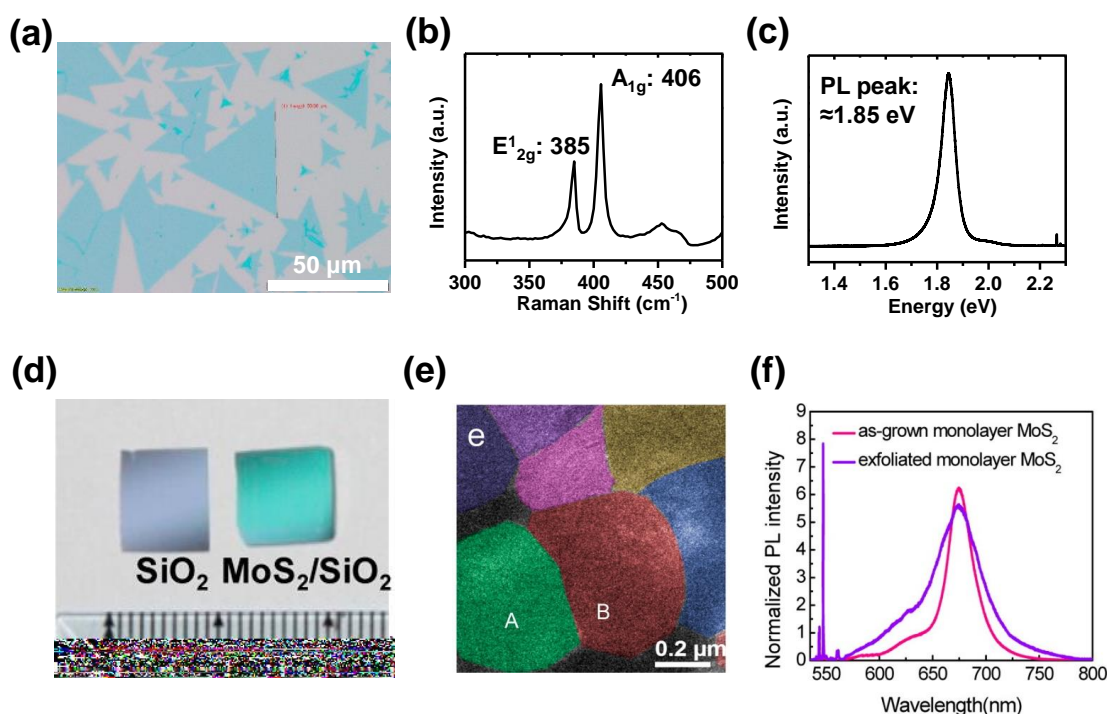


**Figure 4.1 Monolayer MoS<sub>2</sub> synthesized by APCVD method at Jing Kong lab, Massachusetts Institute of Technology (MIT) [126]: (a) optical image, (b) Raman, and (c) PL. Monolayer MoS<sub>2</sub> film synthesized by LPCVD method: (d) optical image, (e) single-crystalline domains, and (f) PL, reprinted from [128], Copyright (2014), with permission from ACS.**

Here, after the construction of the LPCVD system, the optimization of key growth

## Chapter 4 Controlled Synthesis of SWCNTs and MoS<sub>2</sub> based Nanomaterials and their Application in Photovoltaic Devices

parameters for 2D monolayer MoS<sub>2</sub> film growth by control variate method are discussed from experimental results. Basically, the strategy is to increase the nucleation density of MoS<sub>2</sub> to form a continuous film, with the care of film quality and CVD handiness.

### 4.1.2 Controlled Synthesis of Monolayer MoS<sub>2</sub>

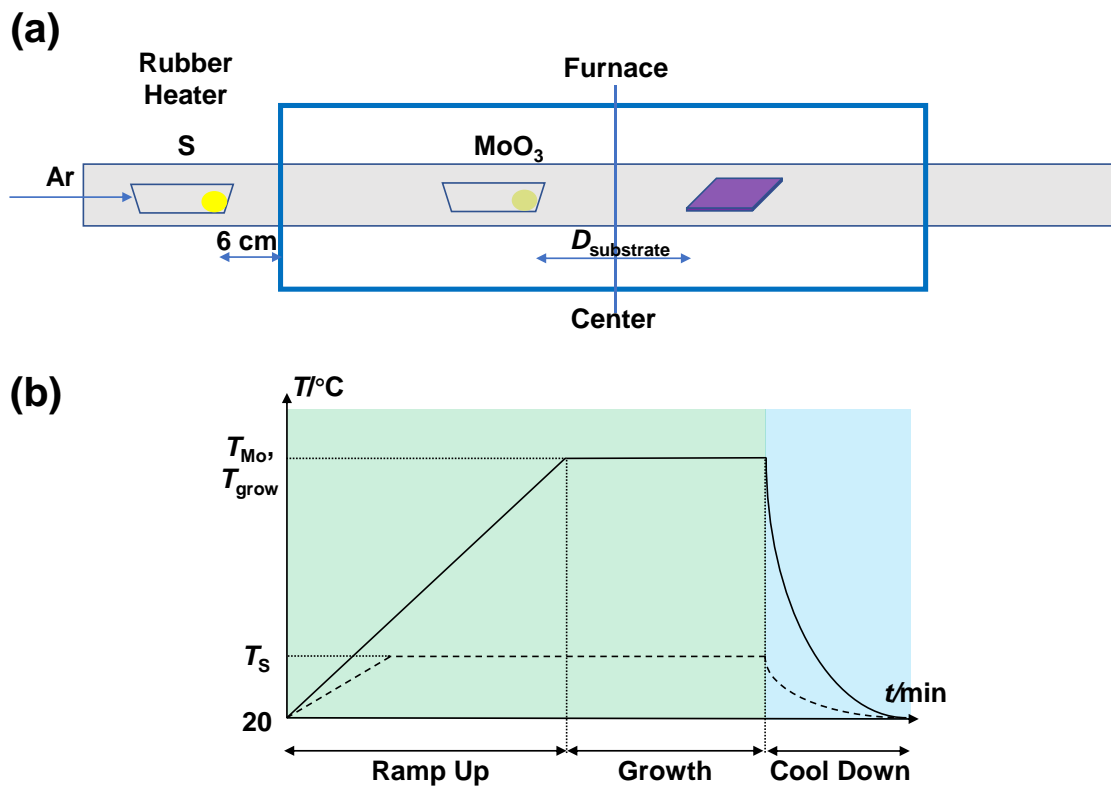


Figure 4.2 (a) A schematic of LPCVD synthesis. (b) Experimental flow of a MoS<sub>2</sub> LPCVD process.

As shown in Figure 4.2a, in the LPCVD synthesis of MoS<sub>2</sub>, the precursors of S and MoO<sub>3</sub> are employed. They are put in different quartz boats and placed in different positions. The precursors need to be evaporated or sublimated into the gas phase and be carried onto the substrate in the downstream for MoS<sub>2</sub> growth. Figure 4.2b shows a typical

## Chapter 4 Controlled Synthesis of SWCNTs and MoS<sub>2</sub> based Nanomaterials and their Application in Photovoltaic Devices

experimental flow of a MoS<sub>2</sub> LPCVD process. During the ramp-up period, the rubber heater and CVD furnace are heated to designated temperatures respectively. These temperatures are kept constant during the growth period. After the growth period, it is essential to determine when to open the furnace for fast cool-down, in order to terminate the growth and to prevent the introduction of strain energy into MoS<sub>2</sub>. Usually, the furnace was opened for fast cool-down at a temperature of < 450 °C.

The crucial parameters for this LPCVD synthesis process are the growth temperature, S evaporation temperature, Ar carrier gas flow rate, amount of S and MoO<sub>3</sub>, growth time, and the distance between MoO<sub>3</sub> boat and substrate. Literature review helped to determine the rough ranges of these growth parameters [125].

### 4.1.2.1 Effect of Substrate Preparation Method

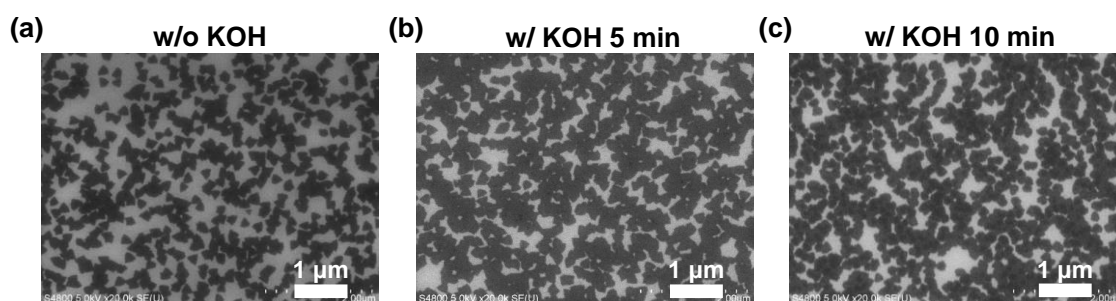


**Figure 4.3 Effect of substrate preparation method on MoS<sub>2</sub> synthesis results, characterized by SEM. (a) Without KOH pre-processing. (b) With 5-min KOH pre-processing. (c) With 10-min KOH pre-processing.**

Firstly, the effect of substrate preparation method was investigated. KOH (1M, Wako) was used to pre-process the Si/SiO<sub>2</sub> substrate, after the routine cleaning by acetone, IPA, and distilled water, 5 min each. After the KOH pre-processing, the substrate was

## Chapter 4 Controlled Synthesis of SWCNTs and MoS<sub>2</sub> based Nanomaterials and their Application in Photovoltaic Devices

cleaned again by distilled water for 5 min and 3 times.

As shown in Figure 4.3, a 5-min KOH pre-processing of Si/SiO<sub>2</sub> substrate can enhance the nucleation density of MoS<sub>2</sub>. Because MoS<sub>2</sub> is hydrophilic [133], the KOH etching makes the substrate more hydrophilic to facilitate MoS<sub>2</sub> nucleation. However, 10-min KOH pre-processing did not make better nucleation density than that of 5-min pre-processing, indicating that although KOH pre-processing is necessary for increasing nucleation density, this process has a saturation time of  $\leq 5$  min.

### 4.1.2.2 Effect of Carrier Gas Flow Rate

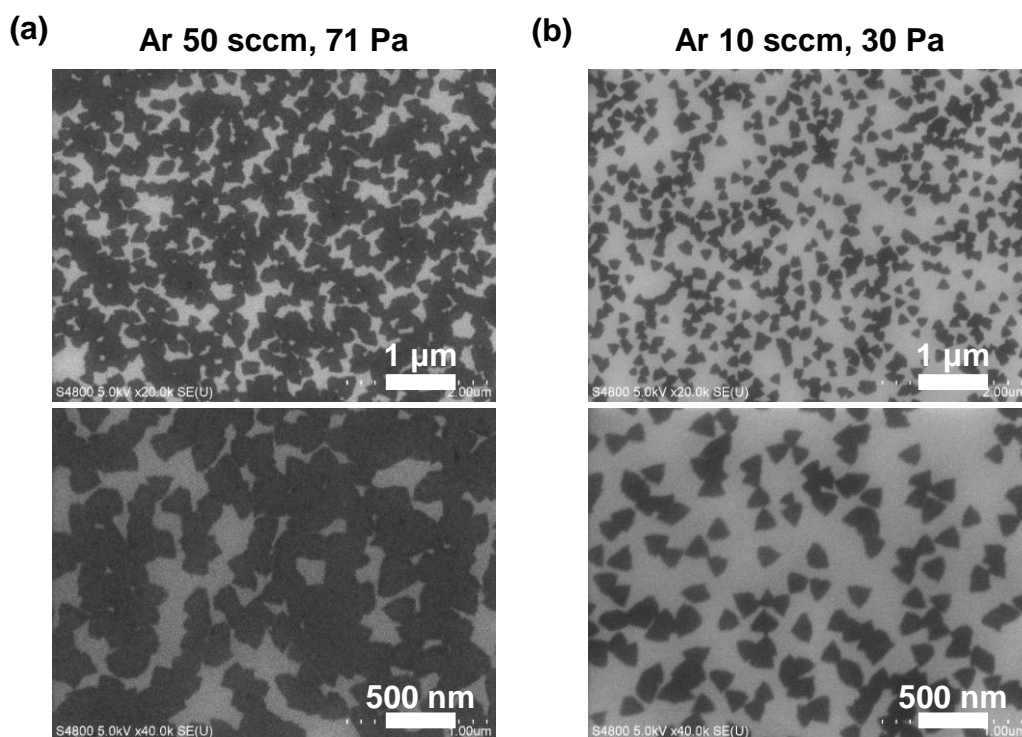


**Figure 4.4** Effect of Ar carrier gas flow rate on MoS<sub>2</sub> synthesis results, characterized by SEM. (a) 50 sccm. (b) 10 sccm.

The effect of carrier gas flow rate on MoS<sub>2</sub> synthesis results was also investigated.

## Chapter 4 Controlled Synthesis of SWCNTs and MoS<sub>2</sub> based Nanomaterials and their Application in Photovoltaic Devices

As shown in Figure 4.4, a higher Ar flow rate can result in higher nucleation density, because more MoS<sub>2</sub> nuclei can be carried onto the substrate by Ar. It is worth noting that from empirical experience, there is another factor governing the spread range of MoS<sub>2</sub>: the pump's evacuation ability. This ability gradually decreases after time, so we need to closely monitor the MoS<sub>2</sub> nuclei spread range by looking at the yellow-green MoS<sub>2</sub> deposited on the wall of the quartz tube.

### 4.1.2.3 Effect of Sulfur Evaporation Temperature

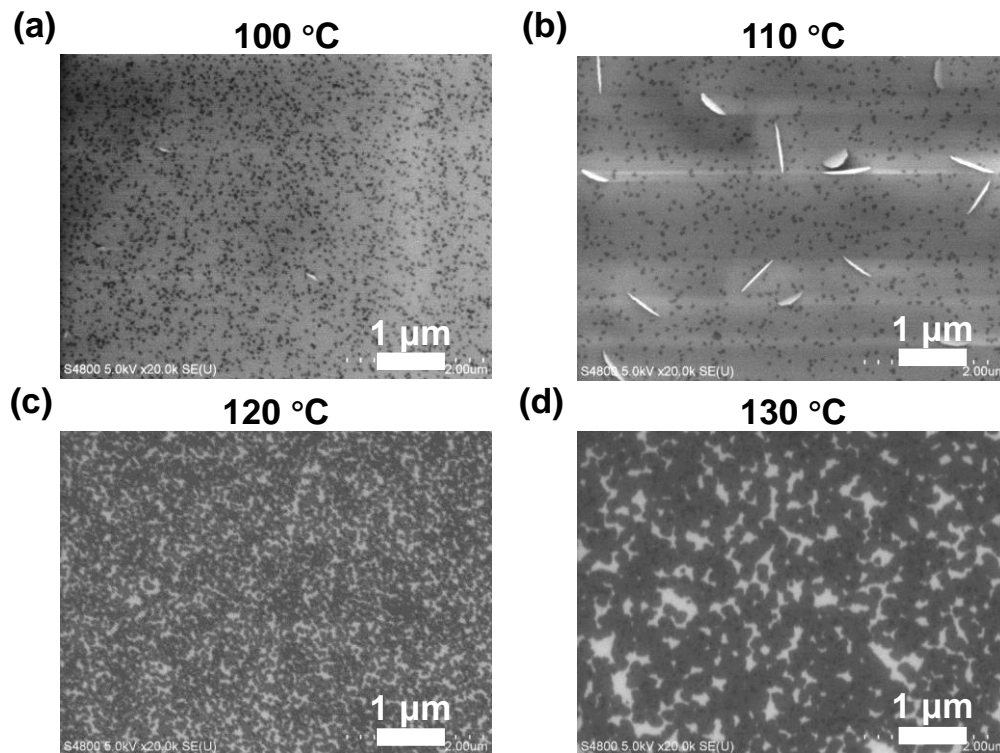
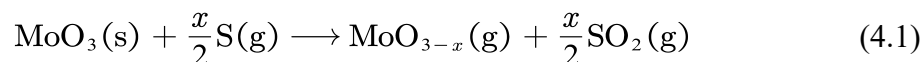


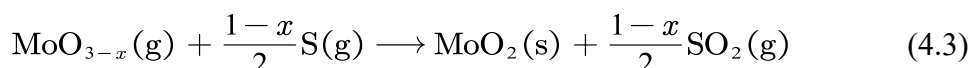
Figure 4.5 Effect of S evaporation temperature on MoS<sub>2</sub> synthesis results, characterized by SEM. (a) 100 °C. (b) 110 °C. (c) 120 °C. (d) 130 °C.

It is important to supply enough S during growth. Because from the reaction during the LPCVD process,

## Chapter 4 Controlled Synthesis of SWCNTs and MoS<sub>2</sub> based Nanomaterials and their Application in Photovoltaic Devices



MoO<sub>3</sub> is firstly reduced by S to be MoO<sub>3-x</sub>, which is easier to sublimate. Then, the reactions can be:



The MoO<sub>3-x</sub> can be sulfurized into either MoS<sub>2</sub> or MoO<sub>2</sub>, depending on the amount of the supplied S. If the S is not enough, the MoO<sub>2</sub> flakes will show up, as shown in Figure 4.5b. So by increasing the S evaporation temperature to around 130 °C and using excess S (1–3 g), enough S supply was achieved and the morphology of the as-synthesized MoS<sub>2</sub> becomes better with larger single-crystalline domain sizes, as shown in Figure 4.5d.

### 4.1.2.4 Effect of MoO<sub>3</sub> Sublimation and Growth Temperature

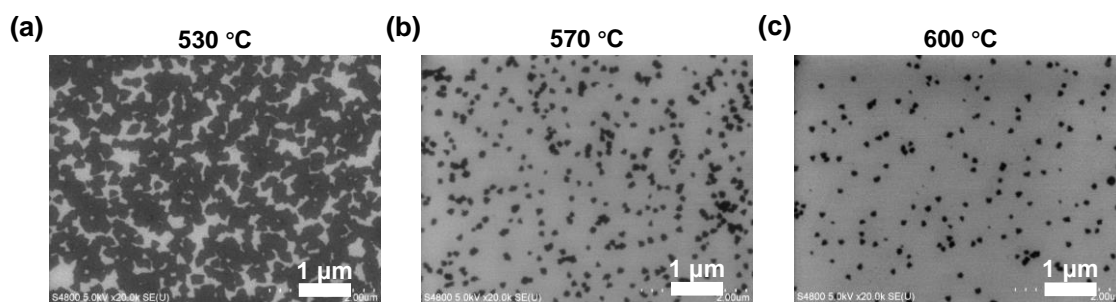


**Figure 4.6** Effect of MoO<sub>3</sub> sublimation and growth temperature on MoS<sub>2</sub> synthesis results, characterized by SEM. (a) 530 °C. (b) 570 °C. (c) 600 °C.

The temperature for MoO<sub>3</sub> sublimation is important for controlling the growth. If this temperature is too high, S will not be enough to cause MoO<sub>2</sub> being deposited onto

## Chapter 4 Controlled Synthesis of SWCNTs and MoS<sub>2</sub> based Nanomaterials and their Application in Photovoltaic Devices

the substrate. In contrast, if this temperature is too low, MoO<sub>3</sub> or MoO<sub>3-x</sub> cannot be sufficiently sublimated to allow efficient growth.

In this work, the growth temperature is coupled with MoO<sub>3</sub> sublimation temperature to have the same furnace temperature. As shown in Figure 4.6, when we decreased the furnace temperature from 600 °C to 530 °C, the nucleation density got improved significantly, as well as the domain size. This indicates that 530 °C provides a relatively optimized condition for the coupling of growth parameters.

As we adopted a two-zone furnace, we can actually control the MoO<sub>3</sub> sublimation temperature and MoS<sub>2</sub> growth temperature separately for approximately up to 200 °C difference. It has been reported that higher growth temperature can induce higher quality MoS<sub>2</sub> [125]. Future work about differentiating these two temperatures is expected to help improve MoS<sub>2</sub> quality.

### 4.1.2.5 Effect of Growth Duration and MoO<sub>3</sub> Amount

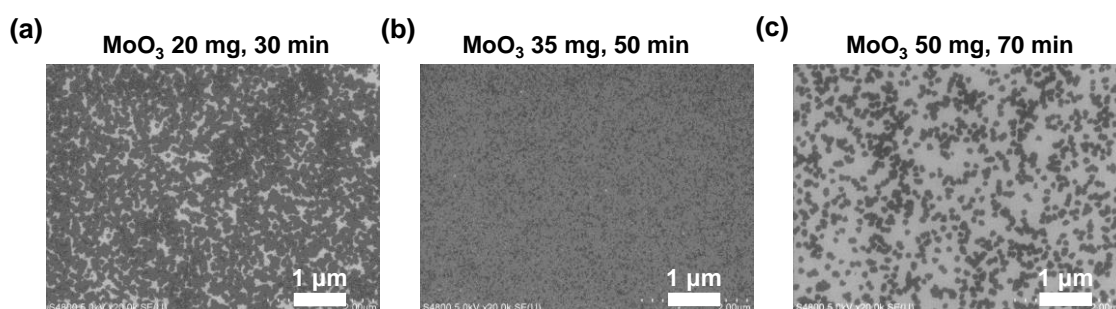


**Figure 4.7** Effect of MoO<sub>3</sub> amount and growth time on MoS<sub>2</sub> synthesis results, characterized by SEM. (a) 30 min. (b) 50 min. (c) 70 min.

Growth duration is apparently an important parameter for the yield of MoS<sub>2</sub>, which is coupled with the amount of precursors that are supplied during the LPCVD process. As

## Chapter 4 Controlled Synthesis of SWCNTs and MoS<sub>2</sub> based Nanomaterials and their Application in Photovoltaic Devices

---

we used excess S to ensure enough S supply, the amount control mainly lies in the amount of MoO<sub>3</sub>, which is proportional to the growth duration. As shown in Figure 4.7a, for 30-min growth, we used 20 mg MoO<sub>3</sub>, and the MoS<sub>2</sub> is not fully covering the substrate. Then, after we increased the growth duration to 50 min with 35 mg MoO<sub>3</sub>, full coverage of MoS<sub>2</sub> onto the substrate can be realized (Figure 4.7b). However, if the growth duration is longer, *e.g.*, 70 min with 50 mg MoO<sub>3</sub>, the coverage is lower again (Figure 4.7c). The reason for this phenomenon may be that too many MoS<sub>2</sub> nuclei etched the MoS<sub>2</sub> away from the substrate.

### 4.1.2.6 Continuous Monolayer MoS<sub>2</sub> Film

After tuning the various growth parameters, a monolayer MoS<sub>2</sub> film with > 99% coverage on SiO<sub>2</sub>/Si substrate can be synthesized, as shown in Figure 4.8a. The growth parameters are: Ar flow rate: 50 sccm; S evaporation temperature: 128 °C; MoO<sub>3</sub> sublimation/growth temperature: 530 °C; S amount: 2–3 g; MoO<sub>3</sub> amount: 35 mg; growth duration: 50 min;  $D_{\text{substrate}}$ : 8 cm.

SEM characterizations confirmed that the coverage is > 99%, as shown in Figure 4.8b. Because MoS<sub>2</sub> tends to grow at the rough surface and edge of the substrate, characterizing the center of the substrate can help us know the lowest coverage. As the center of the substrate has been almost fully covered by MoS<sub>2</sub>, we can say that the MoS<sub>2</sub> film is continuous.

The Raman in Figure 4.8c shows the typical E<sub>2g</sub><sup>1</sup> and A<sub>1g</sub> peaks of MoS<sub>2</sub>. The distance between these two peaks is 21 cm<sup>-1</sup>, indicating the MoS<sub>2</sub> film has 1–2 layers. However, as the PL characterization in Figure 4.8d shows a strong PL feature of monolayer MoS<sub>2</sub>, we can confirm that the major parts of the film are monolayer. From the SEM image in

## Chapter 4 Controlled Synthesis of SWCNTs and MoS<sub>2</sub> based Nanomaterials and their Application in Photovoltaic Devices

Figure 4.8b, we can confirm that there are bilayer nuclei in the single-crystalline MoS<sub>2</sub> domains, which is a common problem for the CVD synthesized MoS<sub>2</sub> [126], though not always mentioned.

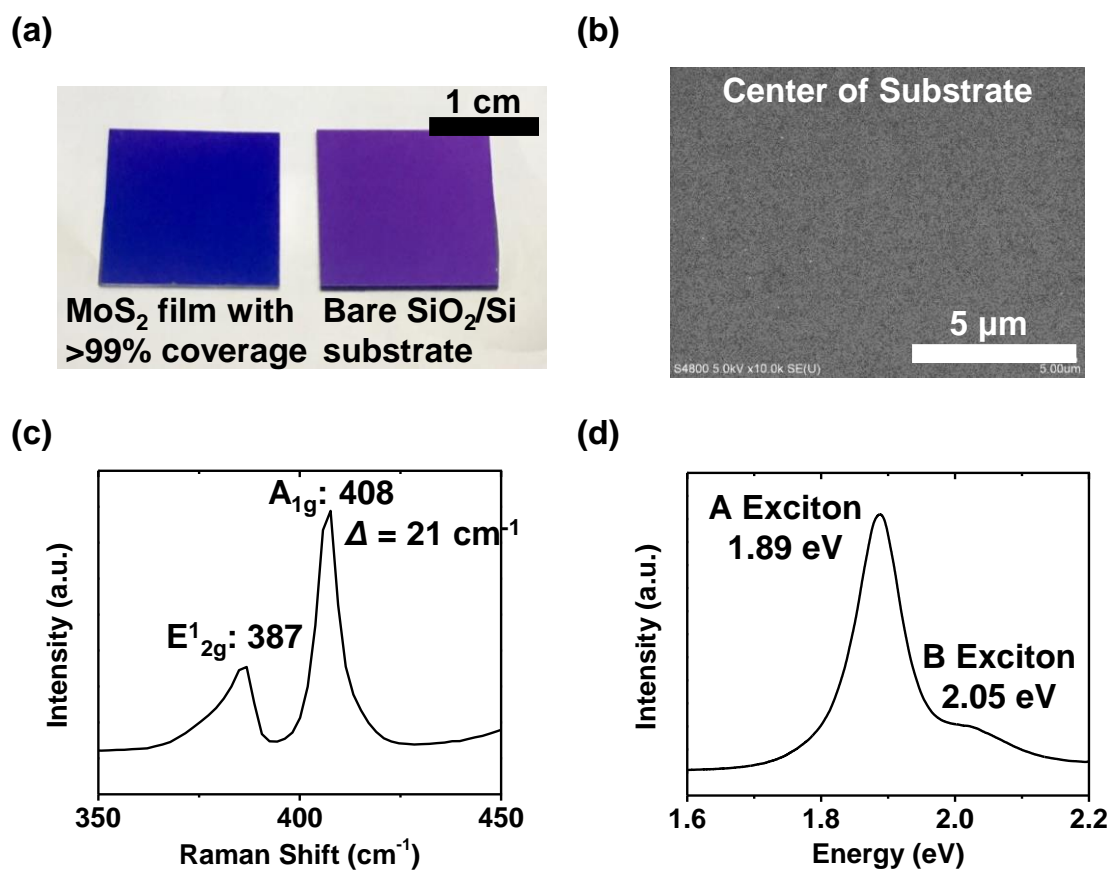


Figure 4.8 As-synthesized continuous monolayer MoS<sub>2</sub> film by LPCVD. (a) Optical image, along with the comparison with bare SiO<sub>2</sub>/Si substrate. (b) SEM image of the center of substrate. (c) Raman. (d) PL.

### 4.1.3 Summary

In summary, after I constructed the MoS<sub>2</sub> LPCVD, MoS<sub>2</sub> has been successfully synthesized by controlling various growth parameters. After the optimization of these

## **Chapter 4 Controlled Synthesis of SWCNTs and MoS<sub>2</sub> based Nanomaterials and their Application in Photovoltaic Devices**

---

parameters, the morphology of the as-synthesized MoS<sub>2</sub> became better, which finally resulted in a continuous monolayer MoS<sub>2</sub> film with > 99% coverage. The successful improvement of nucleation density and domain size enable us to synthesize MoS<sub>2</sub> on various substrates with various structures.

## 4.2 Controlled Synthesis of 1D SWCNTs and MoS<sub>2</sub> based vdW Heterostructures

### 4.2.1 Literature Review and Introduction

As 2D graphene has inspired the research of "2D nanomaterials beyond graphene", the discovery of 1D CNT structure has also given us more room at the bottom of the material world. This kind of tubular structure is actually not only for carbon-based nanomaterials, but also has been realized for MoS<sub>2</sub> [134–137] and WS<sub>2</sub> [136,138]. Although these reports have shown the potential for the diversity of 1D nanomaterials, the methods used to synthesize 1D MoS<sub>2</sub>NT were not clean, and the evidence for single-walled MoS<sub>2</sub>NT was not clear.

2D nanomaterials with interlayer vdW forces have enabled the demonstration of vdW heterostructures [6,139,140], in which atomic layers are stacked on each other and different ingredients can be combined beyond symmetry and lattice matching. However, this concept has been limited in 2D nanomaterials so far.

From the previous research, 2D MoS<sub>2</sub> has been synthesized on the 2D substrate, *e.g.*, a SiO<sub>2</sub>/Si substrate. As MoS<sub>2</sub> has shown various dimensionality, an interesting idea is that how about we grow MoS<sub>2</sub> on the 1D substrate, *e.g.*, an SWCNT. If we can grow 1D nanostructure of 2D nanomaterial, then a new class of 1D vdW heterostructure can be realized, such as MoS<sub>2</sub>NT-BNNT-SWCNT, as shown in Figure 4.9a. From this starting point, we tried to synthesize MoS<sub>2</sub> on the film that is containing 1D nanostructures (*i.e.*, 1D film) with the previously optimized parameters in Section 4.1.

## 4.2.2 Experimental Methods

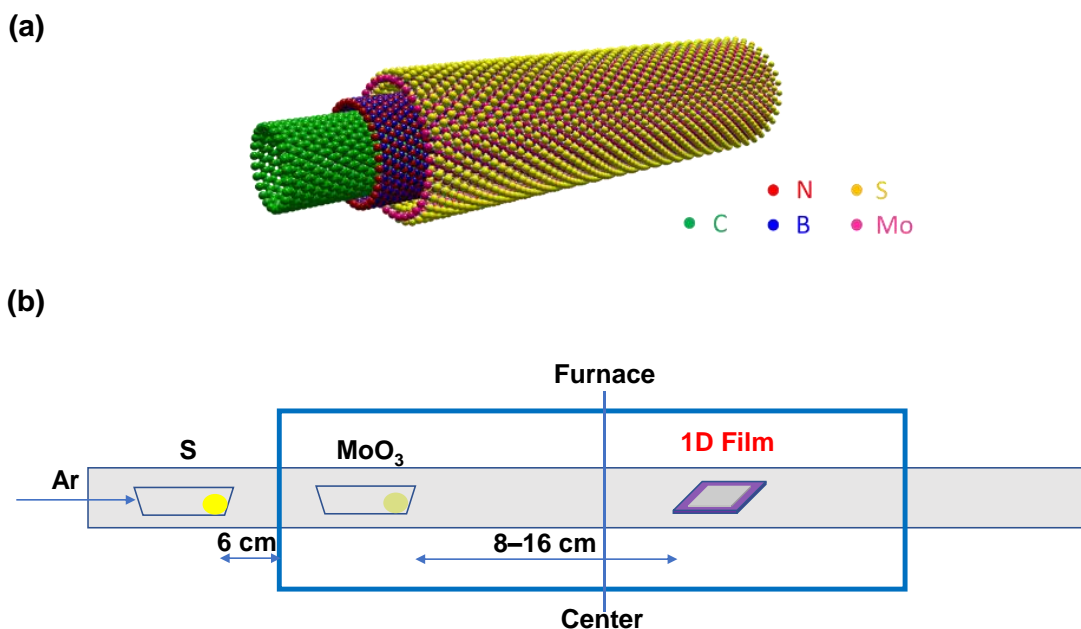


**Figure 4.9 (a) A schematic of a 1D vdW heterostructure of MoS<sub>2</sub>NT-BNNT-SWCNT. (b) A schematic of the LPCVD synthesis of MoS<sub>2</sub>NT onto 1D nanostructures.**

The starting SWCNT film used in this chapter was synthesized by aerosol CVD, as described in Section 2.3.1. The SWCNTs then can be dry-transferred onto a Si substrate, a Mo TEM mesh, or a ceramic washer for the building of heterostructures.

BNNT-SWCNT heterostructures were synthesized by an LPCVD using H<sub>3</sub>NBH<sub>3</sub> as the BN precursor. Briefly, the starting SWCNT film was placed at the center of the furnace. 30 mg BN precursor was loaded at the upstream and heated to 70–90°C. The vapor of BN precursor was taken by a flow of 300 sccm Ar (with 3% H<sub>2</sub>) to the hot zone to form BNNT on the surface of SWCNTs. The reaction temperature was 1000–1100°C and the chamber pressure was maintained at 300 Pa. The growth duration varied from 30 min to 6 hr. After 3-hr CVD, BNNTs were formed at the outer surface of most SWCNTs.

## Chapter 4 Controlled Synthesis of SWCNTs and MoS<sub>2</sub> based Nanomaterials and their Application in Photovoltaic Devices

---

MoS<sub>2</sub>NT-BNNT-SWCNT heterostructures were synthesized by an LPCVD using MoO<sub>3</sub> and S powders as precursors. Typical growth parameters were the same as those for synthesizing continuous monolayer MoS<sub>2</sub> film, with the variation of growth duration (5–50 min) and  $D_{\text{substrate}}$  (8–16 cm). A schematic of the LPCVD synthesis of MoS<sub>2</sub>NT onto 1D nanostructures is shown in Figure 4.9b.

HR-TEM images were taken by a JEM-2010F or JEM-2800 at an acceleration voltage of 200 kV. SAED patterns of the entire film were taken by the same TEMs with a typical selected area aperture diameter of a few  $\mu\text{m}$  and a camera constant of 60 cm. High angle annular HAADF-STEM image and corresponding EELS mapping of MoS<sub>2</sub>NT-SWCNT were taken by JEM-2100F with a cold field-emission gun and an aberration corrector (the DELTA corrector) operating at 60 kV. HAADF-, ABF-STEM images and corresponding EELS mapping of MoS<sub>2</sub>NT-BNNT-SWCNT heterostructures were obtained in the same TEM.

### 4.2.3 Synthesis Results

#### 4.2.3.1 MoS<sub>2</sub>NT-SWCNT 1D vdW Heterostructure

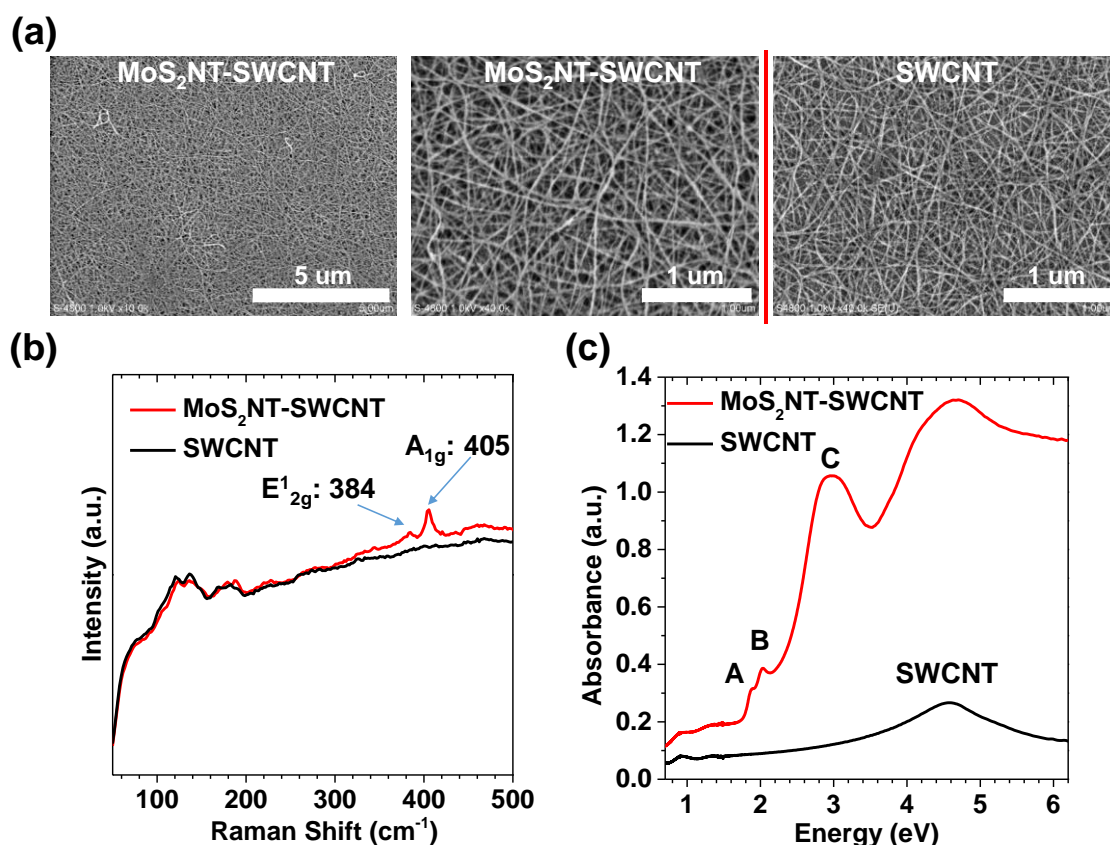


**Figure 4.10** Comparisons of MoS<sub>2</sub>NT-SWCNT and SWCNT films. (a) SEM characterizations. (b) Raman spectra. (c) UV-Vis-NIR absorption spectra.

We firstly tried to synthesize MoS<sub>2</sub>NT onto SWCNT. After synthesis, the sample was firstly characterized in macro scope. The SEM images in Figure 4.10a show that there is little difference from pristine SWCNT film, indicating the almost absence of 2D MoS<sub>2</sub>. The Raman spectra in Figure 4.10b show typical peaks of MoS<sub>2</sub> at E<sub>2g</sub><sup>1</sup> and A<sub>1g</sub>, and the distance between these two peaks indicates a few-layer feature of MoS<sub>2</sub>. We can confirm

## Chapter 4 Controlled Synthesis of SWCNTs and MoS<sub>2</sub> based Nanomaterials and their Application in Photovoltaic Devices

from the absorption spectra in Figure 4.10c that the MoS<sub>2</sub>NT-SWCNT has the A, B, and C absorption peaks, showing the MoS<sub>2</sub>NT is still semiconducting.

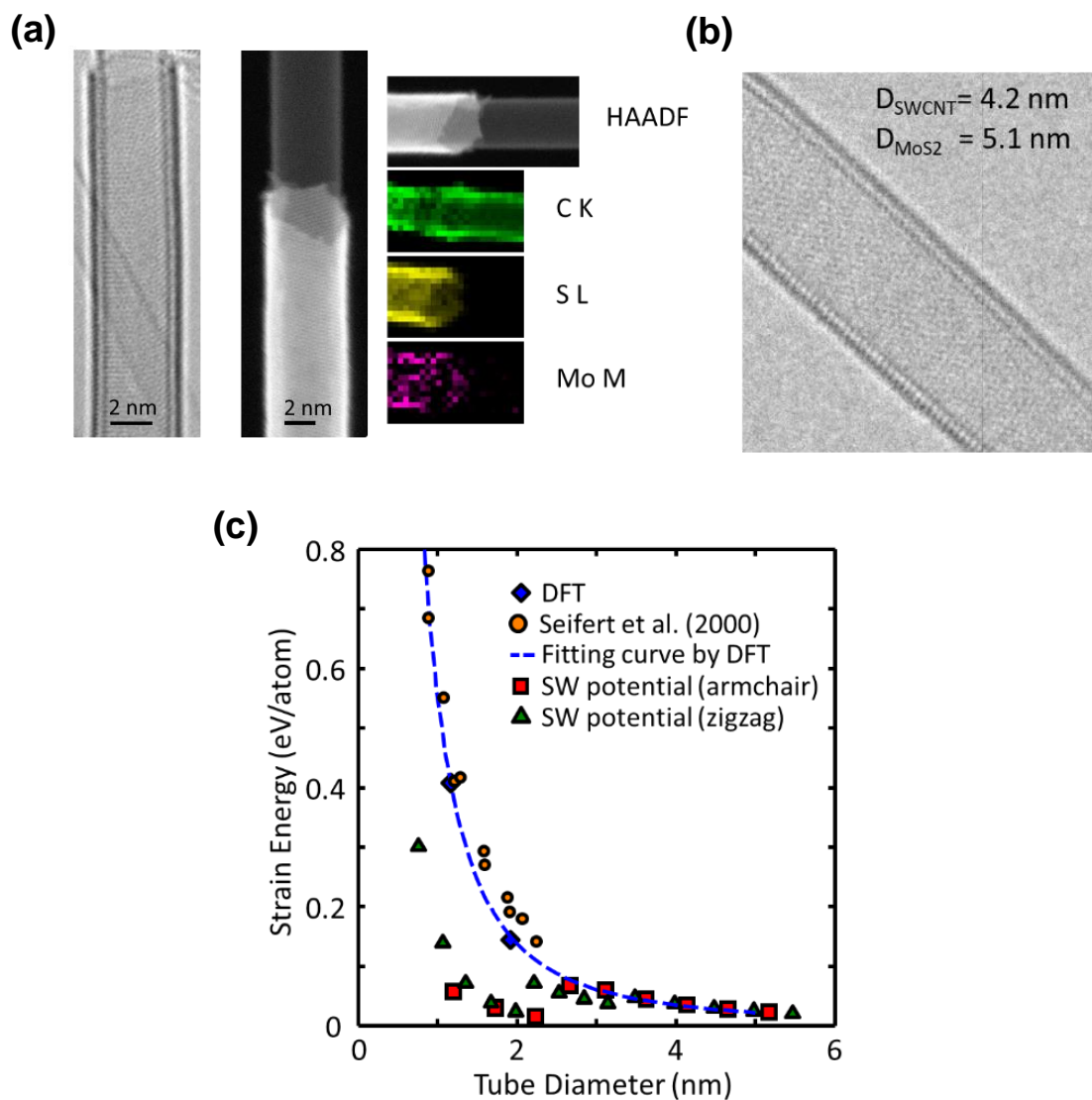


**Figure 4.11 (a) 1D MoS<sub>2</sub>NT-SWCNT nanostructure that was characterized by HR-TEM, HAADF-STEM, and EELS mapping. (b) Typical diameter characterization of a MoS<sub>2</sub>NT-SWCNT. (c) The strain energy of a single-walled MoS<sub>2</sub>NT as a function of tube diameter calculated by Stillinger-Weber (denoted as SW) type potential and DFT simulation.**

## Chapter 4 Controlled Synthesis of SWCNTs and MoS<sub>2</sub> based Nanomaterials and their Application in Photovoltaic Devices

---

In order to reveal the nanostructure of the as-synthesized sample, we characterized the sample in micro scope by TEM. Figure 4.11a shows that an SWCNT is wrapped with a single-walled MoS<sub>2</sub>NT, which is a core-shell or coaxial 1D vdW heterostructure. The MoS<sub>2</sub>NT distinguishes itself by a much stronger contrast than carbon in both TEM and STEM images. This is as far as we know one of the first TEM images evidencing the existence of single-walled MoS<sub>2</sub>NT. We emphasize here the demonstration of single-walled MoS<sub>2</sub>NT because multi-walled MoS<sub>2</sub>NT (with a diameter of usually 20 nm or above) and its hybrid materials have been known for decades. Single-walled MoS<sub>2</sub>NT is predicted to have direct bandgap so its properties can probably be distinctively different from its thicker multi-walled counterparts [141]. Also, quantum confinement is expected to be significant in a single-walled MoS<sub>2</sub>NT with a small diameter [142]. Most importantly, the formation of a MoS<sub>2</sub>NT suggests that other single-walled TMDC nanotubes, *e.g.*, WS<sub>2</sub>, WSe<sub>2</sub>, may also be produced by a similar approach. Hence, for this single-layer featured, largely curved, quantum-confinable TMDC nanotubes, we foresee lots of interesting research topics in spectroscopy, device, and others.

Also, we observe a strong diameter dependence for the formation of single-walled MoS<sub>2</sub>NT. The yield of MoS<sub>2</sub>NT is very low and seamless wrapping is only observed on large-diameter SWCNTs, as shown in Figure 4.11b. To understand this point, we performed some simulations on the strain energy of single-walled MoS<sub>2</sub>NT with different diameters. A clear  $1/D^2$  relationship is observed in Figure 4.11c, which suggests that, in small-diameter range, strain energy is significantly higher. This result is comparable to some previous attempts using density-functional-based tight binding available in the literature [141][143]. If compared to SWCNTs [144], this strain energy is much higher. This can be simply interpreted as a thickness effect: as a single layer of MoS<sub>2</sub> contains

## **Chapter 4 Controlled Synthesis of SWCNTs and MoS<sub>2</sub> based Nanomaterials and their Application in Photovoltaic Devices**

---

three atomic planes and is therefore unstable when rolled into a tubular structure. This is probably why MoS<sub>2</sub>NTs were only seen as multi-walled or on MWCNTs previously [145][146]. According to this result, the minimum diameter of single-walled MoS<sub>2</sub>NTs should be significantly larger than that of SWCNTs. This prediction is surprisingly consistent with our experimental observations. The tubes were found to have diameters of 3.9–6.8 nm, only forming on SWCNTs that have diameters of 3 nm or more. However, most of the starting SWCNTs are thinner than 3 nm, which probably caused the low yield of MoS<sub>2</sub>NT-SWCNT heterostructures. In addition, there is no clear evidence showing preference of zigzag or armchair MoS<sub>2</sub>NT, but we speculate their growth should be kinetically different. Besides this, many features of this single-walled MoS<sub>2</sub>NT are unknown, and we expect more efforts to come for this new nanomaterial.

### **4.2.3.2 MoS<sub>2</sub>NT-BNNT-SWCNT 1D vdW Heterostructure**

The successful post-stacking of BNNT, which is an insulator, onto the outer surface of SWCNTs makes us believe that an even more aggressive 1D vdW heterostructure of MoS<sub>2</sub>NT-BNNT-SWCNT can be realized for the first time.

After the synthesis of BNNT-SWCNT heterostructure, the sample was put into the MoS<sub>2</sub> LPCVD system to coat MoS<sub>2</sub>NT. The coating can be produced in cm scale, and the clear difference can be observed even with naked eyes. As shown in Figure 4.12a, after the synthesis of MoS<sub>2</sub>NT, the film became yellow-green, which is a typical color of MoS<sub>2</sub>. The Raman spectra in Figure 4.12b also confirms the existence of MoS<sub>2</sub>, and is again characterized to be a few-layer feature of MoS<sub>2</sub>. The absorption spectra in Figure 4.12c show the absorption peaks of SWCNT, BN, and MoS<sub>2</sub> clearly.

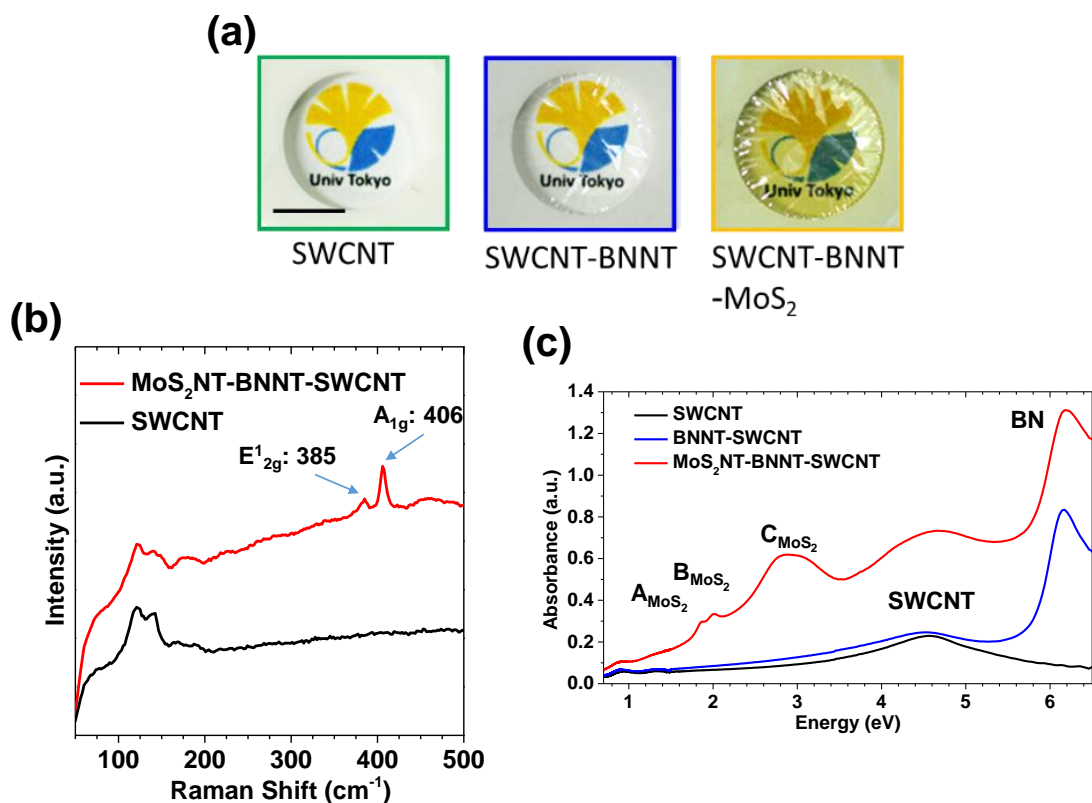
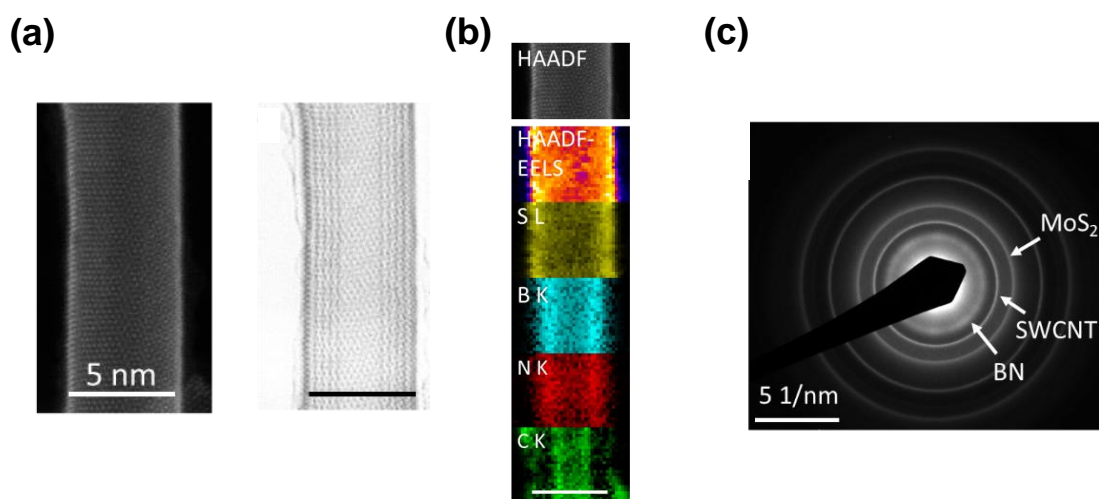


Figure 4.12 Comparisons of SWCNT, BNNT-SWCNT, and MoS<sub>2</sub>NT-BNNT-SWCNT films. (a) Optical images against a printed logo of the University of Tokyo. The scale bar is 5 mm. (b) Raman spectra. (c) UV-Vis-NIR absorption spectra.

TEM characterizations in Figure 4.13a revealed that the nanotube is 5 nm in diameter but consists of three different materials: an inner conducting SWCNT, a middle triple-walled insulating BNNT, and an outside single-walled semiconducting MoS<sub>2</sub>NT. This structure is clearly visualized by the EELS mapping in Figure 4.13b. The existence of SWCNT, BN, and MoS<sub>2</sub> was confirmed by the SAED patterns in Figure 4.13c.



**Figure 4.13** TEM characterizations of the MoS<sub>2</sub>NT-BNNT-SWCNT 1d vdW heterostructures. (a) TEM. The scale bar is 5 nm. (b) EELS mapping. (c) SAED patterns.

Also, as the tube diameter increases from 2 to more than 3 nm after BNNT coating, synthesizing an additional MoS<sub>2</sub>NT becomes much easier. More efficient growth is observed in most of the isolated regions. Such a structure can probably be the smallest MIS vdW heterostructure demonstrated so far. Field effect of the outside MoS<sub>2</sub>NT may be measured using the inner SWCNT gate, and photo-response/PV effect may also be expected in such 1D vdW heterostructures.

#### 4.2.4 Summary

In conclusion, we have discovered 1D vdW heterostructures, extending the concept of vdW heterostructures to a different dimension by tailoring SWCNT and MoS<sub>2</sub> based nanomaterials. Single-walled MoS<sub>2</sub>NT has been synthesized on SWCNT and BNNT-SWCNT, and the realized nanostructures have been characterized by TEM. Most

## **Chapter 4 Controlled Synthesis of SWCNTs and MoS<sub>2</sub> based Nanomaterials and their Application in Photovoltaic Devices**

---

importantly, a novel MoS<sub>2</sub>NT-BNNT-SWCNT 1D vdW heterostructure has been realized for the first time.

It is highly possible that the synthetic technique shown here can be employed to generate a class of new nanotube materials and a series of more sophisticated combinations. 1D vdW heterostructures may bring numerous research interests in material synthesis, crystallography, optics, device physics/applications, catalysis, and probably other areas that are still unforeseen.

## 4.3 Application of SWCNTs and MoS<sub>2</sub> based Nanomaterials in Photovoltaic Devices

### 4.3.1 Literature Review and Introduction

Although 2D semiconducting MX<sub>2</sub> nanomaterials have the thickness of sub-nm level, they have been demonstrated to have unique optical properties [147–150]. The power density of monolayer MoS<sub>2</sub> has been calculated to be one order of magnitude higher than that of traditional PV materials [150]. Moreover, near-unity absorption for sub-15 nm thick MX<sub>2</sub> nanomaterials as active layers has been demonstrated by semiconductor-metal heterostructures [151], showing the potential of high PV efficiency of ultra-thin TMDC nanomaterials.

As MoS<sub>2</sub> is an *n*-type semiconductor, it has the potential to replace *n*-Si in solar cells for cost-cutting, lightweight and flexible applications, semi-transparent applications, and so on. On the other hand, MoS<sub>2</sub> may also contribute to other functional layers of solar cells after tailoring. There have been several efforts to apply monolayer MoS<sub>2</sub> in PV devices. A vertical *p-n* heterojunction of *p*-Si/monolayer MoS<sub>2</sub> has been demonstrated to have a PCE of 5.2% [152]. Furthermore, a lateral *p-n* heterojunction solar cell of WSe<sub>2</sub>-MoS<sub>2</sub> showed an impressive PCE of 2.6%, though the active area was extremely small (4 μm<sup>2</sup>). Thicker MoS<sub>2</sub> nanosheets have also been demonstrated helpful in PV devices. The insertion of a ≈ 17 nm MoS<sub>2</sub> film between graphene-Si solar cell facilitated the hole-transporting/electron-blocking process [153]. The vertical stacking of > 100 nm MoS<sub>2</sub> nanomembranes and Au could function as Schottky barrier solar cells and had PCEs of 0.7–1.8%, depending on the thickness of MoS<sub>2</sub> [154]. Moreover, MoS<sub>2</sub>, along with other

## **Chapter 4 Controlled Synthesis of SWCNTs and MoS<sub>2</sub> based Nanomaterials and their Application in Photovoltaic Devices**

---

TMDC nanomaterials, have been found to be promising candidates for both the HTL and ETL in organic and perovskite solar cells [152–166]. Due to the inorganic nature of MoS<sub>2</sub>, the stability of perovskite solar cells with TMDCs were also significantly enhanced.

From the above literature reviews, MoS<sub>2</sub> based PV devices have been demonstrated to be effective with various structures. Interestingly, these devices can be either vertical or lateral, which have also been reported by other reports of MoS<sub>2</sub> based electronic devices [170,171]. Coupling with the 1D vdW heterostructure that was realized in Section 4.2, the application of this kind of novel structure can allow us to fabricate PV devices with 1D dimensionality. Actually, 1D multi-walled WS<sub>2</sub> was recently proven to show orders of magnitude higher bulk PV effect than that of 2D WS<sub>2</sub>, which demonstrates the potential of 1D TMDC nanotubes for harvesting solar energy more efficiently [172]. The integration of different materials in one substance can also allow easier fabrication than layer-stacking, and thus reduce the size of the device and the amount of used materials. The prototypes of this kind of 1D PV devices are expected to ignite the application of 1D vdW heterostructures, as well as the application of SWCNT and TMDC based nanomaterials in PV devices.

### **4.3.2 MoS<sub>2</sub>NT as Light-Absorbing Layer in Photovoltaic Devices**

The C<sub>60</sub>-MoS<sub>2</sub>NT-SWCNT PV devices were fabricated with MoS<sub>2</sub>NT as the light-absorbing layer, SWCNT as the HTL, and C<sub>60</sub> as the ETL, as shown in Figure 4.14. The C<sub>60</sub> ETL was prepared as follows: 10 mg/ml C<sub>60</sub> was dissolved in 1,2-dichlorobenzene; the obtained solution was spin-coated onto FTO-coated glass substrate with 1500 rpm; the substrate was dried at 60 °C for 2 min. The expected thickness of C<sub>60</sub> layer is  $\approx 37$  nm [173].

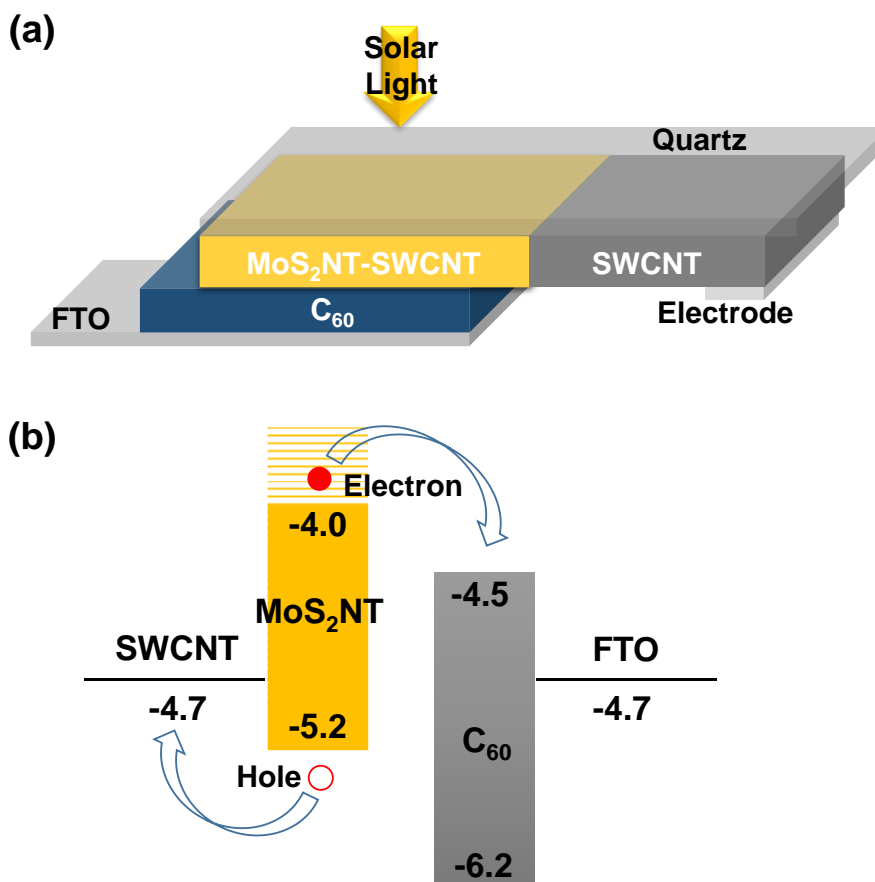


Figure 4.14 (a) A schematic of the C<sub>60</sub>-MoS<sub>2</sub>NT-SWCNT PV device structure. (b) Energy band diagram of the C<sub>60</sub>-MoS<sub>2</sub>NT-SWCNT PV device.

It has been found from DFT calculations that the strain energy causes the bandgap of MoS<sub>2</sub>NT smaller than that of 2D MoS<sub>2</sub> [141,143,174]. Also, while the (*n*, 0) zigzag MoS<sub>2</sub>NTs may have direct bandgaps, other types of MoS<sub>2</sub>NTs (chiral and armchair) may all have indirect bandgaps. From the discussions in Section 4.2.3.1, smaller diameter induces higher strain energy, and thus the bandgap decreases. The as-synthesized MoS<sub>2</sub>NTs on SWCNTs were found to have diameters of 3.9–6.8 nm. Also, there is no clear evidence showing preference of zigzag or armchair MoS<sub>2</sub>NT, and thus the as-

## Chapter 4 Controlled Synthesis of SWCNTs and MoS<sub>2</sub> based Nanomaterials and their Application in Photovoltaic Devices

---

synthesized MoS<sub>2</sub>NT-SWCNT film is a mixture of different MoS<sub>2</sub>NT chiralities. These findings allow us to estimate the bandgap of our MoS<sub>2</sub>NTs: the mixed-chirality large-diameter MoS<sub>2</sub>NTs can be regarded as a bulk MoS<sub>2</sub> substance with a bandgap similar to 2D bulk MoS<sub>2</sub>. However, we expect more discussions about the band structures of MoS<sub>2</sub>NT both theoretically and empirically, especially with the interactions with SWCNT and BNNT.

### 4.3.2.1 C<sub>60</sub>-MoS<sub>2</sub>NT-SWCNT Device Performance

We firstly evaluated the structure of C<sub>60</sub>-MoS<sub>2</sub>NT-SWCNT. The patterned MoS<sub>2</sub>NT-SWCNT film was synthesized using a cover, as shown in Figure 4.15a. The TCF60 SWCNT film was employed to have higher conductivity. The optical image of this film is shown in Figure 4.15b, presenting a clear boundary between SWCNT and MoS<sub>2</sub>NT-SWCNT.

The  $J$ - $V$  curves were measured and it shows a small photocurrent with large leakage, as shown in Figure 4.15c and d. The detailed characteristics are shown in Table 4.1.

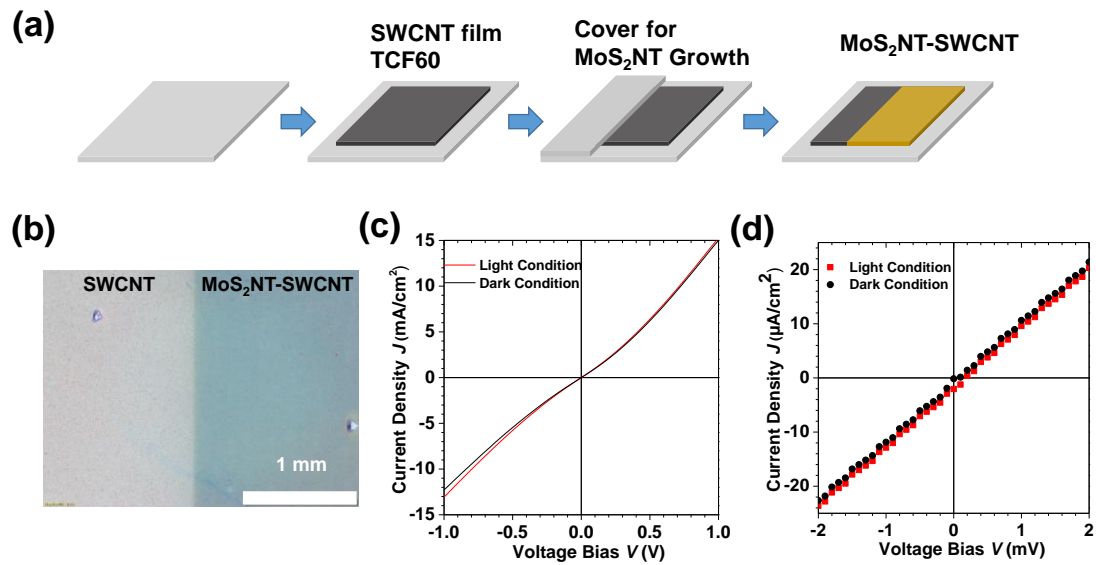


**Figure 4.15** Fabrication and characterizations of the C<sub>60</sub>-MoS<sub>2</sub>NT-SWCNT PV device. (a) A schematic of the sample preparation method. (b) Optical image. (c) *J-V* characteristics in a range of -1 V to 1 V. (d) *J-V* characteristics in a range of -2 mV to 2 mV.

#### 4.3.2.2 C<sub>60</sub>-SWCNT Device Performance

To eliminate the possibility that the photo-response is from C<sub>60</sub> or SWCNT, C<sub>60</sub>-SWCNT device was fabricated and evaluated. As shown in Figure 4.16, the *J-V* curve shows no photocurrent, demonstrating that MoS<sub>2</sub>NT is acting as the light-absorbing layer.

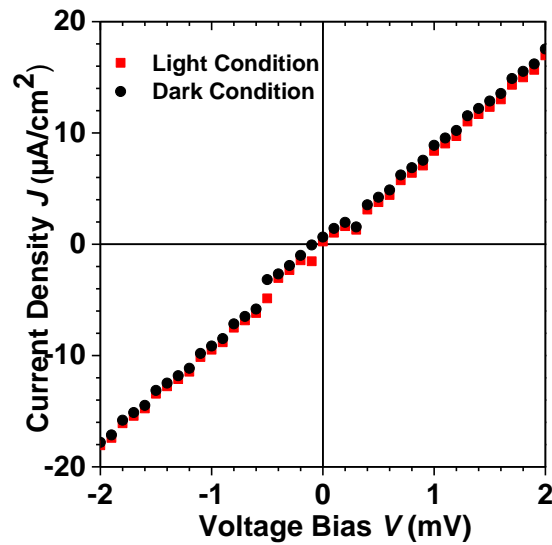


Figure 4.16  $J$ - $V$  characteristics of the C<sub>60</sub>-SWCNT device.

#### 4.3.2.3 C<sub>60</sub>-MoS<sub>2</sub>NT-BNNT-SWCNT Device Performance

We then evaluated the structure using BNNT as an interfacial layer between MoS<sub>2</sub>NT and SWCNT. The structure is again synthesized by a patterned method with a cover, as shown in Figure 4.17a. The growth duration of BNNT CVD is 3 hr. The boundaries can be clearly observed in the optical image (Figure 4.17b).

Figure 4.17c presents the  $J$ - $V$  characteristics of this PV device. It shows a larger photocurrent than the that without BNNT. The detailed characteristics are shown in Table 4.1.

## Chapter 4 Controlled Synthesis of SWCNTs and MoS<sub>2</sub> based Nanomaterials and their Application in Photovoltaic Devices

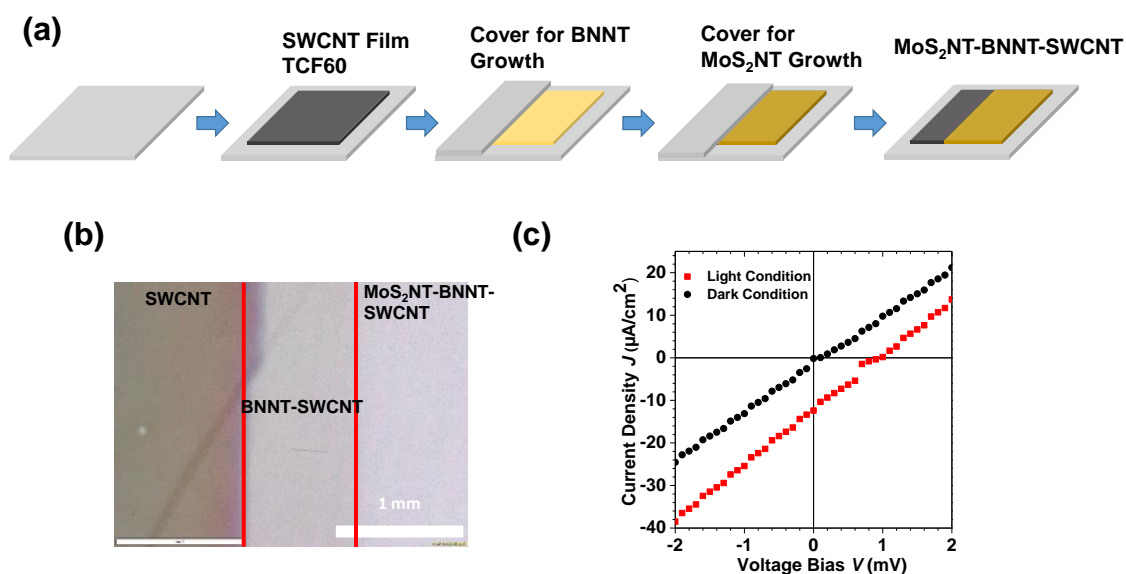


**Figure 4.17** Fabrication and characterizations of C<sub>60</sub>-MoS<sub>2</sub>NT-BNNT-SWCNT PV device. (a) A schematic of the sample preparation method. (b) Optical image. (c)  $J$ - $V$  characteristics in a range of -2 mV to 2 mV.

### 4.3.2.4 Mechanism Discussions

As shown in Figure 4.18a, the comparison of the  $J$ - $V$  curves in light condition shows that by using BNNT as an interfacial insulating layer, PCE has been improved for an order of magnitude. This is because that BNNT partially facilitated the electron-hole separation [175], as shown in Figure 4.18b. More discussions about the functions of BNNT will be presented in Section 4.3.3.

However, the leakage among layers is still dominating the  $J$ - $V$  curve, so we could not confirm a diode characteristic curve. Besides, the contact problem caused by clamping two substrates may account for the low current. The potential application of this device structure could be photodetectors.

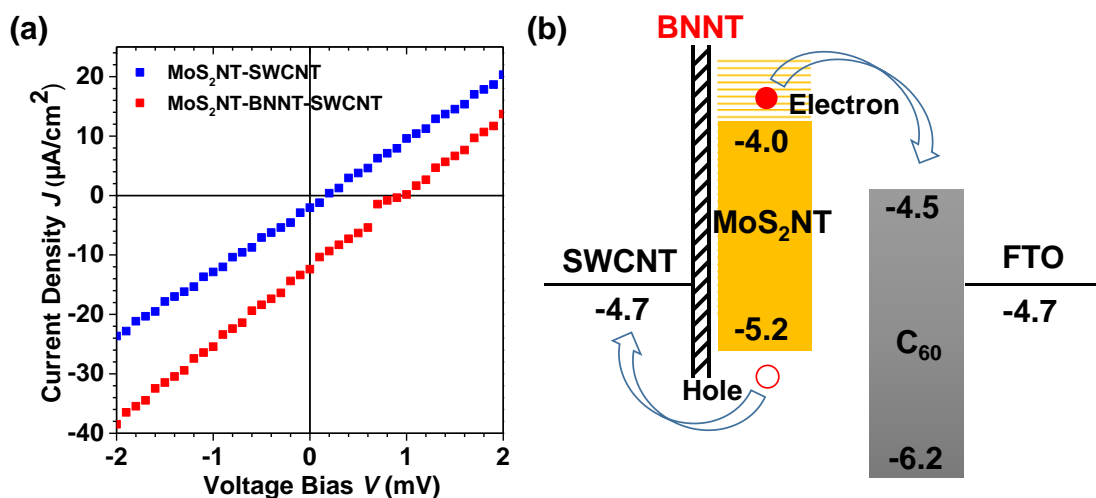


Figure 4.18 (a) Comparison of the  $J$ - $V$  characteristics of the C<sub>60</sub>-MoS<sub>2</sub>NT-SWCNT and the C<sub>60</sub>-MoS<sub>2</sub>NT-BNNT-SWCNT PV devices, under 100 mW/cm<sup>2</sup> AM1.5G illumination. (b) Energy band diagram of the C<sub>60</sub>-MoS<sub>2</sub>NT-BNNT-SWCNT PV device.

Table 4.1 Comparison of the characteristics of the C<sub>60</sub>-MoS<sub>2</sub>NT-SWCNT and the C<sub>60</sub>-MoS<sub>2</sub>NT-BNNT-SWCNT PV devices.

1D Heterostructure	PCE (%)	FF (%)	$V_{oc}$ (V)	$J_{sc}$ (mA/cm <sup>2</sup> )
MoS <sub>2</sub> NT-SWCNT	$1.2 \times 10^{-7}$	47.5	0.12	$2.1 \times 10^{-3}$
MoS <sub>2</sub> NT-BNNT-SWCNT	$3.2 \times 10^{-6}$	27.9	0.93	$1.2 \times 10^{-2}$

### 4.3.3 MoS<sub>2</sub>NT-SWCNT as Electron Transport Layer and Cathode in Perovskite Solar Cells

The as-synthesized MoS<sub>2</sub>NT-SWCNT was applied to inverted-type perovskite solar cells in order to function as both the ETL and cathode at the same time, as shown in Figure

4.19.

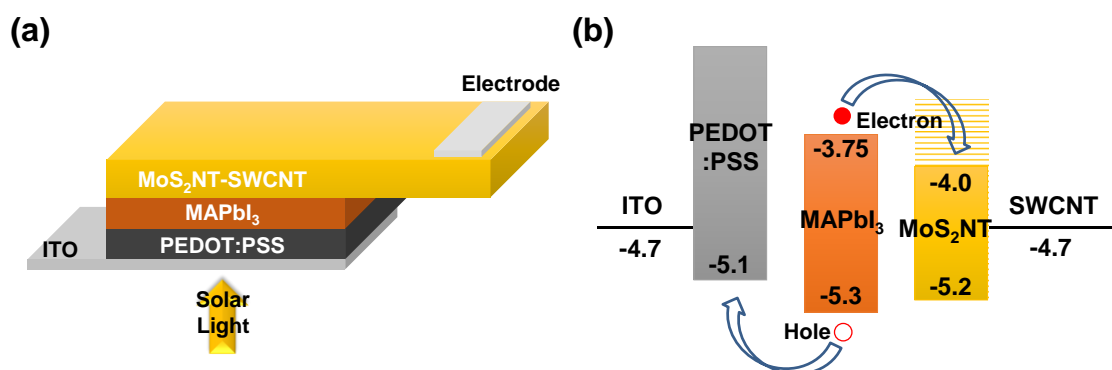


**Figure 4.19 (a) A schematic of the MoS<sub>2</sub>NT-SWCNT on top of an inverted-type perovskite solar cell. (b) Energy band diagram of the MoS<sub>2</sub>NT-SWCNT as ETL and cathode in perovskite solar cells.**

The inverted-type perovskite solar cell substrate consists of an ITO as the anode, a PEDOT:PSS layer as the HTL, a CH<sub>3</sub>NH<sub>3</sub>PbCl<sub>3</sub> (MAPbI<sub>3</sub>) layer as the light-absorbing layer. The detailed fabrication methods of these layers can be found in the literature [34]. Usually, we need PCBM as the ETL, followed by laminating an SWCNT film on the top as the cathode. In this research, the MoS<sub>2</sub>NT-SWCNT film was directly transferred onto the substrate without the PCBM layer.

The MoS<sub>2</sub>NT-SWCNT film (SWCNT: TCF60) was synthesized on a graphite substrate with a designated hole, and was press-printed and floated in chlorobenzene. As chlorobenzene does not react with the layers in this inverted-type perovskite solar cell, we can fish the film out by the perovskite solar cell substrate, which also ensures good contact. For comparison purpose, the SWCNT film (TCF60) was also transferred by this method.

### 4.3.3.1 MoS<sub>2</sub>NT-SWCNT Device Performance

We firstly evaluated the MoS<sub>2</sub>NT-SWCNT on top of inverted-type perovskite solar cells. As shown in Figure 4.20a and Table 4.2, under the light condition, this structure works as a solar cell junction and the PCE is 0.29%. On the other hand, the SWCNT on top of inverted-type perovskite solar cells cannot form a junction with the photo-response only, as shown in Figure 4.20b. As a result, it is the MoS<sub>2</sub>NT that has the function of ETL in inverted-type perovskite solar cells.

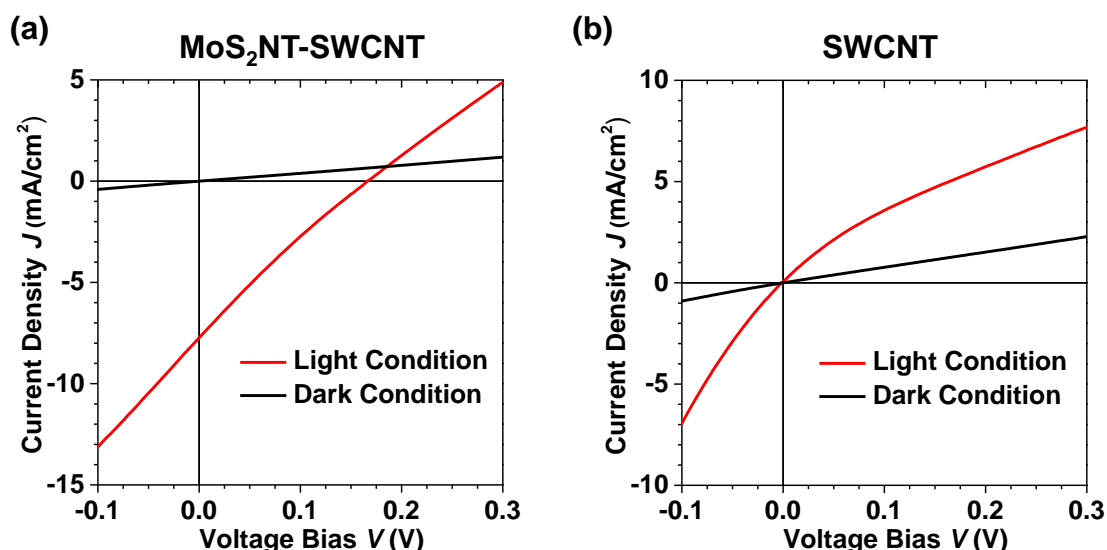


Figure 4.20  $J$ - $V$  characteristics of (a) the MoS<sub>2</sub>NT-SWCNT and (b) the SWCNT on top of inverted-type perovskite solar cells, under 100 mW/cm<sup>2</sup> AM1.5G illumination.

### 4.3.3.2 MoS<sub>2</sub>NT-BNNT-SWCNT Device Performance

From the knowledge we gained in Section 4.3.2, BNNT can partially facilitate the electron-hole separation when applying MoS<sub>2</sub>NT-SWCNT in PV devices. So we evaluated the MoS<sub>2</sub>NT-BNNT-SWCNT on top of inverted-type perovskite solar cells.

## Chapter 4 Controlled Synthesis of SWCNTs and MoS<sub>2</sub> based Nanomaterials and their Application in Photovoltaic Devices

Because the BNNT may block the electrons and holes together, we employed different growth durations of BNNT: 3 hr and 1 hr, to investigate this aspect by different BNNT walls. While 3-hr growth can form 5–8 BNNT walls, 1-hr growth can reduce to 1–2 walls.

As shown in Figure 4.21a and Table 4.2, first, the PCE has been improved slightly by inserting 3-hr BNNT between MoS<sub>2</sub>NT and SWCNT. The enhancement mainly came from  $V_{OC}$ , which was improved from 167 mV to 267 mV. Then, the PCE has been doubled from 0.32% to 0.66% by using 1-hr BNNT instead to improve the  $V_{OC}$  to 395 mV. The conductivity of the film decreased because of the insulating effect of BNNT, as evidenced by the  $J_{SC}$ . FF was improved slightly by BNNT.

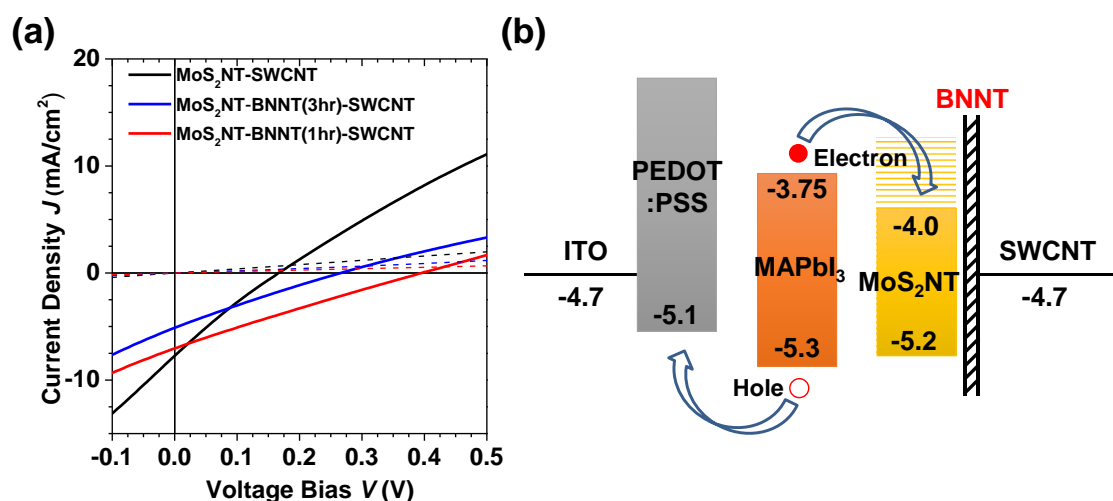


**Figure 4.21** (a) Comparison of the  $J$ - $V$  characteristics of the MoS<sub>2</sub>NT-SWCNT, MoS<sub>2</sub>NT-BNNT(3hr)-SWCNT, and MoS<sub>2</sub>NT-BNNT(1hr)-SWCNT on top of inverted-type perovskite solar cells, under 100 mW/cm<sup>2</sup> AM1.5G illumination. The dashed lines are the dark current. (b) Energy band diagram of the MoS<sub>2</sub>NT-BNNT-SWCNT as ETL and cathode in perovskite solar cells.

**Chapter 4 Controlled Synthesis of SWCNTs and MoS<sub>2</sub> based Nanomaterials and their Application in Photovoltaic Devices**

**Table 4.2 Comparison of the characteristics of the MoS<sub>2</sub>NT-SWCNT, MoS<sub>2</sub>NT-BNNT(3hr)-SWCNT, and MoS<sub>2</sub>NT-BNNT(1hr)-SWCNT on top of inverted-type perovskite solar cells.**

ETL & Cathode	PCE (%)	FF (%)	$V_{oc}$ (V)	$J_{sc}$ (mA/cm <sup>2</sup> )
MoS <sub>2</sub> NT-SWCNT	0.29	22.6	167	7.7
MoS <sub>2</sub> NT-BNNT(3hr)-SWCNT	0.32	23.2	267	5.1
MoS <sub>2</sub> NT-BNNT(1hr)-SWCNT	0.66	23.8	395	7.0

#### 4.3.3.3 Mechanism Discussions

From the experiment results, the contribution of BNNT to the performance enhancement has been confirmed again. As shown the energy band diagram in Figure 4.21b, the MoS<sub>2</sub>NT is not a perfect ETL by the high HOMO level, which causes leakage of holes to the cathode. After the insertion of BNNT between MoS<sub>2</sub>NT and SWCNT, part of the leaked holes can be blocked by BNNT, resulting in higher  $V_{oc}$  and PCE. In addition, as some of the SWCNTs are not fully covered by MoS<sub>2</sub>NT (Figure 4.11a), BNNT can eliminate the negative effect of multi-junctions, *e.g.*, *p-n-p-n-p*.

It has also been confirmed that BNNT blocks electrons and holes together by the results of different BNNT walls. While 1–2 BNNT walls may allow more holes to tunnel to SWCNT side than the 5–8 walls, it can help more electrons to tunnel too. As a result, there is a trade-off between the tunneling and blocking effects of BNNT for electrons and holes (*e.g.*, the trade-off between charge separation and recombination).

## Chapter 4 Controlled Synthesis of SWCNTs and MoS<sub>2</sub> based Nanomaterials and their Application in Photovoltaic Devices

We have substituted two layers of PCBM and SWCNT in inverted-type perovskite solar cells with one multifunctional layer of MoS<sub>2</sub>NT-(BNNT)-SWCNT. The integration of ETL and cathode in one layer can allow easier fabrication than the layer-stacking, and thus reduce the size of the device and the amount of used materials. Although the PCE at this stage is not high, further tailoring of the 1D vdW heterostructures is expected to enhance the solar cell performance.

### 4.3.4 MoS<sub>2</sub>NT-SWCNT as Hole Transport Layer and Anode in Perovskite Solar Cells

The as-synthesized MoS<sub>2</sub>NT-SWCNT was also applied to normal-type perovskite solar cells in order to function as both the HTL and anode at the same time, as shown in Figure 4.22.

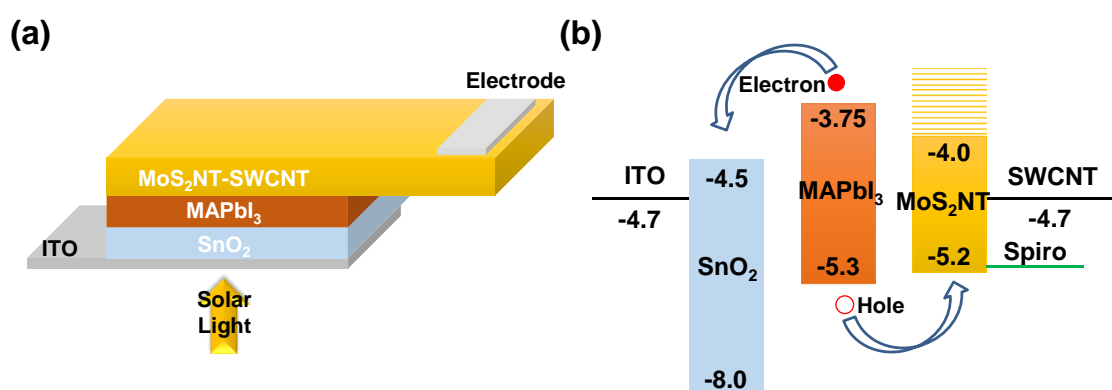


Figure 4.22 (a) A schematic of the MoS<sub>2</sub>NT-SWCNT on top of a normal-type perovskite solar cell. (b) Energy band diagram of the MoS<sub>2</sub>NT-SWCNT as HTL and anode in perovskite solar cells.

The normal-type perovskite solar cell substrate consists of an ITO as the cathode, a

## Chapter 4 Controlled Synthesis of SWCNTs and MoS<sub>2</sub> based Nanomaterials and their Application in Photovoltaic Devices

SnO<sub>2</sub> layer as the ETL, a MAPbI<sub>3</sub> layer as the light-absorbing layer. The detailed fabrication methods of these layers can be found in the literature [160]. The MoS<sub>2</sub>NT-SWCNT film (SWCNT: TCF60) was transferred onto the substrate by the method described in Section 4.3.3, with hexane as the liquid phase. Again, for comparison purpose, the SWCNT film (TCF60) was also transferred by this method. After the transfer process, 50-nm Au was deposited along the side of the film (outside the active area) by vacuum evaporation for measurement purpose.

### 4.3.4.1 Device Performance

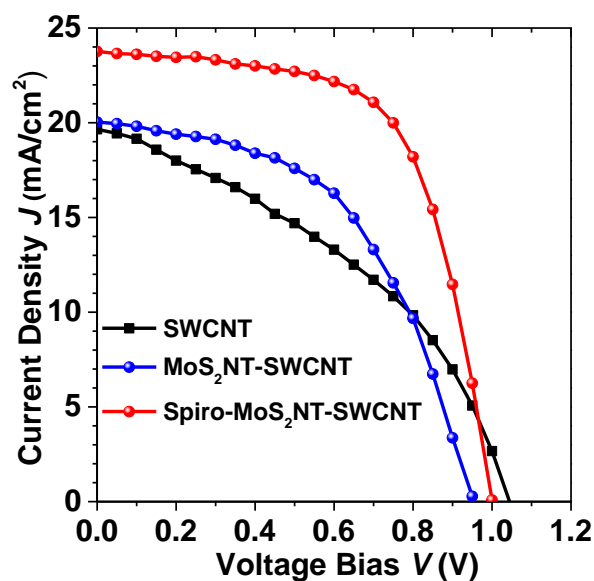


**Figure 4.23** Comparison of the  $J$ - $V$  characteristics of the SWCNT, the MoS<sub>2</sub>NT-SWCNT, and the MoS<sub>2</sub>NT-SWCNT with the spiro-MeOTAD coated on top, on top of normal-type perovskite solar cells, under 100 mW/cm<sup>2</sup> AM1.5G illumination.

As shown in Figure 4.23 and Table 4.3, the application of MoS<sub>2</sub>NT improved the PCE from 8.2% to 9.8%, mainly due to the substantial enhancement of FF, which is from

## Chapter 4 Controlled Synthesis of SWCNTs and MoS<sub>2</sub> based Nanomaterials and their Application in Photovoltaic Devices

39.9% to 51.0%. The spiro-MeOTAD (denoted as spiro in Figure 4.22b, Figure 4.23 and Table 4.3) solution was spin-coated on top of the MoS<sub>2</sub>NT-SWCNT perovskite solar cell to boost the PCE. A PCE of 15.0% has been achieved with all the characteristics improved from those of the pristine MoS<sub>2</sub>NT-SWCNT perovskite solar cell.

**Table 4.3 Comparison of the characteristics of the SWCNT, the MoS<sub>2</sub>NT-SWCNT, and the MoS<sub>2</sub>NT-SWCNT with the spiro-MeOTAD coated on top, on top of normal-type perovskite solar cells.**

HTL & Anode	PCE (%)	FF (%)	$V_{oc}$ (V)	$J_{sc}$ (mA/cm <sup>2</sup> )
SWCNT	8.2	39.9	1.04	19.7
MoS <sub>2</sub> NT-SWCNT	9.8	51.0	0.96	20.0
Spiro-MoS <sub>2</sub> NT-SWCNT	15.0	63.0	1.00	23.8

### 4.3.4.2 Mechanism Discussions

From the energy band diagram in Figure 4.22b, the LUMO level of MoS<sub>2</sub>NT is not so favorable, and thus the  $V_{oc}$  decreased slightly. On the other hand, the MoS<sub>2</sub>NT wrapped around SWCNT can facilitate the hole transport by smoothing the HOMO level alignment. Moreover, from the Raman spectra in Figure 4.24, after the coating of MoS<sub>2</sub>NT, the G band blue-shifted from 1592 cm<sup>-1</sup> to 1596 cm<sup>-1</sup> and the 2D band blue-shifted from 2668 cm<sup>-1</sup> to 2674 cm<sup>-1</sup>, which is a typical *p*-type doping of carbon nanomaterials [176,177].

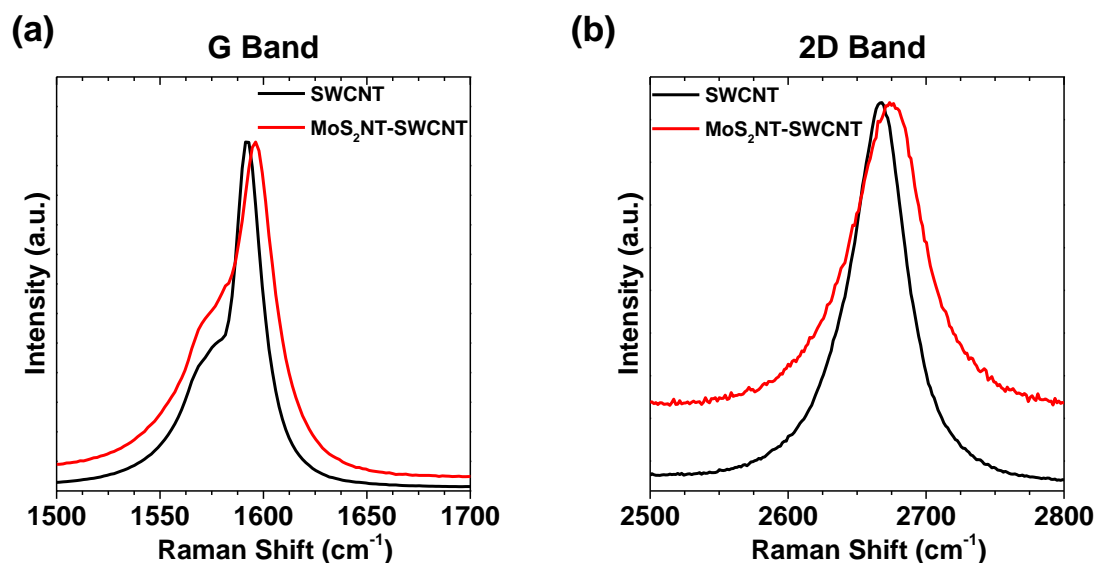


**Figure 4.24 Raman spectra of the SWCNT film before and after MoS<sub>2</sub>NT coating. (a) G band region. (b) 2D band region.**

Although few-layer MoS<sub>2</sub> flakes have been reported to function as HTL in perovskite solar cells [164], the 1D MoS<sub>2</sub>NT wrapping around SWCNT is supposed to be better than 2D MoS<sub>2</sub> in the hole-transporting ability by a closer physical distance. In addition, MoS<sub>2</sub>NT can prevent shunt pathways between MAPbI<sub>3</sub> and SWCNTs. Higher device stability can also be expected because of the inorganic nature of MoS<sub>2</sub>NT. These benefits of MoS<sub>2</sub>NT contributed to better solar cell performance.

### 4.3.5 Summary

In summary, the 1D vdW MoS<sub>2</sub>NT-SWCNT and MoS<sub>2</sub>NT-BNNT-SWCNT heterostructures have been applied to PV devices with different multifunctions. For the light-absorbing layer function, C<sub>60</sub>-MoS<sub>2</sub>NT-BNNT-SWCNT PV device showed higher photocurrent than that of C<sub>60</sub>-MoS<sub>2</sub>NT-SWCNT because of the charge separation

## **Chapter 4 Controlled Synthesis of SWCNTs and MoS<sub>2</sub> based Nanomaterials and their Application in Photovoltaic Devices**

---

facilitation of BNNT. For the ETL and cathode multifunction, we have substituted two layers of PCBM and SWCNT in inverted-type perovskite solar cells with one multifunctional layer of MoS<sub>2</sub>NT-(BNNT)-SWCNT. The integration of ETL and cathode in one layer can allow easier fabrication than the layer-stacking, and thus reduce the size of the device and the amount of used materials. The BNNT again facilitated the charge separation, resulting in the improvement of  $V_{OC}$  and PCE. Moreover, there is a trade-off between the tunneling and blocking effects of BNNT for electrons and holes. For the HTL and anode multifunction, MoS<sub>2</sub>NT-SWCNT was applied to normal-type perovskite solar cells and improved the PCE by the excellent hole-extraction ability of MoS<sub>2</sub>NT. A PCE of 15.0% has been achieved after the application of spiro-MeOTAD. These results have demonstrated prototypes for the promising application of 1D vdW heterostructures in PV devices. The further improvements of the tailoring methods and the device structures will lead to novel applications of both the SWCNT and MoS<sub>2</sub> based nanomaterials and the 1D vdW heterostructures in PV devices.

## Chapter 5 Closing Remarks

### 5.1 Summaries of this Dissertation

This dissertation focused on the tailoring methods for SWCNTs and MoS<sub>2</sub> based nanomaterials, with the application aspect of PV devices.

First, we reported a multifunctional material called Nafion for tailoring SWCNT films in SWCNT-Si solar cells. A simple spin-coating application to the SWCNT film increased the device PCE from 9.5% to 14.4%, manifesting three functions of *p*-doping, a favorable anti-reflection effect, and an exceptional encapsulation effect. The mechanism discussions have given us a comprehensive understanding of the Nafion-tailoring method. The obtained PCE of 14.4% currently stands as the highest stable efficiency among the reported CNT-Si solar cells.

Second, after I constructed the MoS<sub>2</sub> LPCVD, continuous monolayer MoS<sub>2</sub> film has been successfully synthesized by optimizing various growth parameters. Furthermore, we have extended the concept of vdW heterostructures to a different dimension by tailoring SWCNT and MoS<sub>2</sub> based nanomaterials using MoS<sub>2</sub> LPCVD. A novel MoS<sub>2</sub>NT-BNNT-SWCNT 1D MIS vdW heterostructure has been realized for the first time.

Third, the realized 1D vdW MoS<sub>2</sub>NT-SWCNT and MoS<sub>2</sub>NT-BNNT-SWCNT heterostructures have been applied to PV devices with different multifunctions. For the light-absorbing layer function, C<sub>60</sub>-MoS<sub>2</sub>NT-BNNT-SWCNT PV device showed higher photocurrent than that of C<sub>60</sub>-MoS<sub>2</sub>NT-SWCNT because of the charge separation

## Chapter 5 Closing Remarks

---

facilitation of BNNT. For the ETL and cathode multifunction, we have substituted two layers of PCBM and SWCNT in inverted-type perovskite solar cells with one multifunctional layer of MoS<sub>2</sub>NT-(BNNT)-SWCNT. The BNNT again facilitated the charge separation, resulting in the improvement of  $V_{OC}$  and PCE. Moreover, there is a trade-off between the tunneling and blocking effects of BNNT for electrons and holes. For the HTL and anode multifunction, MoS<sub>2</sub>NT-SWCNT was applied to normal-type perovskite solar cells and improved the PCE by the excellent hole-extraction ability of MoS<sub>2</sub>NT. A PCE of 15.0% has been achieved after the application of spiro-MeOTAD. These results have demonstrated prototypes for the promising application of 1D vdW heterostructures in PV devices. The further improvements of the tailoring methods and the device structures will lead to novel applications of both the SWCNT and MoS<sub>2</sub> based nanomaterials and the 1D vdW heterostructures in PV devices.

### 5.2 Vision for Next-Generation Solar Cells

From the case study of nanomaterial solar cells in this dissertation, we can find that the development of cutting-edge technology is focused on the KPIs, such as the PCE, stability, and flexibility. These demonstrated KPIs are helpful for the transition from academia to industry. We can also get hints about how to design next-generation solar cells for real applications and to attract investments. First, the KPIs should be excellent to attract investors' eyes. Second, the fabrication process should be compatible with a scalable industrial process. Third, the comparative advantages should be clarified for obtaining market share. There have already been investments on these next-generation solar cells. For example, OXFORD PV<sup>TM</sup> [178], is a pioneer and technology leader in the field of perovskite solar cells. This company is based on Oxford University, in which Prof. Snaith' group is one of the most famous perovskite solar cell research groups.

It is almost sure that in the next decade, the paradigm shift will occur in the rapidly developing solar cell industry. The question is that what kind of paradigm shift will occur and which type of solar cell will emerge.

As shown in Table 5.1, Si solar cell is already at the high development status; however, the cost is still high. As the FiT is being cut by the government, Si solar cell cannot bring about a paradigm shift in the next decade. The thin-film solar cells are also well-developed, the materials used in these solar cells are still at a high cost and toxic, and the efficiency is not so satisfying. However, we can find comparative advantages to apply them in specific fields, such as the wearable devices, so as to promote the market application. For the next-generation solar cells, we cannot rely on only one type as this is too risky. Each type of next-generation solar cells has its comparative advantages. The

## Chapter 5 Closing Remarks

---

organic solar cells have a relatively longer history of development, and they can be put into the market application promotion stage to help the market get familiar with the next-generation solar cells. The perovskite solar cells still need to solve the stability and toxicity issues, but because its impressive power conversion efficiency, venture capital investment can be in the way to boost the research and also to attract more attention. The nanomaterials solar cells are still in relatively lower development status. The efficiency is low and the gap between academia and industry is still large. However, because of the vast potential of nanomaterials, the continuous support for research is essential to stimulate the researchers. From the experience of the rapid emergence of perovskite solar cells in just a decade, it is still uncertain that which solar cell will be the next king or it can even be the one that we have not discovered yet. However, from the policymaker's perspective, the global consensus of accelerating solar cell application should be continuously maintained. This is not easy as the protectionism is prevalent in some developed countries, and the stakeholders in the opposite side, such as the oil-producing countries, may try to make a negative influence on the negotiation process.

## Chapter 5 Closing Remarks

**Table 5.1 Comparison of different types of solar cells with respect to their different characteristics.**

<b>Solar Cell Type</b>	<b>Development Status</b>	<b>Expected Efficiency</b>	<b>Comparative Advantages</b>	<b>Issues</b>	<b>Policy Change</b>
<b>Si</b>	High	25%	Mature technology	High cost	Decreasing FiT
<b>Thin-Film</b>	Medium-High	15%	Flexible	Low efficiency, toxicity	Market application promotion
<b>Organic</b>	Medium	15%	Public acceptance	Stability, low efficiency, scale-up	Market application promotion
<b>Perovskite</b>	Low-Medium	25%	Impressive performance	Stability, toxicity, scale-up	Venture capital investment
<b>Nanomaterial</b>	Low	15%	Flexible, low cost	Low efficiency, scale-up	Government support

### 5.3 Future Perspectives of this Dissertation

The future perspectives of this dissertation can be focused on:

- 1) Fabrication of SWCNT-perovskite-Si tandem solar cells by Nafion-tailored SWCNT films;
- 2) Further optimization of the synthesis conditions for 2D continuous monolayer MoS<sub>2</sub> films;
- 3) Application of 2D MoS<sub>2</sub> films to PV devices;
- 4) Further optimization of the synthesis conditions for SWCNT and MoS<sub>2</sub> based 1D vdW heterostructures;
- 5) Improvement of the performance of MoS<sub>2</sub>NT-BNNT-SWCNT based PV devices.

## Bibliography

- [1] A. P. Alivisatos, "Semiconductor clusters, nanocrystals, and quantum dots," *Science* **271**, 933 (1996).
- [2] H.W. Kroto, J. R. Heath, S. C. O'Brien, R. F. Curl, and R. E. Smalley, "C<sub>60</sub>: buckminsterfullerene," *Nature* **318**, 162 (1985).
- [3] S. Iijima, "Helical microtubules of graphitic carbon," *Nature* **354**, 56 (1991).
- [4] S. Iijima and T. Ichihashi, "Single-shell carbon nanotubes of 1-nm diameter," *Nature* **363**, 603 (1993).
- [5] K. S. Novoselov, A. K. Geim, S. V Morozov, D. Jiang, Y. Zhang, S. V Dubonos, I. V Grigorieva, and A. A. Firsov, "Electric field effect in atomically thin carbon films," *Science* **306**, 666 (2004).
- [6] A. K. Geim and I. V Grigorieva, "van der Waals heterostructures," *Nature* **499**, 419 (2013).
- [7] B. Radisavljevic, A. Radenovic, J. Brivio, V. Giacometti, and A. Kis, "Single-layer MoS<sub>2</sub> transistors," *Nat. Nanotechnol.* **6**, 147 (2011).
- [8] R. Saito, G. Dresselhaus, and M. S. Dresselhaus., "Physical properties of carbon nanotubes" (1998).
- [9] M. C. Hersam, "Progress towards monodisperse single-walled carbon nanotubes," *Nat. Nanotechnol.* **3**, 387 (2008).
- [10] M. S. Dresselhaus, G. Dresselhaus, R. Saito, and A. Jorio, "Raman spectroscopy of carbon nanotubes," *Phys. Rep.* **409**, 47 (2005).
- [11] Z. K. Tang, N. Wang, G. D. Li, and J. S. Chen, "Materials science: single-walled 4 Å carbon nanotube arrays," *Nature* **408**, 50 (2000).
- [12] J. Golden, M. McMillan, R. T. Downs, G. Hystad, I. Goldstein, H. J. Stein, A. Zimmerman, D. A. Sverjensky, J. T. Armstrong, and R. M. Hazen, "Rhenium variations in molybdenite (MoS<sub>2</sub>): evidence for progressive subsurface oxidation," *Earth Planet. Sci. Lett.* **366**, 1 (2013).
- [13] R. F. Frindt, "Single crystals of MoS<sub>2</sub> several molecular layers thick," *J. Appl. Phys.* **37**, 1928 (1966).
- [14] A. V. Kolobov and J. Tominaga, "Two-dimensional transition-metal dichalcogenides" (2016).
- [15] S. Manzeli, D. Ovchinnikov, D. Pasquier, O. V. Yazyev, and A. Kis, "2D

## Bibliography

---

- transition metal dichalcogenides,” *Nat. Rev. Mater.* **2**, 17033 (2017).
- [16] E. Gibney, “The super materials that could trump graphene,” *Nature* **522**, 274 (2015).
- [17] Q. H. Wang, K. Kalantar-Zadeh, A. Kis, J. N. Coleman, and M. S. Strano, “Electronics and optoelectronics of two-dimensional transition metal dichalcogenides,” *Nat. Nanotechnol.* **7**, 699 (2012).
- [18] Z. M. Wang, “MoS<sub>2</sub>: materials, physics, and devices” (2014).
- [19] K. F. Mak, C. Lee, J. Hone, J. Shan, and T. F. Heinz, “Atomically thin MoS<sub>2</sub>: a new direct-gap semiconductor,” *Phys. Rev. Lett.* **105**, 2 (2010).
- [20] A. Splendiani, L. Sun, Y. Zhang, T. Li, J. Kim, C.-Y. Chim, G. Galli, and F. Wang, “Emerging photoluminescence in monolayer MoS<sub>2</sub>,” *Nano Lett.* **10**, 1271 (2010).
- [21] J. R. Schaibley, H. Yu, G. Clark, P. Rivera, J. S. Ross, K. L. Seyler, W. Yao, and X. Xu, “Valleytronics in 2D materials,” *Nat. Rev. Mater.* **1**, 16055 (2016).
- [22] “World energy outlook 2018” (2018).
- [23] “Renewable energy and jobs - annual review 2018” (2018).
- [24] M. A. Green, Y. Hishikawa, E. D. Dunlop, D. H. Levi, J. Hohl-Ebinger, M. Yoshita, and A. W. Y. Ho-Baillie, “Solar cell efficiency tables (version 53),” *Prog. Photovoltaics Res. Appl.* **27**, 3 (2019).
- [25] W. Shockley and H. J. Queisser, “Detailed balance limit of efficiency of *p-n* junction solar cells,” *J. Appl. Phys.* **32**, 510 (1961).
- [26] “Solar flare - SPV market reseach,”  
<<http://www.spvmarketresearch.com/announcements-and-industry-news.html>>.
- [27] “Solar energy market - allied market research,”  
<<https://www.alliedmarketresearch.com/solar-energy-market>>.
- [28] J. Yuan, Y. Zhang, L. Zhou, G. Zhang, H.-L. Yip, T.-K. Lau, X. Lu, C. Zhu, H. Peng, P. A. Johnson, M. Leclerc, Y. Cao, J. Ulanski, Y. Li, and Y. Zou, “Single-junction organic solar cell with over 15% efficiency using fused-ring acceptor with electron-deficient core,” *Joule* **3**, 1140 (2019).
- [29] D. Yang, X. Zhang, K. Wang, C. Wu, R. Yang, Y. Hou, Y. Jiang, S. Liu, and S. Priya, “Stable efficiency exceeding 20.6% for inverted perovskite solar cells through polymer-optimized PCBM electron-transport layers,” *Nano Lett.* **19**, 3313 (2019).
- [30] Y. Song, X. Li, C. Mackin, X. Zhang, W. Fang, T. Palacios, H. Zhu, and J. Kong, “Role of interfacial oxide in high-efficiency graphene-silicon Schottky barrier solar cells,” *Nano Lett.* **15**, 2104 (2015).
- [31] P. Dong, C. L. Pint, M. Hainey, F. Mirri, Y. Zhan, J. Zhang, M. Pasquali, R. H. Hauge, R. Verduzco, M. Jiang, H. Lin, and J. Lou, “Vertically aligned single-walled

## Bibliography

---

- carbon nanotubes as low-cost and high electrocatalytic counter electrode for dye-sensitized solar cells,” *ACS Appl. Mater. Interfaces* **3**, 3157 (2011).
- [32] K. Cui, A. S. Anisimov, T. Chiba, S. Fujii, H. Kataura, A. G. Nasibulin, S. Chiashi, E. I. Kauppinen, and S. Maruyama, “Air-stable high-efficiency solar cells with dry-transferred single-walled carbon nanotube films,” *J. Mater. Chem. A* **2**, 11311 (2014).
- [33] I. Jeon, K. Cui, T. Chiba, A. Anisimov, A. G. Nasibulin, E. I. Kauppinen, S. Maruyama, and Y. Matsuo, “Direct and dry deposited single-walled carbon nanotube films doped with MoO<sub>x</sub> as electron-blocking transparent electrodes for flexible organic solar cells,” *J. Am. Chem. Soc.* **137**, 7982 (2015).
- [34] I. Jeon, S. Seo, Y. Sato, C. Delacou, A. Anisimov, K. Suenaga, E. I. Kauppinen, S. Maruyama, and Y. Matsuo, “Perovskite solar cells using carbon nanotubes both as cathode and as anode,” *J. Phys. Chem. C* **121**, 25743 (2017).
- [35] J. Wei, Y. Jia, Q. Shu, Z. Gu, K. Wang, D. Zhuang, G. Zhang, Z. Wang, J. Luo, A. Cao, and D. Wu, “Double-walled carbon nanotube solar cells,” *Nano Lett.* **7**, 2317 (2007).
- [36] Y. Jia, A. Cao, X. Bai, Z. Li, L. Zhang, N. Guo, J. Wei, K. Wang, H. Zhu, D. Wu, and P. M. Ajayan, “Achieving high efficiency silicon-carbon nanotube heterojunction solar cells by acid doping,” *Nano Lett.* **11**, 1901 (2011).
- [37] Y. Jung, X. Li, N. K. Rajan, A. D. Taylor, and M. A. Reed, “Record high efficiency single-walled carbon nanotube/silicon *p-n* junction solar cells,” *Nano Lett.* **13**, 95 (2013).
- [38] K. Cui, T. Chiba, S. Omiya, T. Thurakitseree, P. Zhao, S. Fujii, H. Kataura, E. Einarsson, S. Chiashi, and S. Maruyama, “Self-assembled microhoneycomb network of single-walled carbon nanotubes for solar cells,” *J. Phys. Chem. Lett.* **4**, 2571 (2013).
- [39] F. Wang, D. Kozawa, Y. Miyauchi, K. Hiraoka, S. Mouri, Y. Ohno, and K. Matsuda, “Considerably improved photovoltaic performance of carbon nanotube-based solar cells using metal oxide layers,” *Nat. Commun.* **6**, 6305 (2015).
- [40] I. Jeon, T. Chiba, C. Delacou, Y. Guo, A. Kaskela, O. Reynaud, E. I. Kauppinen, S. Maruyama, and Y. Matsuo, “Single-walled carbon nanotube film as electrode in indium-free planar heterojunction perovskite solar cells: investigation of electron-blocking layers and dopants,” *Nano Lett.* **15**, 6665 (2015).
- [41] D. D. Tune and B. S. Flavel, “Advances in carbon nanotube-silicon heterojunction solar cells,” *Adv. Energy Mater.* **8**, 1703241 (2018).
- [42] J. M. Zuo, M. Gao, J. Tao, B. Q. Li, R. Twesten, and I. Petrov, “Coherent nano-area electron diffraction,” *Microsc. Res. Tech.* **64**, 347 (2004).
- [43] P. T. Araujo, S. K. Doorn, S. Kilina, S. Tretiak, E. Einarsson, S. Maruyama, H.

## Bibliography

---

- Chacham, M. A. Pimenta, and A. Jorio, "Third and fourth optical transitions in semiconducting carbon nanotubes," *Phys. Rev. Lett.* **98**, 067401 (2007).
- [44] H. Kataura, Y. Kumazawa, Y. Maniwa, I. Umezū, S. Suzuki, Y. Ohtsuka, and Y. Achiba, "Optical properties of single-wall carbon nanotubes," *Synth. Met.* **103**, 2555 (1999).
- [45] W. Zhou, J. Vavro, N. M. Nemes, J. E. Fischer, F. Borondics, K. Kamarás, and D. B. Tanner, "Charge transfer and Fermi level shift in *p*-doped single-walled carbon nanotubes," *Phys. Rev. B* **71**, 205423 (2005).
- [46] M. Lazzeri, S. Piscanec, F. Mauri, A. C. Ferrari, and J. Robertson, "Phonon linewidths and electron-phonon coupling in graphite and nanotubes," *Phys. Rev. B* **73**, 155426 (2006).
- [47] A. Molina-Sánchez and L. Wirtz, "Phonons in single-layer and few-layer MoS<sub>2</sub> and WS<sub>2</sub>," *Phys. Rev. B* **84**, 155413 (2011).
- [48] C. Lee, H. Yan, L. E. Brus, T. F. Heinz, J. Hone, and S. Ryu, "Anomalous lattice vibrations of single- and few-layer MoS<sub>2</sub>," *ACS Nano* **4**, 2695 (2010).
- [49] H. Zhou, Y. Qu, T. Zeid, X. Duan, J. R. Bolton, D. Gust, T. A. Moore, A. L. Moore, S. C. Roy, et al., "Towards highly efficient photocatalysts using semiconductor nanoarchitectures," *Energy Environ. Sci.* **5**, 6732 (2012).
- [50] L. J. Van der Pauw, "A method of measuring specific resistivity and Hall effect of discs of arbitrary shape," *Philips Res. Reports* **13**, 1 (1958).
- [51] A. Kaskela, A. G. Nasibulin, M. Y. Timmermans, B. Aitchison, A. Papadimitratos, Y. Tian, Z. Zhu, H. Jiang, D. P. Brown, A. Zakhidov, and E. I. Kauppinen, "Aerosol-synthesized SWCNT networks with tunable conductivity and transparency by a dry transfer technique," *Nano Lett.* **10**, 4349 (2010).
- [52] A. G. Nasibulin, A. Kaskela, K. Mustonen, A. S. Anisimov, V. Ruiz, S. Kivistö, S. Rackauskas, M. Y. Timmermans, M. Pudas, B. Aitchison, M. Kauppinen, D. P. Brown, O. G. Okhotnikov, and E. I. Kauppinen, "Multifunctional free-standing single-walled carbon nanotube films," *ACS Nano* **5**, 3214 (2011).
- [53] M. D. McGehee, "Fast-track solar cells," *Nature* **501**, 323 (2013).
- [54] R. L. Crabb and F. C. Treble, "Thin silicon solar cells for large flexible arrays," *Nature* **213**, 1223 (1967).
- [55] B. Tian, X. Zheng, T. J. Kempa, Y. Fang, N. Yu, G. Yu, J. Huang, and C. M. Lieber, "Coaxial silicon nanowires as solar cells and nanoelectronic power sources," *Nature* **449**, 885 (2007).
- [56] M. Jošt, E. Köhnen, A. B. Morales-Vilches, B. Lipovšek, K. Jäger, B. Macco, A. Al-Ashouri, J. Krč, L. Korte, B. Rech, R. Schlatmann, M. Topič, B. Stannowski, and S.

## Bibliography

---

Albrecht, “Textured interfaces in monolithic perovskite/silicon tandem solar cells: advanced light management for improved efficiency and energy yield,” *Energy Environ. Sci.* **11**, 3511 (2018).

[57] M. H. Futscher and B. Ehrler, “Efficiency limit of perovskite/Si tandem solar cells,” *ACS Energy Lett.* **1**, 863 (2016).

[58] B. Chen, Y. Bai, Z. Yu, T. Li, X. Zheng, Q. Dong, L. Shen, M. Boccard, A. Gruverman, Z. Holman, and J. Huang, “Efficient semitransparent perovskite solar cells for 23.0%-efficiency perovskite/silicon four-terminal tandem cells,” *Adv. Energy Mater.* **6**, 1601128 (2016).

[59] D. M. Powell, R. Fu, K. Horowitz, P. A. Basore, M. Woodhouse, and T. Buonassisi, “The capital intensity of photovoltaics manufacturing: barrier to scale and opportunity for innovation,” *Energy Environ. Sci.* **8**, 3395 (2015).

[60] A. Tomasi, B. Paviet-Salomon, Q. Jeangros, J. Haschke, G. Christmann, L. Barraud, A. Descoeurdes, J. P. Seif, S. Nicolay, M. Despeisse, S. De Wolf, and C. Ballif, “Simple processing of back-contacted silicon heterojunction solar cells using selective-area crystalline growth,” *Nat. Energy* **2017 25 2**, 17062 (2017).

[61] I. Jeon, Y. Matsuo, and S. Maruyama, “Single-walled carbon nanotubes in solar cells,” *Top. Curr. Chem.* **376**, 4 (2018).

[62] X. Li, L. M. Guard, J. Jiang, K. Sakimoto, J.-S. Huang, J. Wu, J. Li, L. Yu, R. Pokhrel, G. W. Brudvig, S. Ismail-Beigi, N. Hazari, and A. D. Taylor, “Controlled doping of carbon nanotubes with metallocenes for application in hybrid carbon nanotube/Si solar cells,” *Nano Lett.* **14**, 3388 (2014).

[63] E. Shi, H. Li, L. Yang, L. Zhang, Z. Li, P. Li, Y. Shang, S. Wu, X. Li, J. Wei, K. Wang, H. Zhu, D. Wu, Y. Fang, and A. Cao, “Colloidal antireflection coating improves graphene-silicon solar cells,” *Nano Lett.* **13**, 1776 (2013).

[64] K. Cui, Y. Qian, I. Jeon, A. Anisimov, Y. Matsuo, E. I. Kauppinen, and S. Maruyama, “Scalable and solid-state redox functionalization of transparent single-walled carbon nanotube films for highly efficient and stable solar cells,” *Adv. Energy Mater.* **7**, 1700449 (2017).

[65] D. M. Powell, M. T. Winkler, H. J. Choi, C. B. Simmons, D. B. Needleman, and T. Buonassisi, “Crystalline silicon photovoltaics: a cost analysis framework for determining technology pathways to reach baseload electricity costs,” *Energy Environ. Sci.* **5**, 5874 (2012).

[66] W. Xu, S. Wu, X. Li, M. Zou, L. Yang, Z. Zhang, J. Wei, S. Hu, Y. Li, and A. Cao, “High-efficiency large-area carbon nanotube-silicon solar cells,” *Adv. Energy Mater.* (2016).

## Bibliography

---

- [67] K. Cui and S. Maruyama, "Multifunctional graphene and carbon nanotube films for planar heterojunction solar cells," *Prog. Energy Combust. Sci.* **70**, 1 (2019).
- [68] X. Li, Y. Jung, K. Sakimoto, T.-H. Goh, M. a. Reed, and A. D. Taylor, "Improved efficiency of smooth and aligned single walled carbon nanotube/silicon hybrid solar cells," *Energy Environ. Sci.* **6**, 879 (2013).
- [69] I. Jeon, R. Xiang, A. Shawky, Y. Matsuo, and S. Maruyama, "Single-walled carbon nanotubes in emerging solar cells: synthesis and electrode applications," *Adv. Energy Mater.* **9**, 1801312 (2018).
- [70] I. Jeon, J. Yoon, N. Ahn, M. Atwa, C. Delacou, A. Anisimov, E. I. Kauppinen, M. Choi, S. Maruyama, and Y. Matsuo, "Carbon nanotubes versus graphene as flexible transparent electrodes in inverted perovskite solar cells," *J. Phys. Chem. Lett.* **8**, 5395 (2017).
- [71] S. R. Wenham and M. A. Green, "Silicon solar cells," *Prog. Photovoltaics Res. Appl.* **4**, 3 (1996).
- [72] K. Yoshikawa, H. Kawasaki, W. Yoshida, T. Irie, K. Konishi, K. Nakano, T. Uto, D. Adachi, M. Kanematsu, H. Uzu, and K. Yamamoto, "Silicon heterojunction solar cell with interdigitated back contacts for a photoconversion efficiency over 26%," *Nat. Energy* **2**, 17032 (2017).
- [73] I. Jeon, C. Delacou, A. Kaskela, E. I. Kauppinen, S. Maruyama, and Y. Matsuo, "Metal-electrode-free window-like organic solar cells with *p*-doped carbon nanotube thin-film electrodes," *Sci. Rep.* **6**, 31348 (2016).
- [74] J. Zheng, H. Mehrvarz, F.-J. Ma, C. F. J. Lau, M. A. Green, S. Huang, and A. W. Y. Ho-Baillie, "21.8% efficient monolithic perovskite/homo-junction-silicon tandem solar cell on 16 cm<sup>2</sup>," *ACS Energy Lett.* **3**, 2299 (2018).
- [75] T. Leijtens, K. A. Bush, R. Prasanna, and M. D. McGehee, "Opportunities and challenges for tandem solar cells using metal halide perovskite semiconductors," *Nat. Energy* **3**, 828 (2018).
- [76] E. Shi, L. Zhang, Z. Li, P. Li, Y. Shang, Y. Jia, J. Wei, K. Wang, H. Zhu, D. Wu, S. Zhang, and A. Cao, "TiO<sub>2</sub>-coated carbon nanotube-silicon solar cells with efficiency of 15%," *Sci. Rep.* **2**, 884 (2012).
- [77] R. Li, J. Di, Z. Yong, B. Sun, and Q. Li, "Polymethylmethacrylate coating on aligned carbon nanotube-silicon solar cells for performance improvement," *J. Mater. Chem. A* **2**, 4140 (2014).
- [78] T. Sakaguchi, I. Jeon, T. Chiba, A. Shawky, R. Xiang, S. Chiashi, E. I. Kauppinen, N.-G. Park, Y. Matsuo, and S. Maruyama, "Non-doped and unsorted single-walled carbon nanotubes as carrier-selective, transparent, and conductive electrode for perovskite solar

## Bibliography

---

- cells,” *MRS Commun.* **8**, 1058 (2018).
- [79] S.-J. Kwon, T.-H. Han, T. Y. Ko, N. Li, Y. Kim, D. J. Kim, S.-H. Bae, Y. Yang, B. H. Hong, K. S. Kim, S. Ryu, and T.-W. Lee, “Extremely stable graphene electrodes doped with macromolecular acid,” *Nat. Commun.* **9**, 2037 (2018).
- [80] I. Jeon, C. Delacou, H. Okada, G. E. Morse, T.-H. Han, Y. Sato, A. Anisimov, K. Suenaga, E. I. Kauppinen, S. Maruyama, and Y. Matsuo, “Polymeric acid-doped transparent carbon nanotube electrodes for organic solar cells with the longest doping durability,” *J. Mater. Chem. A* **6**, 14553 (2018).
- [81] Y. Ohama, T. Kobayashi, K. Takeuchi, and K. Nawata, “Chemical resistance of polymethyl methacrylate concrete,” *Int. J. Cem. Compos. Light. Concr.* **8**, 87 (1986).
- [82] “Perma Pure LLC, The basic physical and chemical properties of Nafion,” <<https://www.permapure.com/products/nafion-tubing/nafion-physical-and-chemical-properties/>>.
- [83] Z. Zhang, C. Tian, Z. Yuan, J. Li, W.-P. Wu, and R. Xia, “Temperature and loading sensitivity investigation of nanoindentation short-term creep behavior in Nafion<sup>®</sup>,” *Mater. Res. Express* **6**, 055304 (2019).
- [84] J. H. Lee, K. J. Kim, M. K. Park, H. J. Kim, I. Jeon, S.-H. Choi, J. H. Kim, H. C. Choi, and H. H. Shin, “A new optical film with antismudge function and high durability,” *Jpn. J. Appl. Phys.* **48**, 122401 (2009).
- [85] X.-G. Hu, P.-X. Hou, C. Liu, F. Zhang, G. Liu, and H.-M. Cheng, “Small-bundle single-wall carbon nanotubes for high-efficiency silicon heterojunction solar cells,” *Nano Energy* **50**, 521 (2018).
- [86] S. Wu, L. Yang, H. Wu, Y. Yuan, Z. Ji, and A. Cao, “Performance improvement of assembled multi-walled carbon nanotube network/Si solar cells decorated with metal nanoparticles,” *ChemistrySelect* **3**, 9736 (2018).
- [87] S. Ponzoni, S. Achilli, C. Pintossi, G. Drera, L. Sangaletti, P. Castrucci, M. De Crescenzi, and S. Pagliara, “Hybridized C-O-Si interface states at the origin of efficiency improvement in CNT/Si solar cells,” *ACS Appl. Mater. Interfaces* **9**, 16627 (2017).
- [88] Q. Fan, Q. Zhang, W. Zhou, X. Xia, F. Yang, N. Zhang, S. Xiao, K. Li, X. Gu, Z. Xiao, H. Chen, Y. Wang, H. Liu, W. Zhou, and S. Xie, “Novel approach to enhance efficiency of hybrid silicon-based solar cells via synergistic effects of polymer and carbon nanotube composite film,” *Nano Energy* **33**, 436 (2017).
- [89] M. Bat-Erdene, M. Batmunkh, S. A. Tawfik, M. Fronzi, M. J. Ford, C. J. Shearer, L. Yu, M. Dadkhah, J. R. Gascooke, C. T. Gibson, and J. G. Shapter, “Efficiency enhancement of single-walled carbon nanotube-silicon heterojunction solar cells using microwave-exfoliated few-layer black phosphorus,” *Adv. Funct. Mater.* **1704488**,

## Bibliography

---

1704488 (2017).

[90] X. Li, M. Mariano, L. McMillon-Brown, J.-S. Huang, M. Y. Sfeir, M. A. Reed, Y. Jung, and A. D. Taylor, "Charge transfer from carbon nanotubes to silicon in flexible carbon nanotube/silicon solar cells," *Small* **1702387**, 1702387 (2017).

[91] F. De Nicola, M. Salvato, C. Cirillo, M. Crivellari, M. Boscardin, M. Scarselli, F. Nanni, I. Cacciotti, M. De Crescenzi, and P. Castrucci, "Record efficiency of air-stable multi-walled carbon nanotube/silicon solar cells," *Carbon N. Y.* (2016).

[92] L. Chen, H. Yu, J. Zhong, H. He, and T. Zhang, "Harnessing light energy with a planar transparent hybrid of graphene/single wall carbon nanotube/*n*-type silicon heterojunction solar cell," *Electrochim. Acta* **178**, 732 (2015).

[93] L. Yu, D. D. Tune, C. J. Shearer, and J. G. Shapter, "Application of polymer interlayers in silicon-carbon nanotube heterojunction solar cells," *ChemNanoMat* **1**, 115 (2015).

[94] L. Yu, D. D. Tune, C. J. Shearer, and J. G. Shapter, "Implementation of antireflection layers for improved efficiency of carbon nanotube-silicon heterojunction solar cells," *Sol. Energy* **118**, 592 (2015).

[95] M. Polyanskiy, "Refractive index of PMMA,"  
<[https://refractiveindex.info/?shelf=organic&book=poly\(methyl\\_methacrylate\)&page=Sultanova](https://refractiveindex.info/?shelf=organic&book=poly(methyl_methacrylate)&page=Sultanova)>.

[96] N. F. Bunkin, V. S. Gorelik, V. A. Kozlov, A. V. Shkirin, and N. V. Suyazov, "Colloidal crystal formation at the 'Nafion-water' interface," *J. Phys. Chem. B* **118**, 3372 (2014).

[97] S. S. Li, "Semiconductor physical electronics" (2012).

[98] L. Yu, C. Shearer, and J. Shapter, "Recent development of carbon nanotube transparent conductive films," *Chem. Rev.* **116**, 13413 (2016).

[99] R. Graupner, J. Abraham, A. Vencelová, T. Seyller, F. Hennrich, M. M. Kappes, A. Hirsch, and L. Ley, "Doping of single-walled carbon nanotube bundles by Brønsted acids," *Phys. Chem. Chem. Phys.* **5**, 5472 (2003).

[100] R. Liu, S.-T. Lee, and B. Sun, "13.8% efficiency hybrid Si/organic heterojunction solar cells with MoO<sub>3</sub> film as antireflection and inversion induced layer," *Adv. Mater.* **26**, 6007 (2014).

[101] Y. Zhang, W. Cui, Y. Zhu, F. Zu, L. Liao, S.-T. Lee, and B. Sun, "High efficiency hybrid PEDOT:PSS/nanostructured silicon Schottky junction solar cells by doping-free rear contact," *Energy Environ. Sci.* **8**, 297 (2015).

[102] A. Cuevas and R. A. Sinton, "Prediction of the open-circuit voltage of solar cells from the steady-state photoconductance," *Prog. Photovoltaics Res. Appl.* **5**, 79 (1997).

## Bibliography

---

- [103] K. S. Novoselov, D. Jiang, F. Schedin, T. J. Booth, V. V Khotkevich, S. V Morozov, and A. K. Geim, "Two-dimensional atomic crystals," *Proc. Natl. Acad. Sci. U. S. A.* **102**, 10451 (2005).
- [104] H. Li, J. Wu, Z. Yin, and H. Zhang, "Preparation and applications of mechanically exfoliated single-layer and multilayer MoS<sub>2</sub> and WSe<sub>2</sub> nanosheets," *Acc. Chem. Res.* **47**, 1067 (2014).
- [105] G.-H. Lee, Y.-J. Yu, X. Cui, N. Petrone, C.-H. Lee, M. S. Choi, D.-Y. Lee, C. Lee, W. J. Yoo, K. Watanabe, T. Taniguchi, C. Nuckolls, P. Kim, and J. Hone, "Flexible and transparent MoS<sub>2</sub> field-effect transistors on hexagonal boron nitride-graphene heterostructures," *ACS Nano* **7**, 7931 (2013).
- [106] J. N. Coleman, U. Khan, K. Young, A. Gaucher, S. De, R. J. Smith, I. V Shvets, S. K. Arora, G. Stanton, et al., "Two-dimensional nanosheets produced by liquid exfoliation of layered materials.," *Science* **331**, 568 (2011).
- [107] G. Cunningham, M. Lotya, C. S. Cucinotta, S. Sanvito, S. D. Bergin, R. Menzel, M. S. P. Shaffer, and J. N. Coleman, "Solvent exfoliation of transition metal dichalcogenides: dispersibility of exfoliated nanosheets varies only weakly between compounds," *ACS Nano* **6**, 3468 (2012).
- [108] G. Eda, H. Yamaguchi, D. Voiry, T. Fujita, M. Chen, and M. Chhowalla, "Photoluminescence from chemically exfoliated MoS<sub>2</sub>," *Nano Lett.* **11**, 5111 (2011).
- [109] Z. Zeng, Z. Yin, X. Huang, H. Li, Q. He, G. Lu, F. Boey, and H. Zhang, "Single-layer semiconducting nanosheets: high-yield preparation and device fabrication," *Angew. Chemie Int. Ed.* **50**, 11093 (2011).
- [110] J. Zheng, H. Zhang, S. Dong, Y. Liu, C. Tai Nai, H. Suk Shin, H. Young Jeong, B. Liu, and K. Ping Loh, "High yield exfoliation of two-dimensional chalcogenides using sodium naphthalenide," *Nat. Commun.* **5**, 2995 (2014).
- [111] Y.-C. Lin, W. Zhang, J.-K. Huang, K.-K. Liu, Y.-H. Lee, C.-T. Liang, C.-W. Chu, and L.-J. Li, "Wafer-scale MoS<sub>2</sub> thin layers prepared by MoO<sub>3</sub> sulfurization," *Nanoscale* **4**, 6637 (2012).
- [112] Y. Zhan, Z. Liu, S. Najmaei, P. M. Ajayan, and J. Lou, "Large-Area vapor-phase growth and characterization of MoS<sub>2</sub> atomic layers on a SiO<sub>2</sub> substrate," *Small* **8**, 966 (2012).
- [113] Y. Jung, J. Shen, Y. Liu, J. M. Woods, Y. Sun, and J. J. Cha, "Metal seed layer thickness-induced transition from vertical to horizontal growth of MoS<sub>2</sub> and WS<sub>2</sub>," *Nano Lett.* **14**, 6842 (2014).
- [114] K.-K. Liu, W. Zhang, Y.-H. Lee, Y.-C. Lin, M.-T. Chang, C.-Y. Su, C.-S. Chang, H. Li, Y. Shi, H. Zhang, C.-S. Lai, and L.-J. Li, "Growth of large-area and highly

## Bibliography

---

- crystalline MoS<sub>2</sub> thin layers on insulating substrates,” *Nano Lett.* **12**, 1538 (2012).
- [115] Y. Shi, W. Zhou, A.-Y. Lu, W. Fang, Y.-H. Lee, A. L. Hsu, S. M. Kim, K. K. Kim, H. Y. Yang, L.-J. Li, J.-C. Idrobo, and J. Kong, “van der Waals epitaxy of MoS<sub>2</sub> layers using graphene as growth templates,” *Nano Lett.* **12**, 2784 (2012).
- [116] Y. Li, H. Wang, L. Xie, Y. Liang, G. Hong, and H. Dai, “MoS<sub>2</sub> nanoparticles grown on graphene: an advanced catalyst for the hydrogen evolution reaction,” *J. Am. Chem. Soc.* **133**, 7296 (2011).
- [117] J. Xie, H. Zhang, S. Li, R. Wang, X. Sun, M. Zhou, J. Zhou, X. W. D. Lou, and Y. Xie, “Defect-rich MoS<sub>2</sub> ultrathin nanosheets with additional active edge sites for enhanced electrocatalytic hydrogen evolution,” *Adv. Mater.* **25**, 5807 (2013).
- [118] H. Hwang, H. Kim, and J. Cho, “MoS<sub>2</sub> nanoplates consisting of disordered graphene-like layers for high rate lithium battery anode materials,” *Nano Lett.* **11**, 4826 (2011).
- [119] T. Spalvins, “Morphological and frictional behavior of sputtered MoS<sub>2</sub> films,” *Thin Solid Films* **96**, 17 (1982).
- [120] S. Wu, C. Huang, G. Aivazian, J. S. Ross, D. H. Cobden, and X. Xu, “Vapor-solid growth of high optical quality MoS<sub>2</sub> monolayers with near-unity valley polarization,” *ACS Nano* **7**, 2768 (2013).
- [121] Q. Feng, Y. Zhu, J. Hong, M. Zhang, W. Duan, N. Mao, J. Wu, H. Xu, F. Dong, F. Lin, C. Jin, C. Wang, J. Zhang, and L. Xie, “Growth of large-area 2D MoS<sub>2</sub>(1-x)Se<sub>2x</sub> semiconductor alloys,” *Adv. Mater.* **26**, 2648 (2014).
- [122] Y.-H. Lee, X.-Q. Zhang, W. Zhang, M.-T. Chang, C.-T. Lin, K.-D. Chang, Y.-C. Yu, J. T.-W. Wang, C.-S. Chang, L.-J. Li, and T.-W. Lin, “Synthesis of large-area MoS<sub>2</sub> atomic layers with chemical vapor deposition,” *Adv. Mater.* **24**, 2320 (2012).
- [123] A. M. van der Zande, P. Y. Huang, D. A. Chenet, T. C. Berkelbach, Y. You, G.-H. Lee, T. F. Heinz, D. R. Reichman, D. A. Muller, and J. C. Hone, “Grains and grain boundaries in highly crystalline monolayer molybdenum disulphide,” *Nat. Mater.* **12**, 554 (2013).
- [124] S. Najmaei, Z. Liu, W. Zhou, X. Zou, G. Shi, S. Lei, B. I. Yakobson, J.-C. Idrobo, P. M. Ajayan, and J. Lou, “Vapour phase growth and grain boundary structure of molybdenum disulphide atomic layers,” *Nat. Mater.* **12**, 754 (2013).
- [125] Q. Ji, Y. Zhang, T. Gao, Y. Zhang, D. Ma, M. Liu, Y. Chen, X. Qiao, P.-H. Tan, M. Kan, J. Feng, Q. Sun, and Z. Liu, “Epitaxial monolayer MoS<sub>2</sub> on mica with novel photoluminescence,” *Nano Lett.* **13**, 3870 (2013).
- [126] X. Ling, Y.-H. Lee, Y. Lin, W. Fang, L. Yu, M. S. Dresselhaus, and J. Kong, “Role of the seeding promoter in MoS<sub>2</sub> growth by chemical vapor deposition,” *Nano Lett.*

## Bibliography

---

14, 464 (2014).

- [127] X. Yin, Z. Ye, D. A. Chenet, Y. Ye, K. O'Brien, J. C. Hone, and X. Zhang, "Edge nonlinear optics on a MoS<sub>2</sub> atomic monolayer," *Science* **344**, 488 (2014).
- [128] J. Zhang, H. Yu, W. Chen, X. Tian, D. Liu, M. Cheng, G. Xie, W. Yang, R. Yang, X. Bai, D. Shi, and G. Zhang, "Scalable growth of high-quality polycrystalline MoS<sub>2</sub> monolayers on SiO<sub>2</sub> with tunable grain sizes," *ACS Nano* **8**, 6024 (2014).
- [129] W. Chen, J. Zhao, J. Zhang, L. Gu, Z. Yang, X. Li, H. Yu, X. Zhu, R. Yang, D. Shi, X. Lin, J. Guo, X. Bai, and G. Zhang, "Oxygen-assisted chemical vapor deposition growth of large single-crystal and high-quality monolayer MoS<sub>2</sub>," *J. Am. Chem. Soc.* **137**, 15632 (2015).
- [130] K. Kang, S. Xie, L. Huang, Y. Han, P. Y. Huang, K. F. Mak, C.-J. Kim, D. Muller, and J. Park, "High-mobility three-atom-thick semiconducting films with wafer-scale homogeneity," *Nature* **520**, 656 (2015).
- [131] S. Wang, Y. Rong, Y. Fan, M. Pacios, H. Bhaskaran, K. He, and J. H. Warner, "Shape evolution of monolayer MoS<sub>2</sub> crystals grown by chemical vapor deposition," *Chem. Mater.* **26**, 6371 (2014).
- [132] S. Wang, M. Pacios, H. Bhaskaran, and J. H. Warner, "Substrate control for large area continuous films of monolayer MoS<sub>2</sub> by atmospheric pressure chemical vapor deposition," *Nanotechnology* **27**, 085604 (2016).
- [133] P. K. Chow, E. Singh, B. C. Viana, J. Gao, J. Luo, J. Li, Z. Lin, A. L. Elías, Y. Shi, Z. Wang, M. Terrones, and N. Koratkar, "Wetting of mono and few-layered WS<sub>2</sub> and MoS<sub>2</sub> films supported on Si/SiO<sub>2</sub> substrates," *ACS Nano* **9**, 3023 (2015).
- [134] L. Margulis, G. Salitra, R. Tenne, and M. Talianker, "Nested fullerene-like structures," *Nature* **365**, 113 (1993).
- [135] Y. Feldman, E. Wasserman, D. J. Srolovitz, and R. Tenne, "High-rate, gas-phase growth of MoS<sub>2</sub> nested inorganic fullerenes and nanotubes," *Science* **267**, 222 (1995).
- [136] M. Nath, A. Govindaraj, and C. N. R. Rao, "Simple synthesis of MoS<sub>2</sub> and WS<sub>2</sub> nanotubes," *Adv. Mater.* **13**, 283 (2001).
- [137] M. Remskar, A. Mrzel, Z. Skraba, A. Jesih, M. Ceh, J. Demsar, P. Stadelmann, F. Levy, and D. Mihailovic, "Self-assembly of subnanometer-diameter single-wall MoS<sub>2</sub> nanotubes," *Science* **292**, 479 (2001).
- [138] R. Tenne, L. Margulis, M. Genut, and G. Hodes, "Polyhedral and cylindrical structures of tungsten disulphide," *Nature* **360**, 444 (1992).
- [139] K. S. Novoselov, A. Mishchenko, A. Carvalho, and A. H. Castro Neto, "2D materials and van der Waals heterostructures," *Science* **353** (2016).
- [140] Y. Liu, N. O. Weiss, X. Duan, H.-C. Cheng, Y. Huang, and X. Duan, "van der

## Bibliography

---

- Waals heterostructures and devices,” *Nat. Rev. Mater.* **1**, 16042 (2016).
- [141] G. Seifert, H. Terrones, M. Terrones, G. Jungnickel, and T. Frauenheim, “Structure and electronic properties of MoS<sub>2</sub> nanotubes,” *Phys. Rev. Lett.* **85**, 146 (2000).
- [142] M. Ghorbani-Asl, N. Zibouche, M. Wahiduzzaman, A. F. Oliveira, A. Kuc, and T. Heine, “Electromechanics in MoS<sub>2</sub> and WS<sub>2</sub>: nanotubes vs. monolayers,” *Sci. Rep.* **3**, 2961 (2013).
- [143] D.-B. Zhang, T. Dumitrică, and G. Seifert, “Helical nanotube structures of MoS<sub>2</sub> with intrinsic twisting: an objective molecular dynamics study,” *Phys. Rev. Lett.* **104**, 065502 (2010).
- [144] E. Hernández, C. Goze, P. Bernier, and A. Rubio, “Elastic properties of C and B<sub>x</sub>C<sub>y</sub>N<sub>y</sub> composite nanotubes,” *Phys. Rev. Lett.* **80**, 4502 (1998).
- [145] W. K. Hsu, Y. Q. Zhu, H. W. Kroto, D. R. M. Walton, R. Kamalakaran, and M. Terrones, “C-MoS<sub>2</sub> and C-WS<sub>2</sub> nanocomposites,” *Appl. Phys. Lett.* **77**, 4130 (2000).
- [146] Y. Wang, Z. Ma, Y. Chen, M. Zou, M. Yousaf, Y. Yang, L. Yang, A. Cao, and R. P. S. Han, “Controlled synthesis of core-shell carbon@MoS<sub>2</sub> nanotube sponges as high-performance battery electrodes,” *Adv. Mater.* **28**, 10175 (2016).
- [147] L. Britnell, R. M. Ribeiro, A. Eckmann, R. Jalil, B. D. Belle, A. Mishchenko, Y. J. Kim, R. V. Gorbachev, T. Georgiou, S. V. Morozov, A. N. Grigorenko, A. K. Geim, C. Casiraghi, A. H. C. Neto, and K. S. Novoselov, “Strong light-matter interactions in heterostructures of atomically thin films,” *Science* **340**, 1311 (2013).
- [148] G. Eda and S. A. Maier, “Two-dimensional crystals: managing light for optoelectronics,” *ACS Nano* **7**, 5660 (2013).
- [149] A. Carvalho, R. M. Ribeiro, and A. H. Castro Neto, “Band nesting and the optical response of two-dimensional semiconducting transition metal dichalcogenides,” *Phys. Rev. B* **88**, 115205 (2013).
- [150] M. Bernardi, M. Palummo, and J. C. Grossman, “Extraordinary sunlight absorption and one nanometer thick photovoltaics using two-dimensional monolayer materials,” *Nano Lett.* **13**, 3664 (2013).
- [151] D. Jariwala, A. R. Davoyan, G. Tagliabue, M. C. Sherrott, J. Wong, and H. A. Atwater, “Near-unity absorption in van der Waals semiconductors for ultrathin optoelectronics,” *Nano Lett.* **16**, 5482 (2016).
- [152] M.-L. Tsai, S.-H. Su, J.-K. Chang, D.-S. Tsai, C.-H. Chen, C.-I. Wu, L.-J. Li, L.-J. Chen, and J.-H. He, “Monolayer MoS<sub>2</sub> heterojunction solar cells,” *ACS Nano* **8**, 8317 (2014).
- [153] Y. Tsuboi, F. Wang, D. Kozawa, K. Funahashi, S. Mouri, Y. Miyauchi, T. Takenobu, K. Matsuda, A. K. Geim, et al., “Enhanced photovoltaic performances of

## Bibliography

---

- graphene/Si solar cells by insertion of a MoS<sub>2</sub> thin film,” *Nanoscale* **7**, 14476 (2015).
- [154] M. Shanmugam, C. A. Durcan, B. Yu, Z. B. Zhou, R. Q. Cui, Q. J. Pang, G. M. Hadi, Z. M. Ding, W. Y. Li, et al., “Layered semiconductor molybdenum disulfide nanomembrane based Schottky-barrier solar cells,” *Nanoscale* **4**, 7399 (2012).
- [155] X. Gu, W. Cui, H. Li, Z. Wu, Z. Zeng, S.-T. Lee, H. Zhang, and B. Sun, “A solution-processed hole extraction layer made from ultrathin MoS<sub>2</sub> nanosheets for efficient organic solar cells,” *Adv. Energy Mater.* **3**, 1262 (2013).
- [156] J.-M. Yun, Y.-J. Noh, J.-S. Yeo, Y.-J. Go, S.-I. Na, H.-G. Jeong, J. Kim, S. Lee, S.-S. Kim, H. Y. Koo, T.-W. Kim, and D.-Y. Kim, “Efficient work-function engineering of solution-processed MoS<sub>2</sub> thin-films for novel hole and electron transport layers leading to high-performance polymer solar cells,” *J. Mater. Chem. C* **1**, 3777 (2013).
- [157] Y. Wang, S. Wang, X. Chen, Z. Li, J. Wang, T. Li, and X. Deng, “Largely enhanced  $V_{OC}$  and stability in perovskite solar cells with modified energy match by coupled 2D interlayers,” *J. Mater. Chem. A* **6**, 4860 (2018).
- [158] G. Yin, H. Zhao, J. Feng, J. Sun, J. Yan, Z. Liu, S. Lin, and S. (Frank) Liu, “Low-temperature and facile solution-processed two-dimensional TiS<sub>2</sub> as an effective electron transport layer for UV-stable planar perovskite solar cells,” *J. Mater. Chem. A* **6**, 9132 (2018).
- [159] G. Kakavelakis, I. Paradisanos, B. Paci, A. Generosi, M. Papachatzakis, T. Maksudov, L. Najafi, A. E. Del Rio Castillo, G. Kioseoglou, E. Stratakis, F. Bonaccorso, and E. Kymakis, “Extending the continuous operating lifetime of perovskite solar cells with a molybdenum disulfide hole extraction interlayer,” *Adv. Energy Mater.* **8**, 1 (2018).
- [160] S. Seo, I. Jeon, R. Xiang, C. Lee, H. Zhang, T. Tanaka, J. W. Lee, D. Suh, T. Ogamoto, R. Nishikubo, A. Saeki, S. Chiashi, J. Shiomi, H. Kataura, H. M. Lee, Y. Yang, Y. Matsuo, and S. Maruyama, “Semiconducting carbon nanotubes as crystal growth templates and grain bridges in perovskite solar cells,” *J. Mater. Chem. A* **7**, 12987 (2019).
- [161] P. You, G. Tang, and F. Yan, “Two-dimensional materials in perovskite solar cells,” *Mater. Today Energy* **11**, 128 (2019).
- [162] Q. Van Le, T. P. Nguyen, K. S. Choi, Y.-H. Cho, Y. J. Hong, and S. Y. Kim, “Dual use of tantalum disulfides as hole and electron extraction layers in organic photovoltaic cells,” *Phys. Chem. Chem. Phys.* **16**, 25468 (2014).
- [163] Q. Van Le, T. P. Nguyen, and S. Y. Kim, “UV/ozone-treated WS<sub>2</sub> hole-extraction layer in organic photovoltaic cells,” *Phys. status solidi - Rapid Res. Lett.* **8**, 390 (2014).
- [164] A. Capasso, F. Matteocci, L. Najafi, M. Prato, J. Buha, L. Cinà, V. Pellegrini, A. Di Carlo, and F. Bonaccorso, “Few-layer MoS<sub>2</sub> flakes as active buffer layer for stable perovskite solar cells,” *Adv. Energy Mater.* **6**, 1600920 (2016).

## Bibliography

---

- [165] Y. G. Kim, K. C. Kwon, Q. Van Le, K. Hong, H. W. Jang, and S. Y. Kim, "Atomically thin two-dimensional materials as hole extraction layers in organolead halide perovskite photovoltaic cells," *J. Power Sources* **319**, 1 (2016).
- [166] P. Huang, Z. Wang, Y. Liu, K. Zhang, L. Yuan, Y. Zhou, B. Song, and Y. Li, "Water-soluble 2D transition metal dichalcogenides as the hole-transport layer for highly efficient and stable *p-i-n* perovskite solar cells," *ACS Appl. Mater. Interfaces* **9**, 25323 (2017).
- [167] R. Dai, Y. Wang, J. Wang, and X. Deng, "Metal-organic-compound-Modified MoS<sub>2</sub> with enhanced solubility for high-performance perovskite solar cells," *ChemSusChem* **10**, 2869 (2017).
- [168] U. Dasgupta, S. Chatterjee, and A. J. Pal, "Thin-film formation of 2D MoS<sub>2</sub> and its application as a hole-transport layer in planar perovskite solar cells," *Sol. Energy Mater. Sol. Cells* **172**, 353 (2017).
- [169] P. Huang, L. Yuan, K. Zhang, Q. Chen, Y. Zhou, B. Song, and Y. Li, "Room-temperature and aqueous solution-processed two-dimensional TiS<sub>2</sub> as an electron transport layer for highly efficient and stable planar *n-i-p* perovskite solar cells," *ACS Appl. Mater. Interfaces* **10**, 14796 (2018).
- [170] C.-H. Lee, G.-H. Lee, A. M. van der Zande, W. Chen, Y. Li, M. Han, X. Cui, G. Arefe, C. Nuckolls, T. F. Heinz, J. Guo, J. Hone, and P. Kim, "Atomically thin *p-n* junctions with van der Waals heterointerfaces," *Nat. Nanotechnol.* **9**, 676 (2014).
- [171] X. Zhang, J. Grajal, J. L. Vazquez-Roy, U. Radhakrishna, X. Wang, W. Chern, L. Zhou, Y. Lin, P.-C. Shen, X. Ji, X. Ling, A. Zubair, Y. Zhang, H. Wang, M. Dubey, J. Kong, M. Dresselhaus, and T. Palacios, "Two-dimensional MoS<sub>2</sub>-enabled flexible rectenna for Wi-Fi-band wireless energy harvesting," *Nature* **566**, 368 (2019).
- [172] Y. J. Zhang, T. Ideue, M. Onga, F. Qin, R. Suzuki, A. Zak, R. Tenne, J. H. Smet, and Y. Iwasa, "Enhanced intrinsic photovoltaic effect in tungsten disulfide nanotubes," *Nature* **570**, 349 (2019).
- [173] K. Wojciechowski, T. Leijtens, S. Siprova, C. Schlueter, M. T. Hörantner, J. T.-W. Wang, C.-Z. Li, A. K.-Y. Jen, T.-L. Lee, and H. J. Snaith, "C<sub>60</sub> as an efficient *n*-type compact layer in perovskite solar cells," *J. Phys. Chem. Lett.* **6**, 2399 (2015).
- [174] P. Lu, X. Wu, W. Guo, and X. C. Zeng, "Strain-dependent electronic and magnetic properties of MoS<sub>2</sub> monolayer, bilayer, nanoribbons and nanotubes," *Phys. Chem. Chem. Phys.* **14**, 13035 (2012).
- [175] J.-H. Meng, X. Liu, X.-W. Zhang, Y. Zhang, H.-L. Wang, Z.-G. Yin, Y.-Z. Zhang, H. Liu, J.-B. You, and H. Yan, "Interface engineering for highly efficient graphene-on-silicon Schottky junction solar cells by introducing a hexagonal boron nitride interlayer,"

## Bibliography

---

*Nano Energy* **28**, 44 (2016).

[176] A. M. Rao, P. C. Eklund, S. Bandow, A. Thess, and R. E. Smalley, "Evidence for charge transfer in doped carbon nanotube bundles from Raman scattering," *Nature* **388**, 257 (1997).

[177] R. Beams, L. Gustavo Cançado, and L. Novotny, "Raman characterization of defects and dopants in graphene," *J. Phys. Condens. Matter* **27**, 083002 (2015).

[178] "OXFORD PV," <<https://www.oxfordpv.com/>>.

[179] Y. Jia, A. Cao, F. Kang, P. Li, X. Gui, L. Zhang, E. Shi, J. Wei, K. Wang, H. Zhu, and D. Wu, "Strong and reversible modulation of carbon nanotube-silicon heterojunction solar cells by an interfacial oxide layer," *Phys. Chem. Chem. Phys.* **14**, 8391 (2012).

[180] Z. H. Lu, J. P. McCaffrey, B. Brar, G. D. Wilk, R. M. Wallace, L. C. Feldman, and S. P. Tay, "SiO<sub>2</sub> film thickness metrology by x-ray photoelectron spectroscopy," *Appl. Phys. Lett.* **71**, 2764 (1997).

## Appendix

### Surface Analysis of *n*-Si in SWCNT-Si Solar Cells

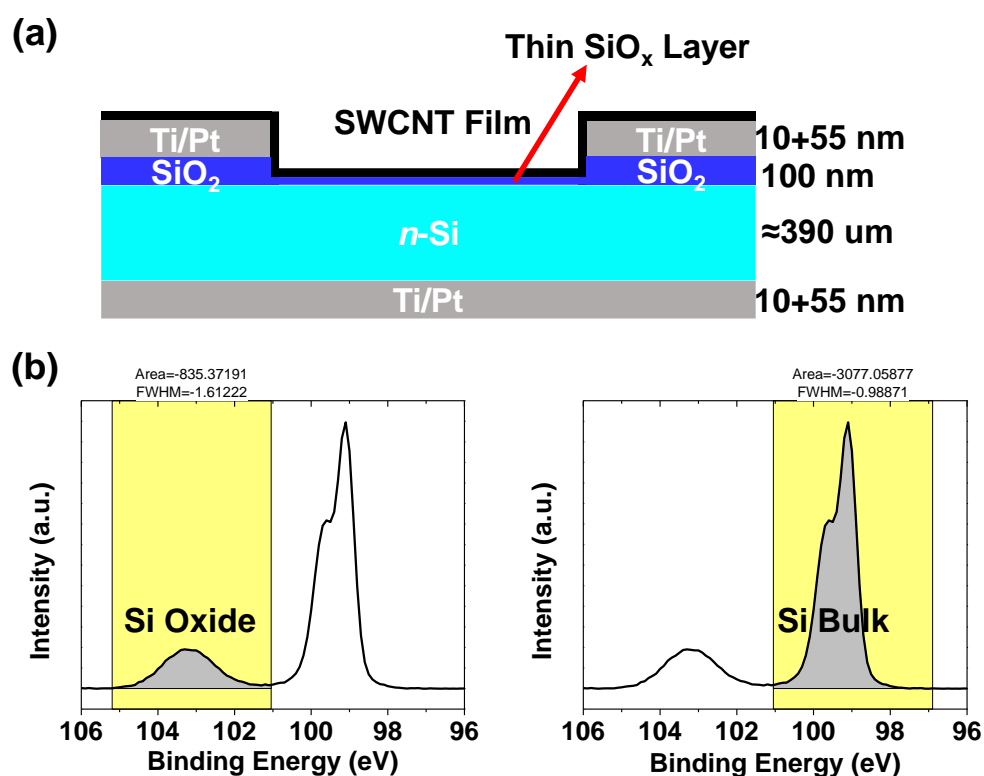


Figure A.1 (a) Schematic of the thin interfacial oxide layer between SWCNT film and *n*-Si. (b) Illustration of the characterization process for Si oxide thickness from XPS spectra.

It has been discussed in SWCNT-Si and graphene-Si solar cells that the interfacial oxide layer (SiO<sub>x</sub>) between SWCNT/graphene and Si (Figure A.1a) has an influence on the solar cell performance [30,32,179]. In this study, the SiO<sub>x</sub> thickness was characterized

## Appendix

---

through XPS. Figure A.1b shows the Si 2*p* spectra that contain separated peaks of Si oxide and Si bulk. The thickness of the oxide layer  $d_{\text{oxide}}$  can be calculated as

$$d_{\text{oxide}} = \lambda_{\text{oxide}} \sin \theta \ln \left( \frac{I_{\text{oxide}}}{\beta I_{\text{Si}}} + 1 \right) \quad (\text{A.1})$$

where  $\lambda_{\text{oxide}}$  is the photoelectron effective attenuation length in SiO<sub>2</sub>,  $\theta$  is the photoelectron take-off angle,  $\beta$  is the Si 2*p* intensity ratio of infinitely-thick SiO<sub>2</sub> and Si ( $I_{\text{oxide}}^{\infty} / I_{\text{Si}}^{\infty}$ ), and  $I_{\text{oxide}} / I_{\text{Si}}$  is the intensity ratio of the measured SiO<sub>2</sub> layer and the Si substrate.  $\theta$  is  $\pi/4$ ,  $\lambda_{\text{oxide}}$  is 2.96 nm, and  $\beta$  is 0.75 [180].  $I_{\text{oxide}}$  and  $I_{\text{Si}}$  can be determined by integrating the peak area after a Shirley background subtraction, as shown in Figure A.1b. The calculated thickness of the oxide layer in Figure A.1b is 6.5 Å.

One understanding obtained from the measurement of interfacial oxide layer should be introduced. After 3-s RCA2 cleaning, one substrate before sputtering and another substrate after sputtering were measured. The SiO<sub>x</sub> thickness before sputtering was 3.9 Å, whereas the thickness after sputtering was 6.5 Å. As a result, the physical mask of Scotch tape actually cannot fully protect the Si from SiO<sub>2</sub> leakage in the sputtering process. After the sputtering deposition process, a 2.6-Å sputtered SiO<sub>2</sub> layer was formed onto the 3.9-Å RCA2-introduced oxide layer.

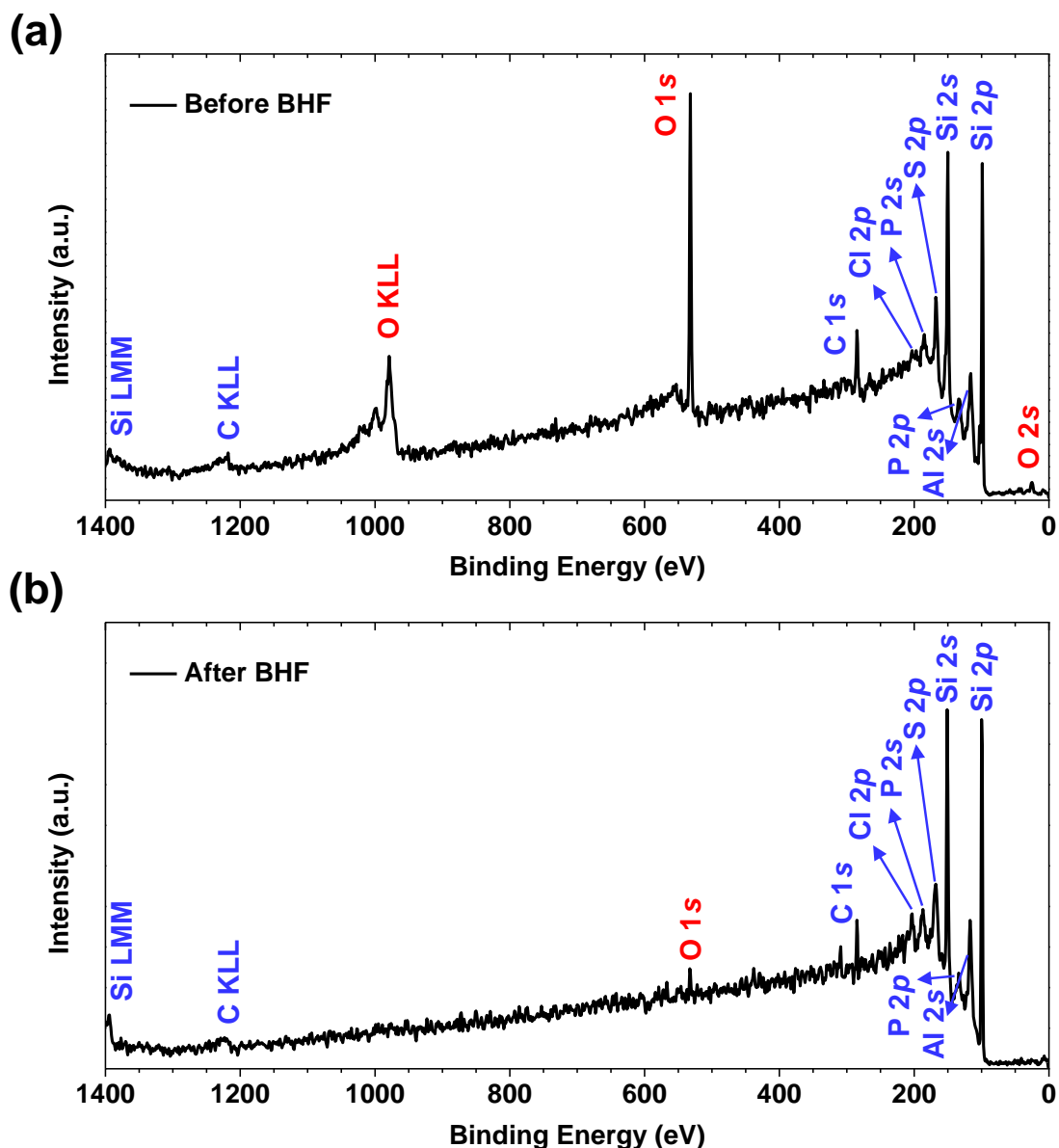


Figure A.2 Full-range XPS surface survey spectra of the RCA2-cleaned *n*-Si substrates. (a) Before BHF cleaning. (b) After BHF cleaning.

The contaminations on the interfacial oxide layer after cleaning were analyzed by full-range XPS surface surveys. BHF ( $\text{NH}_4\text{HF}_2:\text{NH}_4\text{F}:\text{H}_2\text{O} = 15:28:57$ ) was used to clean the *n*-Si surface again after the removal of the physical mask (Scotch tape). As shown in

## Appendix

---

Figure A.2, after BHF cleaning, the O peaks and the Si oxide peak almost disappeared because of the removal of the interfacial oxide layer. There are almost no Na 1s (around 1071 eV) or Cl 2p (around 200 eV) peaks, showing the effectiveness of RCA2 cleaning. After BHF cleaning, the peaks of Cl 2p, P 2s, S 2p, P 2p, and Al 2s still existed as compared with those in Figure A.2a, indicating that these contaminations are mainly from the storage of samples in air or the contaminations in XPS chamber.

## Publication List

### Peer-Reviewed Journal and Proceedings Paper:

1. **Y. Qian** et al., Photovoltaic device applications of one-dimensional van der Waals heterostructures, *in preparation*.
2. **Y. Qian**, I. Jeon, Y.-L. Ho, C. Lee, S. Jeong, C. Delacou, A. Anisimov, E. I. Kaupinnen, Y. Matsuo, Y. Kang, H.-S. Lee, D. Kim, J. J. Delaunay, S. Maruyama, Multifunctional effect of *p*-doping, anti-reflection, and encapsulation by polymeric acid for high efficiency and stable carbon nanotube-based silicon solar cells, *submitted*.
3. **Y. Qian**, H. An, T. Inoue, S. Chiashi, R. Xiang, S. Maruyama, A comparison between reduced and intentionally oxidized metal catalysts for growth of single-walled carbon nanotubes, *Physica Status Solidi (B)*, 255(12), 1800187, (2018).
4. **Y. Qian**, I. Yamada, S. Warisawa, Finger motion detection for human activities recognition using single sEMG channel, *Proceedings of 7th International Conference on Health Informatics (HEALTHINF2014)*, pp60-67, (2014).
5. K. Cui, **Y. Qian**, I. Jeon, A. Anisimov, Y. Matsuo, E. I. Kauppinen, S. Maruyama, Stable and scalable redox functionalization of single-walled carbon nanotube transparent conductive films for high-efficiency solar cells, *Advanced Energy Materials*, 7(18), pp1700449-1700456, (2017).
6. I. Jeon, **Y. Qian**, S. Nakao, D. Ogawa, R. Xiang, T. Inoue, S. Chiashi, T. Hasegawa, S. Maruyama, Y. Matsuo, Room temperature-processed inverted organic solar cells

## Publication List

---

- using high working-pressure-sputtered ZnO film, *Journal of Materials Chemistry A*, 4(48), pp18763-18768, (2016).
7. R. Xiang, T. Inoue, Y. Zheng, A. Kumamoto, Y. Qian, Y. Sato, M. Liu, D. Gokhale, J. Guo, K. Hisama, S. Yotsumoto, T. Ogamoto, H. Arai, Y. Kobayashi, H. Zhang, B. Hou, A. Anisimov, Y. Miyata, S. Okada, S. Chiashi, Y. Li, J. Kong, E. I. Kauppinen, Y. Ikuhara, K. Suenaga, S. Maruyama, One-dimensional van der Waals heterostructures, *arXiv: 1807.06154*, (2019).
  8. Y. Feng, T. Inoue, M. Watanabe, S. Yoshida, Y. Qian, R. Xiang, E. I. Kauppinen, S. Chiashi, S. Maruyama, Measurement of in-plane sheet thermal conductance of single-walled carbon nanotube thin films by steady-state infrared thermography, *Japanese Journal of Applied Physics*, 57(7), pp075101-1-075101-6, (2018).
  9. H. An, A. Kumamoto, H. Takezaki, S. Ohyama, Y. Qian, T. Inoue, Y. Ikuhara, S. Chiashi, R. Xiang, S. Maruyama, Chirality specific and spatially uniform synthesis of single-walled carbon nanotubes from sputtered Co-W bimetallic catalyst, *Nanoscale*, 8(30), pp14523-14529, (2016).
  10. I. Jeon, R. Sakai, S. Seo, G. E. Morse, H. Ueno, T. Nakagawa, Y. Qian, S. Maruyama, Y. Matuso, Engineering high-performance and air-stable PBTZT-stat-BDTT-8:PC<sub>61</sub>BM/PC<sub>71</sub>BM organic solar cells, *Journal of Materials Chemistry A*, 6(14), pp5746-5751, (2018).

**Conference Contributions:**

**Oral (as the presenter):**

1. **Y. Qian**, et al., 2017 International Workshop on "Materials for Future", Melbourne, Australia, oral, (Aug 2017).
2. **Y. Qian**, et al., Bulletin of the American Physical Society, APS March Meeting, Baltimore, USA, oral, (Mar 2016).

**Poster (as the presenter):**

3. **Y. Qian**, et al., 8th International Conference on Nanoscience and Technology (ChinaNANO2019), Beijing, China, poster, (Aug 2019).
4. **Y. Qian**, et al., 20th International Conference on the Science and Application of Nanotubes and Low-dimensional Materials (NT19), Würzburg, Germany, poster, (Jul 2019).
5. **Y. Qian**, et al., 9th A3 Symposium on Emerging Materials: Nanomaterials for Electronics, Energy, and Environment, Kyoto, Japan, poster, (Oct 2018).
6. **Y. Qian**, et al., 19th International Conference on the Science and Application of Nanotubes and Low-dimensional Materials (NT18), Beijing, China, poster, (Jul 2018).
7. **Y. Qian**, et al., 32nd International Winterschool on Electronic Properties of Novel Materials, Kirchberg in Tirol, Austria, poster, (Mar 2018).
8. **Y. Qian**, et al., The 50th Fullerenes-Nanotubes-Graphene General Symposium (FNTG50), Tokyo, Japan, poster, (Feb 2016).
9. **Y. Qian**, et al., The 49th Fullerenes-Nanotubes-Graphene General Symposium (FNTG49), Kitakyusyu, Japan, poster, (Sep 2015).

## Publication List

---

10. Y. Qian, et al., 1st SNU-UTokyo Workshop on Mechanical and Aerospace Engineering, Seoul National University, Seoul, South Korea, poster, (Mar 2015).

# Acknowledgments

First, I would like to express my great appreciation to my supervisor, Prof. Maruyama, his vision and knowledge are always inspiring me during the whole research period. Without him, I would not have had such a wonderful research life in the society of low-dimensional nanomaterials. Also, thanks to the profound insights and suggestions from my Ph.D. defense committee professors of Prof. Daiguji, Prof. Sugiyama, Prof. Matsuo, and Prof. Chiashi, my research outcome has been improved to a better form. Part of Chapter 1 and Chapter 5 in this dissertation is integrated with the Side Paper submitted for the partial fulfillment of the requirements for the graduation from Global Leader Program for Social Design and Management (GSDM), which showcases the bridge among natural science, engineering, and social science. I would like to thank Prof. Okubo and Prof. Suzukan for their kind supervision of the Side Paper.

Second, I would like to thank Prof. Xiang, Prof. Jeon, and Prof. Inoue, for their support of my research. Prof. Xiang helped me with the 1D nanotube growth and TEM characterizations. Prof. Jeon helped me with the solar cell research. Prof. Inoue is always there kindly helping me with experiments.

Third, I would like to thank Watanabe-san, Terao-san, and Shimada-san. Watanabe-san helped me a lot about purchasing suppliers, and he is so enthusiastic a person that I always get cheered up by him. Terao-san and Shimada-san helped me greatly about the documentaries.

For the other laboratory members and my collaborators, both of you are so wonderful

## Acknowledgments

---

people that gave me an impressive life in academia. I enjoyed discussing with you, collaborating with you, having fun with you, both on-campus and off-campus.

At the beginning of my Ph.D. course, I stayed at Prof. Jing Kong's group at MIT for half a year with the financial support from GSDM, which has been a great memory of me. I happened to accompany Prof. Millie Dresselhaus' last half-year, her words of "Keep Working" is still motivating me to fight in my life. Also, I got to know many friends at MIT and Boston, and I would like to thank all of them for helping me and shaping me.

Overall, I would like to thank my friends for helping me and supporting me all the time. Especially I would like to thank Mr. Pan Hu, who was a master's student here, without him, I would not have realized the broad business world outside academia.

Also, thank GSDM and Japan Society for the Promotion of Science (JSPS) for the financial support and research grant.

Last and foremost, I would like to express my utmost gratitude to my parents, for their endless and selfless support of my whole life. This dissertation dedicated to my parents, and the memory of our lovely dog, Xixi.